Università degli Studi dell' Insubria

Dipartimento di Scienza e Alta Tecnologia

PHD THESIS

Analogue Hawking radiation in Bose-Einstein Condensates

Author:
Manuele Tettamanti

Supervisors:
Prof. Alberto Parola
Prof. Sergio Cacciatori

Como, 25th February 2019

Contents

Introduction **4**

1 Black Holes **8**
- 1.1 A little bit of history . . . 9
- 1.2 The Schwarzschild metric . . . 13
- 1.3 Quantum field theory in curved spacetimes . . . 15
  - 1.3.1 The Unruh effect . . . 19
  - 1.3.2 Hawking radiation . . . 24
- 1.4 Sonic black holes and analogue spacetimes . . . 30
  - 1.4.1 The analogue gravity paradigm . . . 37
  - 1.4.2 The Schwarzschild geometry as an example of the analogy 43

2 Bose-Einstein condensates **46**
- 2.1 A new phase of matter . . . 47
- 2.2 Ideal Bose gases . . . 50
- 2.3 Dilute gases and the Bogoliubov approach . . . 55
- 2.4 The Gross-Pitaevskii equation . . . 59
  - 2.4.1 Trapped gases in harmonic potentials . . . 61
  - 2.4.2 Quantization and elementary excitations . . . 64
- 2.5 The Tonks-Girardeau limit . . . 67
- 2.6 The acoustic metric in the case of BECs . . . 70
- 2.7 Analogue Hawking radiation from BECs . . . 76
  - 2.7.1 Dispersion relations and mode analysis . . . 77
  - 2.7.2 The density correlation method . . . 80
  - 2.7.3 Black hole lasers . . . 81

3 The 2014 Technion experiment **83**
- 3.1 The experiment: set-up and results . . . 84
- 3.2 Our first numerical simulations . . . 90
  - 3.2.1 The theoretical model . . . 90
  - 3.2.2 Velocities and density profiles . . . 95
  - 3.2.3 The quest for the seed and the correlation pattern . . . 99
  - 3.2.4 The conclusions (maybe) . . . 102
- 3.3 Controversy on the interpretation of the results . . . 103

- 3.3.1 Further works from other groups . . . 103
- 3.3.2 The path toward a unique picture . . . 108
- 3.4 Our latest numerical results . . . 114
  - 3.4.1 The roles of interactions . . . 116
  - 3.4.2 New interpretation of the experimental data . . . 118
  - 3.4.3 Conclusions . . . 123

4 The Tonks-Girardeau gas model 124
- 4.1 A microscopic description of the analogue Hawking radiation . . . 125
- 4.2 The model . . . 126
  - 4.2.1 The case of a step potential . . . 128
  - 4.2.2 The case of a repulsive barrier . . . 134
- 4.3 Analogue Hawking radiation . . . 140
  - 4.3.1 The case of a step potential . . . 142
  - 4.3.2 The case of a repulsive barrier . . . 145
- 4.4 Semiclassical analysis . . . 149
  - 4.4.1 The stationary configuration . . . 151
  - 4.4.2 The excitation spectrum . . . 155
  - 4.4.3 Analogue Hawking radiation . . . 158
- 4.5 Experimental configurations . . . 165
- 4.6 Conclusions . . . 167

5 Future possibilities 169
- 5.1 Including zero-point quantum fluctuations . . . 170
- 5.2 The black-hole laser effect: realistic experimental apparatuses . . . 171
- 5.3 The TG gas model: future directions worth exploring . . . 172

Conclusions 173

Appendices 174

A The role of the axial confinement 175

B Step potential eigenstates 189

C Exact results for a potential barrier 191

D The density profile for a potential barrier 192

Bibliography 194

List of Abbreviations

BCR	**B**ogoliubov-**C**erenkov **R**adiation
BEC	**B**ose-**E**instein **C**ondensate
BH	**B**lack **H**ole
CMB	**C**osmic **M**icrowave **B**ackground
DCE	**D**ynamical **C**asimir **E**ffect
DSW	**D**ispersive **S**hock **W**ave
GPE	**G**ross-**P**itaevskii **E**quation
GR	**G**eneral **R**elativity
HCB	**H**ard-**C**ore **B**ose
IH	**I**nner **H**orizon
NPSE	**N**on-**P**olynomial **S**chrödinger **E**quation
QFT	**Q**uantum **F**ield **T**heory
QM	**Q**uantum **M**echanics
SR	**S**pecial **R**elativity
TF	**T**homas-**F**ermi
TG	**T**onks-**G**irardeau
TWA	**T**runcated **W**igner **A**pproximation
WH	**W**hite **H**ole

e.g.	**e**xempli **g**ratia (“for example”)
h.c.	**h**ermitian **c**onjugate
i.e.	**i**d **e**st (“that is”)
w.r.t.	**w**ith **r**espect **t**o

Introduction

Analogies play a fundamental role in the development of thoughts and ideas and they are used very profusely across a variety of different disciplines. They are a key ingredient in the field of heuristics but their presence is so vast that, according to Leary, "all knowledge is ultimately rooted in metaphorical (or analogical) modes of perception and thought" [1]. Leaving behind the philosophical discussion on the idea of "analogy" as it is an intricate matter (Mill wrote: "there is no word which is used more loosely, or in more variety of senses, than *Analogy*" [2]), I would like to linger for a moment on the role that analogies have played (and still play) in the scientific context.

Analogies are spread throughout the world of physics and mathematics (see, for example, [3, 4]) and have very different purposes and meanings; sometimes they are a mere tool to help understanding the dynamics of a physical system but they do not highlight any particular connection between them (it is the case, for example, of the analogy between electrical circuits and flowing water), while other times they hide a deeper mathematical/physical symmetry: already in the second century B.C. the Greek Chrysippus compared sound and water waves by means of an analogy while Huygens, in 1678, made a parallel between light and sound, in the attempt to prove his claim of the wave-nature of light [5]; in both these cases an analogy between physical phenomena led to a physical symmetry: water waves, sound and classical light, in fact, are all waves (what is known as, respectively, number of crests in a interval, pitch and color all refer to the same physical quantity, i.e. frequency). Other very famous cases in which an analogy between ideas uncovered physical symmetries are A. Einstein's theories of relativity; the theory of Special Relativity (SR) was formulated in 1905 starting from the idea that *the laws of physics* (that is, electromagnetism included) are exactly the same for all the inertial observers (in analogy with the Galilean relativity which stated that *the laws of mechanics* are exactly the same for all the inertial observers): a simple analogy led to a strong metaphysical principle which solved many open problems and shed light on a deep symmetry of the laws in nature [6]. On the other hand, the fundamental pillar of the theory of General Relativity (GR) is the so-called *equivalence principle*, which was formulated starting from the observation that there is an analogy between the motion of masses in a gravitational field and that of a free body in a non-inertial reference frame [7].

Sometimes, though, analogies are proved to be only partially correct or completely wrong; the former is the case, for example, of the theory of atomic structure: Rutherford compared the electrons to the planets of our system, orbiting the nucleus on well-defined circumferences, but this notion became a mere mathematical tool with Bohr and the advent of Quantum Mechanics (QM). Thus, the analogy provided a useful mathematical insight but did not define a real physical symmetry. Instead, a famous example for a misleading use of an analogy is the case of the conclusions that Maxwell drew about properties of light in 1856, in the paper *On Faraday's Lines of Force*: in this work, in fact, the father of electromagnetism explicitly asserted that his results came from "particular physical analogies" between light and and particles' trajectories [8] but his conclusions were proved wrong shortly after. Just like Maxwell, though, many times physicists admit explicitly a strong use (or abuse) of analogies; it is the case, for example, of Nobel laureate S. L. Glashow, who said, about his theory of electroweak interaction [9]: "I was lead to the group SU(2) × U(1) *by analogy* with the approximate isospin-hypercharge group which characterizes strong interactions [...] Part of the motivation for introducing a fourth quark was based on our mistaken notion of hadronic spectroscopy. But *we also wished to enforce an analogy* between the weak leptonic current and the weak hadronic current."

These few examples should already convey the idea that analogies were fundamental blocks in the development of physics, helping building theories and uncovering underling symmetries of our world. Their importance is so acknowledged that Johannes Kepler wrote: "and I cherish more than anything else the Analogies, my most trustworthy masters. They know all the secrets of Nature, and they ought to be least neglected in Geometry" [10];

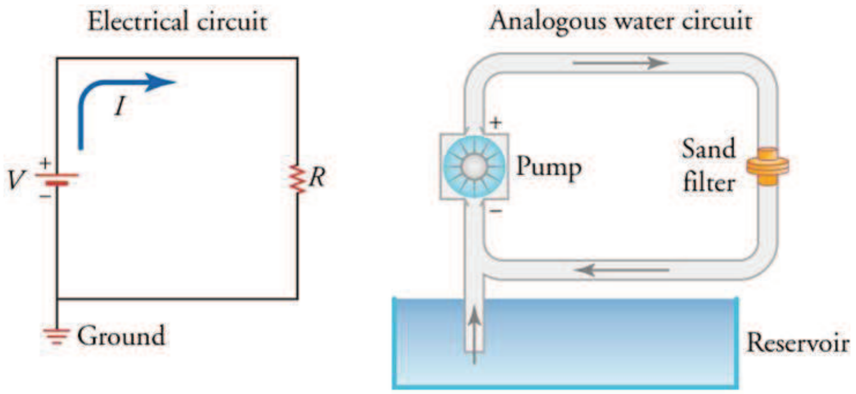

Figure 1: A simple drawing showing the analogous treatment used to compare electrical circuits to water flows.

This Thesis develops in the field of **analogue gravity**, a branch of physics which relies on a specific correspondence (or *analogy*) that exists between fluid dynamics and curved spacetimes; thanks to that, effects which are hard to study in the gravitational context are investigated in the realm of hydrodynamics with the hope that the consequent results could be transferred back to the cosmological domain and give us better insights in the gravitational context. An analogy (which stands rigorous from a mathematical point of view) is the key to this field and it allows us to shift the framework, creating a map between separated physical realms and opening up a broad horizon of new possibilities. Differently from most of the examples listed above, this analogy may not point to any deep symmetry in the laws of nature but it creates the requirements for a challenging and thrilling field of research which spans from Newton's laws to Quantum Mechanics, from flat spacetimes to curved geometries, from black holes to ultra-cold atoms, laser pulses and classical fluids. Grasping the basic notions of this field is not a simple journey, nevertheless I found it extremely stimulating and fascinating. In this Thesis, I will try to introduce the reader to the realm of analogue gravity and to the concepts of Bose-Einstein condensation, Hawking radiation and its analogue counterpart; then I will describe the (little) contributions we tried to give to the theoretical framework of this researching area and, finally, I will outline possible future directions of interest.

Enjoy!

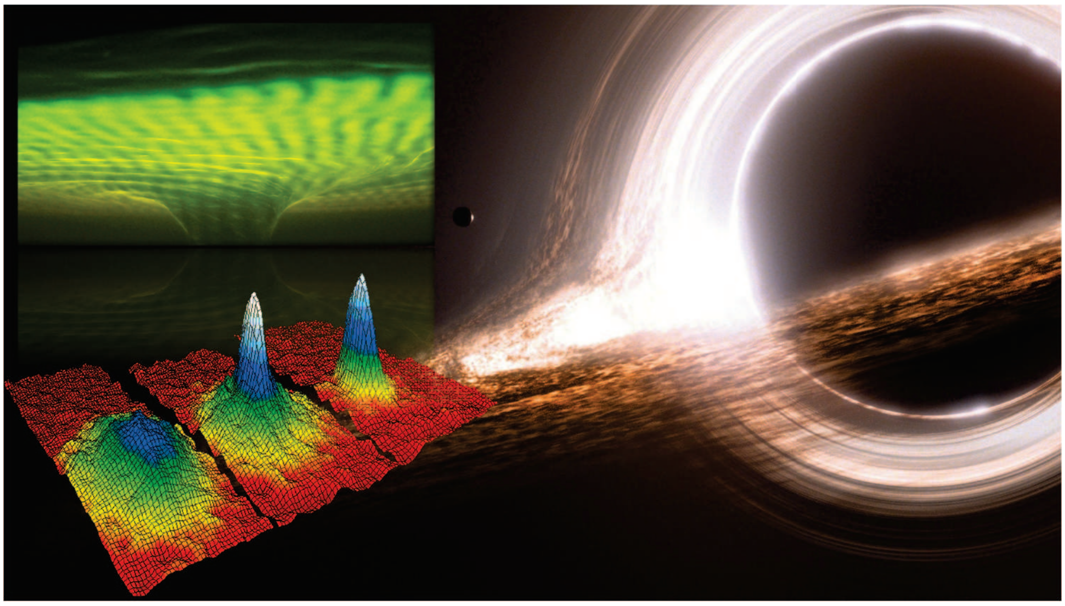

Figure 2: The figure overlaps a representation of a black hole from the movie *Interstellar* (2014), a picture of a sonic black hole taken at the university of Nottingham in the spring of 2017 and the first observation of Bose-Einstein condensation by the JILA group of NIST-University of Colorado at Boulder, in 1995.

Structure of the Thesis

This Thesis consists of five Chapters, whose contents are briefly summarized here.

The purpose of Chapter 1 and 2 is to overview the results and the equations needed in order to understand the work in this Thesis. The concept of analogue Hawking radiation in Bose-Einstein condensates spans over different areas of physics and therefore, in order to fully understand it, notions from very different fields are needed. In the years I have been working in this area I realized that a lot of times confusion and misunderstandings rise from a missing piece of knowledge in one of the two areas we deal with (namely, gravity and quantum hydrodynamics). For this reason, I wanted to describe all the results in details, building everything from scratch, so that any person with some basis in physics and no textbook in hand (maybe a couple) can follow the reasoning throughout this Thesis. Chapter 1 and 2 deal with the concepts of black holes, Bose-Einstein condensates and analogue gravity and they are structured so that any of the Sections can be skipped without losing the stream of thoughts, so the reader expert in any of those may very well do so. Also, the reader who would not want to lose too much time on the introduction may skip to Section 2.7: in a few pages we re-visit the fundamental steps done previously before entering the details of our work.

Chapter 3 and 4 describe the details of our work. In the past years, we have developed two directions of research, both aimed at the characterization of the analogue Hawking radiation in Bose-Einstein condensates. One side of our work had the purpose of investigating the results obtained in recent experiments apt to the detection of the analogue Hawking radiation in a quantum gas. Our results are very important in the description of the phenomena and give insights on how to develop future experiments. This is the content of Chapter 3. The other side of our work aimed at the characterization of this effect from a theoretical point of view by means of an innovative approach, which allows for a much deeper and more detailed description of the radiation and helps shine new light on this effect. This is the content of Chapter 4.

In Chapter 5 we briefly discuss the possible developments of our studying, highlighting the missing pieces of this field and suggesting possible ways to approach the existing problems.

Chapter 1

Black Holes

This Chapter will deal with black holes and the field of analogue gravity. In particular, Sections 1.1 and 1.2 will introduce the basic concepts concerning black holes while Section 1.3 will describe two effects (namely, the *Unruh effect* and the *Hawking effect*) which are usually related to black holes but whose applicability leaps over other areas of physics also. Then, in Section 1.4, we will introduce the basis of analogue gravity, building the general framework and describing the main concepts.

1.1 A little bit of history

Gravity is one of the four fundamental forces of physics and it was the first one to be discovered; already in 1687, English mathematician Isaac Newton published the *Principia*, which contained the hypothesis that “the forces which keep the planets in their orbs must [be] reciprocally as the squares of their distances from the centres about which they revolve” [11]; it was his famous *law of universal gravitation*, which described the motion of any mass in respect to another, from the famous apple falling from a tree to the large scales of the universe. Gravity has been widely studied since then and many more contributions were given during the years, the most important being Einstein’s theory of General Relativity, in 1916; ironically enough, from a certain point of view, gravity stands nowadays as the least understood interaction, as a reconciliation of GR with Quantum Mechanics is yet to be found. This will play a fundamental role in the description of the Hawking effect but we will enter these details in the following Chapters.

Going back to classical mechanics, using Newton’s law of gravitation we can evaluate a quantity called *escape velocity* which is the minimum speed needed for a free object to escape from the gravitational influence of a massive body. Considering a spherically symmetric body such as a star or planet, the escape velocity can be easily derived by evaluating the kinetic energy and the gravitational energy of the object; by doing that, we obtain:

$$v_e = \sqrt{\frac{2GM}{r}}\,, \tag{1.1}$$

where M and r are, respectively, the mass and the radius of our star/planet and G is Newton’s constant. Now, one in principle could ask: what if the velocity calculated above was the speed of light (which, according to SR, is the speed of causality and thus the limit velocity for our reality)? [1] Then we would have theorized an object whose gravitational pull is so intense that not even light can escape. That is, we would have just theorized what is now known as a (classical) **black hole**[2].

---

[1] Note that the radius of massive body whose escape velocity is the speed of light ($v_e = c$) is known as the Schwarzschild radius r_S of the body. We will come back to this concept later.

[2] There is an important difference between this definition of black hole and the one used in GR. Here, in fact, it is not strictly correct to say that nothing can escape as whatever object tries to leave such a gravitational field is destined to fall back, but only after reaching an arbitrary large distance. At that point, if some engine was turned on, the object could escape, as v_e diminishes with the distance. In GR, on the other hand, the horizon can be crossed only in one way and, once passed, no object can get far from it, not even a little. In any case, there is not a general definition of a black hole. The one mentioned here - based on the notion of *trapped regions* - is the one usually adopted by physicists but for a more rigorous mathematical treatment of black holes and horizons see [12].

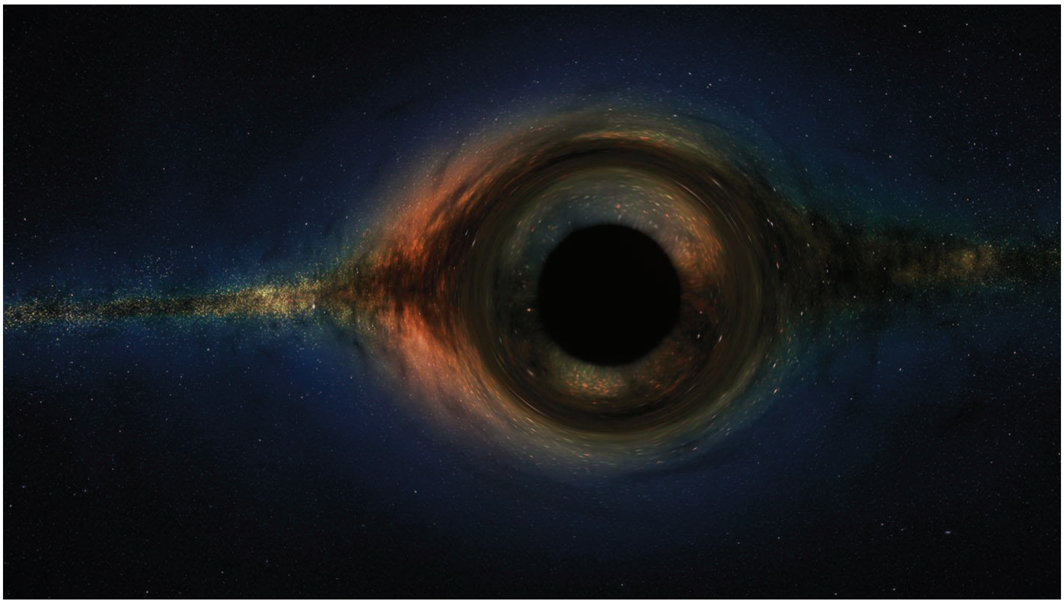

Figure 1.1: An artist's impression of a black hole.

This way of describing a black hole is exactly the approach used by a contemporary of Newton, the English natural philosopher and clergyman John Michell who wrote, in a letter to the Royal Society [13] in 1783: "If there should really exist in nature any bodies [...] whose diameters are more than 500 times the diameter of the sun, [...] their light could not arrive at us; [...] of the existence of bodies under either of these circumstances, we could have no information from sight; " [3]. Because of this peculiar characteristic, the astronomer called these objects "dark stars". A similar idea was investigated a few years later by the French mathematician and astronomer Pierre-Simon Laplace but due to the fact that there was no evidence for the existence of such objects and the concept of "trapped light" was rather bizarre at that time (light was not considered to be influenced by gravity) the idea of dark stars remained a theoretical artefact until the 20th century.

In 1916, a few months after the publication of GR, German physicist Karl Schwarzschild applied Einstein's equation to a spherical symmetric object and, for the first time, the notion of a black hole re-appeared again. The solution, though, predicted also the existence of singularities, which made scientists wonder about the validity of the calculations. The idea was not considered until 1939, when the American physicist Robert Oppenheimer, together with his student Hartland Snyder, demonstrated that a sufficiently large object,

---

[3] It is very interesting to note that the text continues as follows: "yet, if any other luminous bodies should happen to revolve about them we might still perhaps from the motions of these revolving bodies infer the existence of the central ones with some degree of probability"; that is, using Newton's law of gravitation we could infer the existence of a black hole in a certain region of space, which is a widely used technique in astrophysics and is exactly how *SgrA**, the supermassive black hole at the center of our galaxy, was discovered!

such as a really massive star, can collapse under the pull of its own gravity in a runaway process; all the mass then shrinks into an infinitesimally small point of infinite density, called a singularity. This collapse created a region of space so severely warped by gravity that not even light could escape from it [14]. The idea of black hole was emerging again. Unfortunately, World War II brought the brightest scientific minds into projects to develop the atomic bomb and for years the idea languished. It was only around 1959, when Hawking began his undergraduate studies at the University of Oxford, that physicists started to take the idea seriously. It was examined closely by John Wheeler at Princeton University in New Jersey (it was him who, during a conference, gave black holes their name), Roger Penrose in the U.K., and Yakov Zel'dovich in the Soviet Union; the observation, in 1964, of the strong X-rays source *Cygnus X-1* and the general consensus on the identification of the object as a black hole, gave the final push to the matter: black holes were real.

In 1966, after completing his degree in physics, S. W. Hawking started a Ph.D. at the University of Cambridge, under the supervision of cosmologist Denis Sciama. His attention was captured by this resurgence of interest in General Relativity and black holes. Hawking soon realised that a black hole can only increase, never decrease, in size [12]. This may seem obvious: since nothing that gets too close can escape, a black hole can only ever swallow more matter and thus gain mass; the mass of a black hole, in turn, determines its size, measured as the radius of the event horizon, the point beyond which nothing can escape. This boundary will creep inexorably outwards like the skin of an inflating balloon (this results is now known has "Hawking's area theorem"). What is not so obvious is that this theorem holds also for the merging of two black holes; Hawking, in fact, proved that when two black holes merge, the surface area of the final black hole cannot be smaller than the sum of the two single ones (this is not the case, for example, of two water bubbles merging). But Hawking went further and argued that the event horizon's ever-expanding surface area was analogous to another quantity that, according to physics, could only grow: that is, entropy. He pointed out that these two laws - the increasing surface area of a black hole and the increasing entropy of an isolated system - were oddly similar and when Hawking announced his result at the end of 1970, a young physicist named Jacob Bekenstein made a bold proposal: what if this was not just an analogy? Bekenstein suggested that the surface area of a black hole event horizon might be a measure of the black-hole entropy [15]; the result laid the first piece of connection between the realm of black holes with that of Thermodynamics and stimulated further research [16].

Both Bekenstein and Hawking soon realized that something about their results seemed wrong: if an object has entropy, it must also have a temperature and if it has a temperature, then it must radiate energy; yet nothing can get out of a black hole by definition and, because of that, scientist commonly associated a null temperature to these objects [17]. For this reason, most physicists - including Hawking - thought that the proposal about black-hole entropy made no sense and even Bekenstein himself stated that the black hole apparent temperature could not be “real” since it lead to a paradox. But in 1974 Hawking achieved another shocking result, demonstrating that black hole are not entirely black, as they emit radiation and thus could, in principle, evaporate. This is the famous Hawking radiation [18, 19]. The prediction completed the thermodynamical treatment of black holes and it remarkably included QM in the process, resulting in one of the most astonishing achievement of Hawking’s career, as a full reconciliation of GR and QM is still lacking nowadays.

Hawking radiation provided the final piece to a theoretical framework today known as “black-hole thermodynamics” [20, 21], a field that brings together disparate areas of gravity, quantum theory and thermodynamics and which has been a fervent direction of research since then, to which many physicist have contributed. Hawking’s result, above all, stands as the fundamental piece of the picture and we will describe this effect in detail in the following Chapters, as it represents the main subject to this Thesis; due to his importance, many physicist have studied this phenomenon in the past years [22–27] but the debate on the existence of this effect is far from being over: first of all, Hawking radiation opens several issues on the theoretical side (it is worth citing, above all, the information paradox [28] and the Trans-planckian problem [29, 30]); secondly, as of today, we still lack an undisputed, clear evidence of the existence of this radiation. And this is exactly where analogue gravity comes into play.

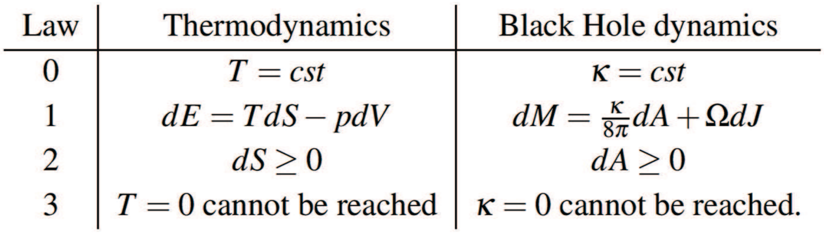

Law	Thermodynamics	Black Hole dynamics
0	$T = cst$	$\kappa = cst$
1	$dE = TdS - pdV$	$dM = \frac{\kappa}{8\pi} dA + \Omega dJ$
2	$dS \geq 0$	$dA \geq 0$
3	$T = 0$ cannot be reached	$\kappa = 0$ cannot be reached.

Figure 1.2: The table summarizes the laws of black-hole thermodynamics. The symbols represent: temperature (T), energy (E), entropy (S), pressure (p), volume (V), surface gravity (κ), mass (M), surface area (A), angular velocity (Ω) and angular momentum (J). For a detailed treatment see [31, 32].

1.2 The Schwarzschild metric

Before entering the details about Hawking radiation and analogue gravity, it is worth deriving some well-known results about black holes, as they will be useful in the following. In particular, we will describe the first real mathematical solution which showed the presence of a event horizon and of a singularity: the Schwarzschild black hole.

As already mentioned, the same year GR was introduced, Karl Schwarzschild applied Einstein's field equations to the case of a spherically-symmetric metric in vacuum and he calculated the exact solution, which is known as the *Schwarzschild metric* [33]; in coordinates (t_S, r, θ, ϕ) that takes the form:

$$ds^2 = \left(1 - \frac{r_S}{r}\right) c^2 dt_S^2 - \left(1 - \frac{r_S}{r}\right)^{-1} dr^2 - r^2 d\Omega^2 \,, \tag{1.2}$$

where $d\Omega^2 = d\theta^2 + \sin^2\theta d\phi^2$ is the angular line element, t_S is the Schwarzschild time coordinate and $r_S = \frac{2GM}{c^2}$ is the already-mentioned Schwarzschild radius[4]. This solution describes the spacetime exterior of slowly rotating astronomical objects, including stars and planets. Asymptotically away from the object, i.e. as $r_S/r \to 0$, the Schwarzschild metric approaches the flat Minkowski metric and the coordinates (t_S, r, θ, ϕ) correspond to the usual spherical coordinates of flat spacetime.

However, the Schwarzschild solution appears to have singularities at $r = 0$ and $r = r_S$, as some of the metric components diverge in these points. Since the Schwarzschild metric is only expected to be valid in vacuum, i.e. for radii larger than the radius of the gravitating body, there is no problem as long as this radius is grater than r_S; these singularities are though relevant only when the entirety of the mass is confined to a radius smaller than r_S, in which case it will inevitably collapse to a single point of infinite density at $r = 0$. These objects are black holes.

The point $r = 0$ is a genuine singularity of the Schwarzschild spacetime [34] (and we shall not be talk about it here) while it is the surface $r = r_S$, the **event horizon**, which is of interest to us. It stands as the surface defining two almost-disconnected regions of spacetime and crossing it has the effect of switching the role of time and space (see the sign in Eq. (1.2)). This apparent singularity ($r = r_S$ is not an actual singularity as it will be more clear in the following) will play a key part in the physics of the Hawking effect and of analogue gravity.

In order to better understand the role of the event horizon, let us briefly review its effects by examining light trajectories, or null curves, by putting $ds^2 = 0$. For simplicity, we shall consider only radial trajectories so we also set $d\Omega^2 = 0$. This leaves us with a differential equation for the radial null curves:

$$\frac{dt_S}{dr} = \pm\frac{1}{c}\left(1 - \frac{r_S}{r}\right)^{-1} \,, \tag{1.3}$$

---

[4] Please note that from now on the signature is taken to be $(+, -, -, -)$.

respectively representing outgoing (+) and incoming (−) waves. Far from the Schwarzschild radius, where $r \gg r_S$, we have that $|\frac{dt_S}{dr}| \rightarrow \frac{1}{c}$, so that light behaves just as it does in flat spacetime. However, as we approach the Schwarzschild radius, $|\frac{dt_S}{dr}|$ diverges in such a way that light takes longer and longer to travel any distance and, especially, if travelling towards the event horizon, can never reach it in a finite time t_S.

This awkward behaviour suggests that Schwarzschild coordinates may not be suited for describing the surface $r = r_S$. To see that this is the case, one must look at coordinate-invariant quantities, that indeed possesses a regular behaviour on r_S. This shows that $r = r_S$ is only a coordinate singularity, which has arisen due to a bad choice of the coordinates. The usual way to treat this problem is to introduce Kruskal-Szekeres [34] coordinates which cover the entire spacetime manifold of the maximally-extended Schwarzschild solution, but we will not enter the details of that method here. We will come back to Schwarzschild solution in the treatment of the Hawking effect and in the analogue gravity paradigm but, before that, we need to first introduce another topic.

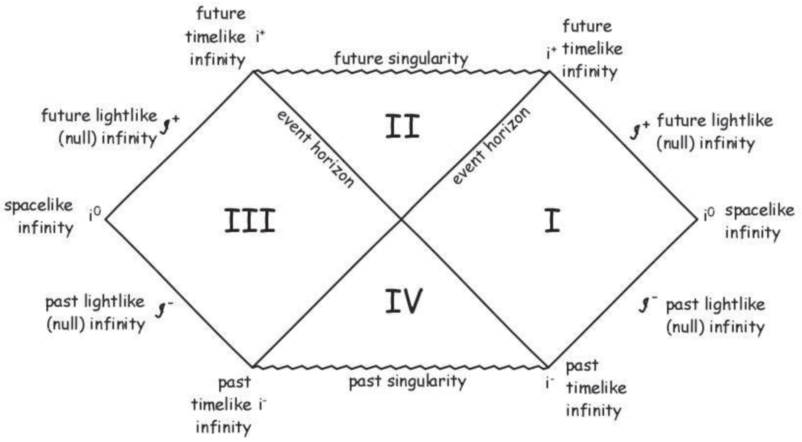

Figure 1.3: Penrose diagram of the maximally extended Schwarzschild solution. Penrose diagrams are frequently used in GR to illustrate the causal structure of spacetimes: a coordinate transformation is chosen such that the entire infinite spacetime is transformed into a diagram of finite size, as the picture shows. For a much more detailed description of Penrose diagrams see [35].

1.3 Quantum field theory in curved spacetimes

Let us consider a free massive scalar field $\phi(x)$ satisfying the Klein-Gordon equation in the Minkowski spacetime[5]

$$\Box\phi + m^2\phi = 0\,, \tag{1.4}$$

where $\Box = \partial^\mu\partial_\mu$. Note that, starting from the action of the system, we immediately obtain the Lagrangian $\mathcal{L}$ and, from that, we can define the conjugate momentum as $\pi = \frac{\partial\mathcal{L}}{\partial\partial_0\phi}$. Now, a set of solutions of Eq. (1.4) is given by plane waves[6]:

$$f = f_0 e^{-ik_\mu x^\mu}\,, \tag{1.5}$$

with $k_\mu = (\omega, -k_i)$, where ω is the frequency and k^i the wave vector. For the rest of this Section we will denote the wave vector k^i with k, for the sake of simplicity. Replacing the solution Eq. (1.5) into the Klein-Gordon equation immediately gives us the dispersion relation, which is

$$\omega^2 = k^2 + m^2\,, \tag{1.6}$$

with $k^2 = \sum_i k^i k^i$; this relation means that the wave vector k completely determines the frequency ω, up to a sign. The usual way to proceed is to set ω to be a positive number and to *define* positive and negative frequency modes in the following way: modes $\{f_k\}$ such that

$$\partial_t f_k = -i\omega f_k\,, \quad \text{with} \quad \omega > 0 \tag{1.7}$$

are called positive frequency modes; similarly, modes $\{f_k^*\}$ such that

$$\partial_t f_k^* = i\omega f_k^*\,, \quad \text{with} \quad \omega > 0 \tag{1.8}$$

are called negative frequency modes, even though $\omega > 0$ always. The next step in classical field theory is to define an inner product between two sets of solutions (f, g) and to use it to normalize the plane wave solutions (that is, to find the value of f_0 in Eq. (1.5)). This way the set of solutions (1.5) forms a complete orthonormal set of modes for the Klein-Gordon equation. That is, the set

$$f_k = \frac{1}{(2\pi)^{3/2}}\frac{1}{\sqrt{2\omega}}e^{-ik_\mu x^\mu}\,, \tag{1.9}$$

with normalization relations

$$(f_k, f_{k'}) = \delta(k-k'), \quad (f_k, f^*_{k'}) = 0, \quad (f^*_k, f^*_{k'}) = -\delta(k-k'), \tag{1.10}$$

is a basis for our problem and thus any classical, real field configuration $\phi(x)$ that is a solution to the Klein-Gordon equation (1.4) can be expanded in

---

[5] For the rest of this Section we will set $\hbar = 1$ and $c = 1$.

[6] By convention, Greek indices run from 0-3, while Roman indices run from 1-3.

terms of the modes $\{f_k, f_k^*\}$, i.e., in a superposition of positive and negative frequencies. In formulas:

$$\phi(x) = \int d^3k\,(a_k f_k + a_k^* f_k^*) = \frac{1}{(2\pi)^{3/2}} \int \frac{1}{\sqrt{2\omega_k}} (a_k e^{i(\mathbf{k}\cdot\mathbf{x}-\omega_k t)} + a_k^* e^{i(-\mathbf{k}\cdot\mathbf{x}+\omega_k t)}) \tag{1.11}$$

or, for the sake of clarity,

$$\phi(x) = \phi^+(x) + \phi^-(x)\,. \tag{1.12}$$

We wanted to work out the details of the general problem of classical fields because that will be useful in understanding the concepts of Quantum Field Theory (QFT) and what issues one encounters when trying to generalize this formalism to the case of curved spacetimes (which is the case of the Hawking effect).

Let us proceed by quantizing our theory following the *canonical quantization* approach; in the same way as the quantum harmonic oscillator is introduced starting from the classical one [36], we quantize our theory by promoting the classical fields to operators acting on an Hilbert space and imposing the canonical commutation relation

$$[\phi(\mathbf{x}, t), \pi(\mathbf{y}, t)] = i\delta^3(\mathbf{x} - \mathbf{y})\,, \tag{1.13}$$

beyond the trivial ones, where π is the canonical momentum operator. This means that, after quantization, the classical field of Eq. (1.11) becomes the operator

$$\phi(x) = \int d^3k\,(a_k f_k + a_k^\dagger f_k^*) = \frac{1}{(2\pi)^{3/2}} \int \frac{d^3k}{\sqrt{2\omega_k}} (a_k e^{i(\mathbf{k}\cdot\mathbf{x}-\omega_k t)} + a_k^\dagger e^{i(-\mathbf{k}\cdot\mathbf{x}+\omega_k t)}) \tag{1.14}$$

where the terms which previously where the coefficients of the expansion are now creation and annihilation operators, with the relation

$$[a_k, a_{k'}^\dagger] = i\delta(k - k')\,, \tag{1.15}$$

which is a consequence of Eq. (1.13) and Eq. (1.11). The meaning of these operators is straightforward: they create (annihilate) a particle (anti-particle) in the k-th state. From the previous relations the standard Fock space can be constructed, starting from the vacuum state $|0\rangle$, which is defined to be such that

$$a_k\,|0\rangle = 0\,, \qquad \forall k \tag{1.16}$$

and it can be demonstrated that, in Minkowski spacetime, the vacuum state is unique; this is because Minkowski space-time is symmetric under the Poincaré group and this property holds for the vacuum state as well. On the other hand, in curved spacetime the Poincaré symmetry is lost, thus there is no preferred set of modes over which decomposing our scalar field [37]. In other words, **positive and negative frequencies have no invariant meaning in curved spacetimes**. This is the peculiarity of QFT in non-flat spacetimes and it is the ground base to the effects which we will describe in the following. In fact, let us consider quantum field theory on a curved background[7]; now, the curved-space version of the Klein-Gordon equation of motion (1.4) is

$$\Box_g \phi + m^2 \phi = 0\,, \tag{1.17}$$

where g_{ab} is the metric of the considered spacetime, $g \equiv det(g_{ab})$ and

$$\Box_g = \frac{1}{\sqrt{-g}} \partial_a [\sqrt{-g} g^{ab} \partial_b]\,. \tag{1.18}$$

Much in the same way as QFT, we can follow the procedure described above and find a complete set of solutions $\{u_k, u_k^*\}$ which are the generalization of the plane-wave solutions; the definition of an internal product allows us to have a complete orthonormal basis and thus any solution ϕ of the Klein-Gordon equation (1.17) can be written as

$$\phi = \sum_k (a_k u_k + a_k^\dagger u_k^*)\,, \tag{1.19}$$

where we have adopted the discrete notation, in order to make things simpler. Once again, we can now start from the vacuum state $|0\rangle_u$ and construct the entire Fock space.

Now, the crucial point is that, in a general non-flat spacetime - in contrast to inertial coordinates for the Minkowski case - there is no distinguished set of coordinates, in particular no distinguished time, with respect to which the expansion (1.19) can be uniquely defined; that is, the basis chosen is not-unique and, therefore, there are different notions of vacuum, one for each possible orthonormal basis. This is the reason why we have written the vacuum state as $|0\rangle_u$ in the first place, with the index 'u' attached to it. This means that we can expand the field into a different set of complete solutions $\{v_p, v_p^*\}$,

$$\phi = \sum_p (b_p v_p + b_p^\dagger v_p^*)\,, \tag{1.20}$$

and, since the two are both complete orthonormal sets, one could also expand one basis with respect to the other; that is

$$v_i = \sum_j (\alpha_{ij} u_j + \beta_{ij} u_j^*)\,. \tag{1.21}$$

---

[7] The procedure described from now on works only for backgrounds (M, g) which are globally hyperbolic; this characteristic is tied to the notion of Cauchy surfaces and we will not enter the details of it here (see, e.g., [32, 38]) as the spacetime we will consider (such as Minkowski or the Kruskal-Szekeres extension of the Schwarzschild spacetime) already possess this characteristic. This is not true, instead, for charged or rotating black holes.

The coefficients α_{ij} and β_{ij} are called the *Bogoliubov coefficients* and they satisfy the relations

$$\sum_k \left(\alpha_{ik}\alpha^*_{jk} - \beta_{ik}\beta^*_{jk}\right) = \delta_{ij}\,, \qquad \sum_k \left(\alpha_{ik}\beta^*_{jk} - \beta_{ik}\alpha^*_{jk}\right) = 0\,, \tag{1.22}$$

which follow from the commutation relations obeyed by the field ϕ and by the modes a_k and b_p. Also, if we momentarily drop the indices ij and we adopt a matrix from, we see that the *Bogoliubov transformations* [39, 40] acquire the simple form

$$\begin{pmatrix} v \\ v^* \end{pmatrix} = \begin{pmatrix} \alpha & \beta \\ \beta^* & \alpha^* \end{pmatrix} \begin{pmatrix} u \\ u^* \end{pmatrix}. \tag{1.23}$$

Finally, we can use the relations above to derive how the two sets of creation/annihilation operators transform; that is

$$a_k = \sum_j \left(\alpha_{jk} b_j + \beta^*_{jk} b^\dagger_j\right), \tag{1.24}$$

$$b_k = \sum_j \left(\alpha^*_{jk} a_j - \beta^*_{kj} a^\dagger_j\right). \tag{1.25}$$

Now, let us introduce the *particle number operator* $N_k = a^\dagger_k a_k$ which measures the number of particle in the k-th state; its expectation value with respect to the vacuum is, of course, zero; however, if we now calculate the expectation value of the number operator referred to the second basis with respect to the first basis vacuum, the result, in QFT on curved backgrounds, does not vanish in general! That is,

$${}_u\langle 0|\, b^\dagger_k b_k \,|0\rangle_u = \sum_j |\beta_{jk}|^2\,, \tag{1.26}$$

which means that, if $\beta_{jk} \neq 0$, the first vacuum contains particle as seen by the second observer; this can be used as a further proof of what we stated above: the definition of a vacuum - and therefore the whole particle concept - is ambiguous if β_{jk} is non-vanishing [8]. This problem, as already stressed, does not occur in flat spacetimes but there is another case in which we can still uniquely define particles: that is, for a **stationary geometry**.

By definition, if a spacetime geometry is stationary, it has a timelike Killing field, i.e. a *Killing vector* of the form $\xi^a \equiv (\partial/\partial t)^a$. Without entering the details about Killing vectors (for a precise characterization see [41]), it is sufficient to know that they represent the symmetries of a metric; roughly speaking, a timelike Killing vector means that the metric is time-independent and, thus, we have a well-defined time variable. Furthermore, the Killing vector field commutes with the Klein-Gordon operator $\Box_g + m^2$ and it is anti-hermitian (that is, its eigenvalues are purely imaginary); these two properties combined

---

[8] This means that, according to Paul Davies: "[in curved spacetimes] particles don't exist" [37]

are everything we need: given the form of ξ^a we can look for its eigenvalues, which will obey equations equivalent to Eqs. (1.7) and (1.8), and they will uniquely identify positive and negative frequencies; furthermore, the modes associated with them will constitute a basis for our problem. Thus, as we just saw, we can still uniquely define the notion of vacuum (and thus, of particles) in a curved spacetime, given that the metric is stationary.

Everything we have been built up until now may seem a rather heavy framework of mathematical machineries but it all leads up to the following reasoning, which resides at the core of Hawking's work of 1974.
As we already said, in quantum field theory on a general spacetime there is no possibility of identifying a unique covariant vacuum state and thus the notion of particles is ambiguous. But what if we imagine a process that starts from a stationary background (or from Minkowski spacetime), undergoes some drastic change and, after a long time, ends in another stationary/flat spacetime? What would an observer see after this evolution? This is exactly how Hawking proceeded when he imagined to describe the final state of a stellar collapse that causes the formation of an event horizon, and it led to the stunning prediction that black holes evaporate. Having introduced the Schwarzschild geometry and QFT in curved spacetimes we have all we need to describe the Hawking effect. However, we will not derive his famous results quite yet, as we want to add another piece first.

1.3.1 The Unruh effect

In this Section, we will analyse the case of an uniformly accelerating non-inertial observer in Minkowski spacetime, or, equivalently, QFT in Rindler space. This will lead to the **Unruh effect** [23] which represents the free counterpart of the Hawking effect. Historically, the Unruh effect was theorized after the Hawking effect but it is more convenient to describe it now as we will introduce many aspects relevant for the discussion of the Hawking radiation. Furthermore, the studies developed on this effect are of paramount importance for the analogue gravity paradigm, as they uncover one particular feature of the Hawking effect; we will talk more about this aspect in the following Sections.

A non-inertial, uniformly accelerating frame can be described by the Rindler coordinate system, according to which, for each uniformly accelerating observer, a Rindler frame can be chosen in which it is at rest. In special relativity, a uniformly accelerating observer undergoes hyperbolic motion. In fact, the trajectory of such an observer is described by $x^\mu(\tau)$, where τ is the proper time, such that $\ddot{x}^\mu \ddot{x}_\mu = -\alpha^2$, where α is the proper acceleration and the dots indicate temporal derivation. Looking for simplicity at a (1+1)-dimensional space, this yields

$$t = \frac{1}{\alpha}\sinh(\alpha\tau)\,, \tag{1.27}$$

$$x = \frac{1}{\alpha}\cosh(\alpha\tau)\,, \tag{1.28}$$

where α is a constant parameter. The acceleration is given by

$$a^2 = g_{\mu\nu}a^\mu a^\nu = g_{\mu\nu}\frac{D^2x^\mu}{d\tau^2}\frac{D^2x^\nu}{d\tau^2} = \alpha^2\,, \tag{1.29}$$

as expected. The world line of the observer $x_\mu x^\mu$ satisfies $t^2 - x^2 = -\frac{1}{\alpha^2}$ which is indeed a hyperbolic motion; the lines $x = t$ are the horizons for this observer because the region $x \leq t$ is forbidden to a Rindler observer. These trajectories are depicted in fig. (1.4). Note that the Rindler chart does not cover the whole Minkowski spacetime, but only a portion of it. In particular we can divide the Minkowski spacetime into four disconnected regions, called “wedges”: left, right, past and future. The accelerated observers can lie on either the left or right region, depending on the sign of their acceleration, yet observers in one region cannot communicate with the ones in the other region. In this framework it is useful to introduce a new set $(\eta,\ \xi)$ of coordinates instead of the Minkowski ones $(t,\ x)$; they are defined in the right Rindler wedge as:

$$x = \frac{1}{a}e^{a\xi}\cosh(a\eta)\,, \tag{1.30}$$

$$t = \frac{1}{a}e^{a\xi}\sinh(a\eta)\,. \tag{1.31}$$

The metric in this coordinate set becomes

$$ds^2 = e^{2a\xi}(d\eta^2 - d\xi^2)\,, \tag{1.32}$$

and it is independent of η, thus ∂/∂_η is a Killing field. An analogous set of coordinates can be chosen in the left Rindler wedge by taking the right wedge's coordinate with opposite sign[9].

As described in the previous Section, in Minkowski spacetime we can decompose any solution on the plane wave basis; now something analogous can be done in Rindler spacetime by taking the set $\{g_k^R, g_k^{R*}\}$, which are the eigenvectors of the Killing field ∂_η in the right Rindler wedge. We have specified the apex 'R' since this set is not complete with respect to Minkowski spacetime and we have to include the basis of the left wedge in order to have a complete set. Thus, given the basis $\{f_k, f_k^*\}$ for the flat spacetime, we have two possible expansions for any field configuration:

$$\phi = \sum_k (a_k f_k + \text{h.c.}) = \sum_k (b_k g_k^R + c_k g_k^L + \text{h.c.}) \tag{1.33}$$

---

[9] One way to choose a set of coordinates which covers the whole four regions is to allow η and ξ to become complex.

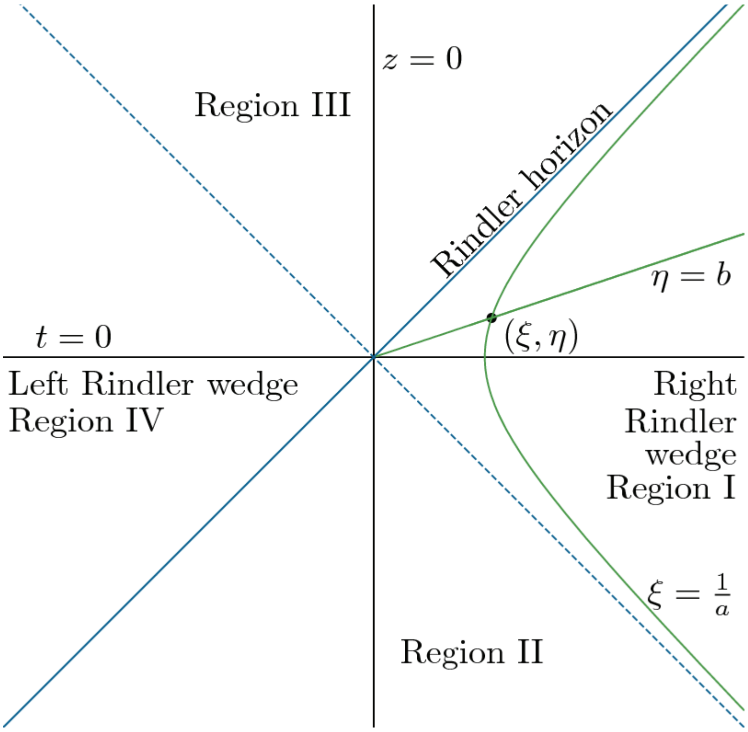

Figure 1.4: Minkowski diagram showing the Rindler chart, which divides the plane into four regions or "wedges": right (region I), past (region II), future (region III) and left (region IV). The blue lines $t = \pm z$ represent the Rindler horizons (here the spatial coordinate is called z instead of x), while the green lines represent curves at constant ξ or η. The lines at constant ξ are the trajectories of accelerated observers with different accelerations. Slowly accelerating observers are represented by almost vertical straight trajectories, positioned on the far left or far right of the diagram. As the acceleration parameter increases the trajectories bend and move closer to the horizons.

Now, one can wonder what an observer in the right Rindler wedge sees if he looks at the Minkowski vacuum. That is, for a given state k, what is

$$_M \langle 0| N_k^R |0\rangle_M = ? \tag{1.34}$$

As already discussed, this quantity can be deduced from the Bogoliubov transformation[10]

$$g_\omega^R = \int d\omega' (A_{\omega\omega'} f_{\omega'} + B_{\omega\omega'} f_{\omega'}^*) ; \tag{1.35}$$

since $f_{\omega'} = \frac{1}{\sqrt{4\pi\omega'}} e^{-ik_\mu x^\mu}$ and $-ik_\mu x^\mu = -i\omega'(t-x) = -i\omega' u$, with $u = t - x$, we have

$$g_\omega^R(u) = \int d\omega' \left(A_{\omega\omega'} \frac{1}{2\pi}\sqrt{\frac{\pi}{\omega'}} e^{-i\omega' u} + B_{\omega\omega'} \frac{1}{2\pi}\sqrt{\frac{\pi}{\omega'}} e^{i\omega' u} \right) ; \tag{1.36}$$

---

[10] Here the transformation is written in continuous notation for convenience and we have considered a massless field for simplicity.

this expression resembles the Fourier transform of $g^R_\omega(u)$. Indeed,

$$\begin{aligned} g^R_\omega(u) &= \frac{1}{2\pi}\int_{-\infty}^{+\infty} d\omega' e^{-i\omega' u}\tilde{g}_\omega(\omega') \\ &= \frac{1}{2\pi}\int_{0}^{+\infty} d\omega' e^{-i\omega' u}\tilde{g}_\omega(\omega') + \frac{1}{2\pi}\int_{0}^{+\infty} d\omega' e^{i\omega' u}\tilde{g}_\omega(-\omega')\,. \end{aligned} \tag{1.37}$$

Thus, by comparing Eq. (1.36) and (1.37), we can write

$$A_{\omega\omega'} = \sqrt{\frac{\omega'}{\pi}}\tilde{g}_\omega(\omega')\,, \quad B_{\omega\omega'} = \sqrt{\frac{\omega'}{\pi}}\tilde{g}_\omega(-\omega')\,. \tag{1.38}$$

Now, it can be demonstrated (we will do that shortly) that

$$\tilde{g}_\omega(-\omega') = -e^{-\pi\omega/a}\tilde{g}_\omega(\omega')\,, \tag{1.39}$$

and, thus,

$$A_{\omega\omega'} = \sqrt{\frac{\omega'}{\pi}}\tilde{g}_\omega(\omega') = -\sqrt{\frac{\omega'}{\pi}}\tilde{g}_\omega(-\omega')e^{\pi\omega/a} = -e^{\pi\omega/a}B_{\omega\omega'}\,. \tag{1.40}$$

This means that, using Eq. (1.22), which can be rewritten as $AA^\dagger - BB^\dagger = 1$, we have

$$|B|^2 = \frac{1}{e^{2\pi\omega/a} - 1}\,. \tag{1.41}$$

This is exactly the quantity we were looking for, i.e., the number of particles in the k-th state seen by a right Rindler observer in the Minkowski vacuum (see Eq. (1.26)). Eq. (1.41) describes a Planck spectrum for bosons with temperature $T = a/2\pi$ and it shows that a Rindler observer is immersed in a thermal bath of particles. This is the Unruh effect.

The last thing we need to do is to demonstrate Eq. (1.39).

Demonstration of Eq. (1.39)

Let us start from the Fourier transform of $g^R_\omega(u)$,

$$\tilde{g}_\omega(\omega') = \int_{-\infty}^{+\infty} du\, e^{i\omega' u} g^R_\omega(u) \tag{1.42}$$

where, it can be demonstrated, $g^R_\omega(u) = \frac{1}{\sqrt{4\pi\omega}}e^{ik_\mu x^\mu}$ with $x^\mu = (\eta, \xi)$ for the right Rindler wedge (that is, for $u < 0$); so $ik_\mu x^\mu = -i\omega(\eta - \xi)$. Now, from the definition Eq. (1.30) we have

$$t - x = u = -\frac{1}{a}e^{-a(\eta-\xi)} \tag{1.43}$$

and thus

$$\eta - \xi = -\frac{1}{a}\ln(-au)\,. \tag{1.44}$$

Taking this into account, the Fourier transform becomes

$$\begin{aligned}
\tilde{g}_\omega(\omega') &= \int_{-\infty}^{0} du\, e^{i\omega' u}\frac{1}{\sqrt{4\pi\omega}}e^{(i\omega/a)\ln(-au)} \\
&= \frac{1}{\sqrt{4\pi\omega}}\int_{-\infty}^{0} du\, e^{i\omega' u}(-au)^{i\omega/a} \\
&= \frac{1}{\sqrt{4\pi\omega}}a^{i\omega/a}\int_{0}^{+\infty} du\, e^{-i\omega' u}u^{i\omega/a} \\
&= \frac{1}{\sqrt{4\pi\omega}}a^{i\omega/a}\frac{1}{a}\frac{\omega}{\omega'}\int_{0}^{+\infty} du\, e^{-i\omega' u}u^{(i\omega/a)-1}\,,
\end{aligned} \tag{1.45}$$

where we integrated by part in the last line. This integral can be rewritten in terms of Gamma functions, given some assumptions. Indeed, let us consider the integral

$$\int_0^\infty dx\, e^{-bx}x^{s-1} \tag{1.46}$$

defined for $\Re(b) > 0$ and $\Re(s) > 0$; that can be rewritten as

$$\int_0^\infty \frac{d(bx)}{b}\, e^{-bx}\frac{(bx)^{s-1}}{b^{s-1}} = b^{-s}\int_0^\infty dy\, e^{-y}y^{s-1} = e^{-s\ln b}\Gamma(s)\,. \tag{1.47}$$

In this integral b is a complex number and thus $\ln(b)$ a multivalued function. We will then adopt the following definition: given the cartesian (A, B) and polar (r, θ) representation of b we define

$$\begin{aligned}
\ln b = \ln(A + iB) = \ln r + i\theta &= \ln(\sqrt{A^2 + B^2}) + i\arctan\left(\frac{B}{A}\right) \\
&= \ln(\sqrt{A^2 + B^2}) + i\arctan\left|\frac{B}{A}\right|\text{sign}\left(\frac{B}{A}\right)\,.
\end{aligned} \tag{1.48}$$

Now, if we set $b = i\omega' + \epsilon$ and $s = i\omega/a + \epsilon$ and we take $\lim_{\epsilon\to 0^+}$ we have

$$\begin{aligned}
&\ln b = \ln(\sqrt{\omega'^2 + \epsilon^2}) + i\arctan\left|\frac{\omega'}{\epsilon}\right|\text{sign}\left(\frac{\omega'}{\epsilon}\right) \\
&\lim_{\epsilon\to 0^+}\ln b = \ln|\omega'| + i\frac{\pi}{2}\text{sign}(\omega')\,;
\end{aligned} \tag{1.49}$$

thus, using this result, Eqs. (1.45) and (1.47) and taking the limit, we obtain

$$\tilde{g}_\omega(\omega') = \frac{1}{\sqrt{4\pi\omega}}a^{i\omega/a}\left(\frac{1}{a}\frac{\omega}{|\omega'|}\text{sign}(\omega')\right)e^{-i\omega/a\ln|\omega'|}\,e^{\omega\pi/(2a)\text{sign}(\omega')}\,\Gamma\left(\frac{i\omega}{a}\right)\,. \tag{1.50}$$

Therefore, for $\omega' > 0$, the two solutions become

$$\tilde{g}_\omega(\omega') = \frac{1}{\sqrt{4\pi\omega}} a^{i\omega/a} \left(\frac{1}{a}\frac{\omega}{|\omega'|}\right) e^{-i\omega/a\ln|\omega'|}\, e^{\omega\pi/(2a)}\, \Gamma\left(\frac{i\omega}{a}\right) , \tag{1.51}$$

$$\tilde{g}_\omega(-\omega') = \frac{1}{\sqrt{4\pi\omega}} a^{i\omega/a} \left(-\frac{1}{a}\frac{\omega}{|\omega'|}\right) e^{-i\omega/a\ln|\omega'|}\, e^{-\omega\pi/(2a)}\, \Gamma\left(\frac{i\omega}{a}\right) . \tag{1.52}$$

A comparison between these two gives

$$\tilde{g}_\omega(-\omega') = -e^{-\pi\omega/a}\tilde{g}_\omega(\omega') , \tag{1.53}$$

which is exactly Eq. (1.39).

1.3.2 Hawking radiation

At this point we are ready to derive the Hawking effect for an astrophysical Schwarzschild black hole. The process described in the following mostly retraces Hawking reasoning from his famous paper [19] but it will differ in the calculations as we will use the math developed in the previous Section. Before attacking the problem from a rigorous point of view, though, it is better to describe the main idea.

It is generally believed that black holes are produced by a gravitational collapse [14], hence, to understand how particle creation can arise, it is essential to consider the time-dependent formation phase as well as the final state. However, in a general spacetime the notions of fields and particles are ambiguous, as we have already described in details; a way out of this consists in dealing with the entire history of a black hole, starting from a situation when matter is diluted with a very low density, so that the spacetime is stationary (or - better - is a weak perturbation of Minkowski) and following the long time evolution of the process: gravity slowly pulls the matter closer and closer and, after a very long time, the increasing amount of mass in a reduced spatial region collapses into a black hole, forming an event horizon; after the whole process has settled, the spacetime ends in another stationary configuration, as a Schwarzschild or a *Kerr black hole* [42]; in both cases the asymptotic region external to the horizon is a flat spacetime. This way of thinking (which is exactly Hawking's approach to the problem) allows us to start and finish from spacetimes equipped with a unique notion of particles; also, by studying the different notions of vacua (that is, comparing the final spacetime to the initial situation) one should be able to see how the collapse and the formation of a horizon has influenced the outside observers. This will lead to the Hawking radiation.

For the sake of clarity, let us summarize once again the main steps to take in order to derive Hawking radiation, starting from the collapse of a star depicted in Fig. (1.5). The idea is to study scalar field propagating throughout the spacetime and perform the canonical quantization with respect to a basis of modes defined at the past null infinity $\mathcal{I}^-$ and also with respect to a set of modes defined at the future null infinity $\mathcal{I}^+$. Then, the physically interesting question is: does an observer in the far future see particles in the vacuum defined in the past? That is, if we calculate the Bogoliubov coefficient for a future observer with respect to the initial vacuum are they vanishing or not? If not, what is the meaning of this effect?

Last, before starting with the calculations, we will make another couple of assumptions. First of all, we will study the case of massless scalar fields (thus the Klein-Gordon equation assumes the simple form $\Box_g \phi = 0$ - the case of massive field can be treated following the same reasoning); second, note that the derivation of the Hawking effect relies on a semi-classical approximation: that is, the matter fields will be treated in the QFT framework while the spacetime metrics will behave classically. Given these assumptions, we are now ready to describe the Hawking effect.

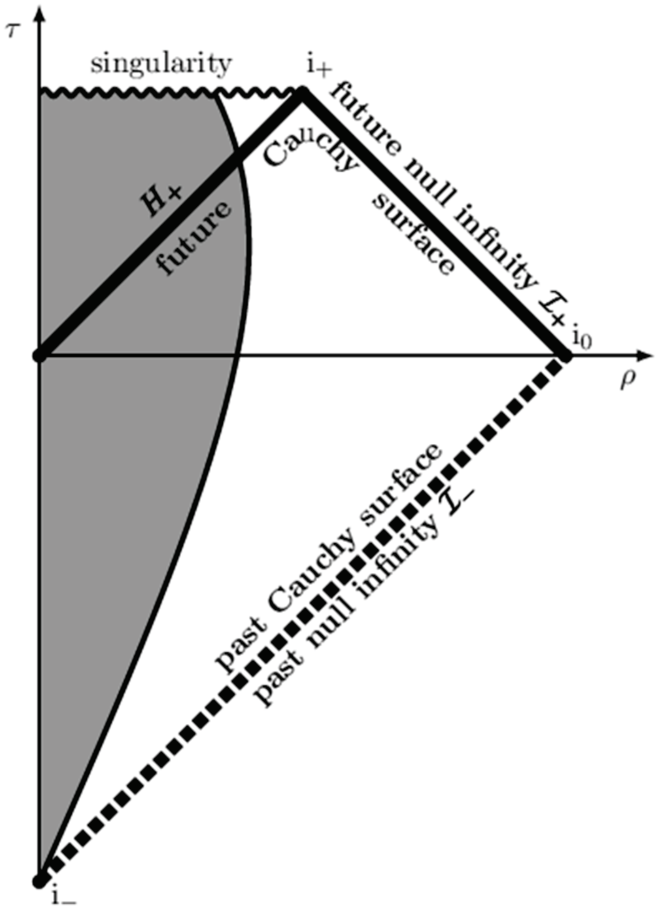

Figure 1.5: Carter-Penrose diagram of a spherically collapsing star. The grey region is the interior of the body.

From the Carter-Penrose diagram of Fig. (1.5) we can see that, while $\mathcal{I}^-$ is a Cauchy surface, $\mathcal{I}^+$ is not, because of the region behind the horizon; however $\mathcal{I}^+ \cup H^+$ is one and, therefore, a set has to be defined on this surface, in order to be complete. Thus, three sets of modes can be defined: $\{f_i, f_i^*\}$ on $\mathcal{I}^-$, $\{g_i, g_i^*\}$ on $\mathcal{I}^-$ and $\{h_i, h_i^*\}$ on H^+ and any field configuration which is solution of the Klein-Gordon equation can be written as

$$\phi = \sum_i (a_i f_i + \text{h.c.}) = \sum_i (b_i g_i + c_i h_i + \text{h.c.})\,. \tag{1.54}$$

As we already said, we will then consider two kinds of vacua: the asymptotic past one, $|0_{in}\rangle$, and the asymptotic future one, $|0_{out}\rangle$. These vacua are defined such that $a_i\,|0_{in}\rangle = 0$ and $b_i\,|0_{out}\rangle = c_i\,|0_{out}\rangle = 0$. We will then look for the Bogoliubov coefficient of the expansion $g_i = \sum_j (A_{ij} f_j + B_{ij} f_j^*)$, which will tell us what the particle content of the initial vacuum as seen by a future observer is.

Now, let us start by re-writing the Schwarzschild metric (1.2) in the form

$$ds^2 = \left(1 - \frac{2M}{r}\right) dt^2 - \left(1 - \frac{2M}{r}\right)^{-1} dr^2 - r^2 d\Omega^2\,, \tag{1.55}$$

where we have used natural units to simplify things. Then, we introduce the "tortoise" coordinate[11] $r_* = r + 2M \ln\left(\frac{r}{2M} - 1\right) = r + r_S \ln\left(\frac{r}{r_S} - 1\right)$ and, since we are in spherical symmetry, we separate the field using the spherical harmonics

$$\phi(x) = \frac{f(t,r)}{r} Y_{lm}(\theta, \varphi)\,. \tag{1.56}$$

Inserting this *ansatz* into the Klein-Gordon equation relative to metric (1.55) we obtain the equation

$$\frac{\partial^2 f}{\partial t^2} - \frac{\partial^2 f}{\partial r_*^2} + V(r_*) = 0\,, \tag{1.57}$$

where the potential is of the form

$$V(r_*) = \left(1 - \frac{2M}{r}\right)\left[\frac{l(l+1)}{r^2} + \frac{2M}{r^3}\right] = \left(1 - \frac{r_S}{r}\right)\left[\frac{l(l+1)}{r^2} + \frac{r_S}{r^3}\right]. \tag{1.58}$$

Note that $\lim_{r\to r_S} V = 0$ as well as $\lim_{r\to\infty} V = 0$ and in between this two values the precise form of V depends on l and it represents a potential barrier so any solution coming from infinity is expected to be partially reflected and partially emitted. It is now convenient to introduce the Eddington-Finkelstein null coordinates [43]

$$u = t - r_*\,, \quad v = t + r_*\,. \tag{1.59}$$

---

[11] The name comes from the fact that dr/dr_* tends to zero as $r \to 2M$, meaning that the function $r = r(r_*)$ becomes more and more constant as one approaches the horizon.

These coordinates are also called *retarded* and *advanced* coordinates respectively, as they play the role of a retarded/advanced time and are suitable to describe outgoing and incoming modes; indeed, in figure (1.5) v runs along $\mathcal{I}^-$ from $-\infty$ to $+\infty$ while u runs along $\mathcal{I}^+$ from $-\infty$ to $+\infty$. Thus we choose to decompose the incoming part of the scalar field ϕ in the asymptotic past in terms of the coordinate v, while in the asymptotic future in terms of the coordinate u.

Now, at $\mathcal{I}^+$ the potential is zero and thus plane waves are solutions of Eq. (1.57). That is

$$f = e^{-ik_\mu x^\mu} = e^{-i\omega u} \tag{1.60}$$

is an outgoing solution to the wave equation at $\mathcal{I}^+$. The key point now is that $u \to \infty$ near the horizon and thus f rapidly oscillates; this means that we can make use the *geometric optics approximation* which is used when a wave has a constant amplitude with respect to the phase; in this formalism, the surface of constant phase of any wave can be traced back in time by following null geodesics. We will now rely on figure (1.6) for the following discussion.

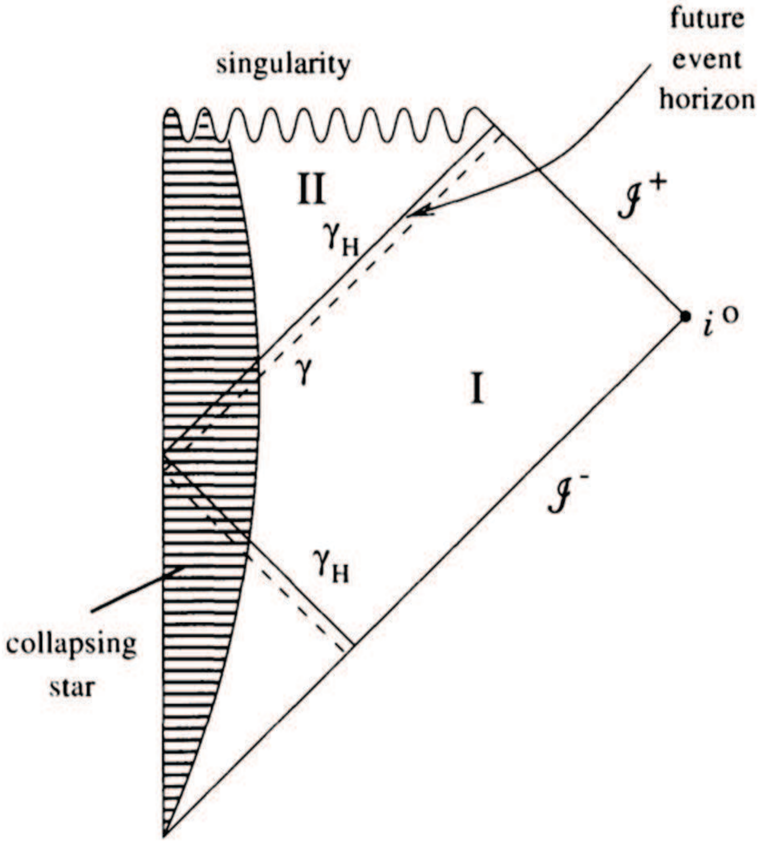

Figure 1.6: The outgoing solution is traced back in time by following the null geodesic γ (dashed line) from $\mathcal{I}^+$ to $\mathcal{I}^-$.

Let γ_H denote the limiting null geodesic staying at the horizon and suppose that the null geodesics γ associated with the outgoing solution (1.60) is close to γ_H. The idea is now to back-evolve a wave from $\mathcal{I}^+$ to $\mathcal{I}^-$; this can be simply done in the geometric optics approximation because this is a highly blue-shifted wave which is not affected by the collapsing body during its transit and interference scattering can also be ignored; this implies, in turn, that the affine distance with the horizon is constant throughout the scattering process and it allows us to compare the phase variation on $\mathcal{I}^+$ with the one in the asymptotic past. That is, the affine distance at $\mathcal{I}^+$ is the Kruskal coordinate U [44] which is linked to u by the relation

$$U = -e^{-u\kappa}\,, \tag{1.61}$$

where κ is the **surface gravity**, defined as the gravitational acceleration at the surface of an object (for a Schwarzschild black hole $\kappa = \frac{1}{4M}$). Now, if we choose the affine distance of the limiting null geodesic γ_H to be $U = 0$ and the one of the null geodesic γ to be $U = -\epsilon$ (we need to be near the horizon for the geometric optic approximation to hold), from Eq. (1.61) the value of u for the geodesic γ can be deduced to be

$$u = -\frac{1}{\kappa}\ln\epsilon \tag{1.62}$$

and thus the respective outgoing plane wave can be rewritten as

$$f = e^{-i\omega u} = e^{i\omega/\kappa \ln\epsilon}\,. \tag{1.63}$$

Then, by tracing back in time, γ reaches $\mathcal{I}^-$ at an affine distance $v = -\epsilon$ giving that the outgoing solution on this surface is $e^{i\omega/\kappa \ln -v}$. This solution has exactly the same form as the one for the Rindler space case, with κ instead of a; thus, the same approach used in the previous Section can be applied (that is, going into Fourier space and comparing the Bogoliubov coefficients) to obtain that the number of particles seen by a future observer looking at the past vacuum is given by

$$|B|^2 = \frac{1}{e^{2\pi\omega/\kappa} - 1}\,. \tag{1.64}$$

This is a Planck spectrum with temperature $T = \kappa/2\pi$ and this phenomenon is known as the **Hawking effect**. One can interpret it by asserting that the time-dependent metric and the formation of a horizon has caused the creation of a certain number of particles of the scalar field. That is, the horizon can be seen as an emitter, causing the black hole to evaporate with a temperature which scales as the inverse of the black hole mass. Other plausible physical interpretations of this effect rely on the creation of virtual pairs of particle/antiparticle in the proximity of a horizon (Fig. (1.7)) getting separated and becoming real particles (we can imagine the negative energy *Partner* to fall into the black hole, reducing its mass, while the positive energy *Hawking radiation* propagates away) or on tunnelling effects from a potential barrier [27]. More details about this phenomenon and its physical implications can be found in the original paper [19]. One last comment we wish to make is that Eq. (1.64) is missing a factor Γ_ω known as the *greybody factor*, which appears when the form of the potential is taken into account and it depends on the angular part of V. In that case Eq. (1.64) becomes

$$|B|^2 = \frac{\Gamma_\omega}{e^{2\pi\omega/\kappa} - 1} \,. \tag{1.65}$$

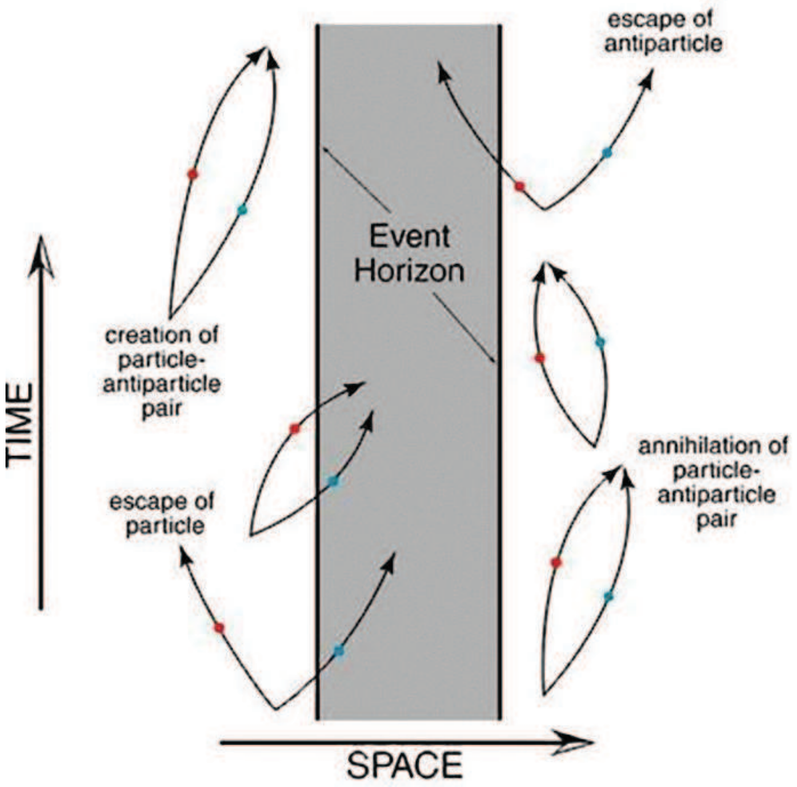

Figure 1.7: Representation of the Hawking effect which relies on vacuum fluctuations in the proximity of a horizon. In QFT, vacuum can be seen as a sea of particle-antiparticle pairs, continuously being created and annihilated in a time lapse given by *Heisenberg's uncertainty principle*, $\Delta t \sim \Delta E/\hbar$. Outside an horizon, however, the gravitational field gradient is very strong and the two particles, may, in principle, become separated right after the creation; if one of them crosses the event horizon into the black hole it acquires negative energy (as in the *Penrose process* [43]) and thus the other, with opposite (i.e. positive) energy, will escape as real radiation. It is important to note that, however, as Hawking himself stated, "these pictures of mechanism [...] are heuristic only and should not be taken too literally" [19].

With these results in hand, we can now take on the realm of analogue gravity and, in particular, on the analogue Hawking effect. We will come back to the results obtained in this Section to highlight a few fundamental points.

1.4 Sonic black holes and analogue spacetimes

In the previous Section we have re-derived one of most surprising phenomena in gravitational physics: that is, the 1974 result by S. Hawking which demonstrates that black holes evaporate [18,19]. The prediction was that black holes, objects whose spacetime structure (Fig. (1.8)) is such that no radiation in principle could propagate from the inside to the outside, nevertheless produce a radiation which gradually shrinks the size of the black hole. Furthermore, the outgoing radiation has the spectrum of a black body with temperature[12]

$$T_H = \frac{\hbar\kappa}{2\pi k_B c}\,, \tag{1.66}$$

where κ is the surface gravity at the horizon (for a Schwarzschild black hole $\kappa = \frac{c^4}{4GM}$). A glance at the various fundamental constants in this equation immediately gives an idea of the paramount importance of this results: not only it combines quantum mechanics and gravity, but it also blends in the field of thermodynamics. This astonishing fusion of disparate realms of physics provided immediately ample motivations to the studies of the Hawking radiation. Unfortunately, it was soon realised that the derivation of this phenomenon presented several issues: while mathematically rigorous, it was hiding severe physical problems. Indeed, there are at least two main problems with the Hawking effect, one on the theoretical side and from the experimental side.

Starting with the possibility of observing the **Hawking radiation** emitted from a real black hole, soon after the discovery of this effect it was shown that this kind of thermal radiation is extremely cold. That is, the temperature depends on the inverse of the black hole mass and if we consider, for example, the case of a realistic solar-mass Schwarzschild black hole, we obtain $T_H \simeq 60$ nK; this is well-below the cosmic microwave background (CMB) radiation temperature, $T \simeq 2.7$ K, and even below its fluctuations (which are the order of the μK) and, therefore, a detection of this phenomenon through an astrophysical observation is very unlikely[13].

Second and foremost, the idea that black holes radiate generated immediately a lot of questions. Where do these particles come from? They cannot be created from inside the horizon so they must come from the outside, but then what creates them there? Also, what causes this temperature? Many more of these questions were evaluated by physicists and they led immediately to possibly the biggest flaw in Hawking's calculation: the *Transplanckian problem.* In fact, it was shown in 1975 [23] that, if one looks at the emitted radiation and asks where it came from, it is straightforward to deduce that it must have been

---

[12] Differently from the previous Section, here we have written all the constants explicitly.

[13] On the other hand, it has been speculated that small black holes created in the early universe might emit detectable Hawking radiation [45] or, perhaps, very small black holes could be created and detected in particle accelerators [46].

closer and closer to the horizon in the past, given that nothing can escape a black hole. However, this means that waves must have been squeezed very near to the horizon as we travel back in the past and thus they have been experiencing a huge gravitational blue-shift[14]. Now, if we try to do the math for a realistic case, we obtain absurdly large numbers: for a case of a solar black hole, in fact, the radiation produced one second after the formation of the horizon should have an energy which corresponds to e^{10^5} the energy of the whole universe [47], literally a physical nonsense. This has been known since as the "Trasplanckian problem" as one could also state the issue by observing that the gravitational Doppler shift due to the horizon implies that wavelengths can reach arbitrarily small values, even below the Planck scale (which is believed to be a physical constraint). The question thus arises: if the derivation relies on such absurd physical assumptions, can the result be trusted?

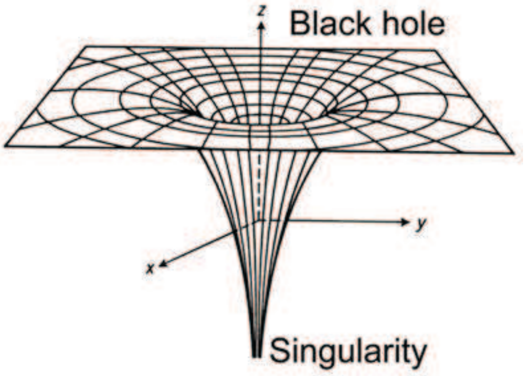

Figure 1.8: A representation of a black hole spacetime.

Needless to say, the discovery of this effect (and its implications) boosted the research in this direction; surprisingly, the Hawking effect stood robust, as many other scientists, approaching the problem from different point of views, reached the same conclusions [22, 24–27][15]. Furthermore, important contributions towards the comprehension of this process were given by S. Fulling [48], P. Davies [49] and W. G. Unruh [23] who understood, from studying particles in a Rindler spacetime, that the Hawking effect was not necessarily related to a gravitational context as it was a more general effect, related to the kinematics of spacetimes. This studies lead to the *Unruh effect* which we have described in details in Section 1.3.1 (in fact, it is sometimes refereed as the *Fulling-Davies-Unruh effect*).

These aforementioned works suggested that the Hawking effect was more fundamental than what previously thought, as it is not relegated to black hole physics but it is solely a quantum-field-in-a-curved-spacetime effect and it

---

[14] Note that it is exactly this reasoning which allowed us to use the geometrical optics approximation in Section 1.3.2 and it represents a key point in Hawking's derivation.

[15] We have listed here some of the other approaches to the Hawking effect but for a more detailed catalogue see [38].

should exist in situations where even gravity itself is not relevant at all (indeed, note that the derivation of Hawking radiation does not rely on Einstein's equations of motion). This may seem obvious given the approach we adopted in the previous Sections but remember that our way of proceeding does not follow the historical development of the discoveries: the Hawking effect was derived first and then physicists found that there were similar effects in QFT on curved backgrounds. Thus, it was realized that **the Hawking effect is a purely kinematic effect** that depends only on the existence of two things: a Lorentzian metric and a horizon. That is, the Hawking radiation is not related *at all* to the dynamics of the system[16] and this result represents the first key ingredient to the analogue gravity paradigm.

In 1980, while teaching a course in fluid mechanics, Unruh realized that there might be another way of approaching the problem of Hawking radiation. Indeed, it was a well-known fact that many waves, including sound waves in a fluid, have a behaviour at low frequencies (long wavelengths) which is almost identical to that of fields in a curved spacetime; that is, the background flow would alter the equations of motion for the sound waves in precisely the same way that a non-flat spacetime metric would alter the equations of motion for fields in the spacetimes corresponding to Einstein's theory of gravity; moreover, sound waves get trapped in regions of supersonic flow in the same way light is trapped inside a gravitational black hole (see, for example, the 1920's work by Gordon [50], or, more recently, the studies by Peregrine on what he addresses as *stopping regions* [51]). This realization led to one of Unruh's most famous work [52] and to the birth of analogue models of gravity, or, in short, **Analogue Gravity**. The underling idea of these models is quite simple and we will now qualitatively explain it.

Just as (classical) light, sound is known to have a wave-like behaviour as well; that is, in a static, homogeneous and inviscid fluid, a perturbation of the dynamical quantities (pressure, velocity and density) obeys the wave equation: sound is *defined* to be these fluctuations in the dynamical quantities [53]. Now, in a static fluid sound is emitted isotropically; on the other hand, a moving fluid will drag sound waves along with it, much in the same way as a moving object drags the sound cones with itself (Fig. (1.9)). Thus, let us imagine a sound wave propagating in a medium which flows with a certain velocity gradient: if the speed of the fluid ever becomes supersonic, then the sound waves will never be able to fight their way back upstream and they become trapped inside the supersonic region. This phenomenon creates what is now known as a "**dumb hole**", the sonic analogue of a black hole, as sound, much as light, gets trapped in a region which resembles the inside of a black hole and can never escape. Figure (1.10) gives a simple and straightforward description of this phenomenon.

---

[16] This is actually true in a quasi-adiabatic regime; that is, if the energy emitted from the black hole is small compared to the mass of the object.

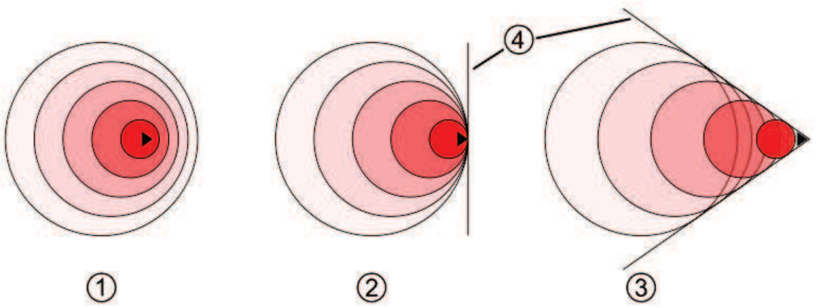

Figure 1.9: Diagram of the sound waves emitted from a moving object. ① shows a subsonic motion, ② a sonic one (otherwise called "Mach 1") and ③ a supersonic motion. ④ points to the shock cone while the different colors help distinguish the wavefronts. In case the object was, say, an aeroplane, this picture would show you the pressure waves of air flowing off of it. It could also represent water waves propagating from a boat that travels faster than the speed at which water waves move.

Now, the key point in this analogy is that the equivalence between the two systems (the hydrodynamical scenario and the case of an astrophysical black hole) is not just qualitative but it can be made rigorous from a mathematical point of view also, as it was already mentioned previously (we will enter these details in the next Section). Furthermore, it was understood that the Hawking effect was uniquely a kinematical effect (as we have already pointed out) and these two things combined brought Unruh to predict that the Hawking radiation should, in principle, be present in these analogue systems also [52]. Since a moving fluid obeys equations which are formally the same of those of a scalar field on a curved background, Unruh followed Hawking's calculation and predicted that the temperature of the radiation, in these cases, should be

$$T_H = \frac{\hbar\kappa}{2\pi k_B c} = \frac{\hbar}{2\pi k_B c}\frac{\partial(c^2 - v^2)}{\partial r}\bigg|_{\text{hor}}, \tag{1.67}$$

where the derivative is evaluated at the horizon, i.e., at the surface where $c^2 = v^2$.

Before going further, it is worth spending some time upon this prediction. Thanks to Unruh it was realized that it was possible to reproduce analogues of black holes in the laboratories and, pushing the analogy further to the quantum level, one could hope, in principle, to observe effects from quantum fields on curved backgrounds (like the Hawking effect) in the acoustic analogue systems. In the years after this discovery many studies were developed on the possible experimental candidates and, as of today, a vast class of systems is studied to this extent, both from an experimental and a theoretical point of view. A few examples include: pulse propagation in non-linear optical media [54–56], quantum fluids of light [57–61], atomic Bose-Einstein condensates of ultracold atoms [62–66], ultra-cold fermions [67–69] and, restricting to a classical

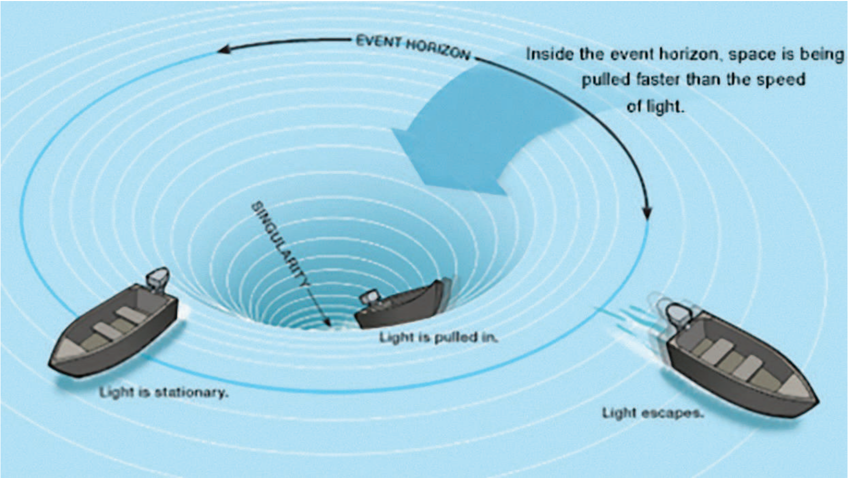

Figure 1.10: This image is usually used as a qualitatively way to describe a black hole; ironically enough, it is a perfect way to give a precise idea of what a **sonic black hole** is. Imagine the in-flowing water being spacetime and the boat a light ray or a sound wave; the boat (light/sound) has constant speed v directed radially and outgoing. As the drawing shows, there is a region where its velocity is enough to escape the drain; on the other hand, there is a region where its speed is not sufficient and the boat gets trapped into the drain and flows towards the "singularity". In the analogy, the boundary dividing these two region is the *sonic horizon*, the analogue of a black-hole horizon, and it is located at the surface $v = c$, where c is now the speed of sound (instead of being that of light).

regime, surface waves on water [70–74] [17]. Furthermore, even though the initial proposal to develop these systems was the detection of the Hawking radiation, it was soon realized that other kinematical effects could be studied in the same frameworks (superradiance, the Dynamical Casimir effect, cosmological particle production to name a few - for a longer list, see [75]) and this helped broaden the analogue gravity field even more. As of today, many people are working either theoretically or experimentally on these objects and studies all around the world have been carried on for years. In this Thesis, we will focus our attention only on a particular class of phenomena in this context, namely the **analogue Hawking effect in Bose-Einstein condensates**, but this introductory description would not be complete without a brief mention of the vast class of possibilities one can encounter in this field.

Going back to the seminal paper by Unruh and to the analogy between fluid dynamics and fields on curved backgrounds, it can be shown (we will do that in the following Section) that the analogy stands accurate, from a mathematical point of view, if one considers the motion of fluids in the *hydrodynamical approximation*, that is, at long wavelengths. Unfortunately, if one remains in the hydrodynamical regime, the derivation of the Hawking effect suffers from the

---

[17] For a more detailed list (but not as updated) we suggest the Review [75].

same difficulties as it does for the black hole case. Unlike for gravity, however, for fluids we understand the short wavelengths, high frequency physics, at least in principle. Fluids are made of atoms and molecules and once the wavelength of the sound waves become comparable to the distance between the molecules, the hydrodynamic approximation fails, as we start to be aware of the discrete pieces that compose our system (this scenario is quite similar to what one expects to happen with our geometrical description of the Universe, when explored with microscopic detail at the Planck scale). The equation of motion of the fluid particles are no longer continuum equations, but become finite difference type equations. While at wavelength much longer that the inter-atomic spacing, continuum, field-theory type approaches are valid, at short wavelengths they no longer suffice. Without a way to treat this problem, it was recognized that the analogue models did not add more to our knowledge of the Hawking radiation.

It was soon realized by T. Jacobson [76] that one of the key effects that this discreetness has is on the dispersion relation of the small fluctuations about some equilibrium flow of the fluid. In these systems the relation between the frequency and the wavelength is no longer the simple

$$\nu\lambda = c \tag{1.68}$$

with ν the frequency and λ the wavelength, but they have a much more complex relation; of course, at large λ the relation becomes the linear one of Eq. (1.68) - which is the Lorentzian one - but the phase velocity and the group velocity drift apart as one approaches the regime of small λ. Thus, one could take a first step at understanding the dependence of the thermal radiation on the nature of the theory of the waves at short wavelengths by examining the behaviour of the prediction under changes in the dispersion relation of the waves at small λ. Going back to the study of the wave propagation, we see that, starting from the outgoing wave-packet and projecting it back from the future, as time unrolls into the past, the packet gets closer and closer to the horizon and its wavelength decreases; eventually, however, its λ becomes small enough that the dispersion relation and the group velocity change: the wave-packet can no longer stay near the horizon and, as one goes back further into the past, that packet must have come from either inside the horizon (if the dispersion relation is such that the group velocity of the wave increases as λ decreases) or outside (in the opposite case). Thus, the system has a natural cut-off to the decrease of the wavelength caused by the horizon. That is, it is precisely the dispersion relation that changes from the long wavelength, relativistic, regime to the cut-off regime, where the atomicity of matter becomes important.

Now, it was shown by a number of numerical studies [77,78] that these systems still emit thermal quantum radiation and that changes in the short wavelength dispersion relation have no (or only very small) effects on the temperature or on the thermal spectrum of the radiation emitted. The conclusion is that the Transplanckian problem is a mathematical artefact, while the Hawking radiation exists quite independently of the physics at the high-energy scale [79, 80][18]. This discovery has prompted a great deal of interest in the analogue black holes and many wonder whether such a phenomenology could be applied to the case of real black holes [82–84]; as of today, the question of the applicability of these results to the gravitational case is still an open issue. However, it is very important to stress that the mechanism by which the Hawking radiation is recovered in these systems is conceptually different, depending on the type of dispersion relation considered. Furthermore, any demonstration of this effect in an dumb hole would not imply anything about Bekestein's entropy or on the laws of black-hole thermodynamics [85], as the two realms rely on completely different equation of motions (Einstein's equations in one case and Navier-Stokes equations in the other)[19]. For this reason, for the sake of clarity, it is preferable to refer to this effect as the **analogue Hawking radiation**, instead of simply the "Hawking radiation". As Unruh himself stated:

> "*Even the direct observation of thermal quantum radiation from an analog horizon does not prove that black holes will radiate. Something could make the gravitational system behave differently from any analog system. It is however very hard to imagine what that could be. The derivation of the thermal radiation from analog horizons follows so closely the derivation of thermal radiation from black hole horizons that it is very hard to imagine that one could occur but not the other*" [47].

Nevertheless, even if these black hole analogies might not teach us about quantum gravity directly, they can demonstrate the ways in which the Hawking spectrum might change in response to new physics at the Planck scale. Perhaps, more importantly, they offer a chance to study Hawking radiation as a general phenomenon related to the restless nature of the quantum vacuum; any insight into the origin of this vacuum radiation [86, 87] is to be welcomed.

This completes the introductory part about the analogue gravity paradigm and the Hawking effect in sonic black holes. As of today, the question of the validity of Hawking's theories is still open, as we lack a clear experimental evidence of this radiation from an (analogue) horizon. Nevertheless, many important results have been obtained in the past years and a few claims on the observation of this effect in analogue black holes were made but none of them generated a general consensus in the scientific community (see, among others, the experiments realized in fused silica [55], water tanks [70, 88, 89], and BECs [65, 66], which have drawn much attention but also criticisms on the interpretation of the results [90–95]). Also, during the writing of this Thesis other two experimental results have claimed the observation of the phenomenon [96, 97].

---

[18] Different conclusions are reached if one includes capillarity in hydrodynamics [81].

[19] For this reason Matt Visser recently proposed to change the name of the field from "analogue gravity" to "analogue spacetimes", in order to avoid confusion.

1.4.1 The analogue gravity paradigm

Up to this point we have described the analogy between hydrodynamics and black holes only in a qualitatively way but we now wish to demonstrate this relation from a rigorous mathematical point of view.

In fluid dynamics a system is defined by means of three fundamental equations [53]: the **equation of continuity** (which expresses mass conservation), the **Euler equation** (equivalent to Newton second law applied to small lumps of fluid) and an **equation of state** (which relates the thermodynamical quantities). Their form is[20]:

$$\begin{cases} \partial_t \rho + \boldsymbol{\nabla} \cdot (\rho \mathbf{v}) = 0\,, \\ \rho \left[\partial_t \mathbf{v} + (\mathbf{v} \cdot \boldsymbol{\nabla})\mathbf{v}\right] = -\boldsymbol{\nabla} p\,, \\ p = p(\rho) \end{cases} \tag{1.69}$$

and since we have five equations and five independent variables, the dynamics of our system is completely determined by this set.

A quick look at the three equations immediately leads to one trivial solution: the case of a static, homogeneous inviscid fluid. In this case we have:

$$\begin{cases} \mathbf{v} = 0\,, \\ \rho = \mathrm{cost} = \tilde{\rho}\,, \\ p(\tilde{\rho}) = \mathrm{cost} = \tilde{p}\,. \end{cases} \tag{1.70}$$

We can now ask the following question: if we take small perturbations around the equilibrium state, how do these fluctuations evolve? We can study that by **linearising** our equations around a known solution. Applying this procedure to the trivial solution (1.70) we obtain a second order equation of the type:

$$\boxed{\partial_t^2 f = c^2 \nabla^2 f} \tag{1.71}$$

with $f = p'$, ρ' or ϕ' (where $\mathbf{v}' = -\boldsymbol{\nabla}\phi'$); they represent, respectively, small perturbations in the pressure, density and velocity field (ϕ' is the velocity potential). As we already stated in the previous Section, sound is *defined* to be these fluctuations in the dynamical quantities [53]. This means that, since Eq. (1.71) is the classical **wave equation**, sound is a wave which moves with a velocity

$$c = \sqrt{\left(\frac{\partial p}{\partial \rho}\right)_0}\,. \tag{1.72}$$

Now we will generalize this result to a fluid which is non-homogeneous or in motion (possibly even in non-steady motion) by proving the following theorem.

---

[20] We are assuming that there is no external forces and that the fluid is inviscid so the only forces present are those due to pressure.

Theorem *If a fluid is barotropic, inviscid and the flow is irrotational (though possibly time dependent) then the equation for the velocity potential describing an acoustic disturbance is identical to the d'Alembertian equation of motion for a minimally-coupled massless scalar field propagating in a (3+1) Lorentzian geometry*

$$\Delta\phi = \frac{1}{\sqrt{-g}}\partial_\mu\left(\sqrt{-g}g^{\mu\nu}\partial_\nu\phi\right) = 0. \tag{1.73}$$

Under these conditions, the propagation of sound is governed by an ***acoustic metric*** $g_{\mu\nu}(t,\boldsymbol{x})$*. This acoustic metric describes a (3+1)-dimensional Lorentzian (pseudo-Riemannian) geometry and it depends algebraically on the density, velocity of flow and local speed of sound of the fluid. Specifically*

$$g_{\mu\nu}(t,\mathbf{x}) \equiv \frac{\rho}{c}\left[\begin{array}{ccc} -(c^2-v^2) & \vdots & -\mathbf{v}^T \\ \cdots & \cdot & \cdots \\ -\mathbf{v} & \vdots & \mathbf{I} \end{array}\right]. \tag{1.74}$$

Here ***I*** *is the* 3×3 *identity matrix. In general, when the fluid is non-homogeneous and flowing, the acoustic Riemann tensor associated with this metric will be non-zero.*

This theorem is the core of the gravitational analogy. That is, it can be proved (and we will do that shortly) that **the equations governing the dynamics of sound propagating in a moving fluid are exactly the same as of a scalar field propagating in a curved geometry (that is, the same as light in a gravitational field)**. Also, the type of geometry we obtain describes certain classes of Lorentzian spacetimes, including black holes. This is quite remarkable if we remember that the underlying fluid dynamics is Newtonian, non-relativistic.

Proof Let us start from an inviscid, irrotational, barotropic, non-homogeneous, moving fluid which, by definition, obeys the dynamics fundamental equations (1.69). The second of these equations[21] can be rewritten as

$$\partial_t\mathbf{v} = \mathbf{v}\times(\boldsymbol{\nabla}\times\mathbf{v}) - \frac{1}{\rho}\boldsymbol{\nabla}p - \boldsymbol{\nabla}\left(\frac{1}{2}v^2\right). \tag{1.75}$$

Since the fluid is taken to be vorticity free (that is, locally irrotational), the first term in the right-hand side of the previous equation disappears. Then, we introduce the velocity potential $\mathbf{v} = -\boldsymbol{\nabla}\phi$ and we use the fact that the fluid is

---

[21] Remember that here, as in Eq. (1.69), we are exploiting the fact that the fluid is inviscid (zero viscosity). That is, in absence of external forces, the only forces present are those due to pressure. It would be straightforward to add external forces, at least conservative ones, such as Newtonian gravity.

barotropic (that is, ρ is a function of p only) so to define the *specific hentalpy* $h(p)$:

$$h(p) = \int_0^p \frac{\mathrm{d}p'}{\rho(p')} \quad \text{so that} \quad \boldsymbol{\nabla} h = \frac{1}{\rho}\boldsymbol{\nabla} p. \tag{1.76}$$

Substituting these in the second equation, our system becomes:

$$\begin{cases} \partial_t \rho + \boldsymbol{\nabla}\cdot(\rho \mathbf{v}) = 0\,, \\ -\partial_t \phi + h + \dfrac{1}{2}(\boldsymbol{\nabla}\phi)^2 = \text{const}\,. \end{cases} \tag{1.77}$$

Up to this point we have just rewritten the Euler equation in another form (a version of Bernoulli's equation). To proceed, we will now linearise the equations obtained around a known solution.

We start from some solution (ρ_0, p_0, ϕ_0) (which represents our background) and we try to see how small perturbations around this equilibrium point evolve. For this reason we take:

$$\begin{cases} \rho = \rho_0(\mathbf{r}, t) + \epsilon\rho_1 + O(\epsilon^2)\,, \\ p = p_0(\mathbf{r}, t) + \epsilon p_1 + O(\epsilon^2)\,, \\ \phi = \phi_0(\mathbf{r}, t) + \epsilon\phi_1 + O(\epsilon^2)\,. \end{cases} \tag{1.78}$$

Then, by using the equations of dynamics, we can study the linearised perturbations. The equations for (ρ_1, p_1, ϕ_1) so obtained describe the propagation of sound in a moving fluid. It is important to point out that traditionally, in the linearisation procedure, the motion of the exact solution (ρ_0, p_0, ϕ_0) and the one of the low-amplitude (acoustic) disturbances $(\epsilon\rho_1, \epsilon p_1, \epsilon\phi_1)$ are treated order by order. That means that, since the perturbations are small, they are assumed to not influence the background motion and so, at order zero, we recover the equations we started from. Moreover, sufficiently low-frequency, long-wavelength disturbances (wind gusts) are conventionally lumped in with the average bulk motion, while higher-frequency, shorter-wavelength disturbances are conventionally described as sound waves [98].

We will now skip the calculations (they can be found, for example, in [75] and [99]) and we will only describe the main steps. They are: take the first order Bernoulli equation and explicit p_1; then derive ρ_1 exploiting the barotropic assumption (that is $\rho_1 = \frac{\partial\rho}{\partial p} p_1$); finally, insert these two quantities into the first order continuity equation to obtain:

$$\partial_t\left(\frac{\partial\rho}{\partial p}\rho_0(\partial_t\phi_1 + \mathbf{v}_0\cdot\boldsymbol{\nabla}\phi_1)\right) - \boldsymbol{\nabla}\cdot\left(\rho_0\boldsymbol{\nabla}\phi_1 - \frac{\partial\rho}{\partial p}\rho_0(\partial_t\phi_1 + \mathbf{v}_0\cdot\boldsymbol{\nabla}\phi_1)\right) = 0. \tag{1.79}$$

Starting from this wave equation we can determine ϕ_1 and, using Bernoulli equation and the barotropic assumption, we completely determine the propagation of acoustic disturbances.

At this point we want to remind that this derivation is exactly the same for the simple wave equation (1.71), the difference being in the fact that now the background fields (ρ_0, p_0, ϕ_0) are time-dependent and position-dependent and so $\rho_0 = \rho_0(\mathbf{r}, t)$, $p_0 = p_0(\mathbf{r}, t)$, $\phi_0 = \phi_0(\mathbf{r}, t)$; in fact, if we now take the background field (our known solution) to be static and homogeneous (the trivial solution) we have p_0 =cost, ρ =cost, $\mathbf{v}_0 = 0$ and if we insert these into Eq. (1.79), we recover Eq. (1.71).

We now substitute the definition of the speed of sound (1.72) (which now becomes space and time dependent) into Eq. (1.79) and construct the 4 × 4 symmetric matrix:

$$f^{\mu\nu}(t, \mathbf{x}) \equiv \frac{\rho_0}{c^2} \left[\begin{array}{ccc} 1 & \vdots & v_0^j \\ \cdots & \cdot & \cdots \\ v_0^i & \vdots & -(c^2 \delta^{ij} - v_0^i v_0^j) \end{array} \right] . \tag{1.80}$$

Then, introducing the (3+1)-dimensional space-time coordinates $x^\mu \equiv (t; x^i)$, equation (1.79) can be rewritten as

$$\partial_\mu (f^{\mu\nu} \partial_\nu \phi_1) = 0. \tag{1.81}$$

Now, in any Lorentzian manifold the scalar d'Alembertian has the form

$$\Delta\phi = \frac{1}{\sqrt{-g}} \partial_\mu \left(\sqrt{-g} g^{\mu\nu} \partial_\nu \phi \right) , \tag{1.82}$$

where $g_{\mu\nu}(t, \mathbf{x})$ is the metric, $g^{\mu\nu}(t, \mathbf{x})$ is the point-wise inverse metric and $g \equiv \det(g_{\mu\nu})$. Thus, we can identify

$$\sqrt{-g}\, g^{\mu\nu} = f^{\mu\nu} \tag{1.83}$$

and this implies that, on one hand,

$$\det(f^{\mu\nu}) = (\sqrt{-g})^4\, g^{-1} = g\,, \tag{1.84}$$

and, on the other hand,

$$\det(f^{\mu\nu}) = -\frac{\rho_0^4}{c^2}. \tag{1.85}$$

Thus

$$g = -\frac{\rho_0^4}{c^2} \quad \text{and} \quad \sqrt{-g} = \frac{\rho_0^2}{c}\,, \tag{1.86}$$

which automatically leads us to the inverse acoustic metric tensor:

$$g^{\mu\nu}(t, \mathbf{x}) \equiv \frac{1}{\rho_0 c} \left[\begin{array}{ccc} 1 & \vdots & v_0^j \\ \cdots & \cdot & \cdots \\ v_0^i & \vdots & -(c^2 \delta^{ij} - v_0^i v_0^j) \end{array} \right] . \tag{1.87}$$

Inverting this matrix we finally obtain the **acoustic metric tensor** $g_{\mu\nu}(t, \mathbf{x})$:

$$g_{\mu\nu} \equiv \frac{\rho_0}{c} \left[\begin{array}{ccc} (c^2 - v_0^2) & \vdots & v_0^j \\ \cdots & \cdot & \cdots \\ v_0^i & \vdots & -\delta^{ij} \end{array} \right] . \tag{1.88}$$

We have thus proved the theorem and we have given a rigorous mathematical and physical description of the analogy existent between light propagating in a curved spacetime and sound propagating in a moving fluid [22].

A much simpler way to obtain the same result is to work in the geometrical acoustic approximation. At this level we only need to assume that we know two things:

- the speed of sound c, relative to the fluid;
- the velocity of the fluid $\mathbf{v}$, relative to the laboratory.

Then, relative to the laboratory, the velocity of a sound ray propagating, with respect to the fluid, along the direction defined by the unit vector $\mathbf{n}$, is

$$\frac{\mathrm{d}\mathbf{x}}{\mathrm{d}t} = c\,\mathbf{n} + \mathbf{v}. \tag{1.89}$$

That defines a sound cone in spacetime given by the condition $\mathbf{n}^2 = 1$, i.e.,

$$c^2\,\mathrm{d}t^2 - (\mathrm{d}\mathbf{x} - \mathbf{v}\,\mathrm{d}t)^2 = 0. \tag{1.90}$$

That is

$$[c^2 - v^2]\,\mathrm{d}t^2 + 2\mathbf{v}\cdot\mathrm{d}\mathbf{x}\,\mathrm{d}t - \mathrm{d}\mathbf{x}\cdot\mathrm{d}\mathbf{x} = 0. \tag{1.91}$$

This *acoustic line element* defines a conformal class of Lorentzian metrics such as the one of Eq. (1.88). The advantage of the geometrical acoustics approach is that the derivation of the precise mathematical form is very simple and it is extremely general. The limit, though, is that one can only deduce the causal structure of the spacetime and does not obtain an unique effective metric. In order to do so, we need to turn to the other limit (i.e. physical acoustics) which leads to the theorem we have described above.

From the form of this effective metric (1.88) two observations can be made. First of all, note that, if $|v_0| < |c|$, the signature of this effective metric is $(+,-,-,-)$ as it should be to be regarded as "Lorentzian" (a necessary condition for a manifold to be a spacetime). Second, at this level there are two distinct metrics in our model:

- A *physical spacetime metric*, which is just the usual metric of Minkowski spacetime $\eta_{\mu\nu}$. The fluid particles couple only to this metric and since $|v_0| \ll c_{\text{light}}$ it is sufficient to consider Galilean relativity and an Euclidean geometry. In fact, Euler equation in Eq. (1.69) has been written in the non relativistic limit.

---

[22] It is important to note that, historically, the acoustic metric (1.88) was first derived by White in 1973 [100], then by Anderson and Spiegel in 1975 [101] and then again by Moncrief in 1980, while studying the relativistic hydrodynamics of accretion flows surrounding black holes [102].

- An *effective acoustic metric*, which is the one we derived in this Section. Sound waves (that is, acoustic perturbations) couple only to this one, as they "do not see" the underlying physical metric at all.

Now, as we mentioned in the previous Section, the Hawking effect is a purely kinematic effect that depends only on the existence of two things: a Lorentzian metric and a horizon. Having derived an effective metric, we can now complete the analogy by demonstrating the presence of an analogue of a black-hole horizon. In principle, defining the black-hole horizon in general relativity is no trivial task but in our case things simplify much.

As we already mention, a black hole is an object which traps everything in a region, light included. The boundary of this trapping region is known as the black-hole horizon. In GR there are two types of horizons: the *absolute* (or *event*) *horizon* and the *apparent horizon*. These two differ in the sense that the latter is an observer-dependent notion (so it is not strictly related to the spacetime itself) while the former is an invariant property of the spacetime itself and so it does not depend on the frame of reference. In the context of analogue gravity, though, these two notions coincide thanks to the background Minkowski metric, which provides us with a natural time parameter. Thus, we can define our acoustic horizon starting from any of the two definitions that appear in general relativity[23].

In analogy with the gravitational case, we can define **the acoustic event horizon (acoustic absolute horizon)** as the boundary of the region from which null geodesics (phonons, in our case) cannot escape. This implies that the fluid velocity needs to be greater than the sound velocity in the medium. In fact, starting from the acoustic metric (1.88) we can parametrize a geodesic as $x^\mu(t) = (t; \mathbf{x}(t))$. Again, this is possible thanks to the real spacetime metric, which provides a natural time parameter. Given this path, the null condition implies

$$g_{\mu\nu}\frac{\mathrm{d}x^\mu}{\mathrm{d}t}\frac{\mathrm{d}x^\nu}{\mathrm{d}t} = 0\,, \tag{1.92}$$

which is, neglecting the conformal factor,

$$(c^2 - v_0^2) + 2v_0^i\frac{\mathrm{d}x^i}{\mathrm{d}t} - \frac{\mathrm{d}x^i}{\mathrm{d}t}\frac{\mathrm{d}x^i}{\mathrm{d}t} = 0 \quad\Longrightarrow\quad \left\|\frac{\mathrm{d}\mathbf{x}}{\mathrm{d}t} - \mathbf{v}_0\right\| = c \tag{1.93}$$

where the norm is taken in the flat physical metric. This last equation tells us that rays which travel on null geodesics move at the speed of sound relatively to the moving fluid; this means that, in order to have a trapped region - i.e. a horizon -, we need the velocity of the fluid to be greater than the speed of sound in the medium.

---

[23] Also, note that the Hawking radiation requires only an apparent horizon (the presence of an event horizon is a stronger requirement which is not needed [103]).

If we recall the form of the effective metric (1.88), we see that the signature is $(-,-,-,-)$ if $|v_0| > |c|$ and thus the metric is not Lorentzian in this case; this, therefore, implies that the analogy is broken for the region inside the black-hole horizon (as we would have expected, given the completely different nature of the physical systems at display).

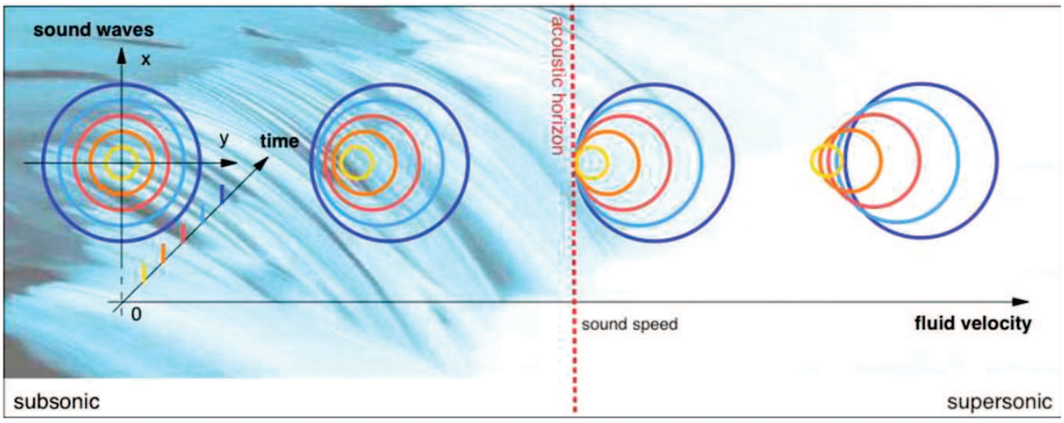

Figure 1.11: A moving fluid can form an acoustic horizon when supersonic flow prevents upstream motion of sound waves.

Finally, it is worth pointing out one last thing: that is, how stationary geometries properties translate to our acoustic analogues. As we already described, in GR a spacetime is said to be stationary if it has a Killing field which is time-like. If we now recall the form of our acoustic metric (1.88), we see that the condition

$$\frac{\partial P}{\partial t} = 0\,, \tag{1.94}$$

where P is any of the dynamical variables ρ_0, v_0 or c, implies that the acoustic metric is time-independent. Thus, in terms of the analogy,

$$\text{stationary spacetimes (relativity)} \quad \Longleftarrow \quad \text{steady flows (acoustics)}\ .$$

This, in turn, gives us an easy way to define a surface gravity constant on the horizon, which is a requirement Hawking radiation has to fulfil.

1.4.2 The Schwarzschild geometry as an example of the analogy

At this point it is interesting to step back and recall the results about the Schwarzschild metric that we derived in Section 1.2. During that discussion we noted how the Schwarzschild coordinates (t_S, r, θ, ϕ) were not fitted to generally describe the physics of the spacetime, as they treated the horizon as a singularity (which, we now know, it is not). The way to address this problem is to choose coordinates that behave regularly at the horizon, such as the ones introduced by Painlevé [104], Gullstrand [105] and Lemaître [106] (as mentioned at the end of Section 1.2, we can opt for other choices too). They suggested the introduction of a new time

$$t = t_S + 2\frac{\sqrt{r_S r}}{c} + \frac{r_S}{c}\ln\left(\frac{\sqrt{\frac{r_S}{r}}-1}{\sqrt{\frac{r_S}{r}}+1}\right), \tag{1.95}$$

which, when substituted in Eq. (1.2), yields the transformed metric

$$ds^2 = c^2dt^2 - \left(dr + c\sqrt{\frac{r_S}{r}}dt\right)^2 - r^2d\Omega^2. \tag{1.96}$$

In these coordinates the metric clearly has no singularity at $r = r_S$, since the coefficients are all regular there.

Now, let us try to interpret the metric (1.96). We shall consider only radial trajectories, setting $d\Omega^2 = 0$. The key point is that, if $dr/dt = -c\sqrt{\frac{r_S}{r}}$, the metric reduces to $ds^2 = c^2dt^2$. Since this condition clearly maximizes ds^2, these trajectories are geodesics and t measures proper time along them. It is as space consists of a (Galilean) fluid, flowing inwards with velocity $-c\sqrt{\frac{r_S}{r}}$ to converge on the point $r = 0$ and the geodesics just defined are those which are stationary with respect to this fluid. They define a locally inertial frame which we shall call the **co-moving frame**, and in this frame, i.e. with respect to the fluid, the speed of light is c. At the Schwarzschild radius the fluid flows inwards with speed c and anything that falls beneath this radius, no matter its velocity with respect to the spacetime fluid, will inexorably be dragged towards the centre at $r = 0$. This view is reinforced by looking at the light cones, which are determined by setting $ds^2 = 0$ and $d\Omega^2 = 0$. We find two possible trajectories for light:

$$\frac{dt}{dr} = \frac{1}{c}\left(\pm 1 - \sqrt{\frac{r_S}{r}}\right)^{-1}. \tag{1.97}$$

The $(+)$ trajectory represents rays propagating against the fluid, while the $(-)$ trajectory represents rays propagating with the fluid. In the latter case rays propagate (with respect to the frame in which the fluid is still) with total velocity $-c - c\sqrt{\frac{r_S}{r}}$, the sum of the light velocity and the fluid velocity. It is clear that this trajectory is perfectly regular at the horizon, in contrast with the Schwarzschild coordinates' case. Instead, in the $(+)$ case rays have a total velocity of $c - c\sqrt{\frac{r_S}{r}}$. This trajectory is not regular at the horizon, since the velocities of the fluid and the light exactly cancel out, giving a total velocity of zero. Rays at higher radii will have a positive total velocity, and will eventually escape to infinity; rays at smaller radii will have a negative total velocity, unable to overcome the fluid flow, and will propagate inwards to $r = 0$.

This reasoning is an alternative way to arrive at the analogy we have defined earlier. We may simply replace $-c\sqrt{\frac{r_S}{r}}$ in Eq. (1.96) with the more general velocity profile $v(x)$ to obtain, in $(1+1)$-dimensional spacetime, the metric

$$ds^2 = c^2 dt^2 - (dx - v(x)dt)^2 \,, \tag{1.98}$$

where now c is to be interpreted as the velocity with respect to the medium in question (not necessarily the speed of light). This is exactly the acoustic line element introduced in the previous Section. The co-moving frame, then, is the frame in which this medium is at rest, and in which the wave speed is exactly c. By contrast, the frame with coordinates x and t shall henceforth be called the **lab frame**. We underline that the general metric (1.98) need not be gravitational in origin. It may, for example, be applied to a system as far cry from astrophysics as a flowing river, as illustrated in Fig. (1.12). In this case the above metric suffices to describe the trajectories of sound waves in this river, which are analogous to the trajectories of light near an event horizon.

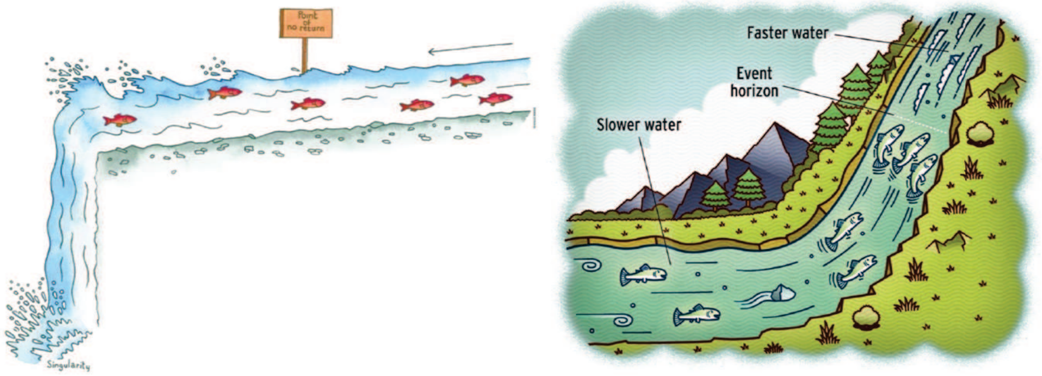

(a) (b)

Figure 1.12: In both these drawings the fish do not have enough speed to flow against the current. In figure (a) they are forced to flow towards the waterfall (thus it represents the analogue of a black-hole horizon) while in (b) they cannot enter the region of the waterfall (this is the analogue of a white-hole horizon). The first drawing is taken from [107] while the second is from [108].

Chapter 2

Bose-Einstein condensates

In this Chapter we spend some time introducing the concept of Bose-Einstein Condensation and discussing the main features of these systems, as they will provide the framework in which this work on the analogue Hawking radiation developed. In particular, Section 2.1 and 2.2 describe the concept of ideal Bose gases while Section 2.3 refines the picture by introducing interactions. In Section 2.4 and 2.5 we discuss the main results that we will use in our work (namely the *Gross-Pitaevskii equation* and the *Tonks-Girardeau gas*) and in Section 2.6 and 2.7 we extend the analogue gravity paradigm to the case of quantum gases, describing the main features of the analogue Hawking radiation.

2.1 A new phase of matter

Bose-Einstein condensation is a very interesting and purely quantum phenomenon. It takes place in systems of bosons cooled down to extremely low temperature and it is associated with a new phase of matter. Indeed, due to their quantum nature, a system of non-interacting bosons at $T \to 0$ behaves like a single entity, since all the particles are allowed to stay in the single-particle ground state. In other words, if N_0 is the number of atoms in the single-particle ground state and N is the total number of atoms in the system, Bose-Einstein condensation occurs when $N_0 \gg 1$ and the ratio N_0/N remains finite in the thermodynamic limit $N \to +\infty$ [109].

The reason behind the vast interest that concerns the physics of ultra-cold atoms resides in the fact that quantum phenomena, which are confined at atomic scales and thus are usually imperceivable, become macroscopic given that we lower the temperature under a critical threshold. These phenomena are so important (and fascinating) that between 1995 and 2003 four Nobel prizes were given to works associated to macroscopic quantum behaviours[1]. To this extent, among the most astonishing discoveries of the last decades, we need to mention the phenomena of superconductivity and superfluidity (discovered in 1911 and 1937 respectively); they are macroscopic manifestations of coherent behaviours, which are due purely to the quantum nature of the systems. The study of these phenomena has vastly contributed to many disparates fields, such as medicine or computer technology. In particular, the physics of ultra-cold atoms has experienced an intense growth in the past two decades, after the first experimental realizations of a Bose-Einstein condensate (BEC) in 1995 [110, 111] (Fig. 2.1).

The founding idea of Bose-Einstein condensation dates back to the 1920s. In 1924, Indian physicist S. N. Bose published a paper devoted to the statistical description of quanta of light [112]; the year after, A. Einstein on the basis of the aforementioned work, predicted the occurrence of a phase transition in a gas of non-interacting atoms [113]. This phase transition was associated with the "condensation" of atoms in the lowest energy state due to quantum statistical effects. For a long time these predictions had no practical impact but in 1938, immediately after the discovery of superfluidity in liquid helium [114, 115], F. London realized that superfluidity could be the manifestation of Bose-Einstein condensation [116]. The first self-consistent theory of superfluids was developed by L. Landau in 1941 [117] and in 1947 N. N. Bogoliubov (the Russian physicist who gave the name to the previously introduced "Bogoliubov transformations") derived the first microscopic theory of interacting Bose gases, based on the concept of BEC [118]. In the following years, great steps forward were taken,

---

[1] They were given for: the discovery of the superfluidity in ^{3}He (1996), the discovery of the fractional quantum Hall effect (1998), the observation of Bose-Einstein condensation (2001) and for the contributions to the theory of superconductors and superfluids (2003).

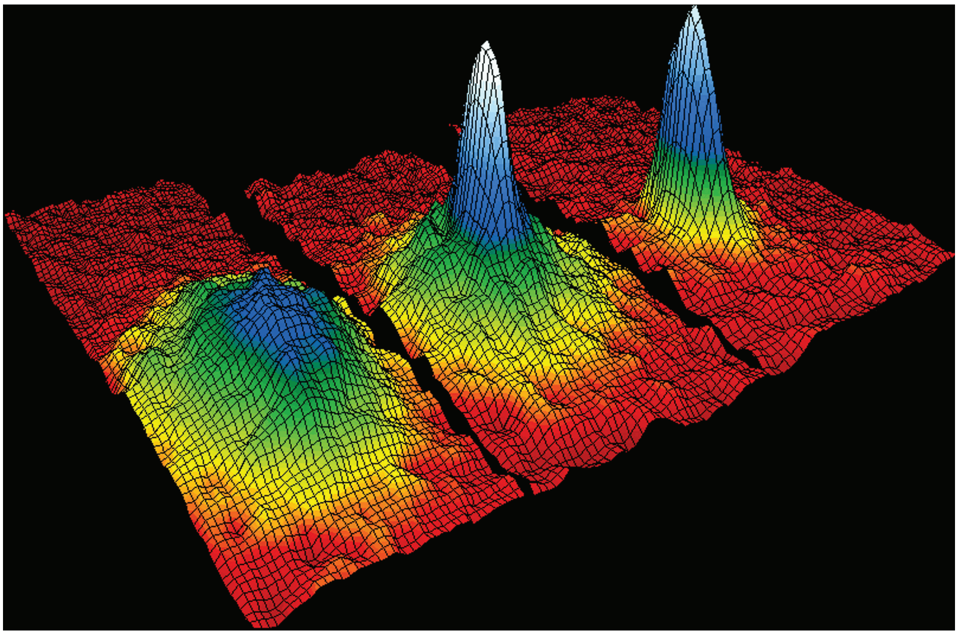

Figure 2.1: The famous image from the experiment held in 1995 at the laboratories of JILA (Joint Institute for Laboratory Astrophysics), an American faculty jointly operated by the University of Colorado (CU) and the National Institute of Standards and Technology (NIST). It shows the velocity distribution for a gas of ^{87}Rb at the temperature of 170 nK and it holds as the proof of the existence of a new phase of matter. The left panel shows the system at a temperature just before the appearance of a BEC, the center one the temperature of formation and the right panel shows the system after further evaporation, which leaves a sample of nearly pure condensate. The observation of Bose-Einstein condensation has rewarded E. Cornell, C. Wieman and W. Ketterle with the 2001 physics Nobel prize.

thanks to the works of L. Landau, E. Lifshitz, O. Penrose (not to be confused with R. Penrose, whom we have cited for the "Penrose diagrams" used in GR), L. Onsager and R. Feynman. However, experimental works on dilute atomic gases were developed much later, starting from the 1970s, and made use of new techniques based on magnetic and optical trapping. In the 1980s, laser-based techniques (such as magneto-optical trapping and laser cooling) were developed to trap and cool atoms, in particular alkali (for a detailed list of works see, e.g., [119]). Finally, in the 1990s, by combining different cooling techniques, the experimental teams of E. Cornell and C. Wieman at Boulder and of W. Ketterle at MIT succeeded in reaching the temperatures and the density required to observe BEC in vapours of ^{87}Rb [110] and ^{23}Na [111]. It is important to notice that, in these conditions, the equilibrium configuration of the system is the solid state and thus, in order to observe BEC, one has to preserve the gas in a metastable state for a sufficiently long time, which is one of the main challenges about the experimental realization of this phase of matter. Indeed, in the 1995 experiment at Boulder, a few hundred thousands atoms of Rubidium were cooled at the temperature of 170 nK in order to enter the quantum regime; it is well-known, in fact, that quantum effects become relevant when the *de Broglie wavelength* of the particle becomes bigger than the characteristic size of the system. In terms of the gas density, that means

$$\lambda = \frac{h}{\sqrt{3mk_BT}} > n^{-1/3} \tag{2.1}$$

which gives an idea of why such low temperature is needed[2]. At the same time, though, as temperature lowers, atoms get closer and closer and when they reach the binding distance R_0 the system enters the solid state, preventing any further phase transition. Thus, the atoms needs to be kept at distance so that they "cannot realize" the energetic gain that solidification implies; in terms of the density this means

$$nR_0^3 \ll 1 \tag{2.2}$$

and this justifies the low densities needed. To summarize, the experimental achievement of these systems implied a problem of fine tuning of the density in order to reach sufficiently low scales but without losing the gas phase. Months after the success by the team at JILA with ^{87}Rb atoms, the BEC phase was obtained also in ^{23}Na [111] and ^{7}Li [120].

The number of experiments of BECs have increased rapidly over the years [119]. One of the main characteristics of these trapped gases is that they are inhomogeneous and finite sized with number of atoms ranging from a few thousands to several millions. In most cases the confining traps can be well-approximated by harmonic potentials, which makes the theoretical treatment of these systems quite simple. Also, the fact they are highly inhomogeneous has several important consequences, first and foremost the fact that BEC can appear not only in the momentum space (Fig. 2.1) but also in coordinate space as a sharp peak in the velocity/spatial distribution (this is not the case, for example, of uniform gases). In order to detect this, in the first case one lets the condensate expand freely by turning off the trap and then measures the density of the expanded cloud with light absorption (it is the case, for example, of the 1995 JILA experiment); if the particles do not interact, the expansion is ballistic and the imaged spatial distribution of the cloud can be related to the initial momentum distribution. In the second case, one measures directly the density of the atoms in the trap by means of dispersive light scattering [121]. In both cases, BEC appears as a sharp peak in the relative distribution.

In the following, after an introduction on the ideal Bose gases and on the fundamental results regarding identical particle statistics, we will turn our attention to dilute BECs, which allow us to describe the effects of the interactions in a rather fundamental way and represent a good approximation for the set-ups

---

[2] We are using a rough approximation to convey the idea of the temperature regimes one needs to enter in order to see the quantum effects. In reality, in order to observe the condensed phase of bosons, there is a specific critical temperature T_c that rules the appearance (or not) of the condensed phased; we will describe this fact in details in the next Section.

and the calculations we will encounter in our quest for the analogue Hawking radiation. Therefore, we will introduce the Gross-Pitaevskii equation and use the Bogoliubov formalism for the characterization of the excitation spectrum.

2.2 Ideal Bose gases

The *spin-statistic theorem* [122] is a well-known result in physics, which asserts that particles can obey only one of two possible statistics, depending on their spin. That is, they can only be *fermions* (semi-integer spin) or *bosons* (integer spin). This fact is related to the evidence that particles, at quantum level, are intrinsically undistinguishable. This implies that the wave function of an ensemble of identical particles needs to be symmetrized (that is, it has to be either symmetric or antisymmetric). As a consequence, there exist only two possible statistics for quantum particles: *Bose-Einstein statistic* [112, 113] for bosons (systems whose wave function is symmetric) and *Fermi-Dirac statistic* [123, 124] for fermions (systems whose wave function is antisymmetric). They have the form

$$\bar{n}_i = \frac{1}{e^{\beta(E_i-\mu)} \pm 1} \,. \tag{2.3}$$

where the + stands for fermions and the − for bosons, $\beta = 1/K_B T$, E_i is the energy of the i-th state and $\bar{n}_i$ is the average number of particles in that state.

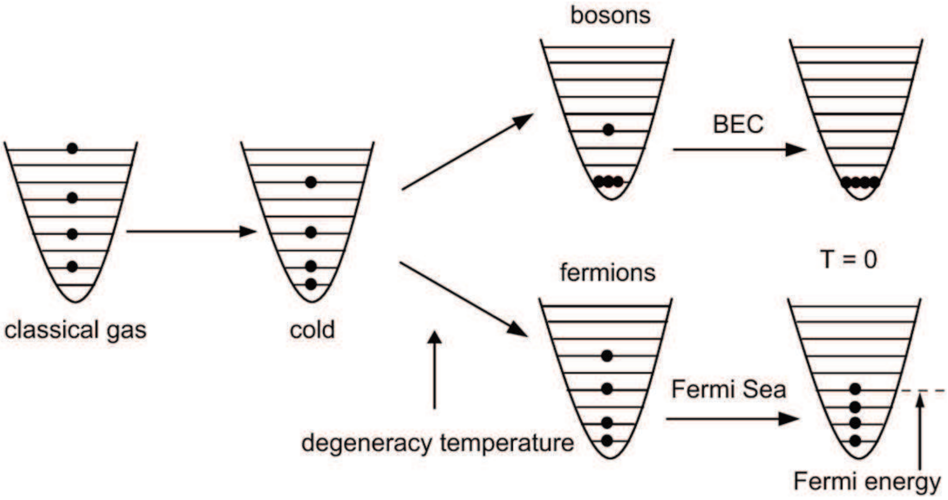

Figure 2.2: Behaviour for classical and quantum particles as the temperature decreases. The symmetry of the total wave function allows the bosons to share the same quantum state (the condensed phase) while fermions can occupy only different states, filling the so-called *Fermi sea* up to the *Fermi energy*.

The formulas (2.3) describe, from a statistical point of view, the behaviour of ideal Bose/Fermi gases and they can be derived starting from the grand canonical ensemble formalism. We will not enter the details of the calculations as they can be found in [109] but it is nevertheless useful to outline the procedure.

In the grand canonical ensemble, the probability of having N' particles in a state k of energy E_k is given by

$$P_{N'}(E_K) = \frac{1}{Z(\beta,\mu)}\, e^{\beta(\mu N' - E_k)}\,, \tag{2.4}$$

where μ is the chemical potential of the reservoir with which the system is in thermal equilibrium and the grand partition function is

$$Z(\beta,\mu) = \sum_{N'=0}^{\infty} e^{\beta\mu N'} Q_{N'}(\beta)\,. \tag{2.5}$$

$Q_{N'}(\beta) = \sum_k e^{-\beta E_k}$ is the canonical partition function for a system of N' particles and the sum $\sum_k$ runs over a complete set of eigenstates of the Hamiltonian with respective energies E_k. From the grand partition function one can calculate the grand canonical potential Ω, which gives the connection to the thermodynamics of the system:

$$E - TS - \mu N = \Omega = -k_B T \ln Z\,. \tag{2.6}$$

Now, let us consider a system of ideal particles (that is, non-interacting) so that we can write the Hamiltonian as

$$\widehat{H} = \sum_i \widehat{H}_i\,. \tag{2.7}$$

In this case the eigenstates k are defined by specifying the set $\{n_i\}$ of the microscopic occupation numbers n_i of the single-particle states, obtained by solving the Schrödinger equation

$$\widehat{H}_i \varphi_i(\mathbf{r}) = E_i \varphi_i(\mathbf{r})\,. \tag{2.8}$$

Then, in the formalism of *second quantization*, the state

$$|k\rangle = (a_0^\dagger)^{n_0}(a_1^\dagger)^{n_1} ... \,|0\rangle \tag{2.9}$$

completely specifies the many-body eigenstate of the Hamiltonian (2.7). Here $a_i^\dagger$, a_i are the particle creation (annihilation) operators relative to the ith single-particle state. They obey the commutation rule $[a_i, a_j^\dagger] = \delta_{ij}$ for bosons and the anti-commutation rule $\{a_i, a_j^\dagger\} = \delta_{ij}$ for fermions, while $|0\rangle$ is the particle vacuum state, that is $a_i\,|0\rangle = 0\ \forall i$.

Now, the main idea is that for a system of independent particles - that is, with an Hamiltonian of the form (2.7) - the grand partition function (2.5) can be evaluated exactly. One only has to remember that sums regarding number of

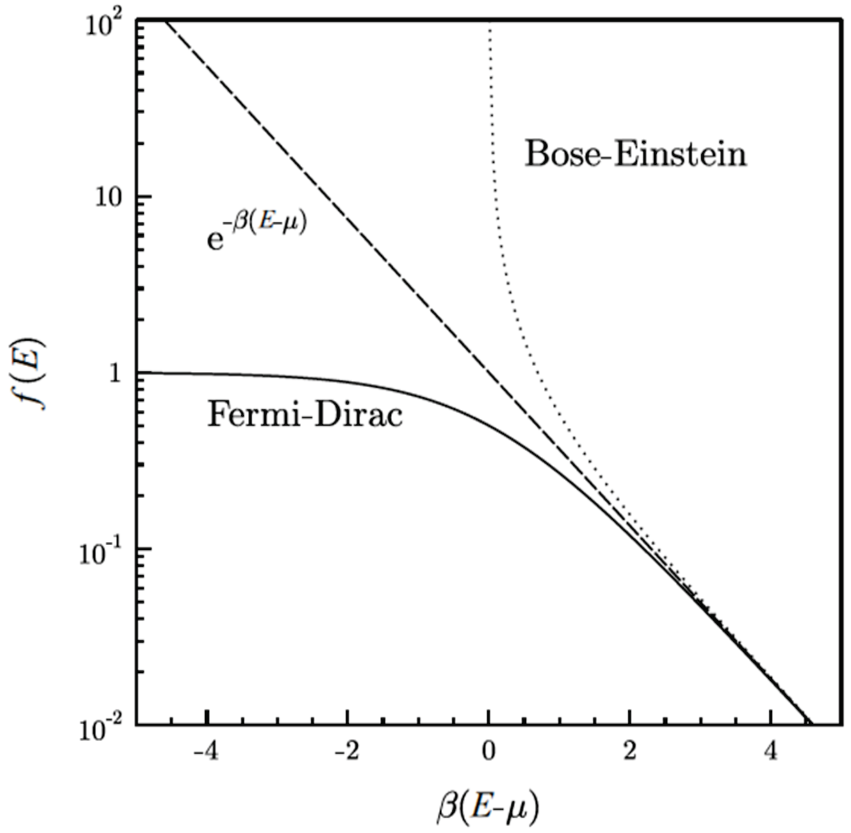

Figure 2.3: The classical Boltzmann distribution and the two possibilities for the quantum statistics as $\beta(E_i - \mu)$ varies.

particles in the same state can run up to ∞ for bosons while they can only assume values 0 or 1 in the case of fermions (this is *Pauli exclusion principle* and it comes from the anti-commutation of fermionic operators). The results, then, are exactly Eqs. (2.3).

Note that, in the limit $\beta(E_i - \mu) \gg 1$, both functions tend to the Boltzmann distribution $e^{-\beta(E_i-\mu)}$ which is the thermal distribution for classical particles (Fig. (2.3)). This is because this limit corresponds to low densities and high temperatures ($\beta\mu$ large and negative) and there are many more states thermally accessible to the particles than there are particles; thus, double occupancy never occurs and the requirements of exchanging symmetry become irrelevant and both fermions and bosons behave like classical particles. Also, note that for the case of bosons Eq. (2.3) diverges if $\mu = E_i$ and thus the chemical potential must always be smaller than the ground state energy; in particular, when $\mu \to E_0$ the number or particles in the ground state

$$N_0 \equiv \bar{n}_0 = \frac{1}{e^{\beta(E_0-\mu)} - 1} \tag{2.10}$$

becomes increasingly large. This is the mechanism at the origin of Bose-Einstein condensation and we will now briefly describe it. We will not talk now about the behaviour of the fermion gas as $T \to 0$ but will come back to this matter in a further Section.

Let us now turn our attention to the ideal Bose gas. We see from Eq. (2.10) that, as $\mu \to E_0$, the ground state becomes macroscopically occupied. In order to better understand the physics behind this phenomenon, let us write the total number of atoms of our system as the condensed phase + the thermal fraction; that is

$$N = N_0 + N_T \,, \tag{2.11}$$

where

$$N_T(T, \mu) = \sum_{i \neq 0} \bar{n}_i(T, \mu) \,, \tag{2.12}$$

is the number of particles out of the condensate, also called the "thermal component" of the gas. It can be shown [109] that, for a fixed temperature, the function N_T has a smooth behaviour as a function of μ and it reaches a maximum N_c at $\mu = E_0$; on the other hand, N_0 is always of order 1, except when μ becomes close to E_0, where N_0 diverges. This means that if N_c is larger than N then Eq. (2.11) is satisfied for values of μ smaller than E_0 and N_0 is negligible with respect to N. Since $N_c(T)$ is an increasing function of T, this scenario takes place for temperatures higher than a critical temperature T_c defined as

$$N_T(T_c, \mu = E_0) = N \,. \tag{2.13}$$

Instead, if $N_c(T) < N$ (or, equivalently, $T < T_c$) then the contribution of the condensate is crucial in order to satisfy Eq. (2.11) and the value of μ will approach E_0 in the thermodynamic limit (that is, for $N \to +\infty$). This is represented in Fig. (2.4). Thus, the temperature T_c defines the critical temperature below which the phenomenon of Bose-Einstein condensation (that is, the macroscopic occupation of a single-particle state) takes place.

Now, let us apply this formalism to the case of a gas of non-interacting bosons confined in a box of volume V. Again, more details about the calculations can be found in [109] and here we will only mention the main steps in order to quickly arrive at the first important results of this treatment.

It this case the single-particle Hamiltonian has the well-known form $H = p^2/2m$ and solutions are plane waves

$$\varphi_{\mathbf{p}} = \frac{1}{\sqrt{V}} e^{i\mathbf{p}\cdot\mathbf{r}/\hbar} \,, \tag{2.14}$$

where we have used cyclic boundary conditions $\varphi(x, y, z) = \varphi(x + L, y, z)$ etc., with $L = V^{1/3}$, so that the energy is $E = p^2/2m$ and the momentum $\mathbf{p} = 2\pi\hbar\mathbf{n}/L$, where the components of the vector $\mathbf{n}$ can be any value $\tilde{m} \geq 0$ with $\tilde{m} \in \mathbb{N}$. Now, since $E_0 = 0$, the chemical potential is always negative.

Furthermore, if the thermal energy $k_B T$ is much larger than the energy spacing $\hbar^2/2mV^{2/3}$, we can make the replacement $\sum_{\mathbf{p}} \to V/(2\pi\hbar)^3 \int d\mathbf{p}$ so that

$$N_T = \sum_{\mathbf{p}\neq 0} \frac{1}{\exp[\beta(p^2/2m - \mu)] - 1} = \frac{V}{\lambda_T^3} g_{3/2}(e^{\beta\mu}) \,, \tag{2.15}$$

where

$$\lambda_T = \sqrt{\frac{2\pi\hbar^2}{mk_B T}} \,, \tag{2.16}$$

is the *thermal wavelength* and $g_{3/2}(e^{\beta\mu})$ belongs to the class of special functions

$$g_p(z) = \frac{1}{\Gamma(p)} \int_0^\infty dx\, x^{(p-1)} \frac{1}{z^{-1}e^x - 1} \,. \tag{2.17}$$

Now, from Eq. (2.13) this yields

$$k_B T_c = \frac{2\pi\hbar^2}{m} \left(\frac{n}{g_{3/2}(1)} \right)^{2/3} \,, \tag{2.18}$$

which shows that the critical temperature for a 3D gas confined in a box is completely determined by the density $n = N/V$ and the mass of the particles. For $T < T_c$ we have $\mu = 0$ so that, using Eq. (2.15) and (2.18), we obtain

$$N_T = \left(\frac{T}{T_c} \right)^{3/2} N \,, \tag{2.19}$$

which finally leads to, applying Eq. (2.11),

$$N_0(T) = N \left[1 - \left(\frac{T}{T_c} \right)^{3/2} \right] \,. \tag{2.20}$$

Another quantity we can evaluate for $T < T_c$ is the energy

$$\begin{aligned} E &= \sum_{\mathbf{p}} \frac{p^2/2m}{\exp[\beta(p^2/2m - \mu)] - 1} \\ &\to \frac{V}{(2\pi\hbar)^3} \int d\mathbf{p} \frac{p^2/2m}{\exp[\beta(p^2/2m - \mu)] - 1} = \frac{3}{2} \frac{V}{\beta\lambda_T^3} g_{5/2}(1) \,. \end{aligned} \tag{2.21}$$

If we now make use of the thermodynamical relation

$$P = \frac{2}{3} \frac{E}{V} \tag{2.22}$$

we obtain that the pressure has the form

$$P = \frac{k_B T}{\lambda_T^3} g_{5/2}(1) \,, \tag{2.23}$$

which does not depend on the volume. This means that the pressure stands constant against variation of the volume and thus it implies that the BEC compressibility is infinite, which is a physical nonsense. This pathological feature originates from the absence of particle-particle interactions, as we shall see in the next Section.

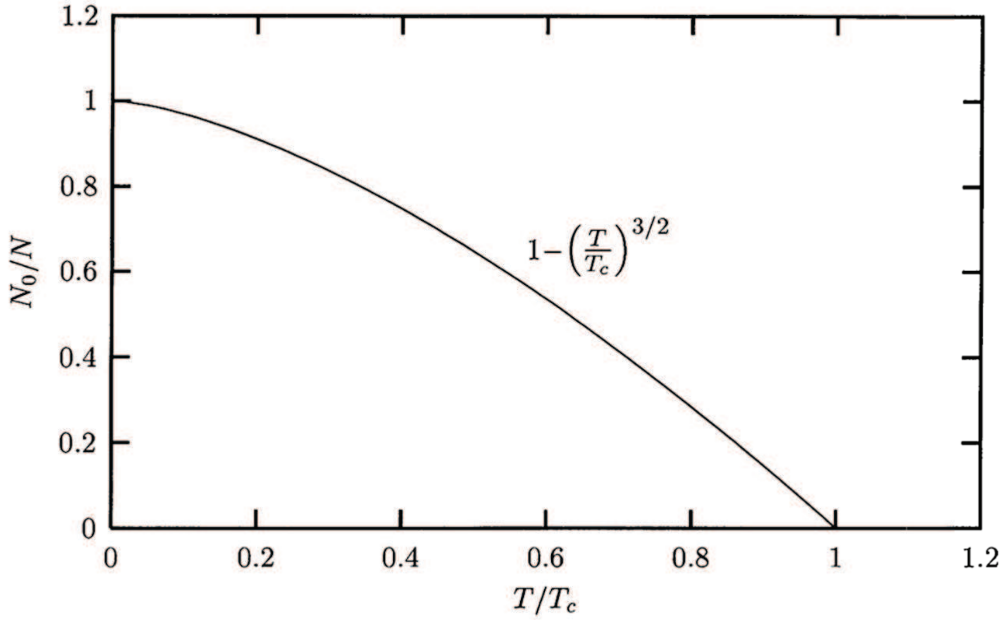

Figure 2.4: Condensate fraction N_0/N versus temperature for the case of an ideal Bose gas confined in a box. The curve refers to Eq. (2.20) and it is reminiscent of a phase transition.

2.3 Dilute gases and the Bogoliubov approach

The problem of generalizing the results of the ideal Bose gas is not trivial since traditional perturbation techniques cannot be applied. This problem was solved in 1947 by N. N. Bogoliubov [118] who applied a new perturbation method which stands as the basis of modern approaches to Bose-Einstein condensation in rarefied (or "dilute") Bose gases.

In dilute gases the range r_0 of interatomic forces is much smaller than the average distance $d = n^{-1/3}$ between particles, fixed by the density of the gas $n = N/V$. In formulas

$$r_0 \ll d = n^{-1/3} \,. \tag{2.24}$$

This allows one to consider only configurations involving pairs of interacting particles, while configurations with three or more particles interacting simultaneously can be safely neglected. This way, the Hamiltonian of the system, written in the second quantization formalism, becomes

$$\widehat{H} = \int \left(\frac{\hbar^2}{2m} \nabla \widehat{\Psi}^\dagger \nabla \widehat{\Psi} \right) d\mathbf{r} + \frac{1}{2} \int \widehat{\Psi}'^\dagger \widehat{\Psi}^\dagger V(\mathbf{r}' - \mathbf{r}) \widehat{\Psi}' \widehat{\Psi} d\mathbf{r}' d\mathbf{r} \,, \tag{2.25}$$

where $V(\mathbf{r}' - \mathbf{r})$ is the two-body potential and we have not included external fields for the moment. The field operators satisfy the well-known commutation relations

$$[\widehat{\Psi}(\mathbf{r}), \widehat{\Psi}^\dagger(\mathbf{r}')] = \delta(\mathbf{r} - \mathbf{r}') \,, \qquad [\widehat{\Psi}(\mathbf{r}), \widehat{\Psi}(\mathbf{r}')] = 0 \,, \tag{2.26}$$

and the density of the system is defined as

$$n(\mathbf{r}) = \langle \widehat{\Psi}^\dagger(\mathbf{r}) \widehat{\Psi}(\mathbf{r}) \rangle \,. \tag{2.27}$$

Another important consequence of the dilute gas regime is that the distance between two particles is always large enough to justify the use for the asymptotic expressions for the wave function of their relative motion, which is fixed by the scattering amplitude. Moreover, since we will always work with temperatures below the critical temperature, the scattering amplitude becomes independent of the energy as well as of the angle and we can replace its value by the s-wave scattering length a_s. That means that, in the regime of dilute gases the effects of the interaction are described in a rather fundamental way since, in practice, a single physical parameter is sufficient to obtain an accurate description. The condition of diluteness can now be written as

$$|a_s| \ll n^{-1/3} \,, \tag{2.28}$$

or, equivalently,

$$n|a_s|^3 \ll 1 \,. \tag{2.29}$$

If a gas of bosons fulfils the requirement of Eq. (2.29) it is said to be **dilute** or **weakly interacting**. However, this does not necessarily mean that the interaction effects are small, as we will demonstrate later on.

Now, because of the previous discussion about properties of the dilute gases, we can replace the actual potential with an effective one, given that both share the same value for a_s; thus, we choose a suitable effective potential U_{eff} to which perturbation theory can be applied [109]. Then, if we go back to the problem of a uniform gas in a box of volume V, keeping the second quantization formalism, we can now conveniently write the field operators as

$$\widehat{\Psi}(\mathbf{r}) = \sum_{\mathbf{p}} \widehat{a}_{\mathbf{p}} \frac{e^{i\mathbf{p}\cdot\mathbf{r}/\hbar}}{\sqrt{V}} \,, \tag{2.30}$$

where $\widehat{a}_{\mathbf{p}}$ is the operator annihilating a particle in the single-particle state with momentum $\mathbf{p}$, which satisfies the usual cyclic boundary conditions. Substituting Eq. (2.30) into Eq. (2.25) we obtain

$$\widehat{H} = \sum_{\mathbf{p}} \frac{p^2}{2m} \widehat{a}^\dagger_{\mathbf{p}} \widehat{a}_{\mathbf{p}} + \frac{1}{2V} \sum_{\mathbf{p}_1,\mathbf{p}_2,\mathbf{q}} U_{\mathbf{q}} \widehat{a}^\dagger_{\mathbf{p}_1+\mathbf{q}} \widehat{a}^\dagger_{\mathbf{p}_2-\mathbf{q}} \widehat{a}_{\mathbf{p}_1} \widehat{a}_{\mathbf{p}_2} \,, \tag{2.31}$$

where $U_{\mathbf{q}} = \int U_{\text{eff}}(\mathbf{r}) \exp[-i\mathbf{q}\cdot\mathbf{r}/\hbar] \, d\mathbf{r}$. Moreover, since only small momenta are involved, we can consider only the $q = 0$ value of the Fourier transform of the effective potential $U_0 = \int U_{\text{eff}}(\mathbf{r}) \, d\mathbf{r}$ so that Eq. (2.31) becomes:

$$\widehat{H} = \sum_{\mathbf{p}} \frac{p^2}{2m} \widehat{a}^\dagger_{\mathbf{p}} \widehat{a}_{\mathbf{p}} + \frac{1}{2V} U_0 \sum_{\mathbf{p}_1,\mathbf{p}_2,\mathbf{q}} \widehat{a}^\dagger_{\mathbf{p}_1+\mathbf{q}} \widehat{a}^\dagger_{\mathbf{p}_2-\mathbf{q}} \widehat{a}_{\mathbf{p}_1} \widehat{a}_{\mathbf{p}_2} \,. \tag{2.32}$$

Now, the crucial point of the approach adopted by Bogoliubov is to replace the operator $\widehat{a}_0$ with a number, that is $\widehat{a}_0 \equiv \sqrt{N_0}$. This will not be a good approximation for a realistic potential but it works perfectly for a smoother potential such as the effective one. Now, in an dilute gas at $T = 0$ the occupation numbers for states $\mathbf{p} \neq 0$ are finite but small (differently for an ideal gas where they would be vanishing since all the particles are in the ground state). Then we can make the approximation $N_0 \sim N$ and thus, replacing $\widehat{a}_0$ with $\sqrt{N}$, the ground state energy is

$$E_0 = \frac{N^2 U_0}{2V} \,. \tag{2.33}$$

Using Born approximation we can derive U_0 in terms of the scattering length as $U_0 = 4\pi\hbar^2 a_s/m$; this quantity is mostly known as g and it describes the relevant interaction coupling constant[3]

$$g = \frac{4\pi\hbar^2 a_s}{m} \,. \tag{2.34}$$

Then, Eq. (2.33) can be rewritten as

$$E_0 = \frac{1}{2} N n g \,, \tag{2.35}$$

which shows that, contrary to the ideal case, the pressure of a weakly-interacting Bose gas does not vanish at zero temperature; in fact

$$P = -\frac{\partial E_0}{\partial V} = \frac{g n^2}{2} \,. \tag{2.36}$$

Accordingly, the compressibility is also finite:

$$\frac{\partial n}{\partial P} = \frac{1}{g n} \,. \tag{2.37}$$

Using the hydrodynamic relation $\frac{\partial n}{\partial P} = \frac{1}{mc^2}$, one obtains the important result

$$c = \sqrt{\frac{g n}{m}} \tag{2.38}$$

which is the sound velocity in a BEC. Furthermore, this shows that, unlike the ideal gas, the chemical potential for the interacting gas is not equal to zero; in fact

$$\mu = \frac{\partial E_0}{\partial N} = g n \tag{2.39}$$

---

[3] This is not a redundancy since the fact that $U_0 = g$ here is a mere coincidence. The coupling constant g is *defined* as in Eq. (2.34) while the form of U_0 is due to the fact that we have considered the lowest-order Born approximation; if we go beyond that - as we will do shortly - U_0 acquires a completely different value.

and thus, because of Eq. (2.38), we have $\mu = mc^2$.

At this point it is better to summarize the few elements described so far, in order to highlight the results we will need in the future and to give a better understanding to the reader on why we wanted to deal with such a long mathematical derivation.

We started by describing the behaviour of particles at the quantum level and we derived the two statistics present at the atomic scale in nature. In particular, Bose-Einstein condensation is the framework of this Thesis (we have not talked about the behaviour of fermions as $T \to 0$ yet but we will do that shortly, as it will be useful in our work). In particular, in the context of analogue gravity one has to deal with BECs accelerated to supersonic speeds and thus it is important to understand how sound is defined in these systems. In the following we will briefly discuss how to demonstrate that the result of Eq. (2.38) coincides with the value obtained by starting from the dispersion relation of the elementary excitations in the long wavelength limit. The way to derive it follows Bogoliubov prescription, which we will use a few times in our work.

Let us now consider Eq. (2.33): it was derived from Eq. (2.32) by means of the canonical transformation $\widehat{a}_{\mathbf{p}} = \sqrt{N_0}\,\delta_{\mathbf{p},0} + \widehat{A}_{\mathbf{p}}$ and expanding in powers of N: the term in N^2 gives Eq. (2.33) while the term in N gives a quadratic form. Following Bogoliubov's approach, we can diagonalize this term through a suitable canonical transformation. In particular, we can rewrite the operators $\widehat{a}^\dagger_{\mathbf{p}}$, $\widehat{a}_{\mathbf{p}}$ as

$$\widehat{a}_{\mathbf{p}} = u_{\mathbf{p}}\widehat{b}_{\mathbf{p}} + v^*_{-\mathbf{p}}\widehat{b}^\dagger_{-\mathbf{p}}\,, \qquad \widehat{a}^\dagger_{\mathbf{p}} = u^*_{\mathbf{p}}\widehat{b}^\dagger_{\mathbf{p}} + v_{-\mathbf{p}}\widehat{b}_{-\mathbf{p}}\,. \tag{2.40}$$

which are know as (again) *Bogoliubov transformations*. The new operators $\widehat{b}^\dagger_{\mathbf{p}}$, $\widehat{b}_{\mathbf{p}}$ (which satisfy precise commutation relations, provided that the coefficients $u_{\mathbf{p}}$ and $v_{\mathbf{p}}$ obey some orthonormality condition [109]) represent a convenient way of rewriting the equations as they diagonalize the Hamiltonian for a suitable choice of the parameters [109]. That is, it can be demonstrated that, with this choice of representation and under certain assumptions, Eq. (2.32) becomes

$$\widehat{H} = E_0 + \sum E(p)\widehat{b}^\dagger_{\mathbf{p}}\widehat{b}_{\mathbf{p}}\,, \tag{2.41}$$

where

$$E(p) = \sqrt{\left(\frac{p^2}{2m}\right)^2 + \frac{gn}{m}p^2} \tag{2.42}$$

is the famous **Bogoliubov dispersion relation** for the elementary excitations of the system. Eqs. (2.41) and (2.42) are fundamental results and they have a deep physical meaning, as they show that the original system of interacting particles can be described in terms of an Hamiltonian of independent quasi-particles having energy $E(p)$ and whose creation and annihilation operators are, respectively, $\widehat{b}^\dagger_{\mathbf{p}}$ and $\widehat{b}_{\mathbf{p}}$. In this picture, a real particle $\widehat{a}_{\mathbf{p}}$ is described as the superposition of the forward propagating quasi-particle $u_{\mathbf{p}}\widehat{b}_{\mathbf{p}}$ and the backward propagating quasi-particle $v^*_{-\mathbf{p}}\widehat{b}^\dagger_{-\mathbf{p}}$. Then, the ground state of the interacting system corresponds to the vacuum of quasi-particles $\widehat{b}_{\mathbf{p}}\,|0\rangle = 0$. Now, note that, for small momenta $p \ll m\sqrt{gn/m}$, the dispersion law (2.42) of quasi-particles takes the phonon-like form

$$E(p) = cp\,, \tag{2.43}$$

where $c = \sqrt{gn/m}$, which exactly coincides with Eq. (2.38). We thus demonstrated that the elementary excitations in the long wavelength limit are, indeed, **phonons**. On the other hand, for large momenta, i.e. $p \gg m\sqrt{gn/m}$, the dispersion law (2.42) becomes the free particle one

$$E(p) \simeq \frac{p^2}{2m}\,. \tag{2.44}$$

The transition between the phonon and the particle regimes happens when $p^2/2m \sim gn = mc^2$, i.e. $p \sim mc$. Then, by setting $p^2/2m = gn$ and $p = \hbar/\xi$, one can define the characteristic interaction length

$$\xi = \sqrt{\frac{\hbar^2}{2mgn}} = \frac{1}{\sqrt{2}}\frac{\hbar}{mc}\,, \tag{2.45}$$

which is known as the **healing length**. This quantity will play a fundamental role throughout our treatment.

2.4 The Gross-Pitaevskii equation

At this point we could ask what happens if we apply Bogoliubov prescription to the case of a non-uniform and time-dependent configuration, since this situation describes in a more realistic way the case of experimental BEC configurations. That means to solve the problem described by the Hamiltonian (2.25) by separating the condensate contribution from the thermal contribution as

$$\widehat{\Psi}(\mathbf{r},t) = \Phi(\mathbf{r},t) + \widehat{\Psi}'(\mathbf{r},t)\,. \tag{2.46}$$

Here $\Phi(\mathbf{r},t)$ is a complex function and it is defined as the expectation value of the field operator, that is $\Phi(\mathbf{r},t) = \langle\widehat{\Psi}(\mathbf{r},t)\rangle$; $\Phi(\mathbf{r},t)$ is a classical field which has the meaning of an order parameter for the phase transition and it is often referred to as the "condensate wave function", as it fixes the condensate density through $n_0(\mathbf{r},t) = |\Phi(\mathbf{r},t)|^2$. For this reason this approach is also known as a **semi-classical approach** or a **mean-field approach**.

The time evolution of the field operator is derived from the requirements of Heisenberg representation, that is

$$\begin{aligned} i\hbar\frac{\partial}{\partial t}\widehat{\Psi}^\dagger(\mathbf{r},t) &= [\widehat{\Psi}^\dagger(\mathbf{r},t),\widehat{H}] \\ &= \left[-\frac{\hbar^2\nabla^2}{2m} + V_{\text{ext}}(\mathbf{r},t) + \int \widehat{\Psi}^\dagger(\mathbf{r}',t)V(\mathbf{r}'-\mathbf{r})\widehat{\Psi}^\dagger(\mathbf{r}',t)d\mathbf{r}'\right]\widehat{\Psi}(\mathbf{r},t) \end{aligned} \tag{2.47}$$

where we have made use of Eq. (2.25) and Eqs. (2.26). Then, if the thermal component (or “depletion”) $\widehat{\Psi}'(\mathbf{r},t)$ is small, we can replace the field operator with the classical field $\Phi(\mathbf{r},t)$; furthermore, the two-body interaction $V(\mathbf{r}'-\mathbf{r})$ can be substituted with an effective interaction

$$V(\mathbf{r}'-\mathbf{r}) = g\,\delta_3(\mathbf{r}'-\mathbf{r})\,, \tag{2.48}$$

since only binary collisions at low energy are relevant, due to the diluteness condition. These approximations lead to

$$i\hbar\,\frac{\partial}{\partial t}\,\phi(\mathbf{r},t) = \left[-\frac{\hbar^2}{2m}\nabla^2 + V_{\text{ext}}(\mathbf{r},t) + g\,|\phi(\mathbf{r},t)|^2\right]\phi(\mathbf{r},t)\,. \tag{2.49}$$

This is the **Gross-Pitaevskii equation (GPE)** and it describes the dynamics of a weakly interacting Bose gas. Its stationary form can be easily derived by the substitution

$$\phi(\mathbf{r},t) = \phi(\mathbf{r})\exp\left(-\frac{i\mu t}{\hbar}\right)\,, \tag{2.50}$$

which yields

$$\left[-\frac{\hbar^2}{2m}\nabla^2 + V_{\text{ext}}(\mathbf{r})\right]\phi(\mathbf{r}) + g\,|\phi(\mathbf{r})|^2\phi(\mathbf{r}) - \mu\,\phi(\mathbf{r}) = 0\,. \tag{2.51}$$

The Gross-Pitaevskii equation was derived independently by E. P. Gross [125, 126] and L. P. Pitaevskii [127] in 1961 and it has the form of a non-linear Schrödinger equation. It is a fundamental equation for the description of weakly-interacting Bose gases and we will use it several times through our work. Note that, if we write the condensate wave function in the Madelung representation

$$\phi(\mathbf{r},t) = \sqrt{n(\mathbf{r},t)}\,e^{i\theta(\mathbf{r},t)}\,, \tag{2.52}$$

we obtain an interesting form for the GPE (2.49). In fact, if we define an irrotational velocity field $\mathbf{v} \equiv \hbar\boldsymbol{\nabla}\theta/m$ and[4] we insert (2.52) into (2.49), the Gross-Pitaevskii equation can be rewritten as

$$\begin{cases} \dfrac{\partial}{\partial t}n + \boldsymbol{\nabla}\cdot(n\mathbf{v}) = 0, \\ m\dfrac{\partial}{\partial t}\mathbf{v} + \boldsymbol{\nabla}\left(\dfrac{mv^2}{2} + V_{\text{ext}}(\mathbf{r},t) + g\,n - \dfrac{\hbar^2}{2m}\dfrac{\nabla^2\sqrt{n}}{\sqrt{n}}\right) = 0. \end{cases} \tag{2.53}$$

---

[4] This vector is exactly the velocity of the condensate flow and the fact that it is irrotational is a typical feature of superfluids [109].

These are the equations which define the dynamics of an irrotational, inviscid fluid, i.e. *equation of continuity* and *Euler equation*, which we have introduced in Section 1.4.1, apart from a term of *quantum potential*

$$V_{\text{quantum}} = -\frac{\hbar^2}{2m}\frac{\nabla^2\sqrt{n}}{\sqrt{n}}\,, \tag{2.54}$$

which has the dimensions of an energy. Eqs. (2.53) are exactly equivalent to the original Gross-Pitaevskii equation and they show that GPE is the equivalent, at the quantum level, to the equations of hydrodynamics for a classical fluid[5]. The quantum pressure term is a direct consequence of Heisenberg uncertainty principle and it reveals that the importance of quantum effects is emphasized in non-uniform gases. In fact, if the density of the gas changes slowly in space then this term can be neglected. That is, if we define R as the typical distance characterizing the density variations inside the system, we see that $\nabla^2\sqrt{n}/\sqrt{n} \sim R^{-2}$, which becomes negligible if $R \gg \xi$, the characteristic length defining the transition between the phonon and the single-particle regime in the Bogoliubov excitation spectrum (2.42). Furthermore, if we can neglect the quantum pressure term, then the second of Eqs. (2.53) becomes the Euler equation for a classical non-viscous gas with pressure $P = gn^2/2$. Then, by using the classical relation $\frac{\partial P}{\partial n} = mc^2$, we obtain that the sound velocity in this gas is $c = \sqrt{gn/m}$, which is in agreement with Eq. (2.38).

Now, much in same way as we have done in the previous Section, the Bogoliubov approach for the excitations of the system can be used in this context too. Before doing so, though, there is one subject we want to discuss, as it will be very useful in our work.

2.4.1 Trapped gases in harmonic potentials

As we already mentioned, the cooling of atoms at such low temperatures requires usually some kind of trapping (magnetic, optical, laser). Most of the times these confining potentials have the nice feature that they can be safely approximated by the quadratic form typical of harmonic potentials. Since this is the approximation we will use through most of our work for the shape of the confining traps, it is worth exploring some features of the GPE when the external potentials are harmonic.

First of all, when the external trapping is harmonic, we can define the harmonic oscillator length $a_\perp$ as

$$a_\perp = \sqrt{\frac{\hbar}{m\omega_\perp}}\,, \tag{2.55}$$

---

[5] Equation of continuity highlights one of the conserved quantities of GPE, i.e. momentum. Note that GPE also conserves the number of atoms and the energy (given that the potential is time-independent).

where $\omega_\perp$ is the external trap angular frequency. If the trap is 2- or 3-dimensional and the angular frequencies are different, $\omega_\perp$ is usually defined as the geometric average of the different oscillator frequencies, that is $\omega_\perp = (\omega_x \, \omega_y \, \omega_z)^{1/3}$. We can also define a parameter expressing the importance of the atom-atom interaction by comparing the interaction energy E_{int} of particles in the ground state with the kinetic energy of the atoms; in formulas, the former is of the order of gNn while the latter is of the order of $N\hbar\omega_\perp$; thus, using Eq. (2.55)

$$\frac{E_{int}}{E_{kin}} \propto \frac{N a_s}{a_\perp} \, . \tag{2.56}$$

This parameter expresses the relevance of the atom-atom interaction in comparison to the kinetic energy. It can be easily larger than 1 even if the dilute condition $n|a_s|^3 \ll 1$ is satisfied [119].

Now, if the interactions between atoms are repulsive ($a_s > 0$), an interesting case occurs if $N a_s / a_\perp \gg 1$. In fact, if we solve numerically the GP stationary equation (2.51) in a spherical trap, at $T = 0$, we obtain the results shown in Figure 2.5 (the graph is taken from [119]).

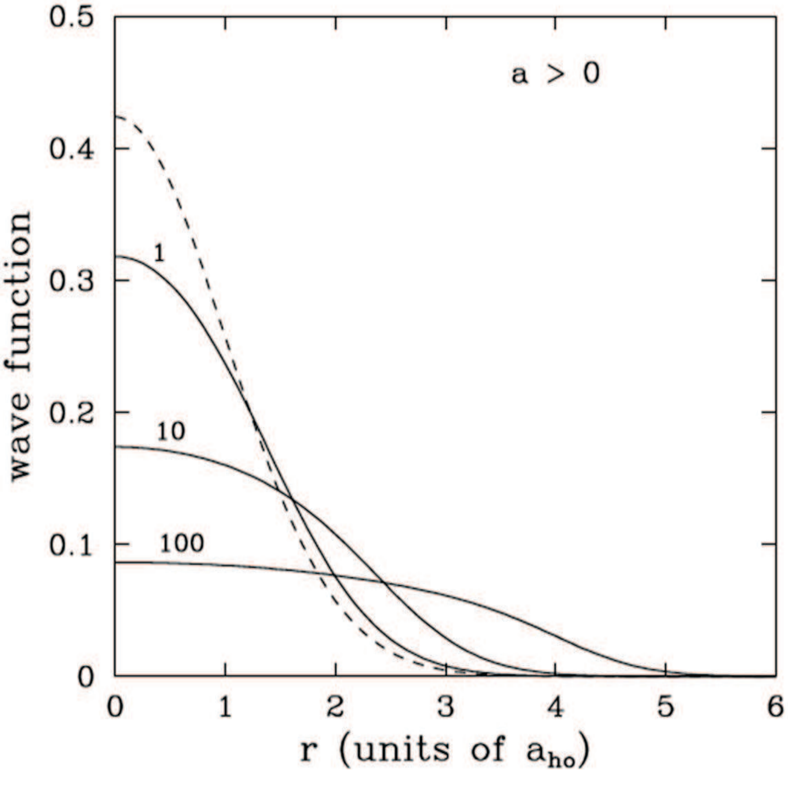

Figure 2.5: Condensate wave function at $T = 0$ for a BEC in a spherical harmonic trap. The interactions are repulsive (i.e. $a_s > 0$) and $N a_s / a_\perp = 1, 10, 100$. The dashed line is the prediction for the ground state of the ideal gas in a harmonic trap (indeed, it is a Gaussian). The parameter 'a$_{\mathrm{ho}}$' is $a_\perp$ while 'a' is a_s.

This clearly shows that when the parameter $N a_s / a_\perp$ grows the atoms are pushed outwards, the central density becomes rather flat and the radius grows. As a consequence, the first term in the stationary GPE (2.51) can be safely neglected. That means that

$$n(\mathbf{r}) = |\phi(\mathbf{r})|^2 = g^{-1}[\mu - V_{\text{ext}}(\mathbf{r})]\,, \tag{2.57}$$

which is known as the **Thomas-Fermi (TF) approximation**.

Now, let us start from the time-dependent 3D GPE (2.49):

$$i\hbar\frac{\partial}{\partial t}\Psi\left(\mathbf{r},t\right) = \left[-\frac{\hbar^2}{2m}\nabla^2 + U(\mathbf{r}) + gN|\Psi\left(\mathbf{r},t\right)|^2\right]\Psi\left(\mathbf{r},t\right)\;, \tag{2.58}$$

where

$$\int d_3r|\Psi\left(\mathbf{r},t\right)|^2 = 1, \qquad g = \frac{4\pi\hbar^2 a_s}{m}, \tag{2.59}$$

N is the number of bosons in the gas and $U(\mathbf{r})$ is the external trapping potential. Consider now a potential with cylindrical symmetry. This is usually the case for experiments aimed at studying 1D systems since, if the transverse confinement is strong enough, the physics is quasi-1D, as the particles can only flow on the longitudinal axis. In particular, we now analyse a trapping potential that is harmonic in the transverse directions and generic in the axial direction (as we already said, a harmonic potential is a good approximation for most of the real traps):

$$U(\mathbf{r}) = \frac{1}{2}m\omega_\perp^2\left(x^2+y^2\right) + V(z)\,. \tag{2.60}$$

The way to proceed, usually, is to minimize the action functional S by constraining the wave function of the transverse direction to be in the ground state of the harmonic potential, i.e., to be a Gaussian wave function of defined width. This leads to the usual 1D GPE for harmonic confinements, which has the form

$$i\hbar\frac{\partial}{\partial t}\psi\left(z,t\right) = \left[-\frac{\hbar^2}{2m}\frac{\partial^2}{\partial z^2} + U(z) + g_{1\text{D}}N|\psi\left(z,t\right)|^2 + \hbar\omega_\perp\right]\psi\left(z,t\right)\;, \tag{2.61}$$

where $g_{1\text{D}} = g\frac{m\omega_\perp}{h}$ and a term due to the zero-point energy of the transverse trap has appeared. A better model, though, can be developed, as done in 2002 by L. Salasnich, A. Parola and L. Reatto [128]. The previous procedure, in fact, can be repeated allowing the transverse Gaussian function width to vary along the axis of motion; this is a better approximation for a realistic harmonic confinement as it takes into account the repulsion between atoms (which can affect the transverse size of the condensate). To obtain the equation of motion, then, we minimize the Action functional S with the trial wave function

$$\Psi\left(\mathbf{r},t\right) = \varphi\left(x,y,t;\sigma\left(z,t\right)\right)f\left(z,t\right)\;, \tag{2.62}$$

where both φ and f are normalized and φ is a Gaussian

$$\varphi\left(x, y, t; \sigma\left(z, t\right)\right) = \frac{e^{-\frac{x^2+y^2}{2\sigma(z,t)^2}}}{\sqrt{\pi}\sigma(z,t)}\,, \tag{2.63}$$

whose width can vary along the axis of motion. We obtain an Euler-Lagrange equation for σ, which gives[6]

$$\sigma^2 = a_\perp^2\sqrt{1+2a_sN|f|^2}\,, \tag{2.64}$$

and another Euler-Lagrange equation for f which - using (2.64) - gives a one-dimensional time-dependent **non-polynomial Schrödinger equation (NPSE)**:

$$\begin{aligned} i\hbar\frac{\partial f}{\partial t} = \left(-\frac{\hbar^2}{2m}\frac{\partial^2}{\partial z^2} + V + \frac{gN}{2\pi a_\perp^2}\frac{|f|^2}{\sqrt{1+2a_sN|f|^2}}\right)f + \\ +\frac{\hbar\omega_\perp}{2}\left(\frac{1}{\sqrt{1+2a_sN|f|^2}} + \sqrt{1+2a_sN|f|^2}\right)f\,. \end{aligned} \tag{2.65}$$

In the weak coupling limit $Na_s \to 0$ this equation reduces to the usual 1D GPE with the usual effective coupling

$$g_{1\mathrm{D}} = \frac{g}{2\pi a_\perp^2}\,. \tag{2.66}$$

Equation (2.65) gives the one-dimensional dynamics for a BEC confined in the transverse plane by a cylindrical symmetric harmonic potential when we allow the width of the transverse wave function to vary and it will be very useful in our work.

2.4.2 Quantization and elementary excitations

Let us now apply Bogoliubov formalism to the GPE in order to recover the excitations, spectrum and phonons. We will first describe the classical case and only later we will quantize the theory (that is, we will derive the same results in the formalism of second quantization). Note that the approach we will use is exactly the one of Bogoliubov and thus the procedure is the same we have described in Section 2.3.

We start by considering the small-amplitude oscillations which are the solutions of the GPE when the changes of the condensate wave function, with respect of to the stationary solution, are small. A convenient way to study

---

[6] A term involving the axial spatial derivative of the Gaussian width $\sigma(z,t)$ has been disregarded.

small oscillations of the system around the equilibrium is to write the order parameter as

$$\Psi(\mathbf{r},t) = \Psi'(\mathbf{r},t)\, e^{-i\mu t/\hbar} = [\phi(\mathbf{r}) + \bar{\theta}(\mathbf{r},t)]\, e^{-i\mu t/\hbar} \tag{2.67}$$

and then look for solutions of the form

$$\bar{\theta}(\mathbf{r},t) = \sum_i [u_i(\mathbf{r})e^{-i\omega_i t} + v_i^*(\mathbf{r})e^{i\omega_i t}]\,, \tag{2.68}$$

which are exactly Eqs. (2.40) adapted to this case, the functions $u_i(\mathbf{r})$ and $v_i(\mathbf{r})$ being the analogues of the parameters $u_{\mathbf{p}}$ and $v_{-\mathbf{p}}$. The procedure now retraces the steps taken to derive GPE, namely to start from the Hamiltonian form of the equation of motion (now in first quantization formalism) and to use the diluteness condition for the interactions. Then, a key assumption needs to be made: we assume that, since oscillations from the equilibrium configuration are small, they do not influence the dynamics of bulk motion (that is, of the ground state) so that, at the lowest order, GPE equation for $\phi(\mathbf{r})$ is valid. Furthermore, we neglect second order terms for the same reasons. This *linearization* technique was vastly used in the previous Sections.
Then, we are left with an equation for the functions $u_i(\mathbf{r})$ and $v_i(\mathbf{r})$ which can be split into two by regrouping the terms $e^{-i\omega_i t}$ and $e^{i\omega_i t}$. Thus, we obtain the pair of equations

$$\begin{aligned} \hbar\omega_i u_i(\mathbf{r}) &= [\widehat{H}_0 - \mu + 2g|\phi(\mathbf{r})|^2]u_i(\mathbf{r}) + g\phi(\mathbf{r})^2 v_i(\mathbf{r}) \\ -\hbar\omega_i v_i(\mathbf{r}) &= [\widehat{H}_0 - \mu + 2g|\phi(\mathbf{r})|^2]v_i(\mathbf{r}) + g\phi^*(\mathbf{r})^2 u_i(\mathbf{r})\,, \end{aligned} \tag{2.69}$$

where $\widehat{H}_0 = -(\hbar^2/2m)\nabla^2 + V_{\text{ext}}(\mathbf{r})$. Using matrix representation, we can write these equations in the much more convenient form

$$\begin{pmatrix} \widehat{H}_0 - \mu + 2g|\phi(\mathbf{r})|^2 & g\phi(\mathbf{r})^2 \\ g\phi^*(\mathbf{r})^2 & \widehat{H}_0 - \mu + 2g|\phi(\mathbf{r})|^2 \end{pmatrix} \begin{pmatrix} u_i(\mathbf{r}) \\ v_i(\mathbf{r}) \end{pmatrix} = \hbar\omega_i \begin{pmatrix} u_i(\mathbf{r}) \\ -v_i(\mathbf{r}) \end{pmatrix}, \tag{2.70}$$

where the matrix is usually referred as the *Bogoliubov matrix* $\mathcal{L}$. These equations provide the normal modes of the system and, in general, they must be solved numerically. Nevertheless, an analytic solution can be found if we consider a uniform gas when no external potential is applied. In that case ϕ can be chosen to be real ($\phi = \sqrt{n}$) and the solutions are plane waves $u_i(\mathbf{r}) = ue^{i\mathbf{k}\cdot\mathbf{r}}$ and $v_i(\mathbf{r}) = ve^{i\mathbf{k}\cdot\mathbf{r}}$ [129] and Eq. (2.70) gives the dispersion relation

$$\omega = \pm\sqrt{\left(\frac{\hbar k^2}{2m}\right)^2 + \frac{k^2}{2m}gn} = \pm\sqrt{c^2k^2 + \left(\frac{\hbar k^2}{2m}\right)^2}\,. \tag{2.71}$$

This is exactly Bogoliubov dispersion relation (2.42) with $p = \hbar k$ and $E = \hbar\omega$.

Now, let us go back to Eqs. (2.70) as they exhibit important properties. First, by taking suitable combinations of these equations one finds

$$(\omega_i - \omega_i^*) \int d\mathbf{r}\, (|u_i|^2 - |v_i|^2) = 0\,, \tag{2.72}$$

which shows that, unless $\int d\mathbf{r}|u_i|^2 = \int d\mathbf{r}|v_i|^2$, Eqs. (2.70) only admit solutions with a real frequency. The occurrence of a complex frequency is associated with a dynamical instability of the system. A second important property is that two solutions with frequencies $\omega_i \neq \omega_j$ satisfy the orthogonality relation

$$\int d\mathbf{r}\, (u_i^* u_j - v_i^* v_j) = 0\,. \tag{2.73}$$

Moreover, for each solution u_i and v_i with frequency ω_i there exists another solution u_i^* and v_i^* with frequency $-\omega_i$ which represents the same physical oscillation.

Furthermore, it can be demonstrated [109] that the energy of the system is the sum of the ground state energy E_0 plus the contribution of the oscillations, which is

$$E^{(2)} = \sum_i \int d\mathbf{r}\, (|u_i|^2 - |v_i|^2)\hbar\omega_i\,. \tag{2.74}$$

This shows that the quantity $\int d\mathbf{r}\, (|u_i|^2 - |v_i|^2)\hbar\omega_i$ must be positive for each mode in order to ensure the stability of the system. The occurrence of solutions for which the above quantity is negative is a direct signature of an energetic instability, which means that the stationary solution ϕ does not correspond to a minimum of the Action functional[7].

We can now transport this whole derivation in second quantization formalism. Starting from the decomposition (2.67) we replace the classical function $\bar{\theta}(\mathbf{r}, t)$ with the field operator $\widehat{\theta}(\mathbf{r}, t)$, which we can write in the form

$$\widehat{\theta}(\mathbf{r}, t) = \sum_i [u_i(\mathbf{r})\widehat{b}_i e^{-i\omega_i t} + v_i^* \widehat{b}_i^\dagger(\mathbf{r}) e^{i\omega_i t}]\,, \tag{2.75}$$

which resembles Eq. (2.68), the difference being that we have introduced the annihilation/creation operators of the i-th elementary particle which satisfy the usual commutation rule for bosons, i.e. $[\widehat{b}_i, \widehat{b}_j^\dagger] = \delta_{ij}$. Note that u_i,v_i and ω_i are solutions of Eqs. (2.70). With this choice, we obtain that, if we rewrite the Hamiltonian as $\widehat{H} = E' + \widehat{H}^{(1)} + \widehat{H}^{(2)}$ where E' is a real number and $\widehat{H}^{(1)}$ is the contribution which leads to GPE, we have

$$\widehat{H}^{(2)} = \epsilon + \sum_i \hbar\omega_i \widehat{b}_i^\dagger \widehat{b}_i\,. \tag{2.76}$$

---

[7] The energetic instability just mentioned should not be confused with the dynamical instability associated with the appearance of an imaginary part in the frequency ω_i.

That is, apart from a constant factor, the Bogoliubov operators thus introduced diagonalize the Hamiltonian and, as already discussed in Section 2.3, they describe a gas of independent quasi-particles: phonons. Note that this is true only if the solutions of Eq. (2.68) are normalized, that is, if they satisfy

$$\int d\mathbf{r}\,[u_i^*(\mathbf{r})u_j(\mathbf{r}) - v_i^*(\mathbf{r})v_j(\mathbf{r})] = \delta_{ij} \tag{2.77}$$

which tells us that the frequencies ω_i of the elementary excitations are positive if the i-th solution is energetically stable, while they are negative in the opposite case. Finally, the contribution ϵ to the ground state energy can be calculated by taking the expectation value of (2.76) on the vacuum:

$$\epsilon = -\sum_i \hbar\omega_i \int d\mathbf{r}\,|v_i(\mathbf{r})|^2\,. \tag{2.78}$$

This concludes the treatment of dilute gases and of Bogoliubov approach to phonons and excitations. We now have everything we need to work with BECs in the analogue gravity framework, except for one last result.

2.5 The Tonks-Girardeau limit

Before heading to the analogue gravity paradigm there is one last, important result we would like to discuss, regarding BECs in 1D. For reasons that will be clear later on, in our work we will mostly deal with one-dimensional condensates; therefore, in Chapter 4, we will exploit one peculiar limit of these configurations.

Exactly solvable models of interacting bosons in 1D have been known for many years [130]. The most celebrated off-lattice system in this class is the δ-interacting Bose gas [131] defined by the Hamiltonian:

$$\widehat{H} = \int dx \left[\frac{\hbar^2}{2m}\,\partial_x\widehat{\psi}^\dagger(x)\partial_x\widehat{\psi}(x) + \frac{1}{2}\,g\,\widehat{\psi}^\dagger(x)\widehat{\psi}(x)\widehat{\psi}^\dagger(x)\widehat{\psi}(x)\right], \tag{2.79}$$

where $\widehat{\psi}(x)$ is the usual bosonic annihilation field operator. This model has been solved via Bethe-ansatz for arbitrary interaction strength g in 1963 by E. H. Lieb and W. Liniger and the full spectrum was calculated [131,132]. Nevertheless, the structure of the wave function is very complex and few analytical results can be effectively extracted. Studying the dynamics of this system in an external potential is even more challenging and only recently some progress has been made in this direction [133,134]. However, in the particular (but physically relevant) limit of hard-core repulsion between bosons (i.e. $g \to \infty$ in Eq. (2.79)) the problem becomes remarkably simple and the interacting Hamiltonian can be exactly mapped, by a Jordan Wigner transformation, into that of a free Fermi gas [135] making considerably easier the analysis. This Bose-Fermi correspondence, **valid only in one dimension**, is based on two observations:

1. Having chosen a basis set labelled by all possible particle configurations in real space, the matrix elements of the kinetic term of the Hamiltonian (2.79) do not depend whether the field operators $\widehat{\psi}(x)$ commute or anti-commute;
2. the hard-core constraint is automatically satisfied by fermions due the anti-symmetry of the wave function.

Due to this mapping, which holds also in the presence of arbitrary external potentials, the full energy spectrum and all the static and dynamic correlation functions involving only density operators of the Bose gas coincide with those of the free fermion model[8]. Therefore, we are brought to conclude that the Hard Core Bose fluid (HCB), also known as **Tonks-Girardeau (TG) gas**, represents the minimal model including the essential features of the interacting Bose gas and allowing for an exact analytical and manageable solution. It is also worth noting that, although the hard-core interaction is certainly a limiting case of the more general Hamiltonian (2.79), the physical properties of the interacting Bose gas change smoothly up to $g \to \infty$ which does not correspond to a singular limit [131]. Indeed, recent studies of the quench dynamics of the interacting Bose gas showed that the HCB limit faithfully represents the generic behaviour of the model [133,134]. Most importantly, the HCB limit can be reached in suitably designed experiments with cold atoms (namely ^{87}Rb) as proved in recent experiments [136, 137].

Since we will be exploiting this interesting feature of 1D Bose gases, it is useful to briefly discuss the Fermi gas. Let us now recall the fermion statistics from Eq. (2.3). As we already anticipated, at $T = 0$, due to Pauli exclusion principle, each particle in the gas occupies a different state, filling up the Fermi sea to an energy known as the *Fermi energy* E_F. Moreover, if we set $\mu = E_F$ [138], the form of the occupation number becomes rather simple

$$\bar{n}_i = \frac{1}{e^{\beta(E_i-\mu)}+1} = \theta(\mu - E_i) = \theta(E_F - E_i)\,, \tag{2.80}$$

where θ is the Heaviside function (that is, $\theta(x) = 0$ if $x < 0$ and $\theta(x) = 1$ if $x > 0$). Any temperature in the gas has the effect of smoothing out this step function, as Fig. (2.6) shows. Furthermore, for an ideal Fermi gas at $T = 0$ in 1D, calculations for the ground state are fairly easy. If we allow particles to move on a segment of length L and we set periodic boundary conditions, we obtain that the wave vectors are $k = 2\pi n/L$, with $n \in \mathbb{N}$; the number of particles N can be obtained by summing all the states up to the Fermi level (remember that particles and states are in one-to-one correspondence)[9]. The result gives that $k_F = \pi\rho$, with the density defined as $\rho = N/L$.

---

[8] Note also that the bosonic momentum density (or current) operator $\widehat{\jmath}$ coincides with the fermionic one because it can be written in terms of the commutator between the density and the Hamiltonian.

[9] If we consider spin, more particles per level are allowed (i.e. one for each orientation).

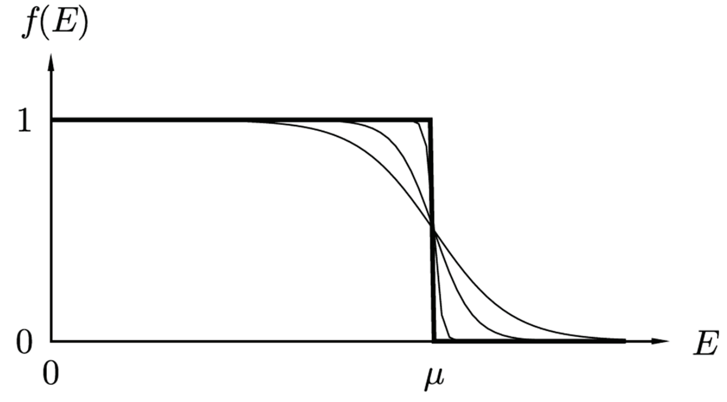

Figure 2.6: The Fermi distribution $f(E)$ for $T=0$ (thick line). The step function is smoothed out as temperature increases.

One can also calculate the energy of the system in terms of the Fermi energy; that turns out to be $E = NE_F/3$ with $E_F = \hbar^2 k_F^2/2m$. Finally, if we calculate the pressure by the thermodynamic relation $P \simeq \frac{2}{3}\frac{E}{L}$ together with $\frac{\partial P}{\partial \rho} = mc^2$, we obtain that the sound velocity, for a 1D free Fermi gas, is

$$c = \frac{\pi\hbar\rho}{m} = \frac{\hbar k_F}{m}\,. \tag{2.81}$$

Now, in the more general case, the exact eigenstates of a collection of non-interacting fermions are written as *Slater determinants* of single particle wave functions and they are labelled by the momentum distribution $f(k)$ defining the set of occupied states. The quantum averages of one- and two- body operators for a given arbitrary momentum distribution function $f(k)$ are defined as follows [139].

- The average of any one body operator $O_1 = \sum_{n=1}^{N} O_1(x_n, -i\hbar\partial_{x_n})$ is written in terms of the single particle eigenstates $|k\rangle$ as

$$\langle O_1\rangle = \int_{-\infty}^{\infty} dk\, f(k)\, \langle k|O_1(x, -i\hbar\partial_x)|k\rangle\,. \tag{2.82}$$

- For a two body operator O_2:

$$\begin{aligned}\langle O_2\rangle = \int_{-\infty}^{\infty} dk\, dk'\, f(k)\, f(k')\, [\langle k, k'|O_2(x, -i\hbar\partial_x; x', -i\hbar\partial_{x'}|k, k'\rangle) + \\ - \langle k, k'|O_2(x, -i\hbar\partial_x; x', -i\hbar\partial_{x'})|k', k\rangle]\,.\end{aligned} \tag{2.83}$$

With these results in hand, we can now turn our attention to the analogue gravity paradigm.

2.6 The acoustic metric in the case of BECs

At this point, it is obvious how the procedure described in Section 1.4.1 can be extended to the case of BECs. In fact, we have showed in Section 2.4 that dilute Bose-Einstein condensates obey, in the mean-field approach, the Gross-Pitaevskii equation, which can be rewritten as a continuity equation and a Euler equation (except for the fact that this last equation exhibits and extra pressure term due to the quantum nature of the system). We could therefore imagine to apply the exact same procedure that we have described for the case of classical fluids and linearise GPE around an equilibrium configuration. This is done first by L. J. Garay, J. R. Anglin, J. I. Cirac, and P. Zoller in 2000 [140].

Thus, we start from Eqs. (2.53) and we linearise a known, classical, ground-state solution (n, θ) by substituting

$$n,\, \theta \longrightarrow n + \widehat{n}_1,\, \theta + \widehat{\theta}_1 \,. \tag{2.84}$$

Note that this is exactly equivalent as starting from the exact dynamics of a δ-interacting Bose fluid in the formalism of second quantisation, i.e.

$$i\hbar \frac{\partial}{\partial t}\, \widehat{\Psi} = \left[-\frac{\hbar^2}{2m} \nabla^2 + V_{\rm ext}(\mathbf{r}, t) + g\, \widehat{\Psi}^\dagger \widehat{\Psi} \right] \widehat{\Psi} \,, \tag{2.85}$$

and then separating the quantum field into a macroscopic classical condensate wave function and a fluctuation: $\widehat{\Psi} = \psi + \widehat{\varphi}$, with $\langle \widehat{\Psi} \rangle = \psi$, where we have written the order parameter in the form $\psi = \sqrt{n} e^{i\theta}$. This is the technique we introduced in Section 2.4 and it is the approach adopted by Bogoliubov, which led to the excitation spectrum of our system. Therefore, by linearising our equation in the way described by Eq. (2.84), we are effectively studying the excitations of our system. Thus, by substituting Eq. (2.84) into Eqs. (2.53), using the GPE at zero-order and neglecting second order terms, we obtain the couple of equations

$$\begin{cases} \partial_t \widehat{n}_1 + \dfrac{1}{m} \boldsymbol{\nabla} \cdot (\widehat{n}_1 \boldsymbol{\nabla} \theta + n \boldsymbol{\nabla} \widehat{\theta}_1) = 0 \,, \\[2ex] \partial_t \widehat{\theta}_1 + \dfrac{1}{m} \boldsymbol{\nabla} \theta \cdot \boldsymbol{\nabla} \widehat{\theta}_1 + g\, \widehat{n}_1 - \dfrac{\hbar^2}{2m} D_2\, \widehat{n}_1 = 0 \,, \end{cases} \tag{2.86}$$

where D_2 is a second-order differential operator of the form

$$D_2\, \widehat{n}_1 \equiv -\frac{1}{2\, (\sqrt{n})^3} \, (\nabla^2 \sqrt{n})\, \widehat{n}_1 + \frac{1}{2\, \sqrt{n}} \nabla^2 \left(\frac{\widehat{n}_1}{\sqrt{n}} \right) \,, \tag{2.87}$$

which comes from the linearisation of the quantum potential. Since we will not need this term we will not expand its expression.

Before going further, we want to point out another way to obtain this set of equations, for the sake of completeness. In fact, we could have started from the

Hamiltonian and, after linearisation, obtain an equation for the depletion $\widehat{\varphi}$, which is usually referred as a *Bogoliubov-de Gennes equation.* Then, by writing the field $\widehat{\varphi}$ in the "quantum acoustic representation"

$$\widehat{\varphi}(t,\mathbf{x}) = e^{-i\theta/\hbar}\left(\frac{1}{2\sqrt{n}}\widehat{n}_1 - i\frac{\sqrt{n}}{\hbar}\widehat{\theta}_1\right) \tag{2.88}$$

and separating the amplitude and the phase contributions, we would have arrived at Eqs. (2.86).

Let us now investigate Eqs. (2.86). First of all, notice that, while the scattering length influences both the background dynamics and the dynamics of the fluctuations, the external potential does not enter in the dynamics of the perturbation. Second, similarly to what we have done in Section 1.4.1, we can write this couple of equations in the form

$$\partial_\mu(f^{\mu\nu}\,\partial_\nu\,\widehat{\theta}_1) = 0\,, \tag{2.89}$$

having introduced the (3+1)-dimensional space-time coordinate $x^\mu \equiv (t; x^i)$ and the 4×4 symmetric matrix

$$f^{\mu\nu}(t,\mathbf{x}) \equiv \left[\begin{array}{ccc} f^{00} & \vdots & f^{0j} \\ \cdots & . & \cdots \\ f^{i0} & \vdots & f^{ij} \end{array}\right], \tag{2.90}$$

where $f^{\mu\nu}$ are differential operators acting on space only. That is,

$$f^{00} = \left[g - \frac{\hbar^2}{2m}D_2\right]^{-1}, \tag{2.91}$$

$$f^{0j} = \left[g - \frac{\hbar^2}{2m}D_2\right]^{-1}\frac{\nabla^j\theta}{m}, \tag{2.92}$$

$$f^{i0} = \frac{\nabla^i\theta}{m}\left[g - \frac{\hbar^2}{2m}D_2\right]^{-1}, \tag{2.93}$$

$$f^{ij} = -\frac{n\,\delta^{ij}}{m} + \frac{\nabla^i\theta}{m}\left[g - \frac{\hbar^2}{2m}D_2\right]^{-1}\frac{\nabla^j\theta}{m}\,. \tag{2.94}$$

This is a key point which separates this case from a relativistic one. Indeed, in GR, tensors are collection of numbers, not operators. Now, if we assumed the $f^{\mu\nu}$ to be numbers we could identify[10]

$$\sqrt{-g}\,g^{\mu\nu} = f^{\mu\nu} \tag{2.95}$$

---

[10] This identification in (1+1) dimensions is highly non-trivial. The reason resides in the fact that, in two dimensions, $\det(kM) = k^2\det M$ if M is a 2×2 matrix and k a number. This implies that $\det(\sqrt{-g}\,g^{\mu\nu}) = -1$ but this might not be the case for $\det f^{\mu\nu}$. Even if it was, though, this relation does not allow to separate the metric from the determinant. Nevertheless, this does not necessarily spoil the analogy, as the determinant enters in the conformal factor which is assumed to be regular on the horizon and, furthermore, the Hawking effect is sensible only to the conformal class of metrics [38].

and Equation (2.89) would become that of a massless minimally coupled quantum scalar field on a curved background:

$$\Delta\widehat{\theta}_1 = \frac{1}{\sqrt{-g}}\partial_\mu\left(\sqrt{-g}g^{\mu\nu}\partial_\nu\widehat{\theta}_1\right) = 0\,, \tag{2.96}$$

as we expected. That is, by proceeding in the exact same way as we did in Section 1.4.1, we could arrive at an identical result, which is the existence of an acoustic metric $g_{\mu\nu}$ that rules the dynamics of fluctuations around the equilibrium configuration. The use of the conditional, though, is essential here since the presence of the D_2 operator makes it impossible to write $f^{\mu\nu}$ as tensor. There is one limit, though, that allows us to neglect the term D_2, as we already discussed in Section 2.4.

Let us go back to the second of Eqs. (2.86) and let us introduce the condensate velocity $\mathbf{v}$, the sound speed c and the healing length ξ, as defined in Section 2.3 (Eq. (2.38) and Eq. (2.45) for the last two). Then the equation becomes

$$\partial_t\widehat{\theta}_1 = -\mathbf{v}\cdot\boldsymbol{\nabla}\widehat{\theta}_1 - g\,\widehat{n}_1 + \frac{1}{2}\frac{\xi^2}{g}\boldsymbol{\nabla}\left[c^2\boldsymbol{\nabla}\left(\frac{\widehat{n}_1}{c^2}\right)\right]\,, \tag{2.97}$$

where the last term of this equation is the differential operator D_2 written in a different way. It is now evident that if we make a spectral decomposition of the fields $(\widehat{n}_1,\,\widehat{\theta}_1)$ and we take wavelengths larger than the healing length we can neglect the terms coming from the linearisation of the quantum potential, that is D_2. This is the **hydrodynamical approximation** and in this context has the effect of keeping only the long-wavelength, low-frequency fluctuations which we know, from Section 2.3, are phonons. Thus, by using the hydrodynamical approximation, we are studying the dynamics of (only) phonons in our condensate. Under this assumption, the acoustic metric (2.90) takes the form

$$g_{\mu\nu}(t,\mathbf{x}) \equiv \frac{n}{m\,c}\begin{bmatrix} (c^2-v^2) & \vdots & v_j \\ \cdots & \cdot & \cdots \\ v_i & \vdots & -\delta_{ij}\end{bmatrix}\,, \tag{2.98}$$

where, we want to remind, $c = c\,(n,g)$. Thus, we have an effective metric which depends on the condensate velocity $\mathbf{v}$, on the atomic mass and on the speed of the phonons in the medium, which is in perfect agreement with the observation made in Section 1.4.1.

We have thus showed that it is possible to establish the gravitational analogy also in the quantum case of Bose gases but this was made possible because of one constraint, i.e., the hydrodynamical approximation. While at first one could be brought to give this approximation not too much consideration, it is better if we stop to discuss this result before continuing.

As we have pointed out, the hydrodynamical approximation is a key factor in our treatment and in the case we would want to probe the system at short length scales (that is, work at small wavelengths) the form of the acoustic metric is not obvious. We will now show that for high energies (small wavelengths) the acoustic metric acquires an explicit dependence on the momentum and the analogy is broken since the metric does not resemble any realistic scenario. Moreover, at high energies excitations cease to behave as non-interacting quasi-particles. This, in turns, tells us that **the hydrodynamic approximation is fundamental for the analogy to hold**. We could have actually foreseen this unfortunate outcome since the condition $\lambda \leq \xi$ means that we are starting to be aware of the microscopic composition of the system (atoms or molecules), as we have deeply discussed in Section 2.3 and 1.4. As already pointed out, this scenario is quite similar to the problem of describing the universe at the Planck scale and thus one could hope that these systems, when probed at sufficiently short length scales, could give us some insight on how physics changes in the gravitational context when one goes at sufficiently short distances, especially in the case of the Hawking effect. Therefore, on one hand, by neglecting the high energy limit (that is, considering analogue systems only under the requirement that $\lambda >$ [coherence length of the system]), we could be hiding the open questions related to the validity of Hawking's results; on the other, we keep ourselves in a regime where a precise mathematical analogy between the gravitational and the hydrodynamical realms subsists. Nevertheless, it is useful to investigate what happens at the acoustic metric once we probe the system at high energies.

In order to explore a regime where the hydrodynamical approximation does not hold (i.e., a high momentum regime) we can make use of another helpful tool, namely the *eikonal approximation*. In this approximation the phase fluctuation $\widehat{\theta}_1$ is itself treated as a slowly-varying amplitude times a rapidly varying phase. This phase is taken to be the same for both $\widehat{n}_1$ and $\widehat{\theta}_1$ since the possibility that the two differ by a time-varying quantity is non physical and any time-constant difference can be absorbed into the definition of the amplitudes. We thus write

$$\widehat{\theta}_1 = A_\theta e^{-i\phi}\,, \tag{2.99}$$

$$\widehat{n}_1 = A_\rho e^{-i\phi}\,. \tag{2.100}$$

As a consequence of our starting assumptions, the gradients of the amplitude and of the background fields are systematically ignored relatively to the gradients of ϕ. We also adopt the notation

$$\omega = \frac{\partial \phi}{\partial t}\,, \quad k_i = \nabla_i \phi\,. \tag{2.101}$$

Then, starting from (2.87), we can approximate the D_2 operator as

$$\begin{aligned} D_2\,\widehat{n}_1 &\equiv -\frac{1}{2\,(\sqrt{n})^3}\,(\nabla^2\sqrt{n})\,\widehat{n}_1+\frac{1}{2\,\sqrt{n}}\nabla^2\left(\frac{\widehat{n}_1}{\sqrt{n}}\right) \\ &\simeq \frac{1}{2n}\nabla^2(\widehat{n}_1) \\ &= -\frac{1}{2n}k^2\widehat{n}_1 \end{aligned} \tag{2.102}$$

and a similar result holds for D_2 acting on $\widehat{\theta}_1$. That is, under the eikonal approximation, we can replace the operator D_2 with a function

$$D_2 \quad \longrightarrow \quad -\frac{1}{2n}k^2\,. \tag{2.103}$$

This means that, from (2.90), our $f^{\mu\nu}$ elements become

$$f^{00}=\left[g+\frac{\hbar^2}{4m}\frac{k^2}{n}\right]^{-1}, \tag{2.104}$$

$$f^{0j}=\left[g+\frac{\hbar^2}{4m}\frac{k^2}{n}\right]^{-1}\frac{\nabla^j\theta}{m}, \tag{2.105}$$

$$f^{i0}=\frac{\nabla^i\theta}{m}\left[g+\frac{\hbar^2}{4m}\frac{k^2}{n}\right]^{-1}, \tag{2.106}$$

$$f^{ij}=-\frac{n\,\delta^{ij}}{m}+\frac{\nabla^i\theta}{m}\left[g+\frac{\hbar^2}{4m}\frac{k^2}{n}\right]^{-1}\frac{\nabla^j\theta}{m}\,. \tag{2.107}$$

From this we see that the metric tensor has become a matrix of numbers and not operators, as one wishes. The problem, now, is that these numbers are explicitly momentum dependent and so we are left to deal with one of many possible "rainbow metrics" [141]. This breaks the analogy in the sense that the acoustic metric is not uniquely specified any more, as it was in the low-momentum limit.

Now, we want to make one final consideration about this high momentum limit. Starting from the $f^{\mu\nu}$ just derived and substituting the new form of the metric in (2.96), we obtain a non-linear dispersion relation [142]. That is

$$f^{00}\omega^2+(f^{0i}+f^{i0})\,\omega k_i+f^{ij}k_ik_j=0 \tag{2.108}$$

which is, after calculations,

$$\omega=v^ik_i\pm\sqrt{c^2k^2+\left(\frac{\hbar}{2m}k^2\right)^2}=v^ik_i\pm\sqrt{c^2k^2+\frac{c^2\xi^2k^4}{2}}\,, \tag{2.109}$$

where c is the speed of sound (2.38)[11]. This result is exactly the dispersion relation found by Bogoliubov for the collective excitations of a homogeneous Bose gas in the limit $T \to 0$, which we have previously derived for the case of a non-moving fluid, i.e. $\mathbf{v} = 0$ (see Eq. (2.71)). We could have foreseen this as, we want to stress, we started this Section by studying the fluctuations around an equilibrium state for a Bose gas, in exactly the same way as Bogoliubov did in 1947. Then we neglected the small-wavelengths, high-frequencies limit but we have now made use of the eikonal approximation in order to study the whole spectrum of k and λ. Thus, recovering Bogoliubov excitation spectrum is a nice consistency check.

Now, as we already discussed in Section 2.3, it is easy to see that the dispersion relation (2.109) interpolates between two different regimes depending on the value of the wavelength $\lambda = 2\pi/||k||$. In fact, if we assume $v = 0$ (or, equivalently, if we put ourselves in the co-moving frame):

1. for $\lambda \gg \xi$ we obtain a standard phonon dispersion relation, $\omega \simeq c||k||$;
2. for $\lambda \ll \xi$ the quasi-particle energy tends to the kinetic energy of an individual gas particle, $\omega \simeq \hbar^2 k^2/(2m)$.

This shows that the dispersion relation is a relativistic one only at low energies (large scales) which is why we refer to the high energy limit as "Lorentz breaking".

Lastly, the dispersion relation (2.109) is referred, in the context of analogue gravity, as *superluminal* since the (positive) term responsible for the deviation from the relativistic form has a positive sign in front.

At the end of this Section we want to remember that this issue - namely, the breaking of Lorentz invariance at high energies - has been studied through the years and the robustness of Hawking radiation against UV violations seems a well-established feature by now, as we have already discussed in Section 1.4 (for further discussions see [143]).

Nevertheless, it would be useful to find a viable method to explore the analogue Hawking effect which does not require the recovery of an acoustic metric, so that we do not have to rely on the hydrodynamic approximation. This is the content of one of our works, which we will describe in Chapter 4.

---

[11] A lot of times, in the literature, one finds the form $v^i k_i \pm \sqrt{c^2k^2 + \frac{c^2\xi^2k^4}{4}}$ where the last term presents a 4 instead of a 2 in the denominator. This is due to the ambiguity in the definition of the healing length: some textbooks define it as we did in Eq. (2.45), others prefer the definition $\xi \equiv \frac{\hbar}{mc}$.

2.7 Analogue Hawking radiation from BECs

We have come a long way to this point, but we have finally arrived at the core of this Thesis, the analogue Hawking radiation in Bose-Einstein condensates. It is useful to summarize the main points of this theoretical framework, in order to make things clear.

1. In 1974 S. Hawking demonstrated that black holes emit a thermal radiation. In the following years, a number of studies led to the understanding that the presence of this effect was tied to the existence of only two things: a horizon and a quantum field living on a curved background. Furthermore, it was understood that Hawking radiation is a solely quantum-field-in-curved-spacetime effect and it is not a peculiarity of gravitational fields (i.e., as long as we have a spacetime with a curved geometry, the presence of gravity is not essential for the effect to be present).
2. In 1981 W. G. Unruh noticed that, since the equations of sound in a moving/inhomogeneous fluid are mathematically equivalent to those of a scalar field living on a curved background, phenomena such as the Hawking effect should appear in these systems also. The field of analogue gravity was born.
3. Since the minimal requirements of the Hawking effect are a quantum field[12] living on a curved geometry and a horizon, a variety of hydrodynamical (or similar) systems can be studied. In particular, referring to Bose-Einstein condensates, if we imagine the fluid to flow from a subsonic region to a supersonic one we would have created an acoustic horizon (the analogue of a black-hole horizon) and thus we expect the appearance of the analogue Hawking radiation, i.e., an emission of a thermal flux of phonons from this region.

These are the main concepts underling this field. Among the other systems, the reason for BECs to be so promising relies in a few factors:

- first and most important, BECs are very controllable systems (they are relatively easy to construct and to manipulate in the laboratories) and they are robust to instabilities;
- they are highly-quantum analogue models;

---

[12] The Hawking radiation is also studied in classical set-ups such as, for example, water. There are reasons to believe that the effects seen in this context are the exact classical counterpart of the Hawking radiation [47]. For the sake of clarity, though, this effect is sometimes referred to as *stimulated Hawking radiation* or *classical Hawking radiation*. We will not enter the details of this topic as this Thesis will only deal with the analogue Hawking radiation in BECs; nevertheless the importance of these studies and the results achieved in this area should not be underestimated (see, e.g., the works [88, 89] or the comments made at the end of [95]).

- it can be shown that the Hawking temperature for small quantities of condensed atoms is of the order of a few nK [144], which is comparable with the temperature of the system;
- they have very low speed of sound ($c \sim$ cm/s);
- they can show density correlations[13].

Now, since Hawking radiation is so weak, the first requirement for any experiment aiming at detecting it is to make sure that there is no other source of noise in the system which could mask the effect. In BECs, this translates into the requirement that there be no quantised vortices, which usually arise due to the interaction of the radial flow with the surface of the container. A way to suppress the formation of such vortices is to take effectively one-dimensional configurations; if this happens, there is no space for the formation of quantum vortices. Such configurations have already been tested experimentally, as we will describe deeply in the following. For this reason, **in this work we deal only with Bose-Einstein condensates in a quasi-one-dimensional geometry**.

In the work developed in this Thesis, we gave contributions on the theoretical characterization of the analogue Hawking radiation in BECs. This field has been particularly active in the past years since a few experiments developed in the Technion laboratories of Haifa, Israel, have shown the presence of phenomena which could be connected to the analogue Hawking radiation. These experiments will be discussed more deeply in Chapter 3, as part of our work developed as a theoretical interpretation of the effects seen. On the other side, we have also built a simple, exactly solvable model to investigate the analogue Hawking radiation from a microscopic point of view and without relying on the mathematical framework of the gravitational analogy. We will describe this model in Chapter 4. Before heading to our work, though, there is still a couple of interesting aspects about the analogue Hawking radiation which are worth discussing.

2.7.1 Dispersion relations and mode analysis

In this Section we would like to discuss the form of the dispersion relation (2.109). Let us start by taking a dispersion relation of the form

$$(\omega - vk)^2 = c^2 F^2(k)\,, \tag{2.110}$$

where

$$F^2(k) = k^2 + \frac{k^4}{k_0^2}\,, \tag{2.111}$$

---

[13] This point will be clearer at the end of Section 2.7.2.

which is exactly the Bogoliubov dispersion relation, given that $k_0^2 = 2/\xi^2$. From these equations we see that the group velocity in the co-moving frame is dF/dk and so wave packets with $k \ll k_0$ propagate near the speed of light/sound, whereas wave packets with $k > k_0$ propagate *superluminally*. Thus, we call the dispersion relation (2.110) "superluminal".

Eq. (2.110) is a fourth-order polynomial equation in the wave vector k so it has four solutions for k at given values of ω and v. The nature of these roots is revealed with a graphical method (Fig. (2.7)). Figure (2.7) shows a plot of the straight lines $(\omega - vk)$ for different values of v and of the curve $\pm F(k)$ as functions of k; $F(k)$ is defined as the positive square root of (2.110). The intersection points are the allowed real wave vector roots of the dispersion relation and, from the figure, it is evident that for $|v| < c$ (i.e. for a subsonic flow) there are only two real roots (the other two roots are complex and, being associated to dynamical instabilities, as we have described in Section 2.4, they are disregarded). On the other hand, when $|v| \geq c$ (i.e. for a supersonic flow) all four roots are real **if** the frequency is smaller than a threshold value $\omega < \omega_{max}$. If $\omega > \omega_{max}$ the case is similar to that of a subsonic flow since there are only two real roots.

Now, let us choose a fluid which flows to the left, i.e. $v < 0$. We can see that the group velocity for a wave packet centred on a given wave vector is

$$v_g = \frac{d\omega}{dk} = -|v| \pm \frac{dF}{dk}\,, \tag{2.112}$$

where $\pm dF/dk$ is the group velocity in the co-moving frame. Thus, for any wave vector, v_g is just the slope of the $\pm dF/dk$ curve minus the slope of the straight line $(\omega - vk)$. If we now restrict our attention to wave vectors on the curve $+F(k)$ we see that dF/dk is positive, hence the sign of v_g is determined by which of the two slopes is larger, which is easily read from Figure (2.7). Furthermore, right-moving wave vectors (outgoing) have positive group velocity, while left-moving (ingoing) have negative group velocity.

We can now imagine to start outside of the horizon with an outgoing wave packet peaked around a wave vector of type $k \in +F(k)$. To make things even simpler, let us choose a wave vector from the first quadrant (i.e. $k \in +F(k) \wedge k > 0$). We now want to follow the same reasoning of Hawking and back-trace the history of the wave. If we follow this packet back in time it will move toward the black hole and blue-shift. This results in an increase in the wave vector which can be seen, from Figure (2.7), by increasing the slope of the straight line while keeping the intercept fixed (that is because the Killing frequency ω is conserved). As the wave vector grows, the group velocity increases in the co-moving frame, until the packet becomes superluminal and crosses the horizon (backward in time). The packet inside the horizon has also a negative component which comes from the fact that near the horizon mode conversion (from the positive wave vector branch to the negative wave vector

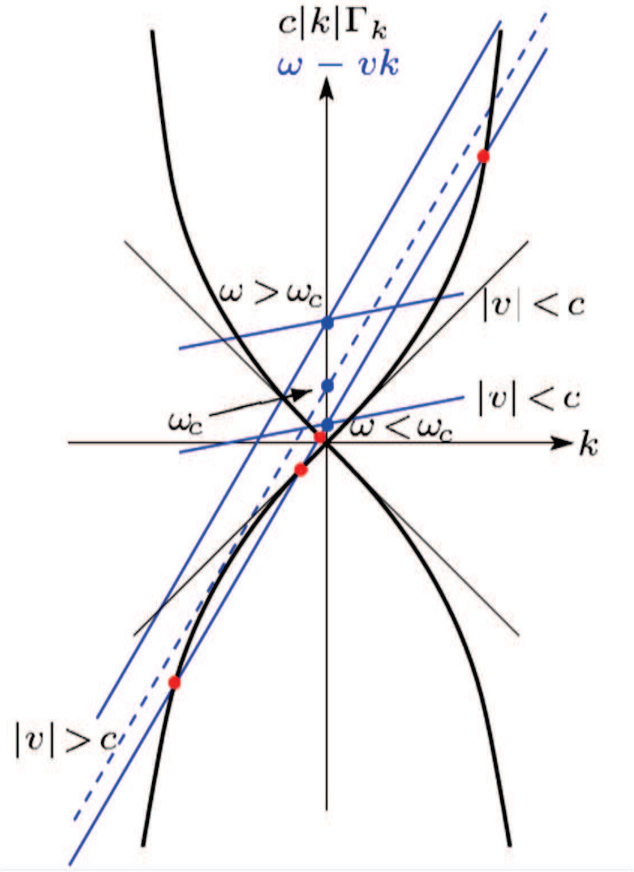

Figure 2.7: Plot of the $\pm cF(k)$ curves (black lines) and of the $(\omega - vk)$ curves (blue lines) as a function of k for different values of v. The intersection points of the curves are the allowed wave vector roots of the dispersion relation (2.110). Both cases of a supersonic and of a subsonic regime are shown and the critical frequency ω_{max} is pointed out (in the graph is labelled as ω_c).

branch of the dispersion relation) occurs. This can be shown analytically and it is made plausible by the fact that, around the horizon, the straight line of Figure (2.7) nearly coincides with a large portion of the curved line of the dispersion curve, thus allowing other wave vectors to become mixed in. This mode-mixing process at the horizon is believed to be at the origin of the Hawking radiation [145, 146].

This simple example was described in order to highlight two points:

1. the Transplanckian problem present in the relativistic case has been fixed by the presence of non-linear terms in the dispersion relation [76], as we had already anticipated in Section 1.4. On the other hand, this also shows that the mechanism underling the occurrence of the analogue Hawking radiation is conceptually different than the one which stands behind its relativistic counterpart.

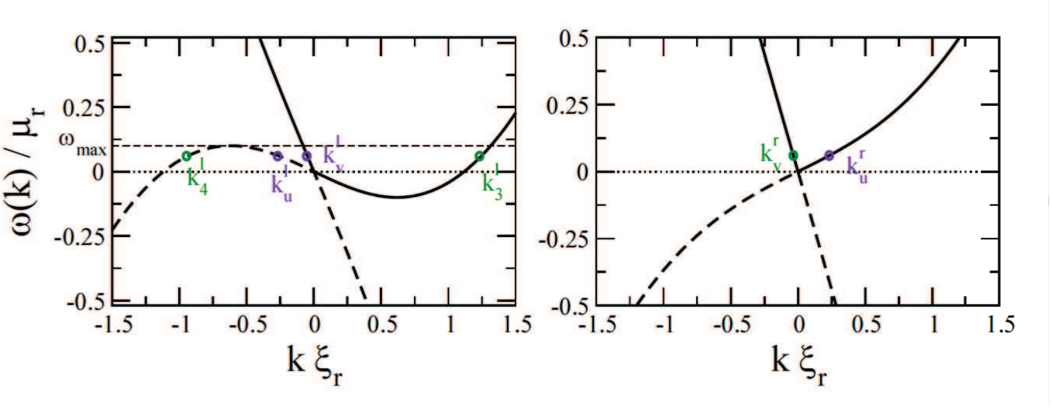

Figure 2.8: The plots give a better understanding on how the dispersion relation changes when we change the flow velocity (left panel: a supersonic scenario; right panel: a subsonic scenario).

2. In order to recover the analogue Hawking radiation, it is fundamental to keep within the limit imposed by ω_{max}. In particular, a few studies have characterized the correct value of this threshold frequency [145, 147].

2.7.2 The density correlation method

As we have described in Section 1.4, the temperature of the analogue Hawking radiation is related to the gradient of the sound and of the flow velocities at the horizon. This gradient cannot be made arbitrarily large and, for the hydrodynamic approximation to hold, one actually needs it to be at least a few times the typical coherence length of the system. This implies that in BECs, with low speed of sound, the expected power loss due to the Hawking emission is too faint to be detectable above the thermal phonon background due to the finite temperature of the condensate [75]. Despite this, the Hawking temperature is still in the nK regime and therefore BECs are still considered a primer candidate for the direct observation of this effect and ways to enforce the signal are being investigated [148].

A different approach to the matter was proposed in 2008 by an Italian collaboration [149, 150] and it is based on the density-density correlations on the two sides of the horizon. One nice feature of the analogue system, in fact, is that we have control on the region inside the horizon, which it is unreachable in the gravitational context (that is why they are called “black” holes). Thus, one could think to evaluate the two-point density correlation function

$$G^{(2)} = \frac{\langle n(x)n(x')\rangle}{\langle n(x)\rangle\langle n(x')\rangle}\,, \tag{2.113}$$

on opposite sides of the acoustic horizon, in order to evidence the correlation pattern between the emitted Hawking quanta and the partner P. This is represented in Figure (2.9).

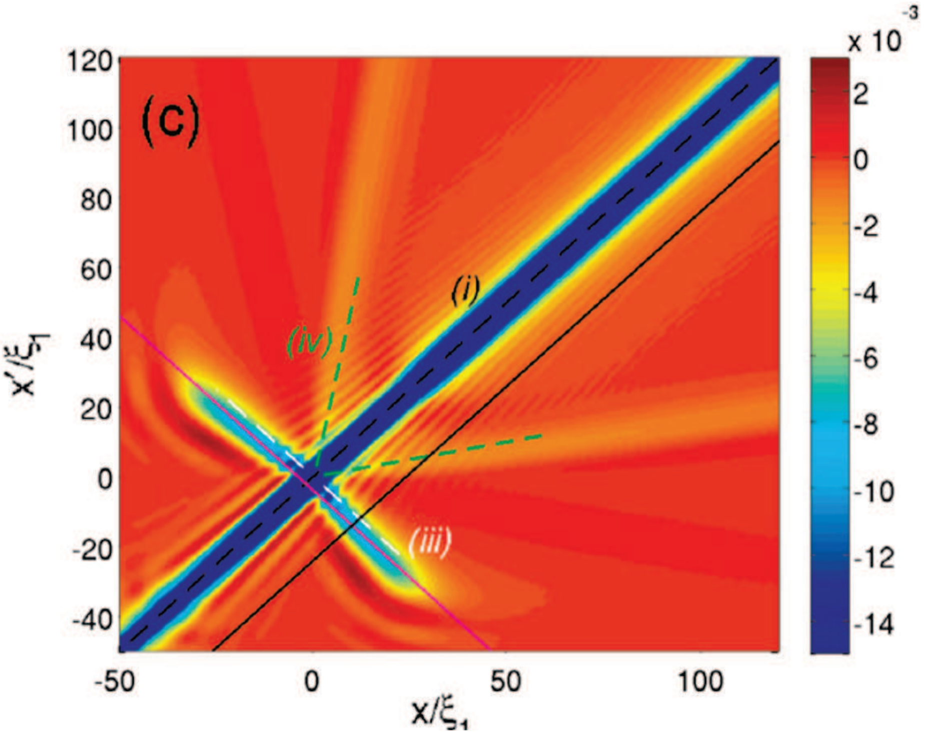

Figure 2.9: The image is taken from [149] and it shows the correlation function (2.113) evaluated at the two sides of the acoustic horizon, which is set in $x, x' = 0$. Features (*iii*) and (*iv*) are associated with the Hawking radiation.

The solidity of this method and its simpleness have quickly made it the “smoking gun” for the observation of the analogue Hawking radiation [151, 152] and recent experimental results use this evidence to claim the observation of analogue Hawking radiation in a BECs [66]. Nevertheless, note that the technique does not give a unique and unambiguous proof of the effect as other sources (e.g. thermal noise) could trigger the same signal [149].

2.7.3 Black hole lasers

One last important result we want to discuss is related to objects which have two horizons. The *black-hole laser* effect was first theorized by Vilenkin in 1978 [153] and then by S. Corley and T. Jacobson in 1999 [154] and is responsible for the amplification of the Hawking radiation in the region between the two horizons. On the astrophysical side, a possible candidate for the occurrence of this effect is represented by charged black holes, as they possess a event horizon and a “inner horizon” (IH). Otherwise, another possibility is the pair of a black-hole (BH) - white-hole (WH) horizon. White holes can be thought as the time-reversal of black holes and, although they are encoded in the Kruskal-Szekeres spacetime of maximally extended solutions, they are actually of limited use in astrophysics. Nevertheless, they can be easily constructed in the analogue systems.

Black hole lasers occurs if there is both an inner and an outer horizon and if the dispersion relation is *superluminal*, which means that wave packets, under certain circumstances, propagate superluminally. If this happens, then the Hawking radiation for a bosonic field is *self-amplifying* while for a fermionic field is *self-attenuating*. This is due to the fact that the region between the horizon behaves like a resonant cavity, where radiation "bounces" back and forth, stimulating further emission. In recent analysis on BECs [155, 156] it has been shown that the complete set of modes to be taken into account in these configurations is composed of a continuous sector with real frequencies, plus a discrete sector with complex frequencies of imaginary part. These discrete frequencies encode the unstable behaviour of these configurations and they are generated as resonant modes inside the supersonic cavity encompassed between the horizons. Furthermore, it was demonstrated that this phenomenon is related to the appearance of a dynamical instability in the Gross-Pitaevskii equation [157, 158].

These systems have been vastly studied in the past years [159–161] and a recent experiment [65] has claimed the observation of this phenomenon. This is exactly the starting point of our work and the content of the next Chapter.

Chapter 3

The 2014 Technion experiment

This Chapter describes the first part of our work which was apt to characterize the effects seen in an experiment in ultra-cold atoms developed in 2014 [65]. The experiment claimed the observation of self-amplifying Hawking radiation and the work had a huge impact in the scientific community, as never before there had been a claim of detection of the Hawking mechanism in a BEC. Starting from the experimental paper, we gave the first theoretical framework of the effects seen, arriving at our own interpretation of the phenomena observed. In the years after our work [92], two other groups developed numerical simulations on the same experiment [93, 94, 162], reaching different conclusions and re-opening the discussion about the detection (or not) of the Hawking effect. We have been working on this matter since then but we think we have finally arrived at a conclusion. The experiment, our first model, the subsequent works and our most recent results are all deeply described in this Chapter.

For the sake of completeness, we want to mention that, in the years after the publication of [65], the same group developed another experiment which claimed the observation of the analogue Hawking radiation [66][1]; this paper also raised some discussion about the interpretation of the results [95, 163]. Nevertheless, the signal investigated in [66] is tied to the quantum nature of the Hawking effect (indeed, they study the correlation pattern described in Section 2.7.2) and, thus, our semiclassical approach cannot be applied to this case. Therefore, our work [92] is not relevant for the solution of the debate [95, 163].

---

[1] Truth to be told, a third work has recently appeared on the web [96] but it has not been published yet.

3.1 The experiment: set-up and results

In October of 2014 Nature Physics published an article which claimed the observation of self-amplifying Hawking radiation from an analogue black hole [65]. The author, Jeff Steinhauer, works at the Technion - Israel Institute of Technology in Haifa, Israel and was also a member of the group that conducted the experiment which led to the first realization of a sonic black hole from a Bose-Einstein condensate in 2010 [64]. Other than his works (the aforementioned ones and the more recent [66,96]), there has never been recorded another realization of a sonic black hole in BECs.

We will now describe in details the 2014 experiment [65] and its results, as they represent the starting point of our work. Through numerical simulations, in fact, we tried to check the validity of the claims made in the article, reaching some interesting results.

The idea of the experiment was simple and straightforward: by means of a combination of magnetic and optical potentials, a Bose-Einstein condensate was accelerated above the speed of sound to recreate an analogue black hole. Actually, since the velocity of the atoms was supersonic only in a limited region and subsonic everywhere else, the configuration showed the presence of two horizons, recreating the analogue of a black hole-white hole pair, rather than a simple black hole. Thus, under suitable conditions, one could hope to detect the self-amplifying Hawking radiation and the black-hole laser effect.

In the experiment, the condensate of ^{87}Rb atoms in the $F = 2$, $m_F = 2$ state is created in a magnetic trap and then transferred to a confining beam which constrains the BEC in a tube-like volume, so to have nearly one-dimensional dynamics (indeed, the transverse confinement has an energy spacing of 6 nK while the chemical potential of the BEC is $\mu = 8$ nK). A magnetic field gradient is also applied to compensate the force of gravity. The focused laser beam (5 μm waist, 123 Hz radial trap frequency and 812 nm wavelength) provides the axial direction (i.e., the direction of motion) with a confining potential which is weaker than parabolic, due to the nature of the Gaussian beam. Then a suitable, step-like longitudinal optical potential (called the "waterfall" potential) is applied in order to accelerate the atoms above the speed of sound. This potential was created by means of a large-diameter Gaussian laser beam and it was swept through the atomic cloud at a constant speed $v_{upstream} = 0.21$ mm/s. The waterfall moves to the right and, therefore, to the right of the step potential the condensate is essentially unperturbed and at rest in the laboratory frame. To the left of the potential drop, however, the atoms gain supersonic speed and an analogue of a black-hole horizon is created. The black-hole horizon (the point where the flow becomes supersonic) is thus set at the position of the waterfall potential and, therefore, it moves to the right at constant speed $v_{upstream}$. Furthermore, due to the profile of the confining potential, the flow

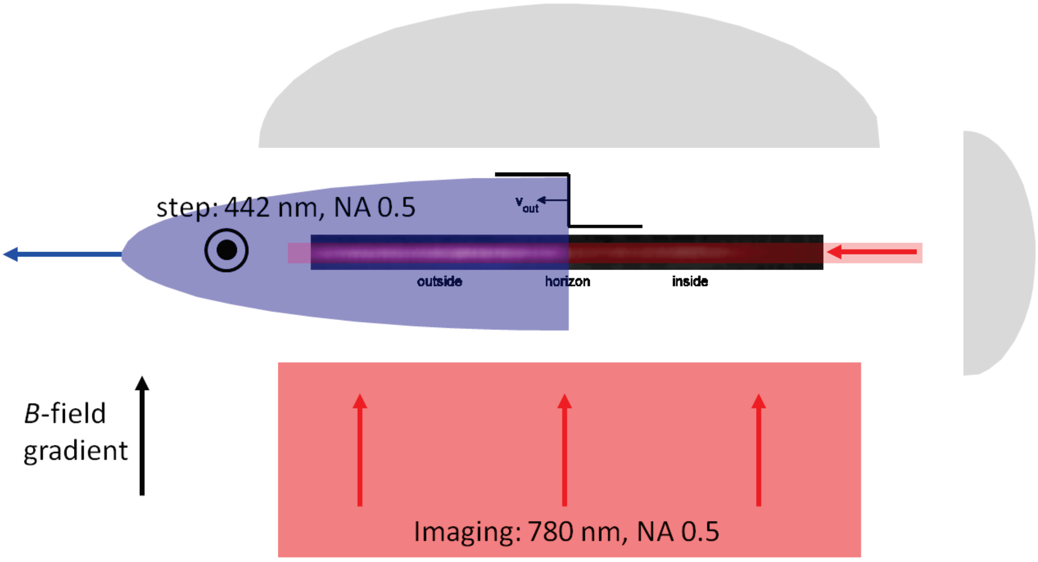

Figure 3.1: Scheme of the experimental set-up for the creation of a sonic black hole in a BEC. The image shows the set-up used at Technion in 2010 [64] but it is very similar to the 2014 experimental set-up (note, though, that the flow velocity is in the opposite direction). The image was taken from the public lecture given by J. Steinhauer at the *21st International Conference on General Relativity and Gravitation* hosted in New York in the summer of 2016.

velocity to the left of the black-hole horizon decreases as atoms flow "uphill" and approach the relevant turning point. The point where the velocity of the atoms drops below the speed of sound is the white-hole horizon, which occurs before the turning point is reached. Thus, the experiment created a pair of analogue black-hole and white-hole horizons since on one side of the region phonons cannot exit while on the other side they are forced to do so. Figure (3.1) shows a scheme of the experimental set-up used in a similar experiment. Figure (3.2), instead, is taken from [65] and shows the form of the longitudinal potential. Note that, in the experiment, different heights were used for the step potential and thus three different turning points are indicated in Figure (3.2). By increasing the potential drop at the waterfall, in fact, the atoms gain a larger velocity and, therefore, the turning point (and, consequently, the WH horizon) moves to the left. The three heights used for the potential step were 3.2 nK, 6.4 nK and 9.6 nK but most of the results in the article are given for the middle value, i.e. 6.4 nK, and therefore, from now on, we will refer to this value only. The step potential has a width of the order of the healing length, which is said to be $\xi = 2\,\mu$m in the supersonic region. Finally, the initial phonon state of the condensate is determined in order to know the temperature of the gas. This was done with an *in situ* technique developed in earlier works [164, 165] which allowed to determine that the initial temperature of the condensate was between zero and $0.1\,\mu$.

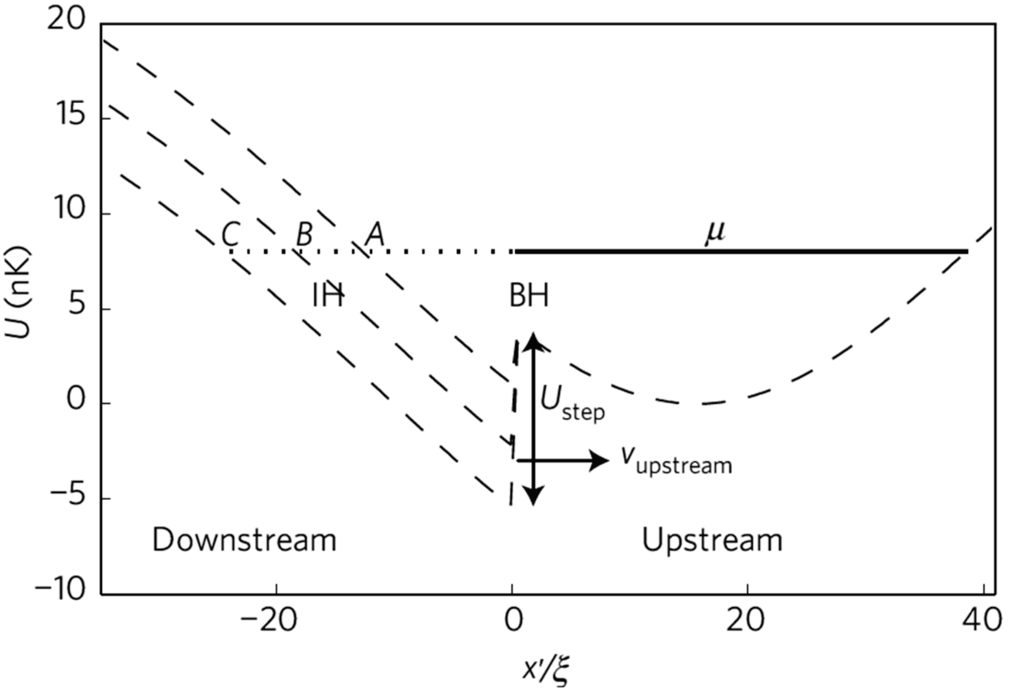

Figure 3.2: Image from [65]. The three potential profiles employed in the experiment of 2014. The dynamics is along the same axis. In particular, the black-hole horizon (BH) and the inner horizon (IH) positions are indicated for the case of the middle value of height of the step while the turning point is indicated for all the three cases (points A, B and C). As described in the text, in the laboratory frame, atoms flow from the right to the left, they gain supersonic speed at the step position and then they gradually slow down as they get closer to the inner horizon. The $x-$axis values are given in term of the healing length, which is 2 μm.

In the experiment, the system is let evolve for 120 ms and the condensate density is imaged at seven instants of time with a phase contrast imaging technique. For each of these times, an ensemble of approximately 80 images is collected and then averaged to reduce noise. From the resulting density profile, the spatial profiles of the condensate velocity and of the speed of sound are finally extracted. In order to verify the presence of two horizons, in fact, the first requirement is to have a supersonic region bounded by two subsonic ones. Thus, from measurements of the density, the velocity of the condensate is extracted by applying the continuity equation (2.53)

$$\boldsymbol{\nabla}\cdot(n\mathbf{v}) = -\frac{\partial n}{\partial t} \tag{3.1}$$

which becomes, in 1D,

$$v = -\frac{1}{n}\int_0^x \frac{\partial n}{\partial t}dx' \,. \tag{3.2}$$

On the other side, the sound speed is calculated using Eq. (2.38), that is

$$c = \sqrt{\frac{gn}{m}}\,, \tag{3.3}$$

where $g = 4\pi\hbar^2 a_s/m$ is, as we have seen, the interaction parameter, m is the atomic mass of ^{87}Rb, n is the density profile and a_s is the s-wave scattering length (in the case of ^{87}Rb $a_s = 5.77$ nm). These measurements, averaged over the evolution time $t = 120$ ms, are plotted in Figure (3.3).

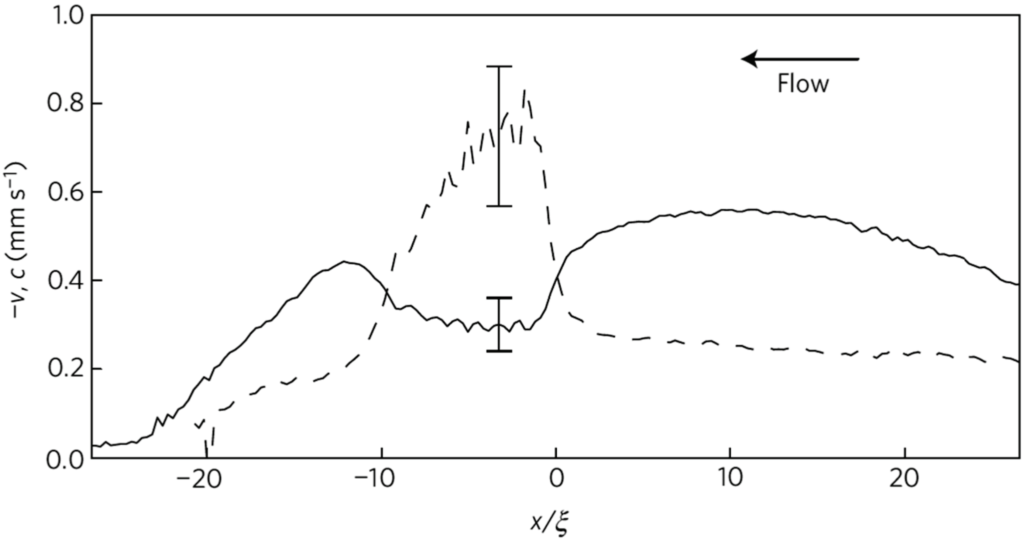

Figure 3.3: Image from [65]. The dashed and solid curves indicate $-v$ and c, respectively. The two curves are the average over the 120 ms of evolution of the condensate, whose density profile change is shown in Fig (3.4). The spatial coordinate is given in unit of the healing length ξ, which is 2 μm inside the lasing region. The plot shows the velocities in the waterfall reference frame, in which the horizons have fixed positions and the atoms flow to the left.

Fig. (3.3) shows that, during the experiment, a well-defined, closed, supersonic region was present. Its width was approximately 20 μm and both the horizons (that is, following the flow direction, the transition from subsonic to supersonic and the transition from supersonic to subsonic) are well-defined. Once this check is made, one can turn the attention to the density profiles evolution, with the hope of detecting the black-hole laser signal.

In an analogue pair of BH-WH we expect the black-hole laser mechanism to appear. As explained in [64,156] and in Section 2.7, the Hawking radiation created at the horizon should propagate away, while the negative-energy partner P should propagate to the other horizon, where it is reflected and it stimulates more Hawking emission. Furthermore, this mode interferences with the negative-energy modes in_- present in the cavity, creating a negative-energy standing wave pattern inside the so called “lasing” region (that is, the supersonic region bounded by the two horizons where the laser effect should take place). Images of the condensate evolution from the experiment are shown in Fig (3.4) (a-i) while the corresponding density profiles are plotted in Fig (3.4) (j-r).

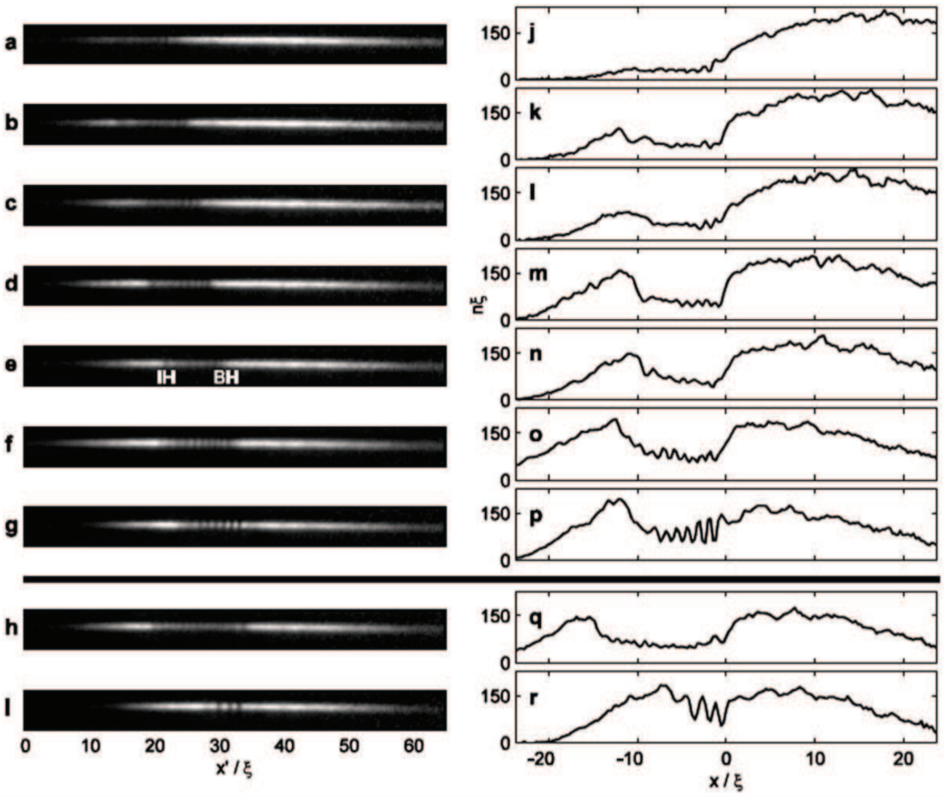

Figure 3.4: Image from [65]. **a-g.** *In situ* images at 20 ms time intervals, starting soon after the creation of the black-hole and inner horizons (respectively BH and IH). The images show the average of the ensemble as viewed in the laboratory frame, in which the horizons move. The intermediate step height is employed. The spatial coordinate is given in unit of the healing length ξ which is 2 μm in the lasing region. **h.** Like the latest time g, but with a higher step. **i.** Like g, but with a smaller step. **j-r.** Integrated profiles corresponding to a-i as viewed in the horizon frame. The black-hole horizon is located at the origin and the $y-$axis is given in healing length units.

Figure (3.4) shows that, during the cloud evolution, a clear "interference pattern" [65] appears inside the supersonic region. Furthermore, from the integrated density profiles we can see that these fringes grow in amplitude as time passes, as one would have expected. Thus, this signal is interpreted as the black-hole laser effect which implies, in turn, the presence of self-amplifying Hawking radiation. The number of maxima in the cavity is the number of modes and it can be seen from Figure (3.4) (q-r) that this number changes as the height of the step varies (that is, for a higher step the number increases while for a lower step it decreases). In order to further test the presence of the black-hole laser mechanism, the two-point correlation function given by

$$G^{(2)}(x_1, x_2) = n_L^{-2}[\langle n(x_1)n(x_2)\rangle - \langle n(x_1)\rangle\langle n(x_2)\rangle - \langle n(x_1)\rangle\delta(x_1 - x_2)] \quad (3.4)$$

is calculated, where the average is over the ensemble of images and n_L is the average density in the lasing region. The results are shown in Figure (3.5).

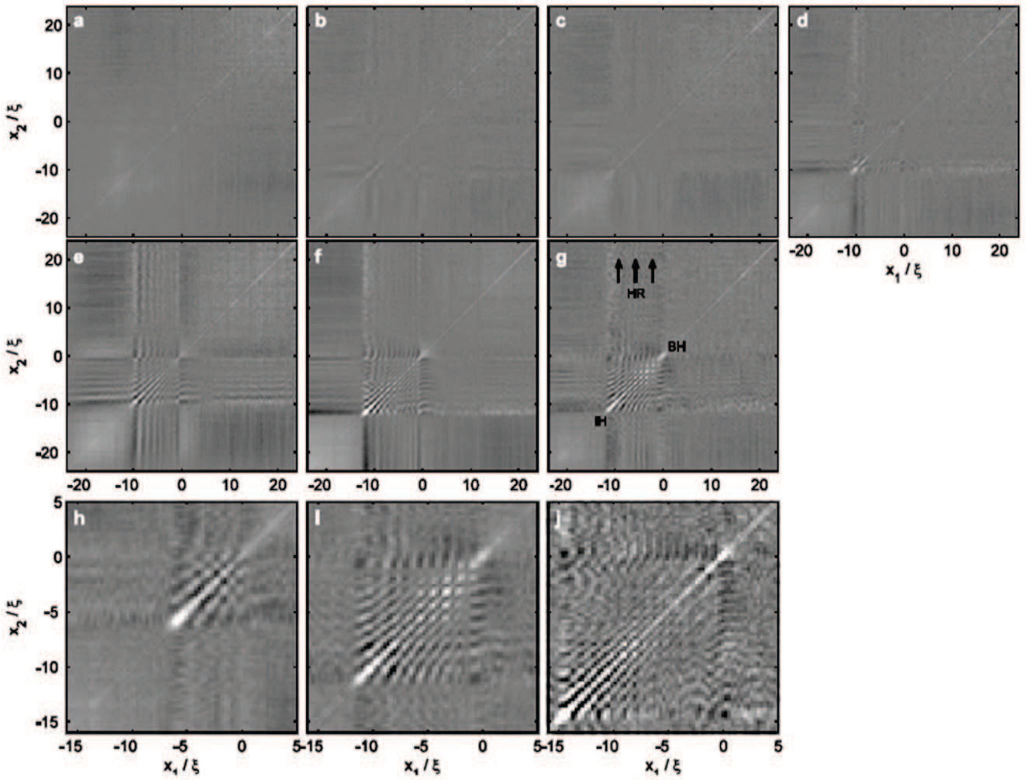

Figure 3.5: Image from [65]. The density-density correlation function pattern is shown, calculated using Eq. (3.4). The points where x_1 and x_2 correspond to the BH horizon and the IH are indicated in g. **a-g.** Increasing times correspond to Fig. (3.4) (a-g), where the intermediate value of the height of the step is used. **h-j.** The lasing region for increasing value of the height of the step at the latest time. **i.** The plot is an enlargement of (g). In (j) the grey scale has been decreased relative to (h) and (i) by a factor two, in order to improve the visibility of the pattern. The spatial coordinate is given in unit of the healing length ξ which is 2 μm in the lasing region.

Figure (3.5) shows the results of the calculation of the density-density function (3.4) for the entire evolution of the cloud. The evidence of the presence of the black-hole laser mechanism is evident from panel (i) of the aforementioned figure; here, in fact, a checkerboard pattern very similar to the predictions of [156] is visible. This implies that the fluctuations have a well-defined wavelength, as well as well-defined nodes. Furthermore, close to the inner horizon in the lasing region, the pattern seems to be more similar to fringes parallel to the diagonal rather than a checkerboard. Such fringes imply that the positions of the of the nodes vary, which occurs because the position of the inner horizon is determined by hydrodynamics, and thus it varies slightly from realization to realization. The location of the BH horizon, in contrast, is determined by the applied potential step, which is the same in every realization.

Finally, the amplitude of these modes is investigated through Fourier transform of the correlation function and the round-trip time of the excitations is extracted. This is an important check because the exponential growth is one way of distinguishing the black-hole laser mechanism from the phenomena of Hawking radiation from one black-hole horizon (no growth), from white-hole radiation (linear or logarithmic growth [166]), or from white-hole undulations (no growth [166, 167]).

In conclusion, in the 2014 experiment a pair of analogue BH-WH was created and effects evident in the density profile evolution were interpreted as the black-hole laser mechanism. Consequently, self-amplifying Hawking radiation was claimed to be detected.

3.2 Our first numerical simulations

A few months after the publication of the experimental results [65] we became aware of the work. In our opinion, the first and most obvious thing to do was to build a numerical simulation in order to characterize the effects seen in the laboratory, as it appeared that no other theoretical study on the experiment had had developed yet. In this Section we will describe the results we achieved, which were published in the summer of 2016 in a Letter [92], after long discussions and deep confrontations with experts in the field (first and foremost, with the author of [65] himself).

3.2.1 The theoretical model

As a first approach, in order to simplify things, we construct a numerical model of the time-dependent Gross-Pitaevskii equation (GPE) (2.49), which we have thoroughly described in Section 2.4 and which represents a good approximation for the dynamics of a dilute Bose gas. Furthermore, to describe a nearly one-dimensional cloud, as the experimental system was, we follow [128] and we trace out the transverse degrees of freedom, so to obtain the Non-Polynomial Schrödinger Equation (NPSE) described in Section 2.4, which is an appropriate form in the case of a harmonic transverse confinement potential. The form of the experimental transverse trap was not exactly harmonic (as the author himself noted during one of our conversations), nevertheless a harmonic confinement represents a very good approximation of the realistic case, as discussed in Section 2.4. We now recall Eq. (2.65) (i.e. the NPSE):

$$\begin{aligned} i\hbar\frac{\partial f}{\partial t} = &\left(-\frac{\hbar^2}{2m}\frac{\partial^2}{\partial z^2} + V + \frac{gN}{2\pi a_\perp^2}\frac{|f|^2}{\sqrt{1+2a_sN|f|^2}}\right)f + \\ &+\frac{\hbar\omega_\perp}{2}\left(\frac{1}{\sqrt{1+2a_sN|f|^2}} + \sqrt{1+2a_sN|f|^2}\right)f - \mu f\,, \end{aligned} \tag{3.5}$$

where $f(z,t)$ is the longitudinal part of the wave function while the transverse profile has been assumed to be Gaussian. Here z is the axis of motion and $a_\perp = \sqrt{\hbar/(m\omega_\perp)}$ is the transverse harmonic length, which was introduced by means of Eq. (2.55).

Since the goal of this simulation is to recreate the experimental conditions, we choose all the parameters in accord with the data given in [65]. In particular, for the transverse harmonic frequency, we choose $\omega_\perp = 965$ rad/s which is in accord with the experimental parameter, given the radial trap frequency ν listed in the article[2]. A further consistency check for our choice can be made by taking the value of the energy spacing given in [65] and extracting $\omega_\perp$ from the harmonic potential energy $\omega_\perp = k_BT/\hbar$.

The longitudinal potential $V(z,t)$ is assumed to have the form:

$$V(z,t) = V_0\sqrt{(z-z_0+vt)^2+a^2} - \frac{V_s}{2}\left[1-\tanh\left(\frac{z}{\sigma}\right)\right] + c, \tag{3.6}$$

with parameters $V_0 = 0.3$ mK/m, $z_0 = 44.63\,\mu$m, $v = 0.21$ mm/s, $a = 19.44\,\mu$m, $V_s = 6.4$ nK, $\sigma = 2.33\,\mu$m and $c = -6.07$ nK, all chosen in order to fit the experimental potential described in Figure (3.2). A snapshot of the resulting total potential at time $t = 20$ ms is represented in Fig. (3.6). Note that, to better match the experiment, the step-like waterfall potential is smoothed with a $\tanh(z)$ function, whose width is in accord with the experimental one ($\sigma \simeq \xi$). Note also that, during the experiment, the confining part of the longitudinal potential remained at rest while the step-like waterfall potential was swept along the condensate at constant speed in the rightward direction. In our simulations, instead, we prefer, for numerical convenience reasons, to move the trap in the leftward, negative-z direction and to keep the waterfall potential at rest. This setting is fully equivalent to the experimental one since the two configurations are related by a Galileian transformation.

Given this configuration, we have that the total number of bosons is approximately $N \simeq 5000$, which is a reasonable number for a cold-atoms experiment (the experimental datum was not listed in the article).

---

[2] Actually, there is a 15% difference between the two numbers (that is, our $\omega_\perp$ and the experimental $\omega = 2\pi\nu$); nevertheless, since the confinement was not exactly harmonic, we adjust $\omega_\perp$ in order to retrace the height of the density profiles shown in Fig. (3.4). Given that in [65] there is no reference to the errors on the values of the parameters, we felt this was the safest way to obtain a good approximation to the experimental case.

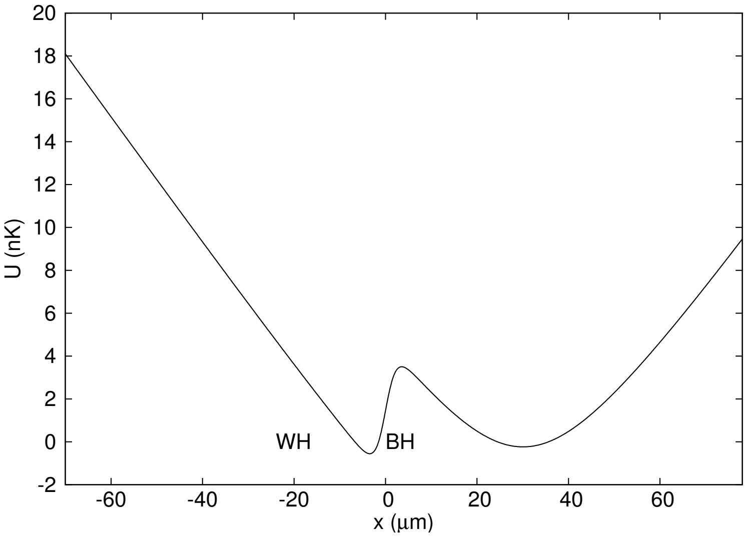

Figure 3.6: Image from [92]. Snapshot of the axial potential used in the simulation at time $t = 20$ ms to be compared to Fig. 1c from [65] which was reported in the previous Section as Figure (3.2). WH and BH indicate the position of the (inner) white-hole horizon and of the black-hole horizon, respectively. In the simulations the condensate flows from the right to the left, which is Galilean-equivalent to the experimental configuration where the step-like waterfall potential is moved in the rightward direction.

To be more precise, before numerically integrating Eq. (3.5) with our suitable choice of longitudinal potential, we want to do some re-scaling, in order to work with adimensional quantities. For this reason we put:

$$x = \frac{z}{a_\perp}\,, \quad \tau = \omega_\perp t \quad \text{and} \quad f = \frac{\psi}{\sqrt{a_\perp}}\,. \tag{3.7}$$

Substituting (3.7) and the value of g in Eq. (3.5) we obtain, after calculations:

$$\begin{aligned} i\frac{\partial\psi}{\partial\tau} = -\frac{1}{2}\frac{\partial^2\psi}{\partial x^2} + \left(\frac{V}{\hbar\omega_\perp}\right)\psi + \frac{g'|\psi|^2\psi}{\sqrt{1+g'|\psi|^2}} + \\ +\frac{1}{2}\left(\frac{1}{\sqrt{1+g'|\psi|^2}} + \sqrt{1+g'|\psi|^2}\right)\psi - \mu'\psi\,, \end{aligned} \tag{3.8}$$

where $\psi(x)$ is normalized and

$$g' = 2\frac{a_s}{a_\perp}N\,, \quad \mu' = \frac{\mu}{\hbar\omega_\perp}\,. \tag{3.9}$$

Furthermore, we can make another modification in order to eliminate the explicit dependence on the number of bosons N (since this parameter is not listed in [65] we can infer it a posteriori). Therefore, if we introduce

$$\phi = \sqrt{N}\psi \tag{3.10}$$

we obtain, by substituting it into Eq. (3.8):

$$
\begin{aligned}
i\frac{\partial\phi}{\partial\tau} = -\frac{1}{2}\frac{\partial^2\phi}{\partial x^2} + \frac{V}{\hbar\omega_\perp}\phi + \frac{\tilde{g}|\phi|^2\phi}{\sqrt{1+\tilde{g}|\phi|^2}} + \\
+\frac{1}{2}\left(\frac{1}{\sqrt{1+\tilde{g}|\phi|^2}} + \sqrt{1+\tilde{g}|\phi|^2}\right)\phi - \mu'\phi\,,
\end{aligned}
\tag{3.11}
$$

where

$$
\int |\phi|^2 dx = N \quad \text{and} \quad \tilde{g} = \frac{g'}{N} = 2\frac{a_s}{a_\perp}\,. \tag{3.12}
$$

At this point, we integrate Eq. (3.11). This task requires the numerical method to be unitary since this is a fundamental property of dynamics at the quantum level. Indeed, given any initial wave function $\phi(x,0)$, the Schrödinger equation keeps the norm constant through the whole evolution.

Now, if we write Schrödinger equation in the form

$$
i\frac{\partial\phi}{\partial t} = H\phi\,, \tag{3.13}
$$

we have that a good way to integrate our equation that respects the aforementioned requirement is through the formula [168]

$$
\left(1+\frac{1}{2}iH\Delta t\right)\phi^{n+1} = \left(1-\frac{1}{2}iH\Delta t\right)\phi^{n}\,, \tag{3.14}
$$

where we have discretized the time variable as $t_n = n\Delta t$ (with Δt the time interval) and we have put $\phi(x,t_n) = \phi^n$. This is a method to integrate Schrödinger equation which is stable, unitary and second-order accurate in space and time. As for the form of H we have, in our case,

$$
\begin{aligned}
H_2 = -\frac{1}{2}\frac{\partial^2}{\partial x^2} + \frac{1}{\hbar\omega_\perp}\left(V_0'\sqrt{(x-x_0+v't)^2+a'^2} - \frac{V_s'}{2}\left[1-\tanh\left(\frac{x}{\sigma'}\right)\right] + c'\right) + \\
+\frac{\tilde{g}|\phi|^2}{\sqrt{1+\tilde{g}|\phi|^2}} + \frac{1}{2}\left(\frac{1}{\sqrt{1+\tilde{g}|\phi|^2}} + \sqrt{1+\tilde{g}|\phi|^2}\right) - \mu'\phi\,,
\end{aligned}
\tag{3.15}
$$

where V_0', v', a', V_s', σ' and c' are the previously-listed V_0, v, a, V_s, σ and c in our re-scaled units. Having replaced this form by its finite-difference approximation, we solve the complex non-linear set of algebraic equations by use of a Predictor-Corrector algorithm to find the wave function at all times.

This last paragraph gives specific details on how we integrate the GPE and this description may as well be put aside, as it does not affect the results (many other approaches to the numerical problem also exist). Nevertheless, we want to give as much detailed description of our work as possible, so to answer any possible question and to give a basis for the reader interested into replicating our results.

Now, going back to Eq. (3.11), having given the precise form of the longitudinal potential V we are only missing $\phi(x, 0)$ in order to solve our problem. As the initial condition, we consider the ground state wave function which is obtained from an imaginary-time NPSE evolution in the presence of interactions and of the harmonic trapping but in the absence of the waterfall potential (we will explain the imaginary-time evolution technique shortly). More precisely, we start the evolution at $t = -50\,\mathrm{ms}$ when the step of the waterfall potential is still far to the left of the trap minimum and the condensate does not touch it. Finally, according to the above-mentioned Galilean transformation, the atoms are also given an initial velocity in the negative z direction which equal to the trap's velocity, so no spurious acceleration stage is introduced. In fact, if we started moving the trap in the leftward directions without giving the atoms an initial velocity, the cloud would feel an acceleration; to avoid that, we modify the initial wave function adding a phase factor to it: that is, we take $\phi(0, x)e^{-ivx}$, instead of simply $\phi(0, x)$, as our initial condition, where $-v$ is the (constant) velocity of the trap in dimensionless units.

Initially we adopted the Thomas-Fermi profile (2.57) as our initial wave condition (the Thomas-Fermi approximation is described in Section 2.4). After further discussions, though, it was deemed better to start from the actual ground state of the trap, in order to avoid any spurious effect. Nevertheless, even though the Thomas-Fermi profile does not have the "tails" typical of a Gaussian profile, the difference between the two turned out to be minimal and no change in the dynamics was noted. In any case, to obtain the real ground state of our problem, one can start from a generic state and let the system evolve with imaginary times. In fact, we can consider the Schrödinger equation in the form

$$i\frac{\partial \phi}{\partial t} = H\phi\,, \tag{3.16}$$

and then take an imaginary time $\tau = it$ so that it becomes

$$-\frac{\partial \phi}{\partial \tau} = H\phi\,. \tag{3.17}$$

This shows that, for $\tau \to +\infty$, the wave function converges to the solution of $H\phi = 0$, which is the ground state of the problem. The procedure is thus simple and straightforward: start with a trial wave function $\phi(t)$ (in our case TF) and let it evolve with imaginary time so to obtain the ground state of the system.

3.2.2 Velocities and density profiles

Having reproduced the experimental configuration, we proceed by numerically integrating Eq. (3.5) and evaluating the axial density[3] $n(x,t) = N|f(x,t)|^2$. As a first step, we want to verify that the configuration of a black hole-white hole pair is recovered by calculating the condensate and the sound velocity. In the same way as [65], the former is obtained by means of the one-dimensional continuity equation[4] as:

$$v(x) = -\frac{1}{n(x)} \int_{-\infty}^{x} \frac{\partial n(x')}{\partial t}\, dx' \,, \tag{3.18}$$

while the latter, averaged over the transverse directions, is

$$c(x) = a_\perp \omega_\perp \sqrt{\frac{g'|f(x)|^2}{\sqrt{1+g'|f(x)|^2}}} \,, \tag{3.19}$$

where $g' = 2a_s N$ is the effective one-dimensional interaction constant.

The averages of these two quantities over the evolution interval are shown in Fig. (3.7(a)). A spatially-limited supersonic region is evident and thus we recover a pair of analogue black-hole and white-hole horizons. It is important to notice that our results agree with the experimental observations shown in Fig. (3.3) also from a quantitative point of view. Indeed, the sound velocity (solid curve) and the width of the lasing region (the region of supersonic flow) agree with the experimental data. The only minor discrepancy between the two figures lies in the stronger contrast of the fringes shown by the speed of sound and, even more visibly, by the condensate velocity (dotted curve) in between the two horizons. Now, in the experimental article it is mentioned that there were some shot-to-shot fluctuations in the position of the white-hole horizon. As the experimental results are obtained by averaging over many different realisations of the experiment, the decrease in the fringe contrast in the region between the two horizons is likely due to these fluctuations. A brief discussion of their origin will be given in the following of this work but now we want to turn our attention to the density profiles.

Figure (3.8) shows the density profiles (dotted lines): the agreement with the corresponding experimental profiles shown in Fig. (3.4) is good both in the overall condensate density and in the width of the lasing region. Most importantly, the characteristic fringe pattern in the region between the two horizons is also quantitatively recovered and it is evident how the amplitude of these fringes grows in time, as observed in the experimental data. As we have already

---

[3] From now on we will work with the real, dimensional quantities and we will denote x the axis of motion.

[4] Note that the result is qualitatively unchanged even if time steps as long as 20 ms are taken, as actually done in the experiment.

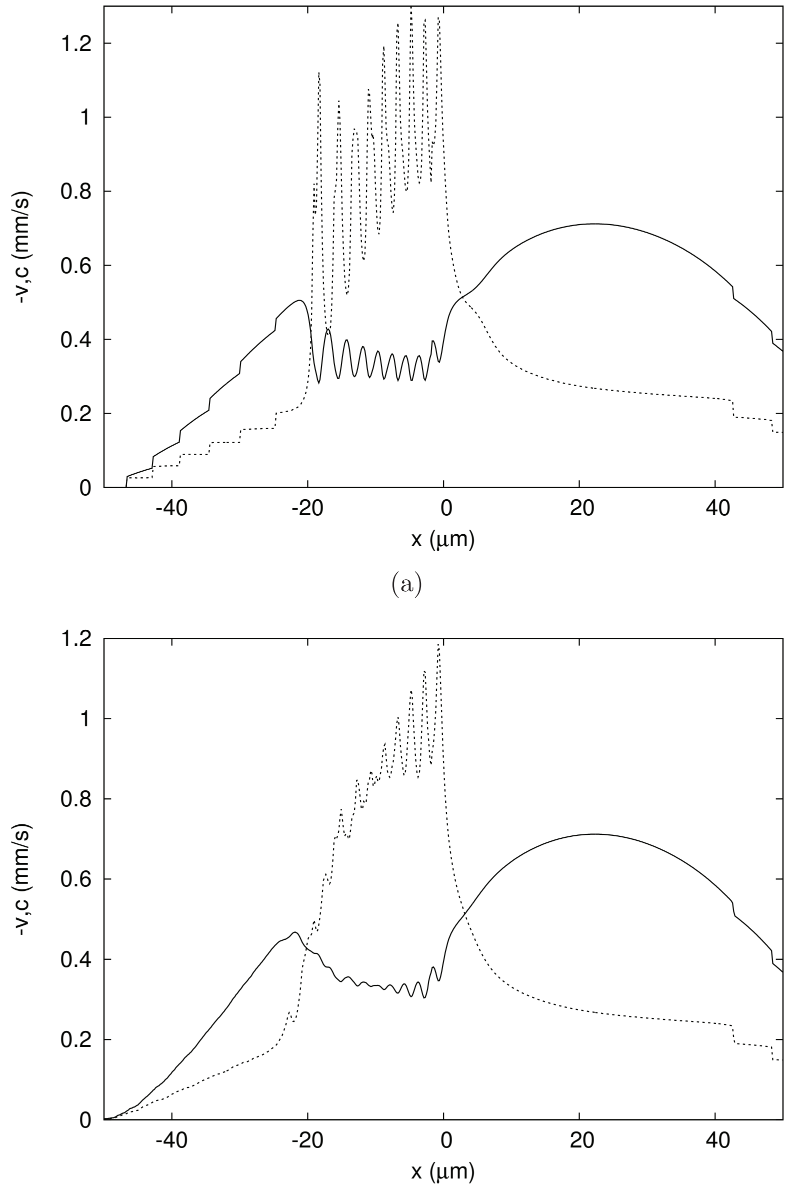

(a)

(b)

Figure 3.7: Image taken from [92]. The dotted and the solid curves indicate $-v$ and c respectively. The upper panel shows the prediction for the two velocities with no additional noise. On the other hand, the lower panel shows the same curves in the presence of fluctuations in the position of the white-hole horizon. As it is discussed in the text, these are included by means of 10% fluctuations on the intensity of the waterfall potential V_s. In both panels the curves are the temporal average over the 120 ms corresponding to Fig. (3.8), as it was done in [65]. In both cases, a well-defined supersonic region is clearly visible inside the two horizons.

mentioned, in [65] this was interpreted as the main signature of the black-hole laser effect.

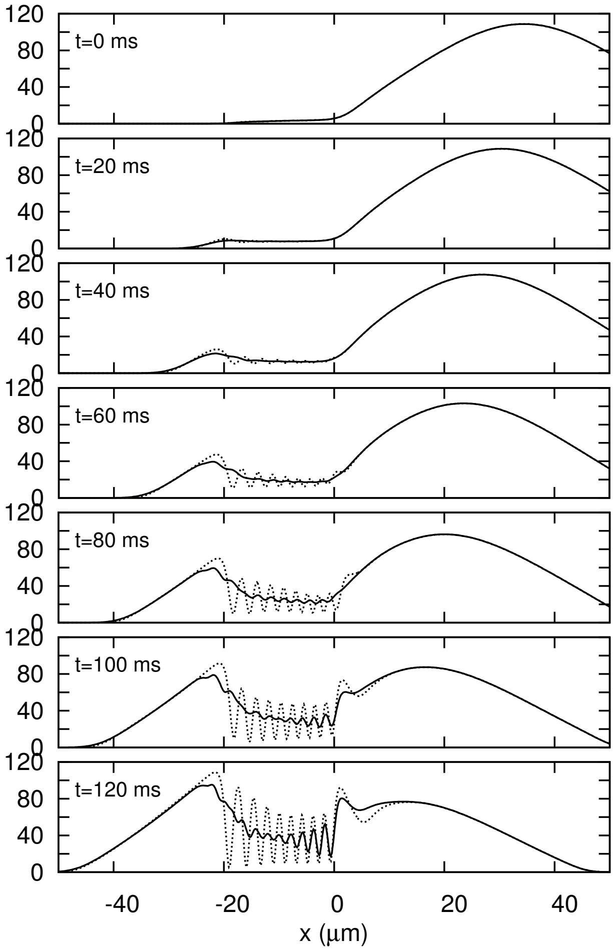

Figure 3.8: Image taken from [92]. The plots show the evolution of the density profile of the condensate for $t = 120$ ms. The snapshots shown are taken at 20 ms time intervals while the unit for the y-axis is μm^{-1}. The dotted curves show the density profile without any additional noise. The solid curves represent the average of the density profiles over 80 realizations when fluctuations in the position of the white-hole horizon are included, as done in Fig. (3.7(b)). Further discussion about these fluctuations can be found in the text.

Now, before commenting of this fact, it is important to note how the fringe pattern predicted by our simulations shows a larger contrast again. As already mentioned for the condensate velocity and the speed of sound, this is likely to be due to the experimental fluctuations in the position of the white-hole horizon. Inspired by a remark in the article [65] (which we have already mentioned) that *"the position of the inner horizon* [...] *varies slightly from realization to realization"*, we investigated the effects of shot-to-shot fluctuations in the precise position of the white-hole horizon. Even though the strength of the optical potentials is actively stabilized to an extremely high degree in the actual experiment, in the absence of more specific information on the physical source of these fluctuations which may originate from the the waterfall potential, the trapping laser, the magnetic field gradient, the total number of atoms, or even external vibrations, we choose the simplest way to introduce this effect into the model, by means a random Gaussian noise on the height of the waterfall potential, whose main consequence is indeed (see Fig. (3.4)) to displace the position of the white-hole horizon while keeping the black-hole one fixed. We then repeated our simulation for different realizations of the random fluctuations, and we take the average of the observable data. The variance of the fluctuations is chosen in a way to optimize the qualitative agreement with the experimental observations. As expected, this choice corresponds to a value of the white-hole horizon displacement of the order of the fringe spacing. The results of the average over 80 realizations of the noise (as well as over time) for the condensate and sound velocities are shown in Fig. (3.7(b)). By comparing these curves with the ones in Fig. (3.7(a)), we can easily see how the contrast of the fringe pattern inside the lasing region diminishes and both curves now closely resemble the experimental ones shown in Fig. (3.3). The density profiles after different evolution times averaged over noise are shown as solid lines in Fig. (3.8). By comparing the dotted and the solid curves, it is apparent how the displacement of the white-hole horizon greatly decreases the visibility of the fringes in the region between the two horizons: the position of the maxima and minima depends on the position of the white-hole horizon and therefore changes from realization to realization, which results in destructive interference once the averages are taken. This interpretation is further confirmed by the fact that the averaging procedure is more effective in washing out the fringes closer to the white-hole horizon, while the ones closer to the black-hole horizon are less affected. This remarkable feature is clearly visible in the simulated density profiles at late times and fully agrees with the experimental observation of Fig. (3.4)p. Finally, for the sake of completeness, we studied the effect of fluctuations in other quantities, e.g. the total number of particles, that do not directly affect the position of the white-hole horizon, and we have verified that such effects do not produce any significant change in the observables, at least for our choice of the shape of the trap (we will discuss more about this in the following).

Having discussed the experimental noise and the way we mimic it, we now want to turn back to the main point which is that our simulations show an “interference pattern” inside the lasing region which is similar to the experimental data and, much as in the experiment, these fringes grow. The key point here is that the same experimental “interference pattern” was reproduced starting from a simulation based on the mean-field Gross-Pitaevskii description of the condensate. In our theory, the phonon field, whose zero-point fluctuations would be responsible for the spontaneous Hawking radiation, is fully classical. Yet the theory recovers the same wave pattern observed in the experiment, which indicates that the phenomenon observed is indeed due to a classical hydrodynamical effect and lacks any quantum origin. In fact, as discussed in Section

2.7, the black-hole laser effect can be explained, at the classical level, in terms of an hydrodynamical instability in the GPE [157]. This fact, which is the key conclusion of our work, suggests that some other effects should be responsible for the birth of the interference pattern observed in the experimental data, as our simulation reproduces purely classical dynamics.

3.2.3 The quest for the seed and the correlation pattern

At this point, it remains to be explained what is the initial seed for the dynamical instability leading to the eventual fast growth of the fringe pattern. The simulations of Fig. (3.8) again provide a clear answer: as it is particularly evident in the third panel from the top for $t = 60$ ms, the wave pattern is seen to first appear at the white-hole horizon and then to propagate towards the black-hole horizon. This suggests that the most natural candidate for the seed is the **Bogoliubov-Cerenkov radiation (BCR)** [169], also called “undulation” in the analogue model literature [167]: this is a process responsible for the appearance of a small static density modulation whenever a condensate flowing at supersonic speed encounters a weak obstacle, in our case the growing harmonic trap potential in the region around the white-hole horizon. This initially small modulation gets then strongly amplified by possible hydrodynamical instabilities. The deterministic nature of the Bogoliubov-Cerenkov emission process reflects in the fact that the fringes also have a deterministic character, with a well-defined position and amplitude.

In fact, to further illustrate the stability of the classical dynamics against additional fluctuation effects, we have repeated our simulations adding some noise to the interacting ground state used as an initial condition of the NPSE evolution,

$$\bar{f}_0(x) = f_0(x)\,[1 + \epsilon\eta(x)], \tag{3.20}$$

where $\eta(z)$ is a random variable with a Gaussian distribution with zero mean and unit variance (independent of z) and ϵ determines the amplitude of noise; both cases of a real and a complex η have been considered but no appreciable difference was present. The results are shown in Fig. (3.9), where we compare the density profile at $t = 60$ ms with the profile at the same time once we apply a noise of intensity $\epsilon = 10^{-1}$ to the initial condition. It is easy to see in this figure that the fringe pattern inside the lasing region is not washed out by the initial random noise and keeps its qualitative structure despite of the added noise. This result is a further confirmation that the observed fringe pattern has a classical origin and that there is no need of invoking quantum phenomena to explain the experimental observations.

As a final check, in order to complete our analysis and confirm that our model is indeed able to reproduce all main features of the experiment, we are left with the study of the correlation function of density fluctuations, encoded in

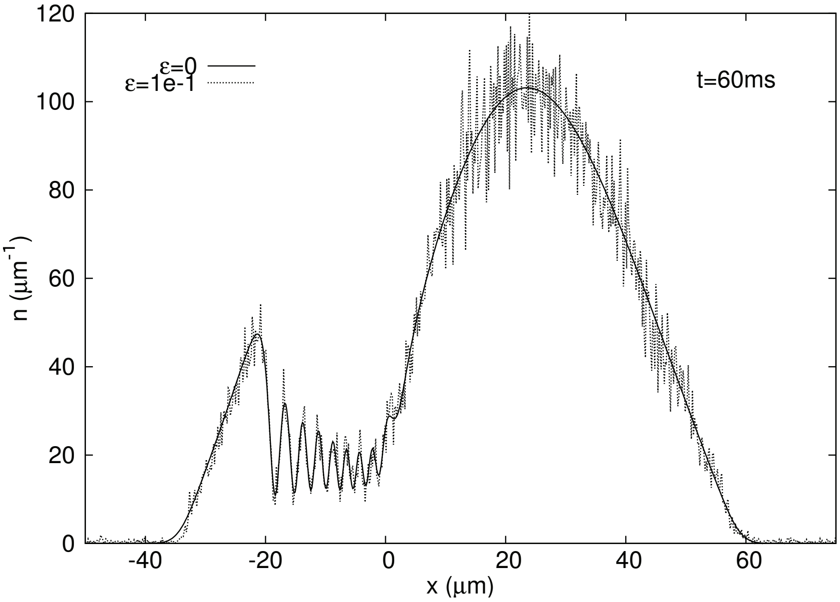

Figure 3.9: Image taken from [92]. The plot shows the density profiles at $t = 60$ ms. The solid curve is the density profile when no noise is added while the dotted one is obtained by adding a random Gaussian noise of intensity $\epsilon = 10^{-1}$ to the initial condition. As explained in the text, the persevering of the interference pattern suggests that the seed triggering it has a deterministic nature.

the two point function:

$$G^{(2)}(x_1, x_2) = \langle n(x_1)n(x_2)\rangle - \langle n(x_1)\rangle \langle n(x_2)\rangle \ . \tag{3.21}$$

As done in the experiment, we calculate Eq. (3.21) for each evolution time by taking the averages over the different realizations of the noise. The results for the latest time are shown in Fig. (3.10) for two cases: in the upper panel, we have added noise on the initial wave function according to Eq. (3.20); in the lower panel, we start from a deterministic initial wave function but we include fluctuations in the position of the white-hole horizon as previously discussed.

The upper panel is characterized by a well-defined checkerboard pattern in the region between the horizons which corresponds to the density modulation of the black-hole lasing mode shown in Fig. (3.8). Here, the role of the initial noise is fairly unimportant, as it just provides a small correction to the deterministic initial amplitude of the mode. The agreement with the experimental results of Fig. (3.5) looks even better for the lower panel where the density fluctuations are caused by the fluctuating position of the white-hole horizon; indeed, the checkerboard pattern is present also in this case, but its clear visibility is restricted to the region close to the black-hole horizon. In the vicinity of the white-hole horizon, around $x_{1,2} = -15\,\mu$m, it is instead partially washed out and is replaced by a series of fringes parallel to the diagonal. This represent another striking similarity with the experimental data

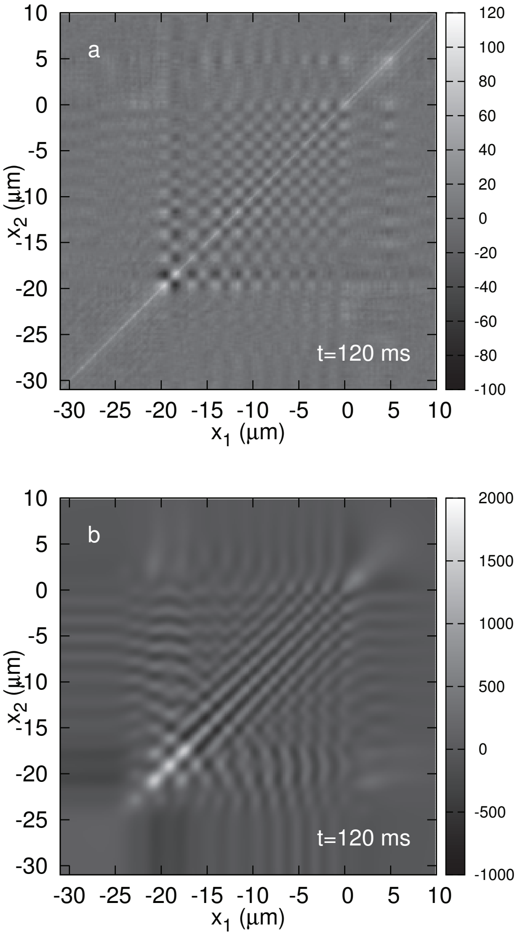

Figure 3.10: Image taken from [92]. Density-density correlation function (3.21) evaluated at the latest evolution time $t = 120$ ms. The two plots differ by the way noise is added: the upper plot includes noise in the initial wave function according to Eq. (3.20) as done in Fig. (3.9). In the lower panel, instead, fluctuations originate from a fluctuating position of the white-hole horizon as done in Fig. (3.8) and explained in the text.

Finally, in order to check that the main characteristics of the dynamics are uninfluenced by fine details, as the shape of the longitudinal trap, we repeated the above tests with an axial potential of the form

$$V(x) = \alpha(x - x_0 + vt)^6 + \frac{V_s}{2}[1 + \tanh\left(\frac{x}{\sigma}\right)]\,. \tag{3.22}$$

We find that the “interference pattern” is still present and it grows in time; it is not washed out by an initial random noise and the checkerboard form of the two-point correlation function is recovered also.

3.2.4 The conclusions (maybe)

Through a series of numerical simulations we have theoretically characterized the 2014 Technion experiment [65] reporting the observation of self-amplifying Hawking radiation. Our work was based on a numerical solution of the Gross-Pitaevskii equation describing the dynamics of the condensate at mean-field level; furthermore, we based our model on the experimental parameters in order to recreate a scenario as similar as possible to the actual experiment. As a main result of our study, we showed how such a classical approach is able to reproduce in a quantitative way the experimental observations without the need of invoking quantum fluctuation effects but only by means of hydrodynamical considerations. In particular, the amplification mechanism behind the phenomena observed in [65] can be explained in terms of a hydrodynamical instability. We also showed that the mechanism seeding it has a deterministic nature, which leads to a well-defined amplitude and phase of the fringe pattern in the density profile, and it can be related to a classical Bogoliubov-Cerenkov emission in the white-hole horizon region. The fine details of the observed density profiles and of the density fluctuation correlation function were also explained in terms of classical shot-to-shot fluctuations in the position of the inner white-hole horizon.

Now, when these results were published, a lot of time had already passed after the publication of the experimental results [65] and we had already discussed our work with a few experts in the field. In particular, around the time of publication, T. Jacobson, of University of Maryland, notified us that he had also been working with his group on simulations on the experiment and that he had reached conclusions in partial agreement with ours. Thus, it appeared that the experiment had two independent verification which led to the same interpretation of the experimental data and, thus, the matter was closed...

.. or maybe not.

3.3 Controversy on the interpretation of the results

Almost a year after the publication of our work, three related studies came out [93,94,162]. All of them describe numerical simulations apt to characterize the 2014 Technion experiment. Two of them [93,94] are back-to-back work from the same group (namely, T. Jacobson group in the U.S.A.), while the latter [162] contains simulations developed by the group of J. Steinhauer, the author of the experiment [65]. In this Section, we will describe these three works, highlighting the main points of controversy as they led to further simulations on our side also. Then, in the second part of the Section, we will discuss our further results which were triggered by these studies.

3.3.1 Further works from other groups

We will now describe the main results and the key points of the three works cited above but without entering in too much details as the purpose is to understand what led to our further works; the reader interested in more details can find them in the original articles.

In the first article by the American group [93], the simulations developed were very similar to ours and led to similar outcomes. Therefore, the interpretation the group gave to the experimental results was very similar to ours, but with some, not-irrelevant, differences. The main point of the work is that a classical simulation starting from a 1D GPE effectively reproduces all of the experimental results, which leads to the conclusion that the results are of hydrodynamic nature solely. Furthermore, the phenomena observed are described in terms of Bogoliubov-Cerenkov radiation only, without the need of invoking any other effect. The article, in fact, claims that both the wave pattern present inside the supersonic region and its growth in time are due to BCR originating from the region near the white-hole horizon. That is, the presence of an obstacle represented by atoms accumulating around the turning-point region leads to Bogoliubov-Cerenkov emission in the supersonic cavity. Furthermore, since the number of atoms accumulated grows in time, the BCR amplitude grows in time also. These effects are demonstrated by a detailed analysis which, at times, retraces ours[5].

In brief, the simulations developed in [93] are based on numerical integration of a 1D GPE with harmonic confinement in the transverse directions and parameters similar to the experimental ones. A deep study of the evolution of the

---

[5] Nevertheless, note that these two studies were developed independently and, in particular, the American group stressed the importance of not sharing any informations with them.

density profiles shows that the wave pattern present in the lasing cavity originates from the WH horizon region and then it extends towards the BH horizon, which leads to think that, given that the simulations are purely classical, the effect might be due to Bogoliubov-Cerenkov emission, which appears when a supersonic flow hits an obstacle. Furthermore, the wave pattern does appear to have zero frequency in the WH frame, as one would expect from BCR. This is a non-trivial point since the mode is seen to have a finite frequency in the laboratory frame. A deeper analysis, though, shows that the white-hole horizon moves slightly during the evolution, with a velocity which is different from the black-hole horizon velocity (this is related to the hydrodynamics of the system). Thus, in order to measure the real frequency of the wave emitted from the WH, we need to move to a frame co-moving with the horizon. This is shown in Figure (3.11): the BCR standing wave has zero frequency in the WH frame (red dashed line), but since the WH is receding from the BH by a velocity difference, the BCR in the BH frame has a non-zero frequency, as can be seen by the phase change of the standing wave along the solid red line.

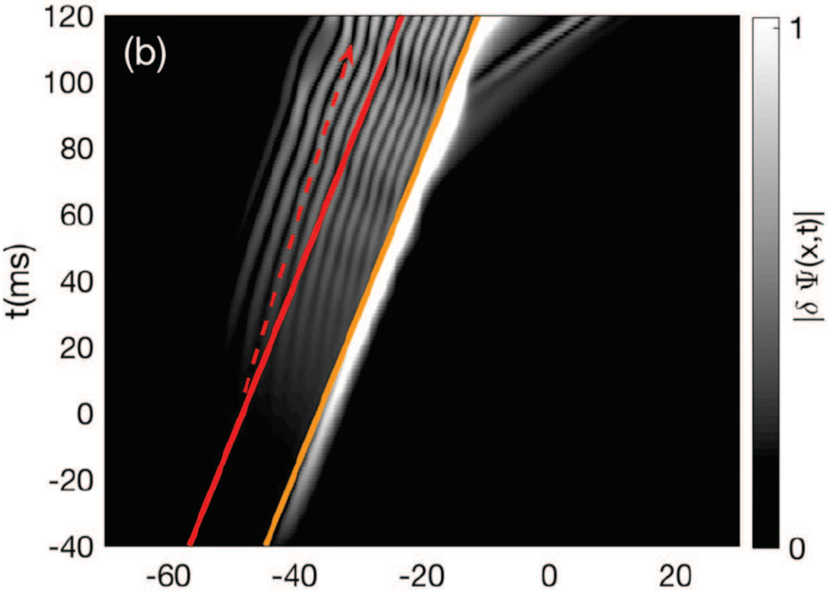

Figure 3.11: Image taken from [93]. Density time evolution. The dashed red line is parallel to the WH world line while the solid red line is parallel to the BH world line, indicated by the diagonal orange line. The figure shows that the WH horizon has a smaller velocity than the BH horizon and the BCR is therefore Doppler shifted to a non-zero frequency in the laboratory frame. In fact, the solid red line crosses few fringes during the evolution. On the other hand, the dashed red line is exactly parallel to the fringes world lines, showing that, in the WH frame, the wave pattern has zero frequency, as expected by BCR.

Thus, the wave pattern seen in the supersonic region is demonstrated to be caused by BCR from the WH horizon region. Furthermore, if we notice that the obstacle which triggers this effect are the atoms themselves, which accumulate around the turning point, we could apply the following, simple reasoning: the amplitude of a BCR standing wave is proportional to both the strength of the obstacle and to the density of the flow [169]. We know the density of the background flow $n_{bf}(t)$ (in [93] this was obtained by Fourier Transform of the density profile inside the supersonic region) and, given than the obstacle here is represented by atoms accumulating in the left region of the supersonic cavity, we can infer that the obstacle itself has a strength proportional to the background flow also. That means that, if we call $n_{nk}(t)$ the amplitude of the BCR emission, we should have

$$n_{nk}(t) \propto n_{bf}^2(t)\,. \tag{3.23}$$

Figure (3.12) shows this relationship as estimated in [93]. We can see that the similar behaviour confirms that the amplification mechanism is still related to the BCR.

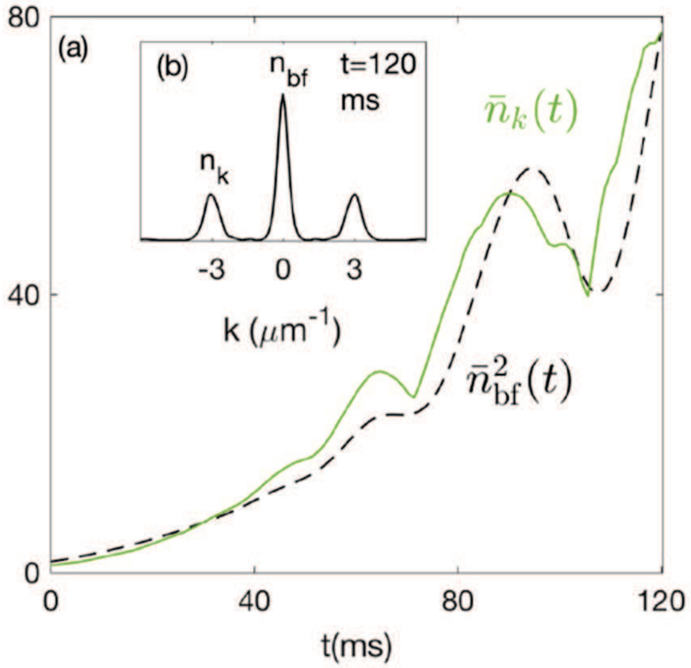

Figure 3.12: Image taken from [93]. The solid green curve is the normalized standing wave amplitude $n_{nk}(t)$ inside the supersonic region. The dashed black curve shows the square of the background density, scaled to match the final standing-wave amplitude. The growth of the two is determined by Fourier Transform inside the supersonic region, as shown in the inset.

The article also adds a discussion on stimulated Hawking emission from the BH horizon and describes a so-called "enhanced parameter regime", a different set of simulations where the set of parameters were chosen differently from the experimental ones so to highlight some features of the phenomena observed. These two parts are not fundamental for our work and thus we will not discuss them.

In the second of their works [94], the American group used the same simulations to study the two-points density correlation function. They also developed their model by introducing the **truncated Wigner approximation (TWA)**: this technique allows to introduce quantum fluctuations in the numerical model by adding to the Gross-Pitaevskii wave function an initial distribution of random fluctuations with the Gaussian statistics of the zero-point fluctuations and then averaging over an ensemble of realizations [170–174]. Thus, they studied the role of the background flow together with the role of quantum fluctuations.

The conclusions of [94] are, again, very similar to ours. They find that quantum fluctuations do not play a relevant role in the picture as shot-to-shot variations of atom number can alone produce all the observed features of the correlation function. In fact, it is demonstrated that a varying number of atoms (something normally present in ultra-cold atom experiments) has the effect of moving the fringes of the wave pattern next to the WH hole horizon, while it does not produce an appreciable effect near the BH horizon. Then, when averages over different experimental runs are taken, the fringes near the WH are partially washed out, which leads to a particular form or the correlation function, as we have discussed in the previous Section. This fact is shown in Figure (3.13).

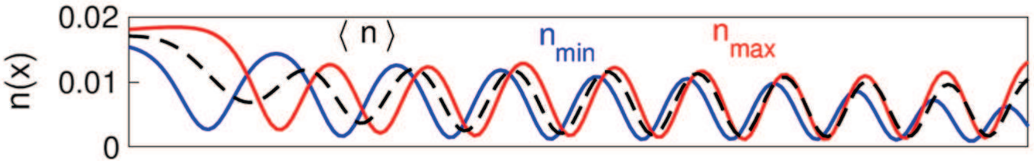

Figure 3.13: Image taken from [94]. Effects of atom-number variation on the standing wave. The dashed black line shows the average density over atom-number fluctuation of $\Delta N/\bar{N} = 0.05$. The solid red line shows the density for a realization with atom number $N = \bar{N} + 0.075\bar{N}$. The solid blue line shows the density for a realization with atom number $N = \bar{N} - 0.075\bar{N}$. In all the simulations $\bar{N} = 6000$ and the variations are introduced by means of a normal distribution with mean $\bar{N}$ and standard deviation ΔN. It is evident from the plot how a varying number of particles greatly affects the fringes near the WH horizon (left region of the plot), while the ones near the BH horizon experience very little change (right region of the plot).

We will not report here all the figures of [94] but we will limit ourselves to say that they show that atom number fluctuations alone are able to reproduce the experimental results both from a qualitatively and a quantitatively point of view. On the other hand, quantum fluctuations are demonstrated to play only a minor role in this description. Thus, once again, this work stresses the point that all the experimental observations are related to the hydrodynamics of the background flow more than to quantum effects.

Note that, since [94] came out after our work, the authors also discussed the fact that in our simulations varying the number of particles did not have any effect. It is pointed out in [94], in fact, that certain features of the condensate evolution are very sensitive to the parameters of the axial potential. Indeed, they illustrate how a change of the 3% in the trap curvature can switch from a regime where fluctuations in the particle number are irrelevant to a regime where they become important. Thus, being our two traps slightly different, this discrepancy is explained.

Finally, the work of J. Steinhauer group [162] arrived at conclusions different from all the other works. In this work, in fact, the phenomena seen in [65] are explained in terms of quantum effects. The numerical model is not discussed as they only mention that "*we numerically study the self-amplifying Hawking radiation via the one-dimensional Gross-Pitaevskii equation. The parameters are similar to those of* [citation of the experimental work]. *Fluctuations are added to the system soon after the formation of the outer black-hole horizon.*" The main point is that the so-called "background ripple" (which our group and T. Jacobson group identified with BCR) is shown to be a separate phenomenon from the self-amplifying Hawking radiation taking place during the experiment.

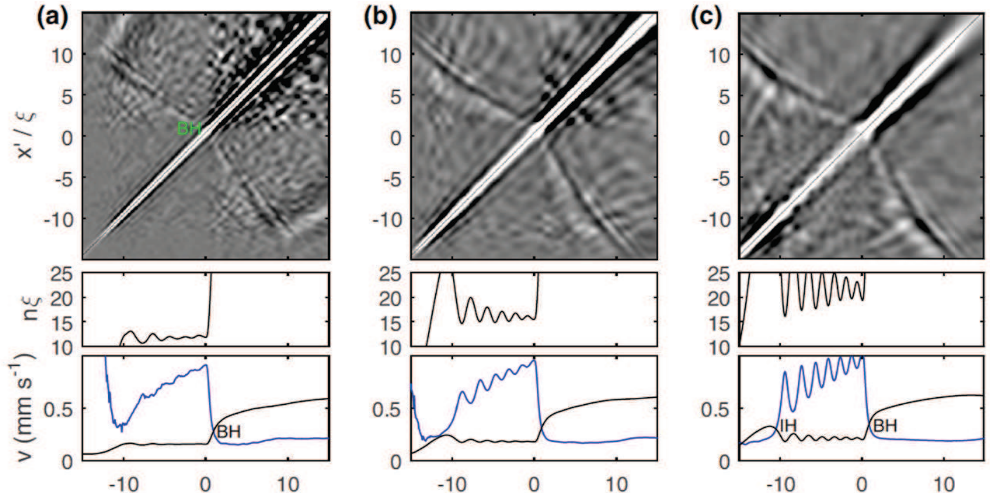

Figure 3.14: Image taken from [162]. The upper panels show the time evolution of the two-point density correlation function while the lower panels show, respectively, the time evolution of the density and the time evolution of the condensate velocity, together with the speed of sound. Only half of the evolution is shown. Nevertheless, two key points are already visible: first, the correlation pattern signature typical of spontaneous Hawking emission (the diagonal stripes described in [149]); second, the fact that the ripple appears before the formation of the WH horizon.

In fact, as shown in Figure (3.14), the ripple is seen to appear before the formation of the WH horizon and, furthermore, the distinctive signature of spontaneous Hawking emission is seen to appear in the correlation function right after the formation of the black-hole horizon (the two diagonal lines, as discussed in Section 2.7). Furthermore, an analysis developed by means of Fourier Transform, shows that the wave pattern has a non-zero frequency independently of the reference frame, that the growth rate increases for decreasing laser cavity length and that it varies widely as a function of the slope of the black-hole horizon, all features that can be associated to self-amplifying Hawking radiation.

In conclusion, two years after the experiment which claimed the observation of self-amplifying Hawking radiation and the black-hole laser effect [65], three different groups had theoretically studied the experiment, reaching different sets of conclusions.

3.3.2 The path toward a unique picture

Given that there were three different interpretations for the same experimental results, we started working on further simulations in order to understand where the differences were lying.

Let us start from the claims made in [162] as they are the easiest to deal with. First of all, since no details of the numerical method is given in the article, it is hard to understand if any difference in the model could have led to different results. Moreover, the technique implied to include quantum effects in the picture is not mentioned and that makes it even harder to interpret the discrepancies with other studies since this procedure (i.e. how to include zero-point fluctuations) is a very delicate matter (we will talk more about it at the end of this Thesis). Nevertheless, at the time we did not have a fully quantum simulation, so we cannot speak about that side of the problem (namely, we cannot comment on the signature of the spontaneous Hawking radiation appearing in the correlation function in [162]). We will thus limit our comments to a few points.

First of all, the claim that the white-hole horizon is born after the formation of the ripple does not rule out the possibility of BCR. This effect, indeed, only requires a supersonic flow (that is guaranteed from $t = 0^+$ by the presence of the black-hole horizon) and an obstacle, which can be represented by the confining trap (in our picture) or by the accumulating number of bosons (in T. Jacobson's picture). None of the two, though, requires a white-hole horizon. Furthermore, it is also true in the case of BCR that the growth rate increases for decreasing laser cavity length and that it varies widely as a function of the slope of the black-hole horizon, and thus these features can be associated either to self-amplifying Hawking radiation or to BCR. Finally, the fact that the mode seen has a zero frequency in the WH frame while a non-zero one in the laboratory frame appeared also in our simulations.

Moving to the other works, testing the discrepancies between our interpretation and the one of [93,94] was not as easy as imagined. Given that the main results of the works were in agreement (that is, that the effects seen in the laboratory were due to hydrodynamical features more than to quantum effects and that

BCR was responsible for the wave pattern), proving that the fine details were also consistent required some work. In particular, we were able to check all the differences easily, except for the nature of the growth. In fact, we verified that the WH moves during the evolution by a small quantity and our results are in agreement with the ones of [93, 94] (see Fig. (3.15)).

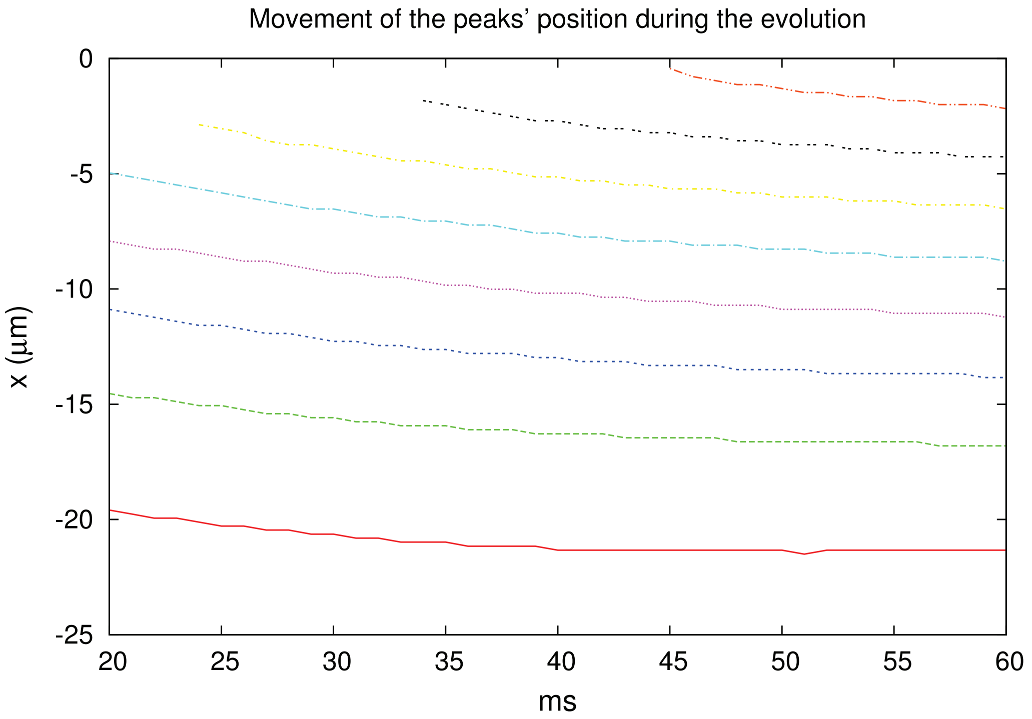

Figure 3.15: Movement of the peaks during the evolution interval. It is evident how all the peaks move to the same direction with a typical speed which agrees with the velocity measured for the WH displacement.

Secondly, we tested the claim that the tuning of the parameters of the axial potential implies a difference in the dynamics of fluctuations. That is, we repeated our simulations with the longitudinal trap used in [93, 94] and we checked that varying the number of atoms implies that the fringes around the WH horizon destructively interference when the different runs are averaged. This was found to be true. Figure (3.16) shows the differences between our trap and the trap used in [93, 94]. Note how the curvature is slightly different: this is because while we chose a form so to perfectly fit the trap plotted in Fig. (3.2), the trap used in [93, 94] was chosen with a Gaussian profile with the parameters equal to the experimental beam, following the description of [65]. This diversity in the approach resulted in two different profiles and the changes in the dynamics are not irrelevant: if simulations are run with our trap then a fluctuating number of atoms does not seem to affect the dynamics al all. The opposite cannot be said for a trap of the form of [93, 94].

Having reconciled almost all the discrepancies between [92] and [93,94], there is

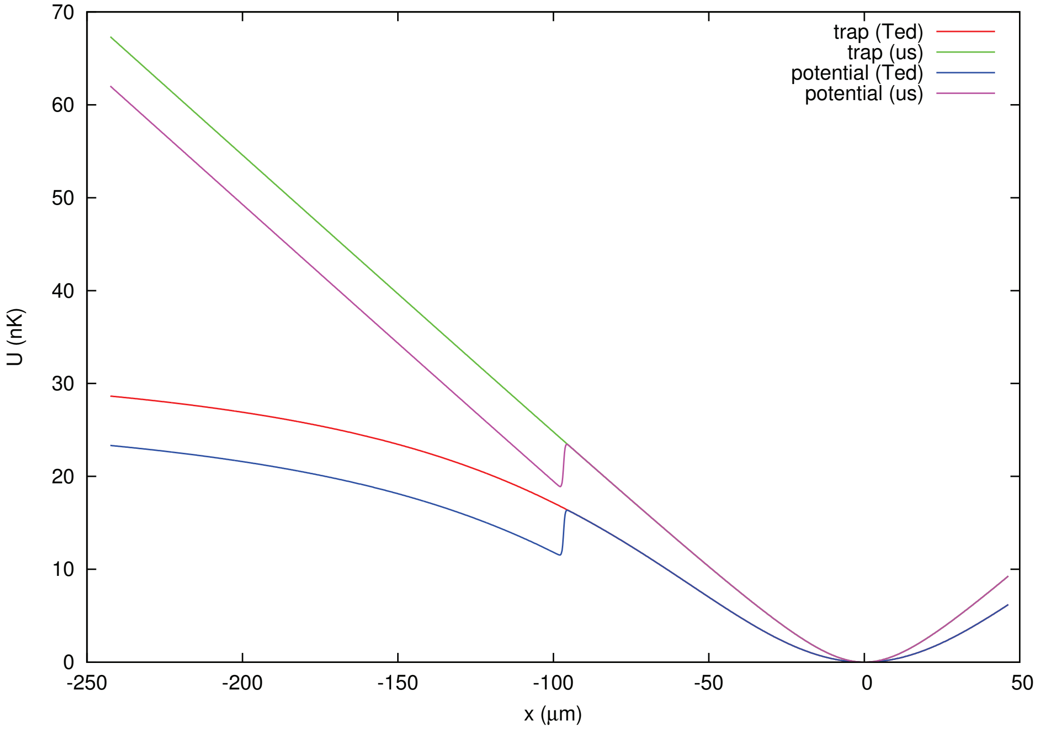

Figure 3.16: The two sets of axial traps and potentials. The green line represents the trap used in [92], with the violet curve being the potential after the addition of the waterfall. The red line represents the trap used in [93,94], with the blue curve being the potential after the addition of the waterfall. Note how the trap used in [93, 94] was slightly more shallow than the one used in [92]. This, as explained in the text, has caused some discrepancies in the results. It is important to notice that this snapshot is taken at very early times, when the waterfall is still far from the condensate. To have a qualitative understanding of the differences between the traps remember that the cloud is centred in the trap minimum and its length is approximately 100 μm.

one last matter to treat, namely the cause of the growth of the wave pattern. In fact, while both studies agree that the seed of this emission is BCR, the two have different interpretations for the growth of the fringes: in [92] the cause is claimed to be an hydrodynamical instability (and thus, one expects an exponential growth) while in [93, 94] the growth is believed to be caused by the same BCR, and thus a polynomial growth is expected. Even though the analysis and the results in [93, 94] appear to be completely legitimate, the growth of the peaks in our simulations seems to be in contrast with that interpretation, as shown in Fig. (3.17). From the figure, in fact, we can see that, if we plot the growth of the fringes peaks on a log-scale, the behaviour seems to be linear, reinforcing the idea of an exponential growth.

Furthermore, from a detailed analysis of the density profiles evolution (where we have studied the density profile with steps of 1 ms) it is clear how, after 60 ms, another mode appears, which is responsible for the oscillations in the

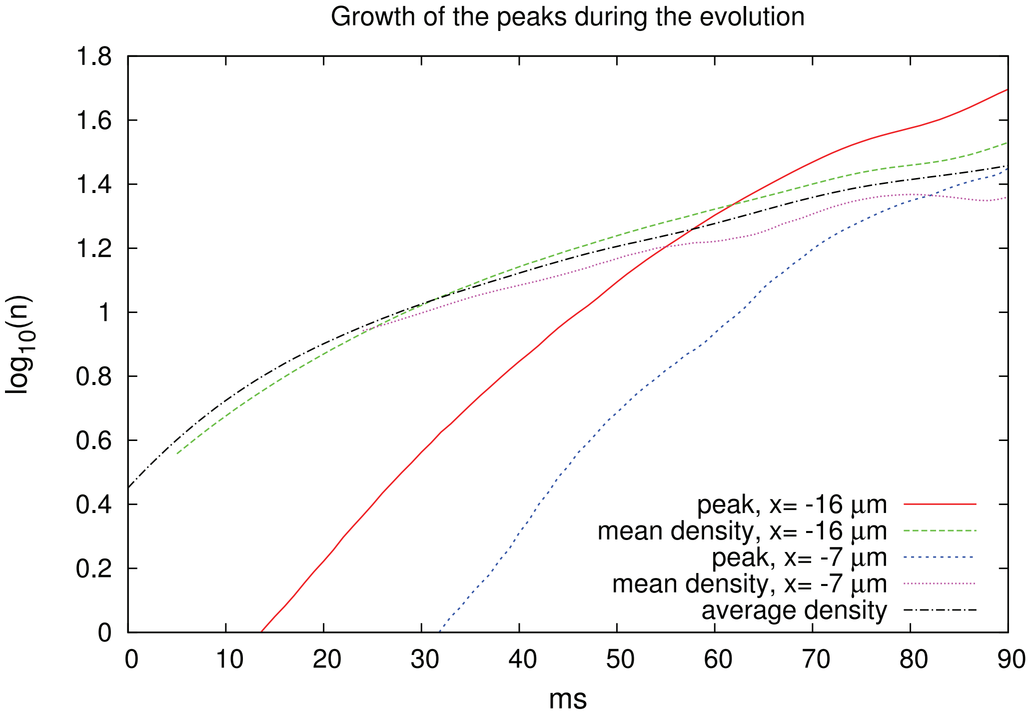

Figure 3.17: Growth of the fringes compared to that of the density. The height of the *peaks* is calculated as $\frac{1}{2}(y_{max} - y_{min})$ while for the *mean density* we take $\frac{1}{2}(y_{max} + y_{min})$. The *average density*, instead, is calculated by taking the mean value of the density in the lasing region. The y-axis is logarithmic, base 10. We want to point our that before $t = 15$ ms the supersonic region is not well-defined yet (this can be seen in the velocity profiles evolution, which have been not reported here).

height of the peaks (this can also be seen from the lower panels of Fig. (3.8)). Thus, any conclusion about the peaks growth has to be extracted from the interval $t =$[10, 60] ms. In this interval, the growth of the peaks in Fig. (3.17) seems to follow a linear trend, while it becomes more flat at later times.

Now, before describing the conclusions we reached on this matter, it is important to note one thing, which plays a fundamental role in this treatment. **The evolution we are studying is a transient**. That is, the evolution of the system never reaches a stationary configuration. This point, which may seem harmless, affects all the conclusions we try to take. As a matter of fact, it would be much easier to discriminate between effects if a stationary configuration was reached, but this does not happen in the real experiment. Furthermore, the evolution time is fairly short due to the size of the system and thus any interpretation of the results is not trivial. Nevertheless, we could think about slowing down the process, so to have a longer time window to observe the growth and discriminate between the two possible processes. Unfortunately, by slowing down the cloud, we also narrow the supersonic region, thus decreasing the effect. Therefore, even if simulations give us the opportunity of repeating the experiment several times with different parameters, this problem seems to require more than just a few trials[6].

In order to test the claim made in [93, 94] we should also plot the quantities evaluated in that work, namely, the height of the peaks with respect of the square of the background density. There are several ways to study these quantities and we plot all of them in Fig. (3.18). The idea is to compare the growth of the wave pattern inside the lasing region to the product of the mean density inside the supersonic region (the background flow which hits the obstacle) and the amplitude of the obstacle (the density around the turning point). Now, if we look at Figs. (3.8, 3.7(b)) we see that just outside the WH horizon, to the left, there is a density peak, which corresponds to the atoms accumulating in the proximity of the turning point. We will call the density of that peak n_P (it is the first peak from the left). To the right of this peak, the supersonic region begins and we will name n_1 the first peak/maximum from the left, n_2 the first valley/minimum from the left (the one between n_P and n_1) and n_3 the second valley/minimum from the left (the one to the right of n_1). Then we see that the strength of the obstacle is just n_P, the actual height of the first peak inside the supersonic region is $n_1 - \frac{1}{2}(n_2 + n_3)$ and the background density can be taken as $n_M = \frac{1}{2}(n_1 + n_2)$ approximately. Thus, if the scenario depicted in [93, 94] is correct, we should obtain

$$\frac{n_1 - \frac{1}{2}(n_2 + n_3)}{n_P\, n_M} \simeq \text{constant}\,. \tag{3.24}$$

This is shown in Fig. (3.18), where other ratios are evaluated also. The plot shows that Eq. (3.24) is correct, as the curve is very flat. The other ways to calculate the same quantity are still legitimate but they do not represent the best approximation.

This outcome provided the final link between the conclusions of [92] and those of [93, 94]. With these further results, in fact, the picture was one and only. Indeed, the experimental results of [65] can be explained in terms of classical hydrodynamical effects in the background flow and thus no quantum effect seems to play an important role in the dynamics. Moreover, the wave pattern inside the supersonic cavity is consisted with the picture of a Bogoliubov-Cerenkov emission from the white-hole horizon region. The growth of the peaks is probably due to the accumulation of atoms around the turning point, even though the short time of evolution makes it hard to discriminate between this phenomena and an hydrodynamical instability. Finally, the particular pattern

---

[6] At this point one could object that we could also change the form of the trap, so to make it more shallow, thus slowing down the dynamics. This has been tried also but it is not an effective way to treat the problem: as we have seen for the case of a fluctuating number of atoms, it seems that the system is fairly sensible to the tuning of the longitudinal potential parameters. Thus, by changing the trap, we could obtain a much more favourable context but then we would not know if the picture obtained resembled the actual experiment.

seen in the two-point correlation function can be explained in terms of BCR together with the presence of realistic experimental noise.

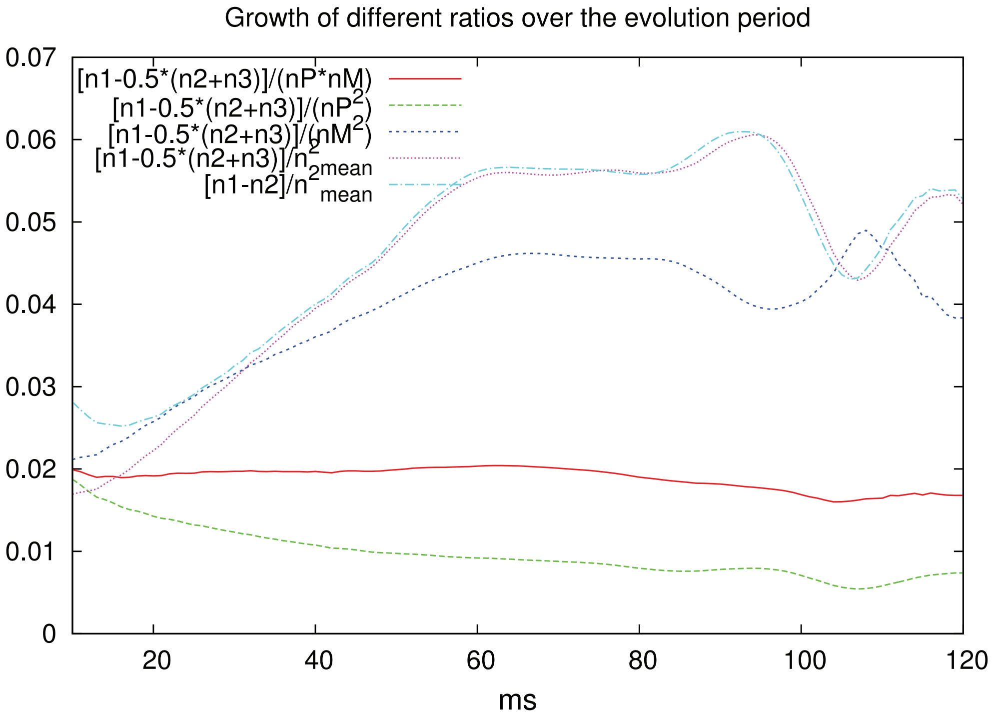

Figure 3.18: Different ratios evaluated in order to study the claim of [93, 94] about the polynomial growth of the fringes. The different quantities are described in the text, except for n_{mean}: this is the mean density calculated on the entire supersonic region. It can be easily seen how the best description of the effect (the quantity described in Eq. (3.24), the solid red curve here) is constant, as expected.

Thus, once again, it seemed that a consistent picture about the interpretation of the experimental results was achieved. But, again, this is not the end of the story...

3.4 Our latest numerical results

After the aforementioned results of our simulations, long discussions with I. Carusotto of the CNR-INO BEC Center of Trento and R. Parentani of the University of Orsay, Paris-Sud, led to the conviction that the next step in our study should have been the characterization of these phenomena (namely, the Bogoliubov-Cerenkov wave and its growth) when the axial confinement varied. This thought came from the observation that even a slightly different axial confinement could lead to measurable differences in the dynamics if some experimental noise (i.e. a fluctuating number of bosons) was introduced. Thus, it was deemed important to characterize the effects produced by variations in the axial trap, so to have a better understanding on the phenomena present and to give insights for the realization of future experiments.

In order to have a configuration as realistic as possible, we started by changing two things in our numerical model. First of all, we decided to use an axial trap obtained from the consideration that the constricting laser beam has a Gaussian shape, as it was done in [93, 94]. That is, keeping the transverse confinement harmonic, we changed the longitudinal potential to the form

$$U(x) = U_0 \, \frac{x^2}{x^2 + x_0^2} \, , \tag{3.25}$$

where the parameters are given by the experimental ones. In fact, if we consider a 3D Gaussian laser beam, we have that the potential is

$$U(r,x) = U_0 \left(1 - \left[\frac{w_0}{w(x)} \right]^2 e^{-\frac{2r^2}{w(x)^2}} \right) \quad , \tag{3.26}$$

where x is our direction of motion, $r = (y,z)$ is the radial distance from the center of the beam (y and z being the transverse directions), $w(0) = w_0$ the so-called *waist* of the beam and

$$w(x) = w_0 \sqrt{1 + \left(\frac{x}{x_0} \right)^2} \quad , \tag{3.27}$$

where x_0 depends on the beam waist and wavelength, i.e. $x_0 = \frac{\pi w_0}{\lambda}$. Thus, if we evaluate the potential on the axis $y = 0$, $z = 0$ we obtain exactly Eq. (3.25). This way the axial trap better represents the real case of a Gaussian laser beam.

The second change we made to our model was on the transverse confinement. A harmonic trap, in fact, is a good approximation but we can improve it by allowing $\omega_\perp$ to vary on the axial direction. Indeed, the transverse confinement, being created by means of a Gaussian beam, does not have a perfectly cylindrical symmetry. In fact, if we expand at the first-order the trap (3.26) around zero we have

$$U(r,x) \simeq U_0 \left[\frac{w_0}{w(x)}\right]^2 \left(1 - \frac{2r^2}{w(x)^2}\right) = -\frac{U_0 w_0^2}{w(x)^2} + \frac{2U_0 w_0^2}{w(x)^4}\, r^2 \,, \qquad (3.28)$$

which shows that

$$\frac{1}{2} m\omega_\perp^2 = \frac{2U_0 w_0^2}{w(x)^4} \qquad (3.29)$$

and, therefore, $\omega_\perp = \omega_\perp(x)$, as we expected. If we now rewrite Eq. (3.5)

$$\begin{aligned} i\hbar\frac{\partial f}{\partial t} = &\left(-\frac{\hbar^2}{2m}\frac{\partial^2}{\partial x^2} + U + \frac{gN}{2\pi a_\perp^2}\frac{|f|^2}{\sqrt{1+2a_sN|f|^2}}\right) f + \\ &+\frac{\hbar\omega_\perp}{2}\left(\frac{1}{\sqrt{1+2a_sN|f|^2}} + \sqrt{1+2a_sN|f|^2}\right) f \,, \end{aligned} \qquad (3.30)$$

we see that this modification affects two terms (remember that $a_\perp = \sqrt{\hbar/(m\omega_\perp)}$). This is a rather important change as we can quickly verify: if we take the $\omega_\perp$ used in [93, 94] (there a fixed $\omega_\perp$ was used) and we calculate the zero-point energy $\hbar\omega_\perp/k_B$ we obtain a value of approximately 6 nK, which, compared to the asymptotical value $U_0 = 33$ nK, gives almost a 20% correction.

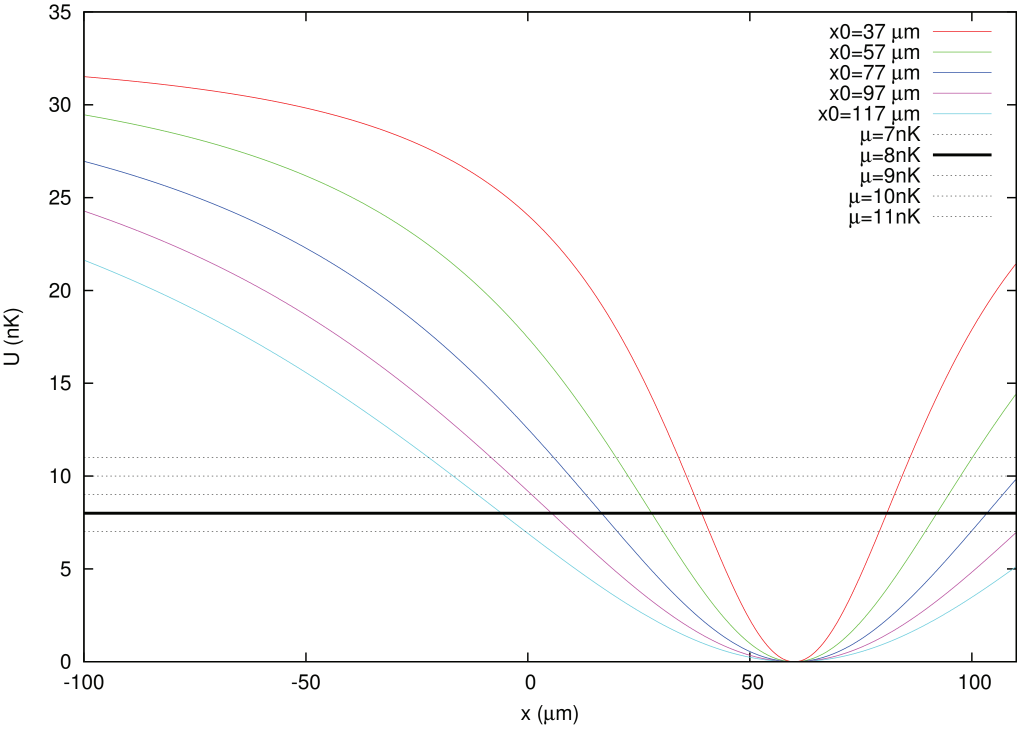

Figure 3.19: Different choices for x_0 and μ for our simulations. Note that, if we use the experimental parameter listed in [65], we have that $x_0 = 97\mu$m and $\mu = 8$ nK.

Thus, we apply these two corrections to our numerical model and then we study the variations in the dynamics when we allow x_0 and the chemical potential μ

to vary. The former determines how shallow/steep the longitudinal confinement is while the latter determines the number of atoms in the trap. Figure (3.19) shows the different values we chose for these two parameters.

The results of this analysis are reported in Appendix A. We do not want to focus on them here as they do not add much to our interpretation of the experimental outcomes and, thus, they are not as important as the following discussion.

3.4.1 The roles of interactions

Let us focus now on two facts that we have formerly mentioned which turn out to be of greater importance than we have previously thought. First of all, being the system far from stationarity, we find that the usual concepts of lasing instability and Bogoliubov-Cerenkov radiation are not immediately applicable. Second, from both the simulations and the experimental data, it is evident that the density is very low in the supersonic region (see Figs. (3.4) and (3.8)). These two facts combined led us to wonder if the role of interactions, which define effects like the black-hole laser and BCR since they depend on the speed of sound, have a major role in these configurations or they can be neglected. This reasoning, as we will see, has led to a completely different interpretation of the experimental results.

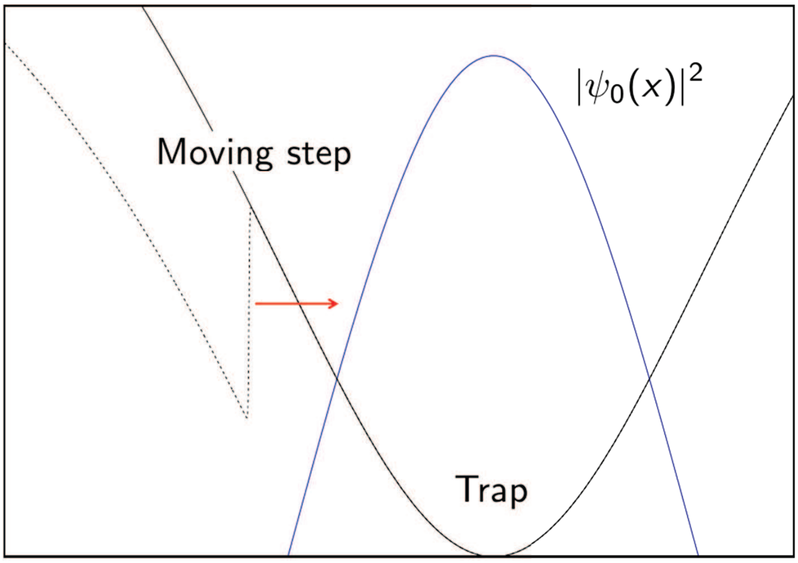

Figure 3.20: Drawing representing the structure of our current model: we start from the ground state of the BEC in the trap and we let the system evolve by sweeping a waterfall potential trough the cloud at a constant velocity.

Let us start from the way we have solved the problem so far and let us apply a Galilean transformation to the system, so to have a configuration like the experimental one, i.e. with a still trap and a moving waterfall potential. This configuration is depicted in Figure (3.20). The system undergoes the same dynamics we have already described: the atoms flow over the waterfall potential, they gain velocity and they progressively slow down as the curvature of the trap increases. By continuity (Eq. (3.1)) we see that an increment in the velocity implies a drop in the density and, thus, we have very few atoms moving very fast. Now, we could then ask ourselves: what happens if we neglect interactions then? It is obvious from Eq. (2.49) that interactions scale as the density and, therefore, one should expect that their role reduces as the density decreases. In order to study this, we run our simulation using a trick: we tune the interactions so that they are present in the initial cloud of unperturbed atoms (that is, to the right of the black-hole horizon) and we set them null in the portion of condensate which experiences an acceleration (that is, to the left of the black-hole horizon). This trick is represented in Fig. (3.21).

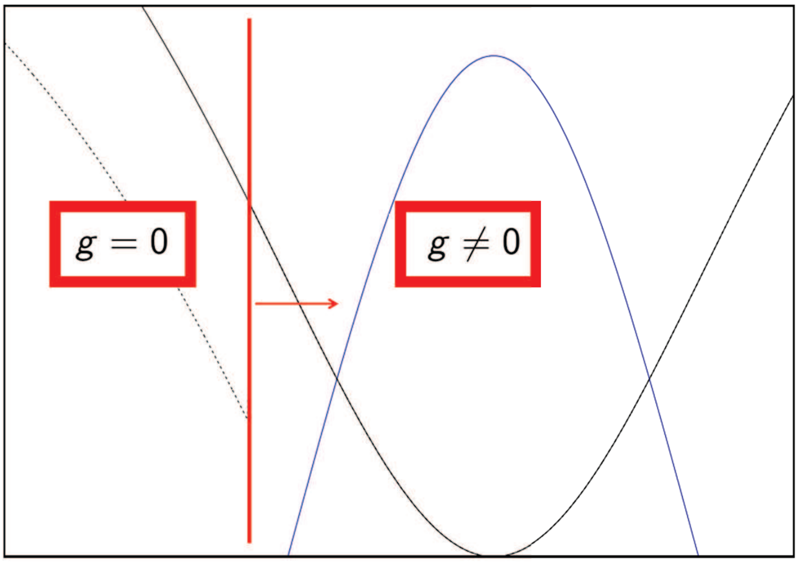

Figure 3.21: Our new set-up, developed in order to study the role of interactions. The waterfall potential (i.e. the balck-hole horizon) flows to the right with a constant speed. To the right of it interactions are present while to the left they are vanishing.

Thus, we start from the ground state of the interacting condensate and, when the atoms encounter the potential drop, interactions are switched off. If we recall the form of the Gross-Pitaevskii equation (2.49) in 1D

$$i\hbar \frac{\partial}{\partial t} \phi(x,t) = \left[-\frac{\hbar^2}{2m} \frac{\partial^2}{\partial x^2} + V_{\text{ext}}(x,t) + g \left| \phi(x,t) \right|^2 \right] \phi(x,t) \qquad (3.31)$$

we see that setting $g = 0$ has the effect of transforming this equation in the well-known Schrödinger equation. Thus to the left of the waterfall we are effectively integrating Schrödinger equation while to the right the full GPE.

3.4.2 New interpretation of the experimental data

The result of this machinery is plotted in Fig. (3.22) where the evolution of the density profile is shown in three different cases. In particular, we plot the results in the BH frame so that the horizon is still and the figures are easier to understand. To the right of the potential step we have GPE in all three cases, while the interaction parameter g is adjusted to the left, in order to show the transition from one case to the other.

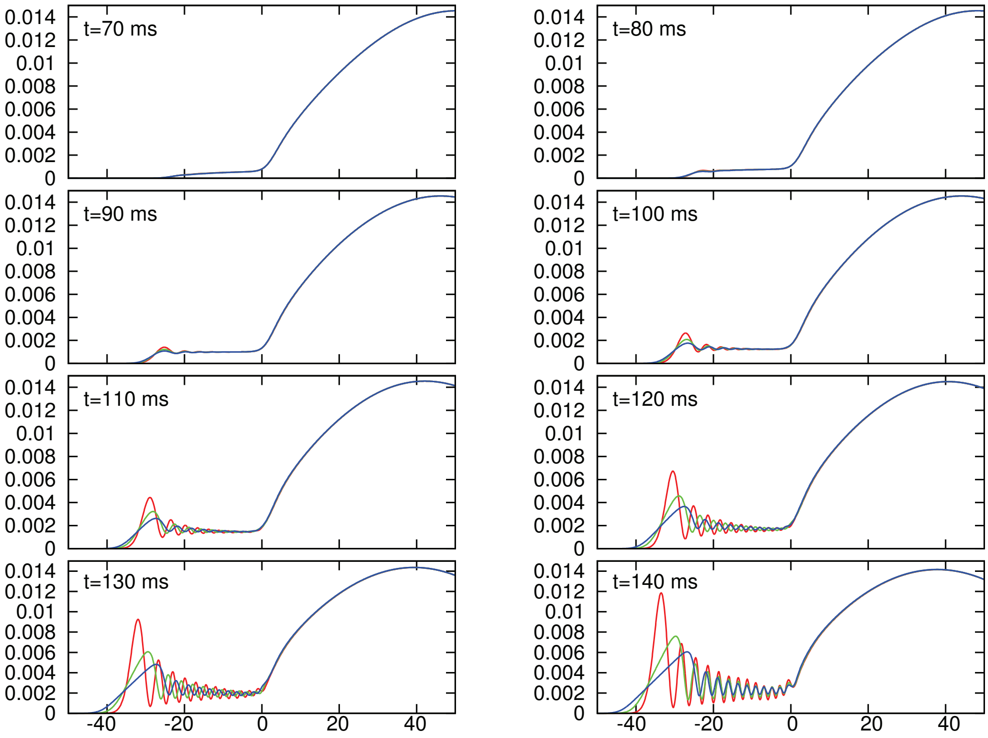

Figure 3.22: The canvas show snapshots of the condensate at subsequent times. The results are given in the step reference frame so that the waterfall is fixed in the origin and the cloud moves to the left. The x-axis unit is micron while the y-axis is $\mu\mathrm{m}^{-1}$. The three curves represent different interaction parameters **to the left** of the potential drop (to the right is GPE in all three cases): the red curve shows the case of null interactions, i.e. the Schrödinger case; the blue curve shows the case of fully-interacting atoms, i.e. the GPE case; the green curve shows the case when the interaction parameter is $\frac{g}{2}$, i.e. the intermediate case.

The results plotted in Fig. (3.22) show one key thing: the wave pattern is recovered in all three cases regardless of the interactions, i.e. also when interactions are null. Furthermore, the height of the fringes changes in the three cases (we will describe this phenomena in the following) but their location and number do not. This leads to the conclusion that the effects seen in the experiment [65] and in the numerical simulations [92–94, 162] cannot be related to the black-hole laser effect nor to Bogoliubov-Cerenkov radiation as the speed of sound, if we do not consider interactions, is not defined[7]. Thus, there is not a notion of "supersonic" or "subsonic" region and all the effects related (like the black-hole laser mechanism and BCR) cannot be applied.

Fig. (3.22) also shows that there is a smooth transition from one case to the other. In fact, we kept the fully interacting cloud to the right of the step so that the condensate could experience the real potential trap and, therefore, we would start from the actual ground state of the experimental system. Furthermore, the peaks become narrower and taller as the interaction decreases exactly because we are diminishing the repulsion between atoms: when interactions are present, this tends to spread out the wave function more as the atoms feel the nearest neighbour's repulsion; on the other hand, taking the interactions away results in a more "concentrated" gas.

If we now re-plot the same red curves of Fig. (3.22) - i.e. the case of non-interacting atoms - superimposed, we can check that the basic features of the wave pattern are recovered, as Fig. (3.23) shows. We see that the fringes grow in time and they slightly move to the right, as the standing wave pattern did, both in the experiment [65] and in the numerical simulations [92–94, 162].

Since the dynamics is completely described by the linear Schrödinger equation, the interpretation of these results is fairly easy. Indeed, by means of a semi-classical approach, we can interpret the wave function in terms of the WKB approximation [36]. More specifically, being in the region near the trap turning point, the Airy functions are good candidates to model our dynamics. Before doing that, though, we want to describe the motion of the peaks.

Let us now proceed by adopting a fully classical approach. We consider a point particle of mass m which enters the non-interacting region $x < x_s(t)$, where $x_s(t)$ is the position of the moving step. In the trap reference frame, $x_s(t) = x_s(0) + vt = vt$. We take the particle to be initially at rest: this represents a good approximation since our initial condition, as we already mentioned, is well-fitted by the Thomas-Fermi condition, which is obtained neglecting the kinetic terms. Now, let us start from Newton equation for the particle subject to a time dependent potential $V_s(x - vt)$

$$m\ddot{x} = -V_s'(x - vt)\,; \tag{3.32}$$

multiplying this by $\dot{x}$ we can rewrite this equation in the form of an "energy conservation equation":

$$\frac{d}{dt}\frac{1}{2}m\dot{x}^2 = -\frac{d}{dt}V_s(x - vt) + mv\ddot{x}\,, \tag{3.33}$$

---

[7] One could equivalently say that, given Eq. (2.38), if we set $g = 0$ then we have a vanishing sound velocity, that is $c = 0$. This would not change the conclusion we will reach (namely, that it is not possible to define an analogue horizon as there is no notion of "supersonic" flow), nevertheless it is clear from Section 2.2 that in a ideal Bose gas - i.e. a non-interacting gas - sound cannot be defined, due to some pathological features of the model.

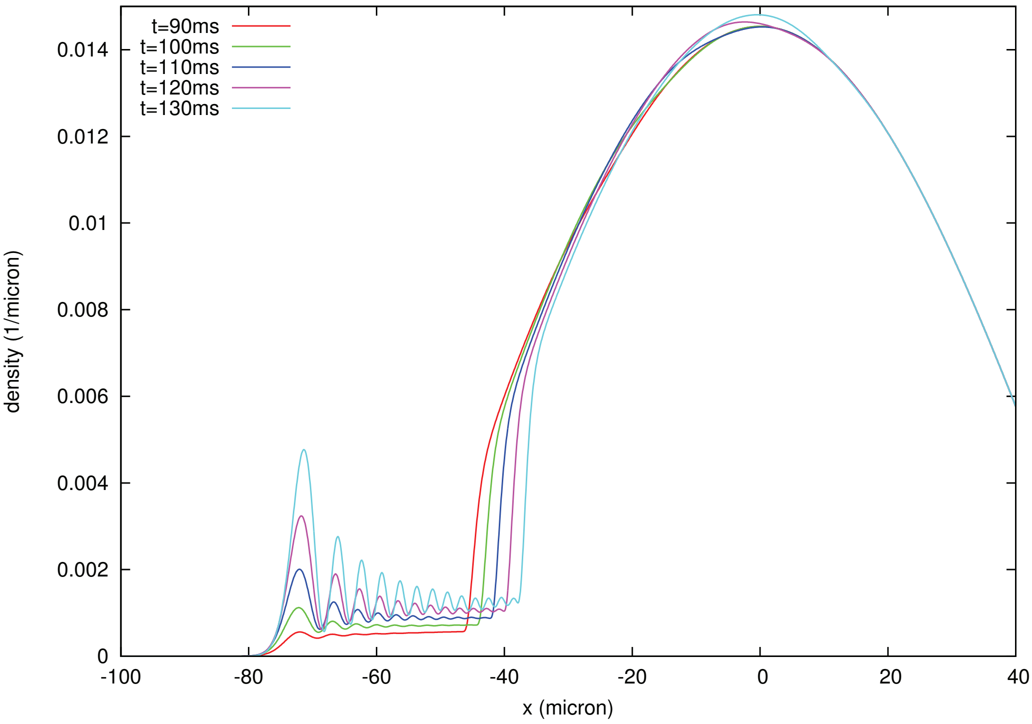

Figure 3.23: The profiles in the figure are the equivalent of the red curves of Fig. (3.22) superimposed in the same canvas, the only difference being in the width of the potential step: in Fig. (3.22), in fact, the width is $\sigma = 2\,\mu$m, which is the value of the experimental setup [65]; here, instead, we have used a sharp step ($\sigma = 0.2\,\mu$m) in order to increase the visibility of the movement of the peaks. The plot shows the time evolution of the condensate when we place a vanishing interaction parameter to the left of the potential drop. To show how the wave pattern grows in time we have moved to the trap reference frame, i.e., to the frame where the step moves and the trap is still.

which leads to the conservation law

$$\frac{1}{2}m\dot{x}^2 + V_s(x - vt) - mv\dot{x} = \text{constant}\,. \tag{3.34}$$

If the step potential is $V_s(x) = V_s[\Theta(x) - 1]$ and the particle is at rest before the kick, the right hand side can be estimated as pure internal energy $gn(x_s(t)) = \mu - U(x_s(t))$. Therefore, after the kick, the particle acquires a velocity $w < 0$ satisfying the equation

$$\frac{1}{2}mw^2 - mvw - V_s = \mu - U(x_s(t))\,. \tag{3.35}$$

After the initial kick the particle moves freely in the trap potential $U(x) = U_0\,\frac{x^2}{x^2+x_0^2}$ and therefore obeys the standard energy conservation equation

$$\frac{1}{2}m\dot{x}^2 + U(x) - V_s = E_{in}\,. \tag{3.36}$$

The initial energy is evaluated at the position of the step just after the kick

$$E_{in} = \frac{1}{2}mw^2 + U(x_s(t)) - V_s \tag{3.37}$$

and, thus, at the turning point (i.e. the point where the kinetic energy vanishes) we have, using Eq. (3.36) and (3.37),

$$U(x_t(t)) = \frac{1}{2}mw^2 + U(x_s(t))\,. \tag{3.38}$$

This gives us an analytical form for the turning point once we use Eq. (3.35) to obtain w. The result of this treatment is plotted in Fig. (3.24) together with the numerical results.

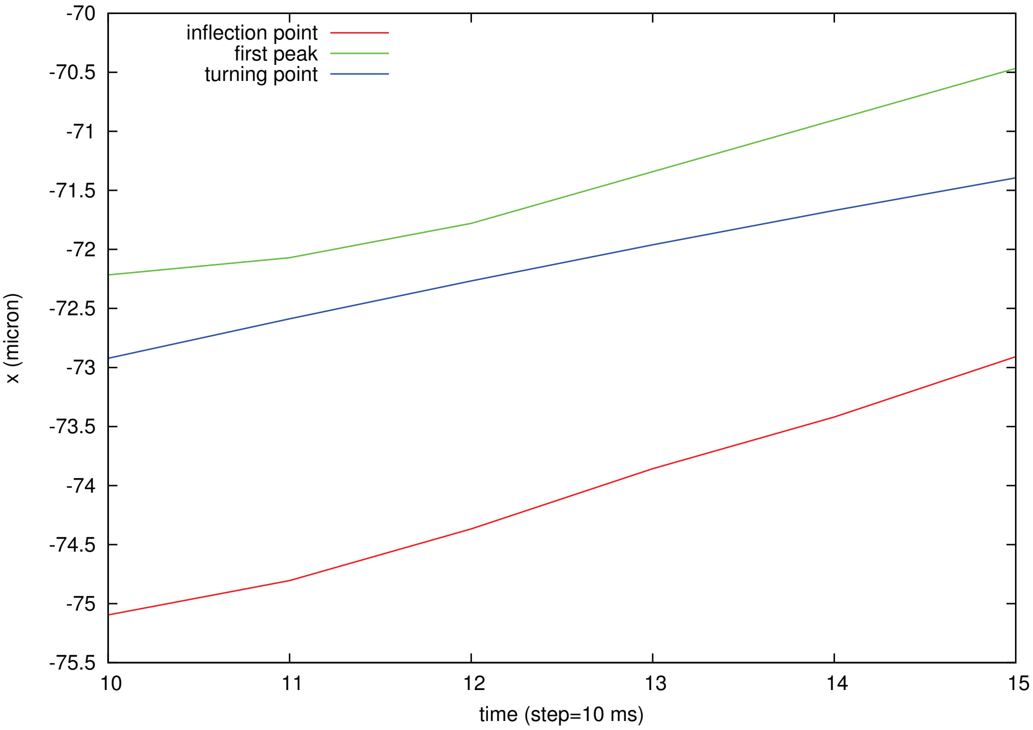

Figure 3.24: Motion of the turning point calculated with Eq. (3.38) (blue curve) together with the movement of the first peak inside the “supersonic” region (green curve) and the motion of the inflection point of the wave function (red curve), both calculated numerically.

Fig. (3.24) shows that the motion of the turning point, calculated from purely classical considerations, is in a good agreement with the motion of the first peak inside the (ex-)supersonic region and with that of the inflection point. This tells us two things: first of all, the fact that the turning point moves is due to system not conserving energy, which was shown in the calculations and it is obvious if we remember that our potential is time-dependent. Second, the motion of the turning point is responsible for the shifting of the peaks during the evolution, as it is evident from the figure.

Then we can try to recover an analytical form for the wave function of our system. We start by linearising the potential around the chemical potential,

$$U(x) - V_s = \mu - F(x - x^*)\,, \tag{3.39}$$

and then we substitute this expansion in the eigenvalue equation valid in the trap reference frame on the left of the step

$$-\frac{\hbar^2}{2m}\phi_\epsilon''(x) + [\mu - \epsilon - F(x - x^*)]\phi_\epsilon(x) = 0\,; \tag{3.40}$$

we can reduce this equation to the Airy form by the change of variable

$$x = -\alpha z + x^* + \frac{\mu - \epsilon}{F}\,, \tag{3.41}$$

with $\alpha = \left(\frac{\hbar^2}{2mF}\right)^{1/3}$. Therefore, imposing that the eigenfunction vanishes for $x \to -\infty$, we find the general solution

$$\phi_\epsilon(x) = Ai(z) = Ai\left(\frac{x^* - x}{\alpha} + \frac{\mu - \epsilon}{\alpha F}\right)\,. \tag{3.42}$$

If we define an energy-dependent turning point position

$$\xi = x^* + \frac{\mu - \epsilon}{F} \tag{3.43}$$

we have that the solution has the form

$$\phi_\xi(x) = Ai\left(\frac{\xi - x}{\alpha}\right)\,, \tag{3.44}$$

with eigenvalue $\epsilon = \mu + F(x^* - \xi)$. Therefore, the most general solution of the time-dependent Schrödinger equation can be written as a superposition of stationary states

$$\psi(x,t) = e^{-\frac{i}{\hbar}(\mu + F x^*)t} \int d\xi K(\xi) Ai\left(\frac{\xi - x}{\alpha}\right) e^{\frac{i}{\hbar}F\xi t}\,, \tag{3.45}$$

for any $x < x_s(t)$. Here $K(\xi)$ is an arbitrary complex function to be determined by imposing the suitable boundary condition at $x = x_s(t)$. One choice could be the Thomas-Fermi profile but the resulting equation cannot be solved analytically. Nevertheless, from the simulations we see that near the potential drop TF fails to reproduce the actual wave function of the condensate (while it still does away from it).

Finally, the fact that the fringes grow in time is related to the shape of the initial wave function: being the ground state not flat, as time passes more and more particles flow towards the left side of the trap, thus increasing the height of the peaks. On the other hand, though, this also causes the width of the (ex-)supersonic region to grow, which competes with the aforementioned process.

3.4.3 Conclusions

In our most recent numerical simulations we developed a simple model which effectively describes the observations of [65]; the results confirmed the previous findings that the phenomena have a purely classical interpretation and, thus, zero-point quantum fluctuations do not play a role in this picture [92–94]. Moreover, these studies interpreted the effects observed in terms of Bogoliubov-Cerenkov radiation and in terms of an hydrodynamical instability present in the Gross-Pitaevskii equation. As we have thoroughly illustrated, a description based on these effects is highly non-trivial: in fact, while the analysis of the numerical data seems to be in agreement with this picture, BCR [169] and the hydrodynamical instability of the GPE [157] are effects which should be evident in stationary regimes, a condition which is not respected in our case. Thus, an interpretation of the effects seen in [65] in terms of these phenomena might not be fully appropriate.

To this purpose, in our latest simulations we have shown that the effects seen in [65] appear to be related not to Bogoliubov-Cerenkov radiation nor to any hydrodynamical instability, as they seem to originate from a simple linear dynamics which can be completely described by the Schrödinger equation. Indeed, the absence of interactions in the simulations rules out these two candidates, as they rely on the existence of subsonic/supersonic regions. In this picture, the structure appearing in the experiment can be described by means of Airy functions; furthermore, the flux of atoms flowing over the step potential increases in time because the condensate profile is not flat and this causes the fringes to grow; the turning point, on the other hand, moves because the semiclassical energy is not conserved and this causes the peaks to shift.

Now, one might argue that the structure observed in the simulations could be interpreted in terms of a dispersive shock wave (DSW) [175, 176]. These are non-stationary waves which appear in weakly dispersive media when the non-physical discontinuity of some solutions (caused by the non-linearity of the equations) is regularized by dispersion. Since the structure present in Fig. (3.22) resembles the aspect of a typical DSW, it has been proposed that the switching off of the interaction to the left of the waterfall potential might have caused this phenomena to appear. A close look to Fig. (3.22), though, suggests that this might not be the case for two reasons: first of all, the structure is seen to appear regardless of the presence of interactions (i.e., the non-stationary wave pattern is present in all cases, in spite of the value of g); secondly, the structure is seen to appear not on the density drop (as one would have expected in the case of a DWS connecting two inhomogeneous regions) but on the turning point of the trap potential. Thus, this interpretation seems unlikely.

The results described above are summarized in an article in preparation and we believe they constitute an important piece in the debate on the observation of the analogue Hawking radiation.

Chapter 4

The Tonks-Girardeau gas model

This Chapter contains the description of the second part of our work. Here, we give a complete characterization of the analogue Hawking radiation in BECs by analysing a microscopic, exactly solvable model, without relying on the gravitational analogy. The approach presented is innovative as the theoretical description of the analogue Hawking effect has been only studied in semiclassical approximation up to date. We are able to test the validity of the semiclassical approach and, moreover, we show that the effect requires other conditions to be met besides the presence of a sonic horizon, which are related to the condensed-matter nature of the system. The density correlations method and a realistic experimental set-up are also discussed.

This work has led to the publication of a first Letter [69], while a more detailed analysis is in preparation[1].

---

[1] During the revision of this Thesis, the aforementioned work has been accepted for publication on *Physical Review D*.

4.1 A microscopic description of the analogue Hawking radiation

As we have seen in the previous Chapter, sonic black holes in Bose-Einstein condensates have been intensively studied in recent years, as the detection of the analogue Hawking radiation seems to finally be in sight. Nevertheless, although the analogue gravity picture leading to spontaneous phonon emission from a sonic horizon is widely accepted from a theoretical point of view, in Bose-Einstein condensates this mechanism has always been studied only in semiclassical approximation, based on the Gross-Pitaevskii equation supplemented by a Bogoliubov analysis of the excitation spectrum. Moreover, very often studies start from the results obtained from the gravitational analogy, without questioning their validity. This is a subtle but important point: a very common approach in this field, in fact, is to start from a fluid, create an analogue horizon by accelerating the flow in a finite region of space and then apply Eq. (1.67) to obtain the Hawking temperature. This way of proceeding, though, implicitly assumes the derivation of the form of T_H for the case of a fluid, which was obtained from the gravitational counterpart having defined the analogue surface gravity [52]. Another way of proceeding, instead, consists in not-relying on the gravitational analogy, therefore starting from a moving fluid and asking the following questions: if we set the fluid in supersonic motion, do we observe a flux of particle in the far upstream region of subsonic motion? If so, can we associate a temperature to this flux of particle? What is its form? This way of approaching the problem provides a description of the analogue Hawking radiation which “does not rely” on the gravitational analogy. A few studies develop in this direction, for example [145, 147, 177]. Nevertheless, the starting point is always the semiclassical approximation and, up to date, a fully microscopic model displaying the analogue gravity mechanism at work in a physically well-defined setting has not been devised yet, although it has been deemed desirable soon after the discovery of the analogy (see, for example, the comments made in [77, 79]). Such an investigation would allow to understand the physical origin of the quasi-particle emission in a condensed matter system and to establish the necessary conditions for the detection and the characterization of this effect. This is therefore a crucial step towards the unambiguous identification of the analogue Hawking radiation in the laboratory.

This is exactly the starting point of our work, which we will describe in this Chapter. Indeed, we give a complete characterization of the analogue Hawking radiation in BECs by analysing a microscopic, exactly solvable model, without relying on the gravitational analogy. In particular, the collapse of a star into a final black hole is simulated by means of a quantum quench perturbing a free stationary flow; then, we analyse the sound spectrum at late times, when the stationary regime is met again, much as Hawking did in his approach [18, 19]. The results are in agreement with the analogue gravity picture but with some, fundamental, differences. Let us now briefly describe the idea of the model and then we will outline the details.

Since experiments in ultra-cold atoms systems have always been performed in quasi one-dimensional geometries (as we have illustrated in the previous Chapter), we conform to this limit and we exploit a particular feature of bosons in 1D, namely the Tonks-Girardeau limit; we have already discussed this particular case in Section 2.5. Thanks to this approach, we can make use of a precise correspondence between bosons and fermions which makes the system exactly solvable and thus allows us to compute the many-body wave function, the spectrum of the emitted quanta and the exact form of all the dynamical quantities. This way, we can completely characterize the analogue Hawking radiation in BECs from a microscopic point of view and, furthermore, we can test the limits of validity of the semiclassical methods. Note that the analogue gravity paradigm has already been explored in systems of fermions [67, 68] but, again, in the semiclassical approximation[2]. Here, instead, we investigate a microscopic model constituted by interacting quantum particles which is exactly solvable, so that we can follow the full dynamics analytically and we have complete control of all the physical details playing a role in the phenomena. Furthermore, even though we will show that the results obtained apply not only to the TG limit, note that experimental realizations of these systems are nevertheless accessible [136, 137, 179, 180].

4.2 The model

Following the line of thought originally devised by Hawking in the astrophysical context [18, 19], we proceed in the following way: first we consider a stationary flux of interacting bosons in the TG limit that is in motion to the left with a constant speed (this represents the vacuum of the gravitational case); the (repulsive) interaction between bosons is essential in order to be able to describe the excitation spectrum in terms of phonons. Then, we switch on an external potential quenching the system, and we let the gas evolve in time[3]. After a while, the system will reach a new stationary state, which, under suitable conditions, may present a sonic horizon, i.e., a point where the flow passes from a subsonic regime to a supersonic one. The usual arguments of the analogue gravity paradigm then predict that, in the final stationary state, there should be a flux of phonons escaping the horizon. Such a flux is expected to be thermal at least in a certain region of the spectrum, with a temperature proportional to the gradient of the difference between the flow velocity and the sound velocity at the sonic horizon, as Eq. (1.67) illustrates.

---

[2] During the writing of this Thesis another work on Fermi gases has appeared [178].

[3] The mapping between bosons and fermions remains unchanged if an external potential is switched on.

Therefore, we start from the ground state of a HCB gas in the absence of external potentials, which is described by a Fermi distribution in the interval $(-k_F, k_F)$; the gas particles fill all the single-particle states up to the Fermi momentum, which is related to the uniform particle density by $k_F = \pi\,\rho$, as illustrated in Section 2.5. Then, following the procedure described above, we perform a Galilean transformation and we shift the wave vectors of all particles by $-k_0$, setting the fluid into motion towards the left, with a uniform velocity $v_0 = \frac{\hbar k_0}{m}$. The fermionic many-body state, then, is a Slater determinant of single particle wave function, which, in this case, are the plane waves

$$\psi_k^0(x) = \frac{e^{ikx}}{\sqrt{2\pi}}\,, \tag{4.1}$$

with wave vectors in the interval $-k_F - k_0 < k < k_F - k_0$. In the following, we will always consider the case $k_0 \leq k_F$, which corresponds to a subsonic flow[4]. Now we perform a quantum quench: at $t = 0$ an external potential $V(x)$ is suddenly turned on, bringing the system out of the initial stationary state. As a consequence, each single-particle plane wave evolves in time according to

$$\begin{aligned} \psi_k(x,t) &= \int_{-\infty}^{\infty} dp\,\langle\phi_p|\psi_k^0\rangle\,\phi_p(x)\,e^{-\frac{i}{\hbar}\epsilon_p t}\,, && (4.2)\\ \langle\phi_p|\psi_k^0\rangle &= \int_{-\infty}^{\infty} \frac{dx}{\sqrt{2\pi}}\,\phi_p^*(x)\,e^{ikx}\,e^{-\eta|x|}\,, && (4.3) \end{aligned}$$

where $\phi_p(x)$ are the exact eigenfunctions of a single particle in the external potential $V(x)$, $\epsilon_p = \frac{\hbar^2 p^2}{2m}$ are the associated eigenvalues and $\eta \to 0^+$ is the usual convergence factor. Now, let us consider the long-time behaviour of these wave functions at a fixed position x. During the unitary time evolution, the many-body wave function preserves its Slater determinant structure with time-dependent orbitals given by Eq. (4.2). A careful analysis of Eqs. (4.2) and (4.3) shows that, for each k, $\psi_k(x,t)$ is given by the sum of an exact scattering eigenfunction of the system in the presence of the external potential multiplied by a time-dependent phase factor, plus a contribution which vanishes as $t \to +\infty$ (we will explicitly demonstrate this in the following). These two terms represent, respectively, the asymptotic stationary state and a travelling wave originated during the quench. The asymptotic stationary wave function describing the long-time behaviour of each single-particle state at fixed position x is just the exact scattering eigenstate corresponding to an incident plane wave of defined wave vector. The evaluation of the asymptotic properties can be made explicit in specific models, where the exact single-particle eigenstates are known. In the following, we will consider two representative potentials, often investigated both theoretically and experimentally.

---

[4] If we recall Eq. (2.81) of Section 2.5 it is straightforward to verify that this inequality is exactly the condition $v_0 \leq c$.

4.2.1 The case of a step potential

We first consider an external potential of the form $V(x) = V_0\Theta(x)$, where Θ is the Heaviside function and we define $V_0 = \frac{\hbar^2 Q^2}{2m}$ for convenience. This "waterfall" potential coincides with the one adopted in the latest experiments in BECs [65, 66, 96][5].

A set of single-particle eigenfunctions for this problem is explicitly reported in Appendix B. With this choice, we can evaluate the long time limit of Eq. (4.2) to obtain the stationary state. We will now give a sketch of the calculations, as they will be useful in the following Sections also.

We start from the exact time evolution Eq. (4.2). We first evaluate the internal products $\langle\phi_p|\psi_k^0\rangle$ (4.3) which, using the explicit expressions of Appendix B, can be written as a sum of simple poles of the form

$$\frac{\alpha_p}{\eta \pm i(p-k)} = \alpha_p \pi\delta(p-k) \mp P\frac{i\alpha_p}{p-k}\,, \tag{4.4}$$

where the Plemelj identity [181] has been used. Inserting this sum into Eq. (4.2) we get

$$\pi\alpha_k\phi_k(x)\, e^{-\frac{i}{\hbar}\epsilon_k t} \mp i\, P\int_{-\infty}^{\infty} dp\, \frac{\alpha_p\phi_p(x)e^{-\frac{i}{\hbar}\epsilon_p t}}{p-k}\,, \tag{4.5}$$

where, besides the term coming from the δ-function, the integral also gives a non-vanishing contribution at long times. In fact, by defining $u = p - k$ and expanding α_{k+u} and ϵ_{k+u} to first order in u, it is straightforward to show that the second term has a finite limit as $t \to +\infty$:

$$\mp\pi\alpha_k\phi_k(x)\, e^{-\frac{i}{\hbar}\epsilon_k t}\,\mathrm{sgn}(\epsilon_k')\,, \tag{4.6}$$

whose sign depends on the slope of the fermionic dispersion ϵ_k so that, for $\pm\epsilon_k' > 0$ it precisely cancels the contribution coming from the δ-function. In conclusion, we can formally write

$$\lim_{t\to+\infty}\frac{e^{-\frac{i}{\hbar}\epsilon_p t}}{\eta \pm i(p-k)} = 2\pi\delta(k-p)\, e^{-\frac{i}{\hbar}\epsilon_k t}\,\Theta(\mp\epsilon_k')\,. \tag{4.7}$$

This analysis is easily extended to all the external potentials that do not admit bound states, because the pole contribution in the internal product (4.3) comes from the asymptotic regions $x \to \pm\infty$ where every eigenfunction $\phi_p(x)$ acquires the form of a scattering state, i.e., can be written as a linear combination of an incident (or transmitted) wave and a reflected wave. Therefore, the form of the eigenfunctions at $x \to \pm\infty$ has the same structure shown in Appendix B, irrespective of the details of the external potential.

---

[5] In the actual experiments the waterfall potential is never a *sharp* step and thus a smooth version of this potential should be considered. We will do that in the following, demonstrating that using a smooth step does not change the conclusions reached in the case of a sharp one.

Thus, the stationary state is defined by the single particle orbitals

$$\psi_k(x,t) \to \begin{cases} \phi_k(x)\, e^{-i\frac{\hbar k^2}{2m}t} & k>0 \\ \sqrt{\frac{|k|}{p}}\, \phi_{-p}(x)\, e^{-i\frac{\hbar p^2}{2m}t} & k<0 \end{cases}, \tag{4.8}$$

with $p = \sqrt{k^2+Q^2}$ while the expressions for $\phi_k(x)$ can be found in Appendix B. The momentum distribution defining the Slater determinant remains unchanged during the evolution and, thus, the stationary state is defined by the orbitals belonging to the interval $-k_F - k_0 < k < k_F - k_0$. As a consequence, after an initial transient, an observer at a given position x will perceive the moving fluid in a stationary state described by the asymptotic single-particle wave functions (4.8). Note that, while the full evolution (4.2) must conserve both the energy and the total number of particles, the stationary state orbitals do not have to, because the waves formed during the quench and travelling in both directions may carry energy (and particles) to infinity at long times. Moreover, in the non-uniform stationary state, the local energy and momentum density may differ from their initial value before the quench, even in the asymptotic regions $x \to \pm\infty$.

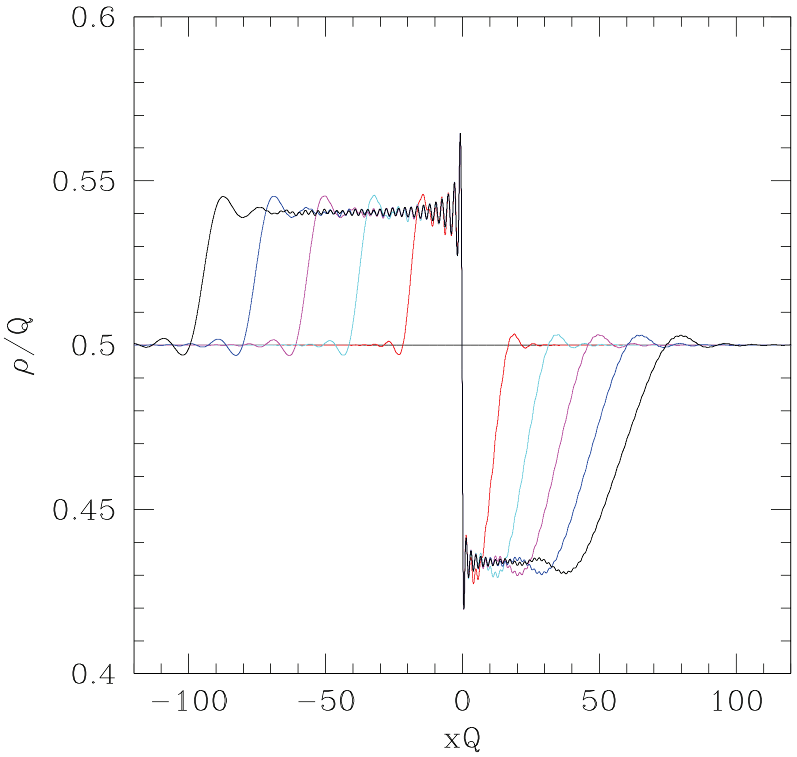

Figure 4.1: Density profile of the HCB gas after the quench for $k_F = \frac{\pi}{2}Q$ and $k_0 = \frac{3\pi}{50}Q$. Initially the fluid has a uniform density $\rho_0 = 0.5\,Q$. Colours refer to different times after the quench: red, cyan, magenta, blue, black. The time lapse between curves is $10\,\frac{m}{\hbar Q^2}$.

The stationary state properties can now be evaluated analytically by use of Eq. (4.8). In Fig. (4.1) we show a few snapshots of the time evolution of the density profile

$$\rho(x,t) = \int_{-k_F-k_0}^{k_F-k_0} dk\, |\psi_k(x,t)|^2 \,, \tag{4.9}$$

as obtained by numerical integration of the Schrödinger equation for a Fermi gas flowing in a waterfall potential.

In the figures, lengths are expressed in units of Q^{-1} and times in units of $\tau = \frac{m}{\hbar Q^2}$. In Fig. (4.1) the initial density is set to $\rho_0 = 0.5\,Q$ and the initial velocity is 0.12 times the sound speed of the fluid $c_0 = \frac{\hbar}{m}\pi\rho_0$. The quench dynamics is clearly visible in the figure: two waves are generated at $t = 0$ in $x = 0$ and propagate at different velocities $c_0 \pm |v_0| = \frac{\hbar}{m}(k_F \pm k_0)$ in the downstream (+) and upstream (−) direction. In the central region the density profile shows a rapid variation near the waterfall, several standing waves develop and the density becomes lower upstream than downstream. In Fig. (4.2) a blow-up of the density profile in the inner region at long times $t = 50\,\tau$ is compared to the analytical solution based on Eq. (4.8).

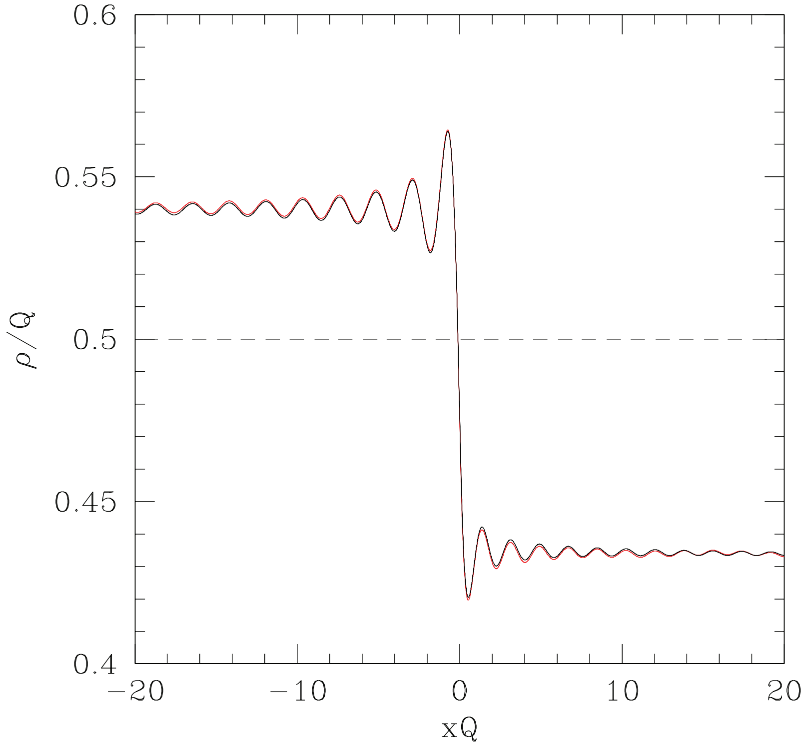

Figure 4.2: Blow-up of the long time results shown in Fig. (4.1) which shows the density profile of the HCB gas long after the quench. The analytical stationary solution (black line) is compared to the numerical solution of the Schrödinger equation after a time $t = 50\,\frac{m}{\hbar Q^2}$ (red curve). The two curves are superimposed on the scale of the figure. The dashed line $\rho = 0.5\,Q$ shows the value before the quench.

The velocity profile of the Fermi gas is defined in terms of the local mass flux

$$j(x,t) = \Re\left[i\,\frac{\hbar}{2}\int_{-k_F-k_0}^{k_F-k_0} dk\,\psi_k(x,t)\,\partial_x\psi_k^*(x,t)\right] \tag{4.10}$$

as $v(x,t) = \frac{j(x,t)}{m\rho(x,t)}$. In Fig. (4.3) the fluid velocity is compared to the local sound speed, which, we recall, is $c(x,t) = \frac{\hbar}{m}\pi\rho(x,t)$ for a HCB gas.

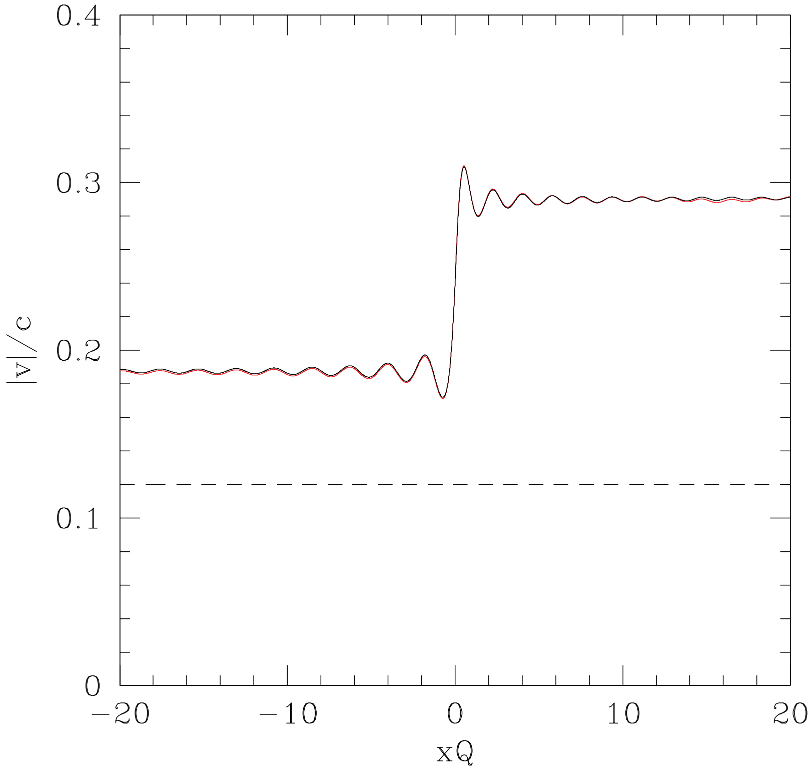

Figure 4.3: Ratio between the absolute value of the fluid velocity and the local sound speed long after the quench, for the same parameters of Fig. (4.1). The dashed line shows the ratio before the quench. The analytical stationary solution (black line) is compared to the numerical solution of the Schrödinger equation after a time $t = 50\,\frac{m}{\hbar Q^2}$ (red curve). The two curves are superimposed on the scale of the figure.

For this parameter choice the flow is always subsonic, the ratio v/c being always less than unity. The excellent agreement between the numerical results and the analytical expressions confirms the correctness of the theoretical analysis.

At fixed initial density ρ_0, for sufficiently small values of the initial velocity v_0, the stationary state is subsonic while, for larger values of v_0, a supersonic region appears near the potential step, although the flow remains subsonic in the asymptotic region $x \to -\infty$. Nevertheless, a sonic horizon is present whenever $k_F - k_0 < Q$. Further increasing v_0, the flow becomes fully supersonic beyond the sonic horizon located close to $x = 0$. Fig. (4.4) shows the ratio

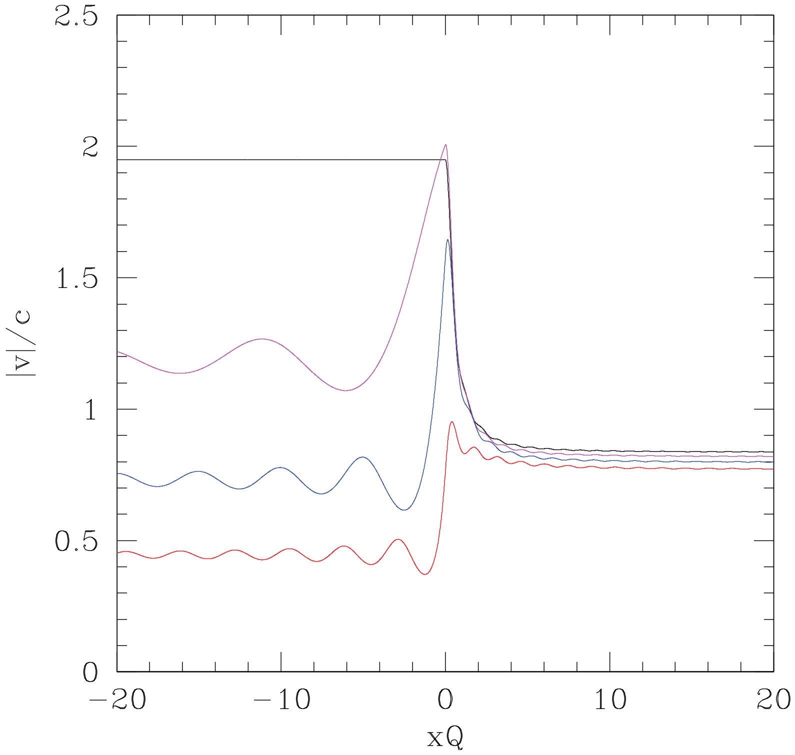

Figure 4.4: Ratio between the absolute value of the fluid velocity and the local sound speed in the stationary state reached starting from $\rho_0 = 0.5\,Q$ and initial velocities $v_0 = -\frac{5\pi}{10}\frac{\hbar Q}{m}$ (black curve), $v_0 = -\frac{4\pi}{10}\frac{\hbar Q}{m}$ (magenta), $v_0 = -\frac{3\pi}{10}\frac{\hbar Q}{m}$ (blue), $v_0 = -\frac{2\pi}{10}\frac{\hbar Q}{m}$ (red). The plot shows that, for a fixed value of the initial density ρ_0, by increasing the initial velocity we develop from a totally subsonic configuration in the $x < 0$ region (red curve), to a configuration which shows a sonic horizon near the origin but is subsonic in the asymptotic region $x \to -\infty$ (blue curve), to configurations which are totally supersonic in the asymptotic region $x \to -\infty$ (magenta and black curves).

between the fluid velocity and the local sound speed in the stationary state for a few values of the initial parameters (k_F, k_0). The behaviour is generally non monotonic and characterized by undulations in the downstream region, except for $k_0 = k_F$ (that is, for $v_0 = -\pi\frac{\hbar\rho_0}{m}$) when the oscillations disappear and the velocity becomes constant beyond the horizon. A few snapshots of the HCB dynamics are shown in Fig. (4.5) for a set of parameters triggering a supersonic transition.

The analytical stationary state and numerical results long after the quench are compared in Fig. (4.6) and the agreement is remarkable. Note that in this case, the development of the stationary state requires considerable longer times and the numerical integration was carried out up to times as large as $t = 250\,\tau$ in order to obtain a stationary solution in the range $|x| \lesssim 10\,Q^{-1}$.

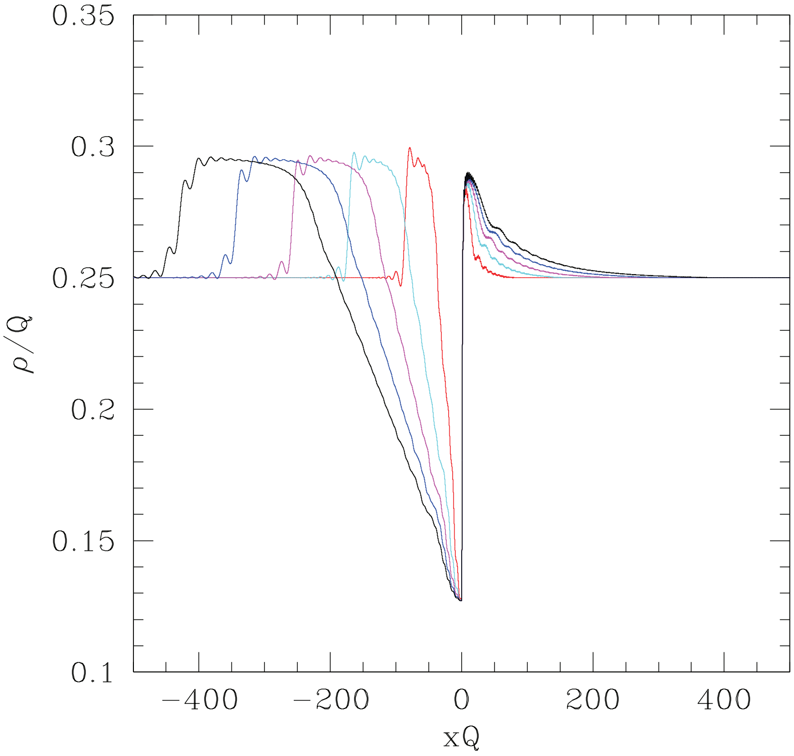

Figure 4.5: Density profile after the quench for $k_F = k_0 = \frac{\pi}{4}\,Q$. Initially the fluid has a uniform density $\rho_0 = 0.25\,Q$. Colors represent different times after the quench: red, cyan, magenta, blue, black. Time lapse between curves is $50\,\frac{m}{\hbar Q^2}$.

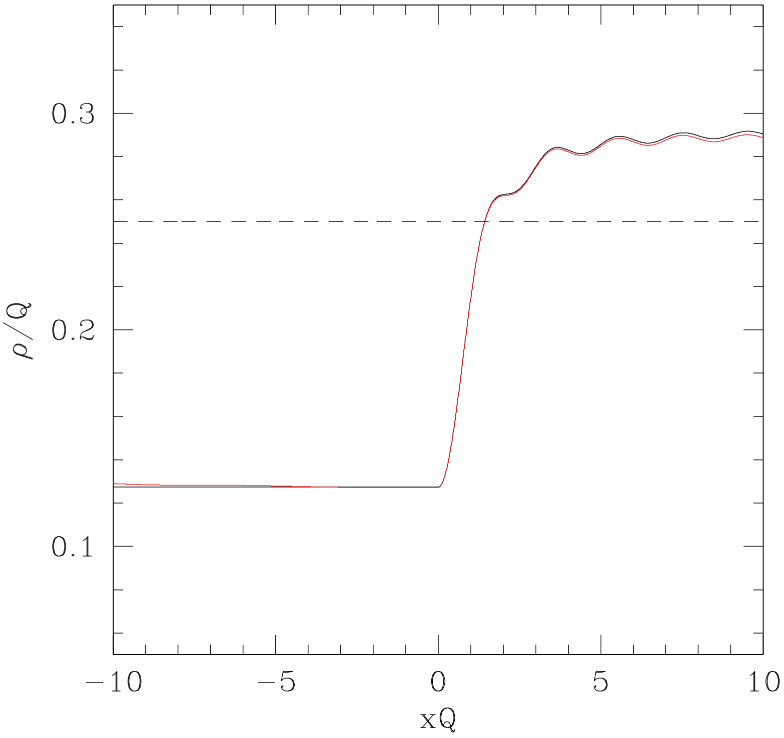

Figure 4.6: Blow-up of the results of Fig. (4.5) which shows the density profile long after the quench. The analytical stationary solution (black line) is compared to the numerical solution of the Schrödinger equation after a time $t = 250\,\frac{m}{\hbar Q^2}$ (red curve). The dashed line shows the value before the quench.

The Mach ratio $|v|/c$ long after the quench is shown in Fig. (4.7) and a supersonic transition is clearly visible. For this choice of parameters, at $t = 0$ the fluid velocity coincides with the sound speed of the uniform gas.

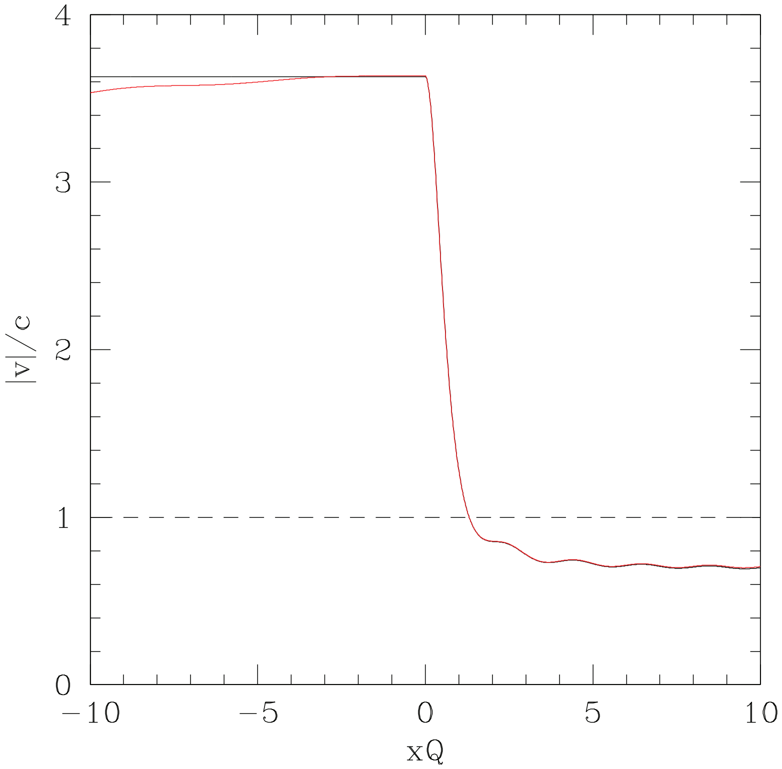

Figure 4.7: Ratio between the absolute value of the fluid velocity and the local sound speed long after the quench for the same parameters of Fig. (4.5). The dashed line shows the ratio before the quench. The analytical stationary solution (black line) is compared to the numerical solution of the Schrödinger equation after a time $t = 250\,\frac{m}{\hbar Q^2}$ (red curve).

4.2.2 The case of a repulsive barrier

Let us now turn our attention to a different form of the external potential, namely a repulsive barrier[6] of the form

$$V(x) = \frac{V_0}{\cosh(\alpha x)^2} \tag{4.11}$$

where the parameter α governs the width and smoothness of the barrier, while V_0 is conveniently parametrized[7] as $V_0 = \frac{\hbar^2 Q^2}{2m} + \frac{\hbar^2 \alpha^2}{8m}$. From the exact solution

---

[6] Barrier potentials can be experimentally reproduced in the laboratory (see, e.g., [182]).

[7] Due to a misprint, the term $\frac{\hbar^2\alpha^2}{8m}$ in the definition of V_0 was disregarded in [69].

of the eigenvalue problem [183] we can write the properly normalized eigenfunctions as:

$$\begin{aligned}\phi_k(x) \; &= \frac{\Gamma(\frac{1}{2}-i\frac{k+Q}{\alpha})\Gamma(\frac{1}{2}-i\frac{k-Q}{\alpha})}{\sqrt{2\pi}\,\Gamma(1-i\frac{k}{\alpha})\Gamma(-i\frac{k}{\alpha})}\left[\zeta(1-\zeta)\right]^{-i\frac{k}{2\alpha}} \\ &\quad F\left(\tfrac{1}{2}-i\frac{k+Q}{\alpha},\tfrac{1}{2}-i\frac{k-Q}{\alpha};1-i\frac{k}{\alpha};\zeta\right)\,, \qquad (4.12)\end{aligned}$$

where $\zeta = \frac{1-\tanh(\alpha x)}{2}$ and $\Gamma(a)$, $F(a,b;c;\zeta)$ are the usual Gamma and Hypergeometric functions, respectively [184]. The above expression, valid for $k > 0$, represents a right-moving scattering solution with energy $\epsilon_k = \frac{\hbar^2 k^2}{2m}$. The degenerate eigenfunction with $k < 0$ is obtained by replacing $k \to -k$ and $x \to -x$.

We can now proceed as previously discussed, thus by setting the free Fermi gas in a Slater determinant of plane waves with momenta in the interval $-k_F - k_0 < k < k_F - k_0$ (with $0 < k_0 \leq k_F$). An analysis similar to the one carried out for the step potential (namely, the evaluation of the limit $t \to +\infty$) shows that, if we switch on the barrier and we wait for equilibration, the system relaxes on a state defined by a Slater determinant of the eigenstates (4.12) with momenta belonging to the same interval. This set of eigenstates, therefore, describes the asymptotic stationary state of the system long after the quench. The analytical form of the asymptotic densities at $x \to \pm\infty$ are reported in Appendix C.

Figs. (4.8) and (4.9) show the comparison between the numerical integration of the Schrödinger equation for long times and the asymptotic analytical expressions for the density and the velocity profiles, respectively. The parameter α has been chosen so to study the case of a sharp barrier $\alpha = Q$. The same comparison for a smoothly varying potential with $\alpha = 0.1\,Q$ instead is presented in Figs. (4.10) and (4.11).

As in the case of the step, we conclude that the stationary state predicted on the basis of the eigenfunctions (4.12) is indeed reached at long times irrespective of the value of the parameter α. An interesting peculiarity of the time evolution in the case of the potential barrier can be readily noticed. In the step case two density modulations originate from the defect (i.e. the waterfall placed at $x = 0$) propagating in the upstream and downstream directions. Instead, for a barrier, as the supersonic transition sets in, a further soliton-like wave propagating downstream is clearly visible. The soliton velocity is indeed very close to the theoretical expectation $v_{sol} \sim c + |v| = \pi\frac{\hbar Q}{m}$. This observation confirms the analysis, based on the Gross-Pitaevskii dynamics, carried out in [185,186] where the effect was attributed to the peculiar form of the Bogoliubov excitation spectrum in the supersonic case. Note also that the stationary-state properties of the system are visibly different from those of the step potential, as they barely change with α in the range we have examined (modulo a trivial rescaling of the length unit), showing that in the case of a potential barrier the "smooth limit" is easily achieved also for moderate values of α/Q.

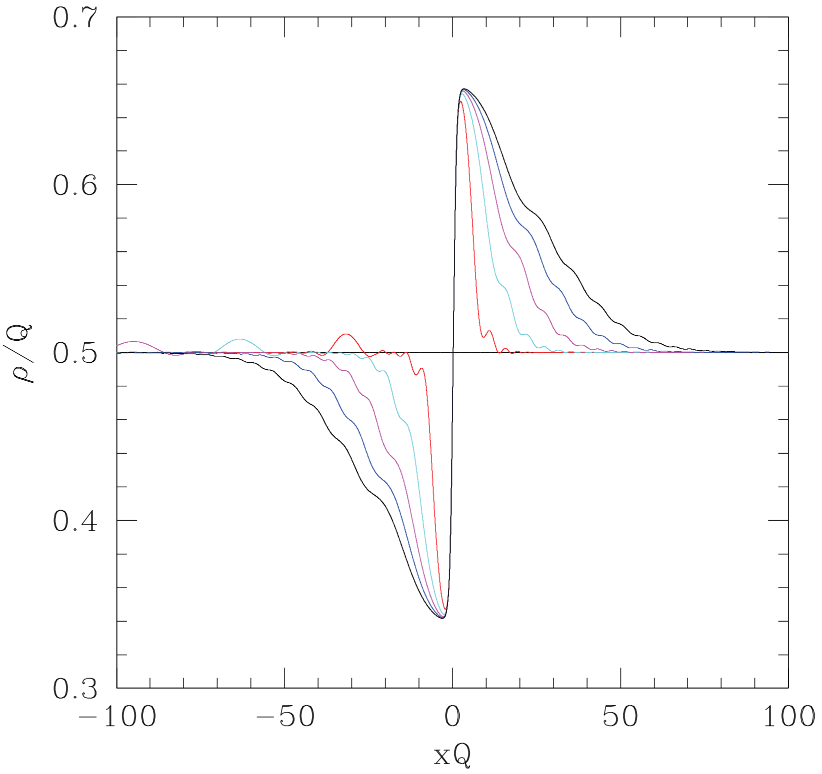

Figure 4.8: Density profile after the quench for $k_F = k_0 = \frac{\pi}{2}\,Q$ and $\alpha = Q$. Initially the fluid has a uniform density $\rho_0 = 0.5\,Q$. Colors refer to different times after the quench: red, cyan, magenta, blue, black. The time lapse between curves is $10\,\frac{m}{\hbar Q^2}$.

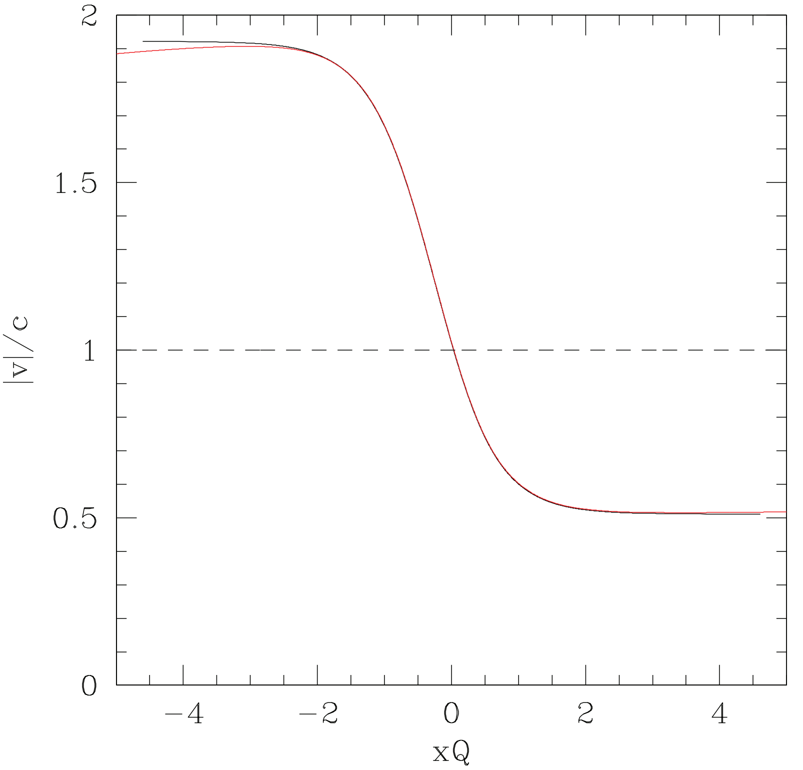

Figure 4.9: Mach number for the same parameter choice as Fig. (4.8). The dashed line shows the ratio before the quench. The analytical stationary solution (black line) is compared to the numerical solution of the Schrödinger equation after a time $t = 50\,\frac{m}{\hbar Q^2}$ (red curve).

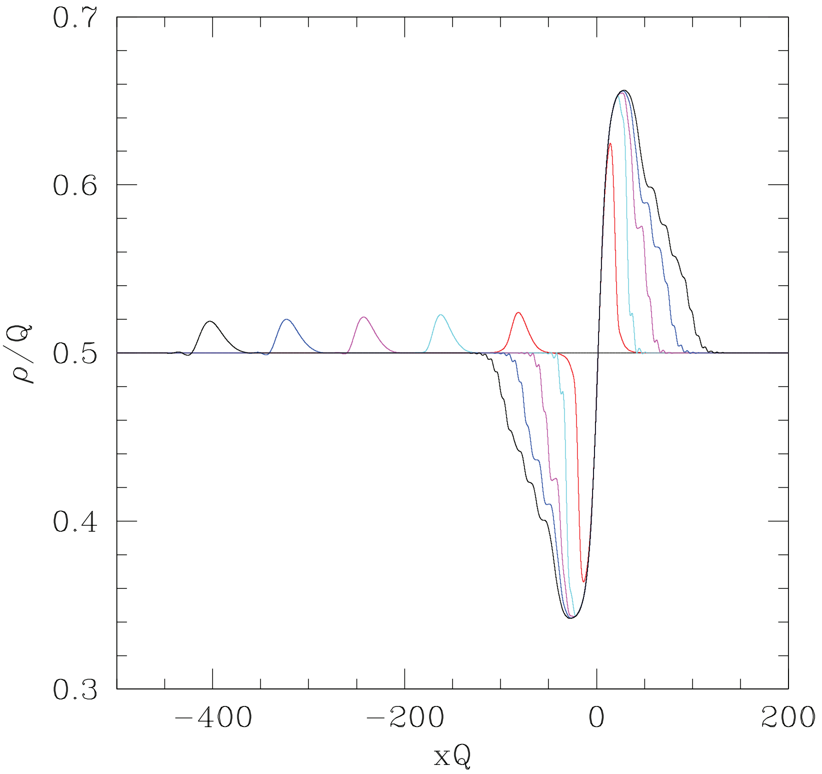

Figure 4.10: Density profile after the quench for $k_F = k_0 = \frac{\pi}{2}\,Q$ and $\alpha = 0.1\,Q$. Initially the fluid has a uniform density $\rho_0 = 0.5\,Q$. Colors refer to different times after the quench: red, cyan, magenta, blue, black. The time lapse between curves is $25\,\frac{m}{\hbar Q^2}$.

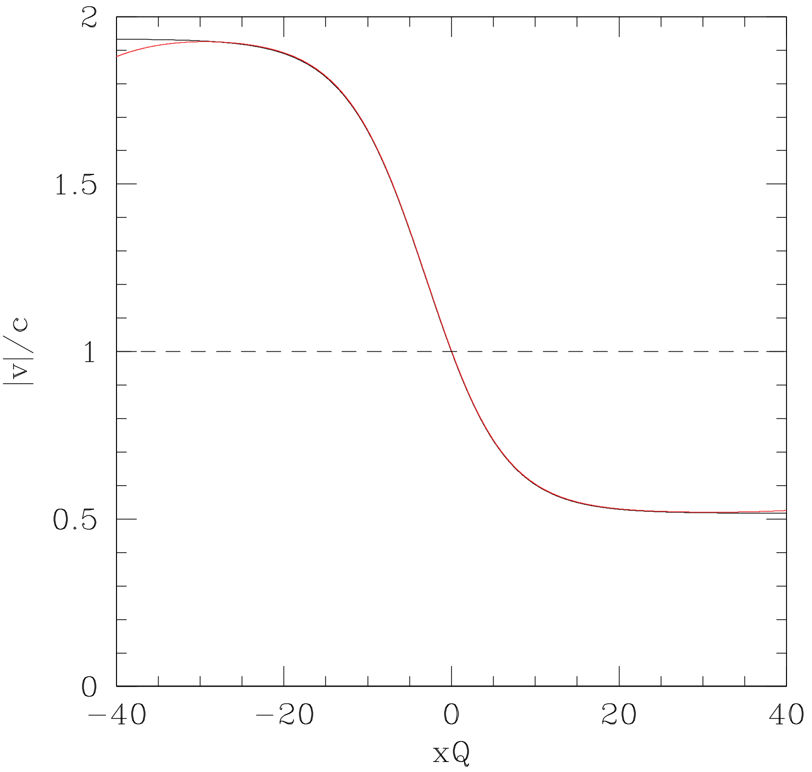

Figure 4.11: Mach number for the same parameter choice as Fig. (4.10). The dashed line shows the ratio before the quench. The analytical stationary solution (black line) is compared to the numerical solution of the Schrödinger equation after a time $t = 200\,\frac{m}{\hbar Q^2}$ (red curve).

Remarkably, in the $\alpha \to 0$ limit, several analytical expressions can be obtained from the asymptotic behaviour of the Hypergeometric functions (see Appendix D). The density profile of the stationary state is readily evaluated by inserting the results (D.12), (D.13) into

$$\rho(x) = \int_{-k_F - k_0}^{k_F - k_0} dk \, |\phi_k(x)|^2 \, . \tag{4.13}$$

It is convenient to define a dimensionless coordinate as

$$\xi = \tanh(\alpha x) \, , \tag{4.14}$$

$$\xi_\pm^2 = 1 - \left(\frac{k_F \pm k_0}{Q} \right)^2 \, . \tag{4.15}$$

Then, the density profile acquires different analytical expressions in three regimes:

- $Q > k_F + k_0$. Here all the fermions have kinetic energy lower than the height of the barrier. Total reflection occurs and the stationary-state density profile is

  $$\rho(x) = \begin{cases} \frac{Q}{\pi} \sqrt{\xi^2 - \xi_-^2} & \text{for } \xi < -\xi_- \\ \frac{Q}{\pi} \sqrt{\xi^2 - \xi_+^2} & \text{for } \xi > \xi_+ \end{cases} \, , \tag{4.16}$$

  while $\rho(x) = 0$ elsewhere. The mass flux in this regime vanishes because particles cannot tunnel through the barrier.

- The most interesting regime is when $k_F - k_0 < Q < k_F + k_0$. Here quantum tunnelling occurs and the constant mass flux is $j = -\frac{\hbar}{4\pi} \left[(k_F + k_0)^2 - Q^2 \right]$. The density profile is now given by

  $$\rho(x) = \Theta(-\xi_- - \xi) \frac{Q}{\pi} \sqrt{\xi^2 - \xi_-^2} + \frac{Q}{2\pi} \sqrt{\xi^2 - \xi_+^2} + \frac{Q}{2\pi} \xi \, , \tag{4.17}$$

  where the Heaviside function $\Theta(x) = 1$ for $x > 0$ and vanishes for $x < 0$. Note that the density profile is generally not monotonic. A sonic horizon is always present in this regime.

- For $Q < k_F - k_0$ the flow is fully subsonic in the stationary state. The mass flux is $j = -\frac{\hbar}{\pi} k_F k_0$ and the full density profile preserves the symmetry of the potential

  $$\rho(x) = \frac{Q}{2\pi} \left(\sqrt{\xi^2 - \xi_-^2} + \sqrt{\xi^2 - \xi_+^2} \right) \, . \tag{4.18}$$

A comparison between the exact solution and the asymptotic analytical results for $\alpha \to 0$ is shown in Fig.(4.12) where the local Mach number $\frac{v(x)}{c(x)} = \frac{j}{\pi \hbar \rho(x)^2}$ is displayed for $\frac{\alpha}{Q} = 0.1$ and different choices of the parameters (k_F, k_0).

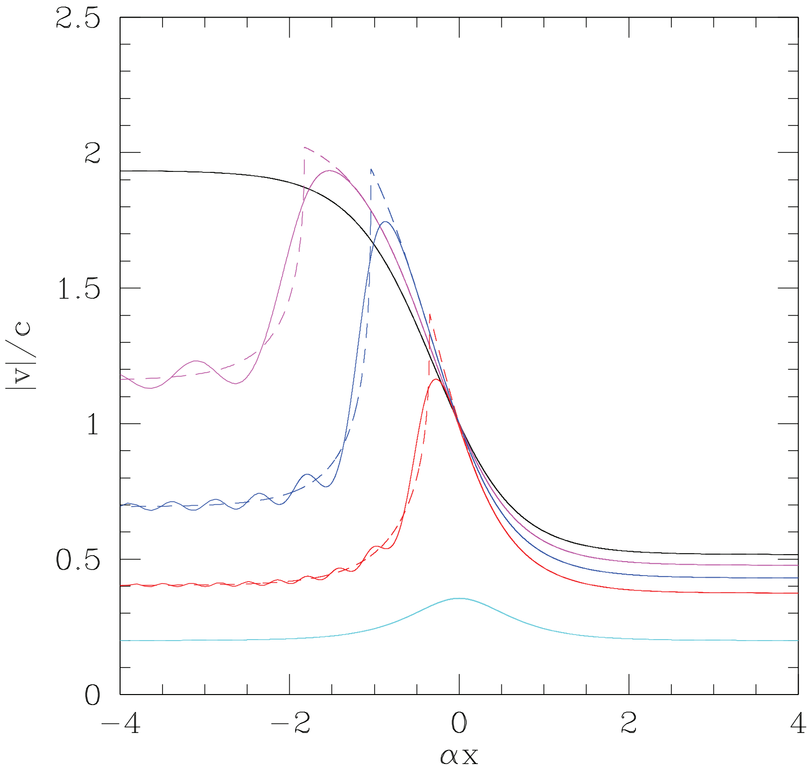

Figure 4.12: Ratio between the absolute value of the fluid velocity and the local sound speed at stationarity for $\alpha = 0.1\,Q$ $k_F = \frac{\pi}{2}\,Q$ and $k_0 = \frac{5\pi}{10}\,Q$ (black curve), $k_0 = \frac{4\pi}{10}\,Q$ (magenta), $k_0 = \frac{3\pi}{10}\,Q$ (blue), $k_0 = \frac{2\pi}{10}\,Q$ (red), $k_0 = \frac{\pi}{10}\,Q$ (cyan). The numerical results are shown in solid curve and they are compared to the analytical expression valid for $\alpha \to 0$ (dashed lines). Note that all the cases obey the condition $Q < k_F + k_0$ while for the black curve $k_F - k_0 = 0$, for the magenta curve $k_F - k_0 = 0.3\,Q$, for the blue curve $k_F - k_0 = 0.6\,Q$, for the red curve $k_F - k_0 = 0.9\,Q$ and for the cyan curve $k_F - k_0 = 1.2\,Q$.

The analytical expressions are able to capture the essential features of the exact solution, showing that the Mach number develops a maximum in the supersonic region while the flow downstream may even become subsonic again (blue and red curves), in close analogy with the case of the step potential (see Fig. (4.4)). After the peak the density profile (and therefore also the Mach number) shows oscillations on a scale $x \sim \alpha^{-1}$ which are washed out in the $\alpha \to 0$ limit. The oscillations disappear both in the fully subsonic regime (cyan curve) and for $k_0 = k_F$, when the Mach number is always monotonic (black curve). From the analytical expressions we can also evaluate the asymptotic uniform density and velocity in the far upstream region $x \to +\infty$: while in the subsonic case $Q < k_F - k_0$ the asymptotic density and velocity remain unchanged during the quench ($\rho_+ = \frac{k_F}{\pi}, v_+ = -\frac{\hbar k_0}{m}$), in the regime of interest

$k_F - k_0 < Q < k_F + k_0$ they become

$$\rho_+ = \frac{k_F + k_0 + Q}{2\pi}\,, \tag{4.19}$$

$$v_+ = -\frac{\hbar}{2m}\left(k_F + k_0 - Q\right). \tag{4.20}$$

Therefore, a hypothetical observer in the far upstream region, unaware of the presence of the potential barrier, would assign an effective value to the key parameters (k_F, k_0) given by

$$k_F^{eff} = \frac{k_F + k_0 + Q}{2}\,, \tag{4.21}$$

$$k_0^{eff} = \frac{k_F + k_0 - Q}{2}\,, \tag{4.22}$$

and, thus, an effective Fermi distribution limited by the two Fermi momenta

$$\begin{aligned} -k_F^{eff} - k_0^{eff} &= -k_F - k_0\,, \\ k_F^{eff} - k_0^{eff} &= Q\,. \end{aligned} \tag{4.23}$$

4.3 Analogue Hawking radiation

At this point, we are ready to investigate the occurrence of a thermal phonons flux emerging from the sonic horizon in the stationary state of the model. This will discriminate the presence of the analogue Hawking effect. Before doing so though, there is one important aspect we need to discuss.

In the gravitational framework the quantized scalar field is defined on a pre-assigned background metric while in analogue models the phonon field represents the excitations of the original quantum system (i.e., the HCB flow) providing the analogue metric. Therefore, a faithful correspondence between the gravitational and the analogue model requires that the quasi-particles of the HCB system behave as an independent, free, quantum scalar field. This crucial condition is verified only in the low energy limit, where the elementary excitations are known to behave as free quantum quasi-particles (this fact is more clear if we recall the approach adopted by Bogoliubov to diagonalize the Hamiltonian of the system, which we have described in Section 2.3. For further discussion on this point see, for example, [187]). This requirement is met provided that the potential is extremely smooth, i.e., $\frac{\alpha}{Q} \ll 1$; steep external potential, in fact, will unavoidably excite high energy modes of the HCB gas, introducing a finite lifetime of the elementary excitations and spoiling the correspondence between the phonon gas and the free quantum field. From a gravitational point of view, not respecting the low-energy limit would break the analogy and the Lorentz invariance, introducing non-physical rainbow metrics in the system, as thoroughly discussed in Section 2.6.

Now, let us consider the energy density of a one-dimensional uniform Bose fluid. The presence of a thermal phonon branch is known to exhibit an additive contribution of the form

$$E_{ph}(T) = \int_0^\infty \frac{dk}{2\pi} \frac{\hbar c k}{e^{\beta \hbar c k} - 1} = \frac{\pi}{12} \frac{(k_B T)^2}{\hbar c} \,, \tag{4.24}$$

where the usual phonon dispersion relation $\omega = c\,k$ has been used. Switching to the representation of the HCB in terms of spinless fermions, the same fluid can be described in terms of an effective Fermi-Dirac distribution

$$f_{FD}(k) = \frac{1}{1 + e^{\beta(\epsilon_k - \mu)}} \,, \tag{4.25}$$

leading to a thermal contribution to the energy density,

$$\begin{aligned} E(T) &= \int_{-\infty}^{\infty} \frac{dk}{2\pi} f_{FD}(k)\, \epsilon_k \qquad (4.26) \\ &= E(0) + \frac{\pi}{6} \frac{m}{\hbar^2 k_F} (k_B T)^2 + O(T^4) \,. \end{aligned}$$

In Eq. (4.26) the first term is the ground state energy of the Fermi gas, while the second term equals the thermal energy density of the two phonon branches (one for each Fermi point), as can be easily checked recalling that the sound velocity in a one-dimensional Fermi gas (or a HCB fluid) coincides with the Fermi velocity, $c = v_F = \frac{\hbar k_F}{m}$. This simple observation shows that, in one dimension, there is a one-to-one correspondence between the quantitative description of the one-dimensional HCB system in terms of a phonon gas and that of a fluid of fermionic particles, if only low energy excitations are present.

Moreover, if phonons originate from the sonic horizon and we study the flow in the far upstream region $x \to +\infty$, only quasi-particles with positive wave vectors $k > 0$ will appear while left moving particles (i.e. with $k < 0$) would be unaffected by the Hawking mechanism and remain at zero temperature. Therefore, we are led to a very specific expectation for the effective momentum distribution of the fermions in the region $x \to +\infty$ if analogue Hawking emission occurs: all local physical observables, in fact, should appear as if the Fermi gas was characterized by a momentum distribution of the form (4.25) with $\beta = (k_B T_H)^{-1}$ for $k > 0$ and $\beta = \infty$ for $k < 0$.

Finally, another signature of the particle emission at the horizon due to the Hawking process is related to the existence of quantum correlations between the upstream and the downstream regions, as discussed in Section 2.7. Physically, these correlations originate from the creation of entangled phonon pairs at the horizon propagating in opposite directions. In our microscopic model, we can check also this prediction, by evaluating the density-density correlations in the stationary state:

$$\begin{aligned} h(x,x') &= \frac{\langle \widehat{\rho}(x,t)\widehat{\rho}(x',t)\rangle}{\rho(x,t)\rho(x',t)} - 1 \qquad (4.27)\\ &= -\frac{\left|\int_{-k_F-k_0}^{k_F-k_0} dk\, \psi_k^*(x,t)\, \psi_k(x',t)\right|^2}{\rho(x)\rho(x')}, \end{aligned}$$

where the local density $\rho(x) = \langle \widehat{\rho}(x,t)\rangle = \langle \widehat{\psi}^\dagger(x,t)\widehat{\psi}(x,t)\rangle$ is defined in Eq. (4.9). We now turn to the evaluation of these properties for the representative choices of potentials previously introduced.

4.3.1 The case of a step potential

Let us start from the case of a step potential. As already mentioned, in the far upstream region $x \to +\infty$ the asymptotic wave function $\psi_k(x,t)$ (4.8) simplifies and it becomes the superposition of an incident and a reflected plane wave regardless of the form of the potential. In the specific, the exact expression for a step potential is

$$\psi_k(x,t) \to \begin{cases} \frac{1}{\sqrt{2\pi}} \frac{2k}{k+\sqrt{k^2-Q^2}}\, e^{ix\sqrt{k^2-Q^2}}\, e^{-i\frac{\hbar k^2}{2m}t} & \text{for } k > Q \\ \frac{1}{\sqrt{2\pi}} \left[e^{ikx} - \left(\sqrt{1+\frac{k^2}{Q^2}} + \frac{k}{Q}\right)^2 e^{-ikx}\right] e^{-i\frac{\hbar(k^2+Q^2)}{2m}t} & \text{for } k < 0 \end{cases}, \qquad (4.28)$$

while for $0 < k \le Q$ the wave function is exponentially small at $x \to +\infty$. When the quantum average of a physical quantity is evaluated starting from this expression, the asymptotic result at large x can be formally written according to Eqs. (2.82), (2.83). Disregarding the interference term between the two counter-propagating waves whose contribution vanishes for $x \to +\infty$, the asymptotic form coincides with that of a uniform free Fermi gas characterized by an effective momentum distribution $f(k)$ given by:

$$f(k) = \begin{cases} 1 & \text{for } -k_F - k_0 < k < K \\ \left(\frac{p-k}{Q}\right)^4 & \text{for } K < k < k_F + k_0 \end{cases}, \qquad (4.29)$$

where we have defined $p = \sqrt{k^2+Q^2}$, $K = \sqrt{(k_F-k_0)^2 - Q^2}$ for $k_F - k_0 > Q$ and $K = 0$ elsewhere. This momentum distribution displays a tail at positive wave vectors, denoting the presence of quasi-particles (phonons) travelling upstream in the stationary state. The analytic form of the tail coincides with the reflection coefficient of the external potential $V(x)$. According to this expression, for $k_F - k_0 > Q$ the flow is purely subsonic, $K > 0$ and the momentum distribution preserves the sharp discontinuity at $k = K$. Conversely, when a supersonic transition is present, $K = 0$ and the two branches of $f(k)$ join smoothly at $k = 0$. Although the qualitative behaviour of the system conforms to the expectations based on the gravitational analogy, the quantitative details do not: a phonon flux is still present even in the absence of a sonic horizon and, most importantly, the "Hawking-like" radiation is never thermal, because the effective distribution differs from the Fermi-Dirac form (4.25). This result denotes a failure of the gravitational analogy, which, being based on semiclassical arguments, is not expected to faithfully represent the actual behaviour of the model when a rapidly varying external potential, like a step, is switched on.

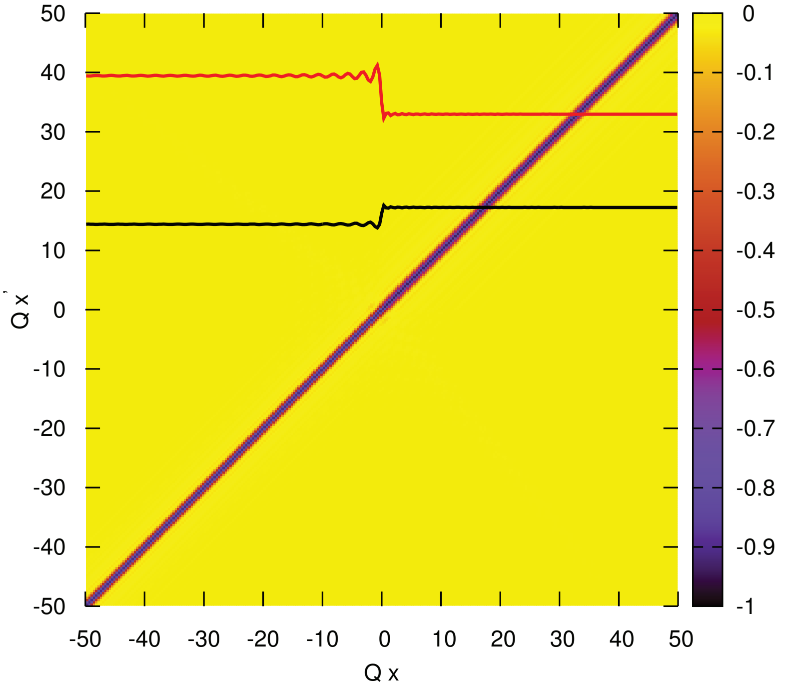

Figure 4.13: Colour density plot of the correlation function (4.27) for a step potential with $k_F = \frac{3\pi}{5} Q$ and $k_0 = \frac{\pi}{5} Q$. The absolute value of the fluid and sound velocities (black and red curves, respectively) are also reported in arbitrary units, to illustrate the absence of a sonic horizon.

This analysis can be generalized for the case of a smooth step of the form $V(x) = \frac{V_0}{2}[1 + \tanh \alpha x]$ where the parameter α controls the sharpness of the potential and the discontinuous step is recovered for $\alpha \to \infty$. By defining $V_0 = \frac{\hbar^2 Q^2}{2m}$ and calculating the reflection coefficient for this case [183], the effective momentum distribution turns out to be

$$f(k) = \begin{cases} 1 & \text{for } -k_F - k_0 < k < K \\ \left[\frac{\sinh\left(\frac{\pi}{2\alpha}(p-k)\right)}{\sinh\left(\frac{\pi}{2\alpha}(p+k)\right)}\right]^2 & \text{for } K < k < k_F + k_0 \end{cases} \tag{4.30}$$

where p and K have been previously defined. We see that the general features of this effective momentum distribution remain unchanged when for a smooth step, even in the limit $\alpha \to 0$, when the phonon tail reduces to $e^{-\frac{2\pi k}{\alpha}}$.

Thus, in the case of an external potential with a step form (sharp or smooth) we have emission of phonons in the far upstream region $x \to +\infty$ from the horizon but the spectrum is never thermal. Furthermore, the emission persists even if a supersonic transition is absent.

The density correlations of the stationary state (4.27) can be easily computed starting from the asymptotic form of the wave functions (4.8). It is interesting to compare the results in the fully subsonic regime $(k_F - k_0 > Q)$ and the ones in the supersonic regime $(0 < k_F - k_0 < Q)$. In Figs. (4.13) and (4.14) the results are shown for the case of a sharp step for two representative choices of the parameters.

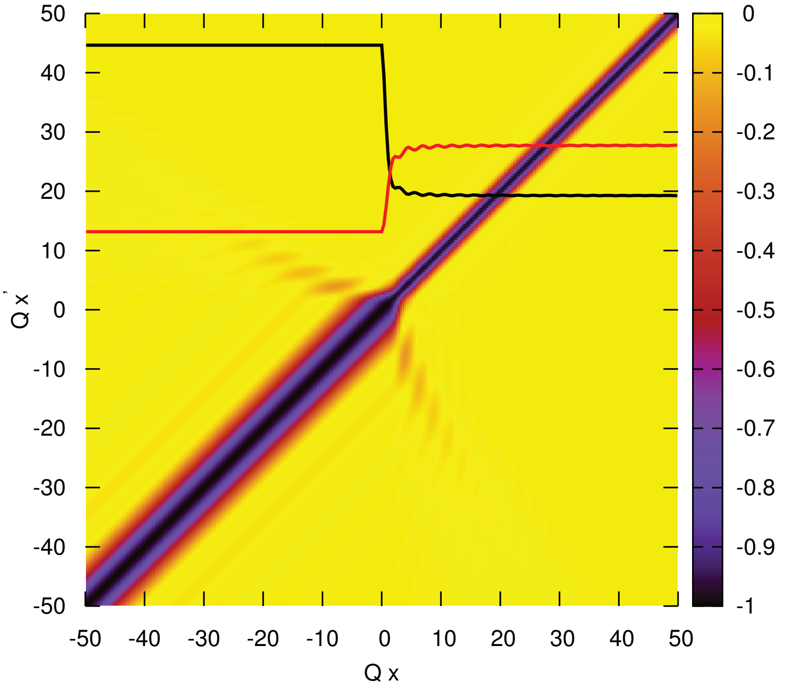

Figure 4.14: Colour density plot of the correlation function (4.27) for a step potential with $k_F = k_0 = \frac{\pi}{5} Q$. The absolute value of the fluid and sound velocities (black and red curves, respectively) are also reported in arbitrary units, to indicate the position of the sonic horizon.

The presence of weak, but clearly-visible, correlations across the sonic horizon in Fig. (4.14) confirms the commonly accepted picture: phonon pairs created at the horizon and propagating upstream and downstream give rise to density correlations between the inner and the outer regions. What is more interesting, though, is that this pattern appears only for a supersonic transition (in contrast to the quasi-particle emission which is always present) but it emerges even though the radiation emitted is not thermal.

4.3.2 The case of a repulsive barrier

For the repulsive barrier (4.11) the asymptotic wave function ψ_k in the upstream region $x \to +\infty$ takes the form

$$\psi_k(x) = \begin{cases} \frac{1}{\sqrt{2\pi}}\, T_k\, e^{ikx} & \text{for } k > 0 \\ \frac{1}{\sqrt{2\pi}} \left[e^{ikx} + R_k\, e^{-ikx} \right] & \text{for } k < 0 \end{cases}, \tag{4.31}$$

where we have omitted an overall time dependent phase factor. Furthermore

$$T_k = \frac{\Gamma(\frac{1}{2} - i\frac{|k|+Q}{\alpha})\Gamma(\frac{1}{2} - i\frac{|k|-Q}{\alpha})}{\Gamma(1 - i\frac{|k|}{\alpha})\Gamma(-i\frac{|k|}{\alpha})}, \tag{4.32}$$

$$R_k = \frac{\Gamma(i\frac{|k|}{\alpha})\Gamma(\frac{1}{2} - i\frac{|k|+Q}{\alpha})\Gamma(\frac{1}{2} - i\frac{|k|-Q}{\alpha})}{\Gamma(-i\frac{|k|}{\alpha})\Gamma(\frac{1}{2} - i\frac{Q}{\alpha})\Gamma(\frac{1}{2} + i\frac{Q}{\alpha})}, \tag{4.33}$$

are the transmission and reflection amplitudes. As before, we can consider this asymptotic form as an equivalent Fermi gas with effective momentum distribution $f(k)$ given by

$$f(k) = \begin{cases} 1 & \text{for } -k_F - k_0 < k < k_F - k_0 \\ |R_k|^2 & \text{for } k_F - k_0 < k < k_F + k_0 \end{cases}, \tag{4.34}$$

with

$$|R_k|^2 = \frac{1 + \cosh(2\pi Q/\alpha)}{\cosh(2\pi Q/\alpha) + \cosh(2\pi k/\alpha)}. \tag{4.35}$$

Notice that $f(k)$ is continuous in $k = k_F - k_0$ only for $k_F = k_0$. For a generic value of $\frac{\alpha}{Q}$, the effective momentum distribution (4.34) differs from the expected Fermi-Dirac form (4.25), which is a sign of the coupling between the quasi-particles (phonons) and the underlying metric (flowing Bose gas). Only for $\frac{\alpha}{Q} \to 0$, i.e. for very smooth barriers, phonons are excited at extremely low energies and quasi-particles behave as a free scalar field. In this limit, the effective momentum distribution acquires the suggestive form

$$f(k) \simeq \frac{1}{1 + e^{\frac{2\pi}{\alpha}(k-Q)}} \tag{4.36}$$

for $k_F - k_0 < k < k_F + k_0$, while $f(k) = 1$ for $-k_F - k_0 < k < k_F - k_0$. This distribution describes a Fermi gas with a sharp jump at the left Fermi point $-k_F - k_0$, while a tail appears for $k > k_F - k_0 > 0$, indicating the presence of excited phonons in the HCB fluid. This, together with the case of a step, is shown in Fig. (4.15). We first note that both in the fully subsonic

($k_F - k_0 > Q$) and in the fully supersonic regime ($Q > k_F + k_0$) the effective Fermi point $k = Q$ lies outside the interval where Eq. (4.36) holds. Then, for $\alpha \to 0$, $f(k)$ either vanishes (for $k_F - k_0 > Q$) or is identically equal to one (for $Q > k_F + k_0$). In both cases the effective distribution for $\alpha \to 0$ coincides with the standard zero temperature result and no phonon flux is present in the HCB fluid at $x \to \infty$. Instead, in the interesting regime where the sonic horizon forms ($k_F - k_0 < Q < k_F + k_0$) we can quantitatively match the result (4.36) with the expected Fermi-Dirac distribution (4.25) at finite temperature. Indeed, let us start from Eq. (4.23) and linearise the energy spectrum near the effective Fermi point $k = Q$, corresponding to the chemical potential $\mu = \epsilon_Q$, giving the quasi-particle dispersion at low energy:

$$\epsilon_k - \mu \simeq \hbar v_{qp} \, (k - Q), \tag{4.37}$$

with quasi-particle velocity $v_{qp} = \hbar Q/m$. Inserting such a form into the Fermi distribution (4.25) we obtain the expression Eq. (4.36) if the effective temperature T_H is given by

$$k_B T_H = \alpha \frac{\hbar^2 Q}{2\pi m}. \tag{4.38}$$

Therefore, as previously discussed, an observer at $x \to +\infty$ will detect a phonon field at the temperature T_H on top of the flowing HCB fluid, given that a sonic horizon is present and if the height of the barrier is smaller than the largest kinetic energy of the fluid particles. Furthermore, since the gravitational analogy subsists, we can test the agreement with Hawking results by comparing the temperature (4.38) with the one which would be obtained by means of the gravitational analogy, i.e.

$$k_B T_H = \frac{\hbar}{2\pi} \frac{d(v - c_s)}{dx} \bigg|_{x = x_h}. \tag{4.39}$$

By use of the asymptotic expression for $\frac{\alpha}{Q} \to 0$, it is easy to check that the sonic horizon is located exactly at the top of the barrier ($x = 0$), where the analogue surface gravity $\kappa = \frac{d(c-v)}{dx}$ can be evaluated as $\alpha \frac{\hbar Q}{m}$, leading, via Eq. (4.39) to exactly Eq. (4.38), in full agreement with the analogue gravity picture. This also shows that $\kappa \to 0$ in the asymptotic limit, implying that the relevant parameter κ/ω_{max}, defying the domain of validity of the gravitational analogy, vanishes as $\frac{\alpha}{Q} \to 0$, satisfying the criterion established in [145]. In fact, we will show that the full excitation spectrum, including the characteristic frequency ω_{max}, remains finite in this limit.

We can also evaluate the density correlations (4.27) on the basis of the analytical form of the scattering states (4.12). A representative result is shown in Fig. (4.16) for $\alpha = 0.1\,Q$ and $k_F = k_0 = \frac{\pi}{5}\,Q$. The fluid velocity in the stationary state is also reported (black line) together with the local sound velocity (red

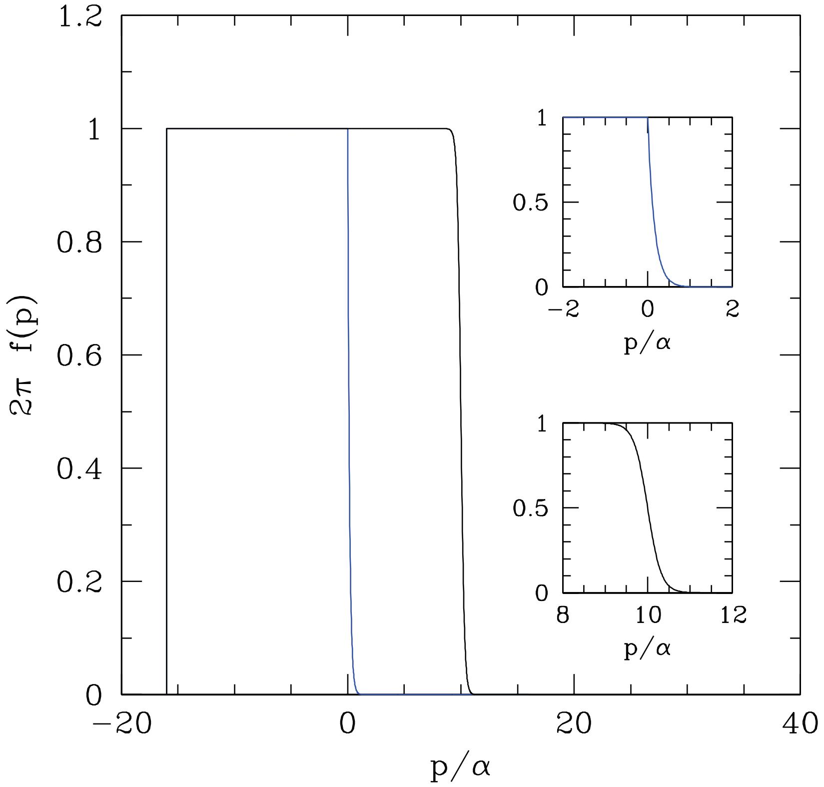

Figure 4.15: Image taken from [69]. Black line: effective Fermi distribution for a barrier defined by $\frac{\alpha}{Q} = 0.1$ with parameters allowing for the presence of a sonic horizon ($k_F = 0.9\,Q$ and $k_0 = 0.7\,Q$). For comparison, the effective Fermi distribution for the case of a waterfall potential with the same parameters is also shown (blue line). In the insets a zoom of the two curves in the relevant ranges is reported. We see that an escaping flux of phonons is always present in the far upstream region $x \to +\infty$ although is never thermal in the case of a waterfall potential, while a temperature can be assigned in the case of a barrier potential, but only if a sonic horizon is present. Moreover, the temperature detected is exactly the one predicted by the Hawking effect.

line). In the bottom-right corner a blow-up of the off diagonal correlations is displayed in order to appreciate the presence of the weak signal related to the emergence of the Hawking radiation.

An analytical understanding of the density correlations is possible in the asymptotic region $(x, x') \to \pm\infty$ in the limit $\alpha \to 0$. Specializing to the interesting range of parameters $k_F - k_0 < Q < k_F + k_0$ where the horizon is present and taking advantage of the explicit expressions of the transmission and reflection coefficients (4.32), (4.33), the asymptotic correlations can be written in terms of $k^{\pm} = k_F \pm k_0$ as

- $x \to +\infty$, $x' \to +\infty$. Here the fluid is subsonic and the correlations

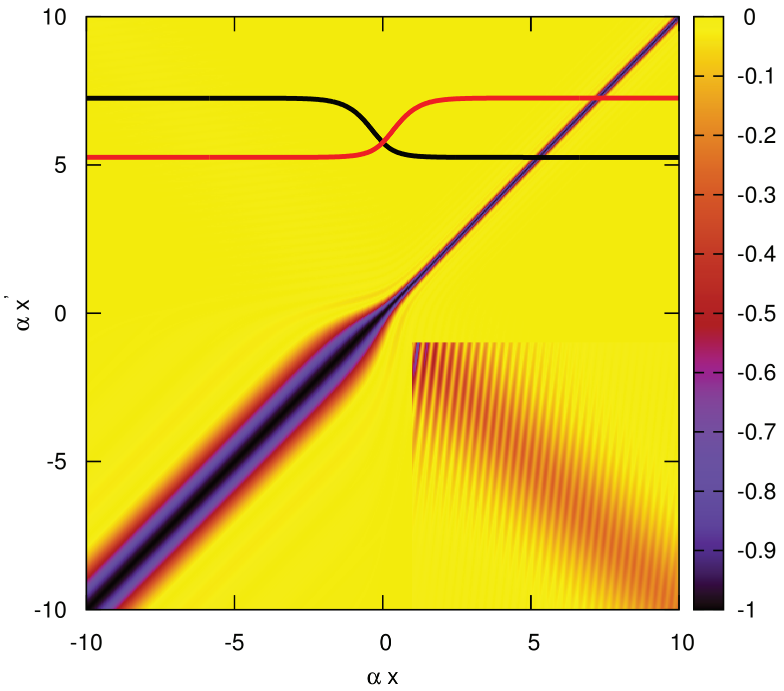

Figure 4.16: Colour density plot of the correlation function (4.27) for a repulsive barrier with $\alpha = 0.1\,Q$ and $k_F = k_0 = \frac{\pi}{5}\,Q$. The absolute value of the fluid (black) and sound (red) velocities are also reported (in arbitrary units) to indicate the position of the sonic horizon. In the bottom-right corner of the figure a blow-up (by a factor 50) of the off-diagonal correlations is shown.

become translationally invariant asymptotically. Setting $s = x - x'$ we obtain, to leading order in α,

$$h_+(s) = -\left[\frac{\sin \frac{k^+ + Q}{2} s}{\frac{(k^+ + Q)\,s}{2}}\right]^2 . \tag{4.40}$$

- $x \to -\infty$, $x' \to -\infty$. In the downstream region density correlations show a more complex structure as a function of $s = x - x'$

$$h_-(s) = -\left|\frac{\sin k^- s + e^{i\frac{k^+ + Q}{2}s}\,\sin \frac{k^+ - Q}{2} s}{\frac{(k^+ + 2k^- - Q)\,s}{2}}\right|^2 . \tag{4.41}$$

- $x \to \pm\infty$, $x' \to \mp\infty$. To leading order in α, the off-diagonal correlations identically vanish far from the horizon. However, a non trivial result appears to second order, proving that density correlations between specular points in the sub- and supersonic regions persist even at large distances

> from the barrier. Setting $u = x + x'$, the asymptotic form of the correlation function is
>
> $$h_{\pm}(u) = -\frac{\alpha^2 \left[\cosh \frac{\alpha u}{2}\right]^{-2}}{4\left(k^+ + Q\right)\left(k^+ + 2k^- - Q\right)} \,. \tag{4.42}$$
>
> Remarkably, this exact result for the Tonks-Girardeau gas reproduces the semiclassical prediction of Ref. [150] obtained in a mean field model where the effective coupling g of the Gross-Pitaevskii equation acquires different values in the upstream and downstream regions.

Thus, in conclusion, a flux of quasi-particles is always present in the far upstream region, regardless of the form of the external potential. Nevertheless, phonons acquire a thermal character with a temperature in agreement with the Hawking emission only if the external potential is a barrier and if a sonic horizon is present. A waterfall potential, in fact, is never a suitable choice for the emission of the analogue Hawking radiation. Finally, the density correlation pattern appears both in the case of a step potential that in the case of a barrier potential.

We will now retrace the derivation of the analogue Hawking effect in this model following the semiclassical prescription, in order to give a complete characterization of the phenomenon and highlight the limit of validity of this approximation.

4.4 Semiclassical analysis

A semiclassical description of the Tonks-Girardeau gas can be obtained considering a Bose fluid in second quantization formalism, described by the Hamiltonian

$$\widehat{H} = \int dx \left\{ \widehat{\psi}^{\dagger}(x) \left(-\frac{\hbar^2}{2m}\frac{d^2}{dx^2} \right) \widehat{\psi}(x) + W \right\} \,, \tag{4.43}$$

where $W = W_c + W_e$ is the sum of a contact term

$$W_c = \frac{g}{\nu} \left(\widehat{\psi}^{\dagger}(x) \right)^{\nu} \left(\widehat{\psi}(x) \right)^{\nu} \tag{4.44}$$

and the linear interaction with an external potential

$$W_e = (V(x) - \mu) \widehat{\psi}^{\dagger}(x) \widehat{\psi}(x) \,. \tag{4.45}$$

For future reference, we consider a generic ν-body interaction so that the usual pair potential corresponds to the choice $\nu = 2$. The bosonic field operator $\widehat{\psi}(x)$ satisfies the canonical commutation relations

$$[\widehat{\psi}(x), \widehat{\psi}^{\dagger}(x')] = \delta(x - x') \,. \tag{4.46}$$

As already done several times, we can decompose the field operator as a sum of a background configuration, described by a complex function $\psi(x)$, and a quantum perturbation so that

$$\widehat{\psi}(x) = \psi(x) + \delta\widehat{\psi}(x)\,, \tag{4.47}$$

provided that $\delta\widehat{\psi}(x)$ satisfies the relations (4.46). Inserting in the Hamiltonian and keeping terms up to order two in the perturbation, we get $\widehat{H} = E + \widehat{H}_1 + \widehat{H}_2$, with

$$\widehat{H}_1 = \int dx\, \delta\widehat{\psi}^\dagger h_1\, \psi + h.c. \tag{4.48}$$

$$\widehat{H}_2 = \int dx \left\{ \delta\widehat{\psi}^\dagger h_2 \delta\widehat{\psi} + \frac{g}{2}(\nu-1)|\psi|^{2\nu-4}\left(\psi^2 \delta\widehat{\psi}^2 + h.c.\right)\right\}\,, \tag{4.49}$$

where E is the reference "classical" energy and

$$h_1(x) = -\frac{\hbar^2}{2m}\frac{d^2}{dx^2} + g|\psi(x)|^{2\nu-2} + V(x) - \mu\,, \tag{4.50}$$

$$h_2(x) = -\frac{\hbar^2}{2m}\frac{d^2}{dx^2} + g\nu|\psi(x)|^{2\nu-2} + V(x) - \mu\,, \tag{4.51}$$

are the first quantization effective Hamiltonians. The stationary background configuration $\psi(x)$ is chosen so that the first order contribution $\widehat{H}_1$ identically vanishes:

$$h_1(x)\psi(x) = 0\,. \tag{4.52}$$

This non-linear differential equation defines the stationary solution in the semiclassical approximation and corresponds, for $\nu = 2$, to the known Gross-Pitaevskii equation for the condensate wave function. While the obvious choice $\nu = 2$ corresponds to the physical many body Hamiltonian (2.79), it has been shown [188] that the semiclassical approximation reproduces the exact spectrum of the strongly interacting Tonks-Girardeau gas in one dimension for the alternate choice:

$$\nu = 3 \qquad \text{and} \qquad g = \frac{\hbar^2\pi^2}{2m}\,. \tag{4.53}$$

These are the values we will consider from now on.

Note that this change in the dynamical equations does not affect the validity of the gravitational analogy. It is possible, in fact, to demonstrate the existence of an effective acoustic metric also starting from this generalized Gross-Pitaevskii equation. The procedure is exactly the one depicted in Section 2.6 and the equations are same except for some small modifications[8] which change the overall conformal factor but do no affect the form of the acoustic metric.

---

[8] In the specific, the term $g\,\widehat{n}_1$ in Eq. (2.86) now becomes $2gn\,\widehat{n}_1$; nevertheless, with the new definition of g and c for this case, the metric acquires the usual form.

4.4.1 The stationary configuration

We will now assume an external smooth potential of the form

$$V(x) = U(\alpha x) \tag{4.54}$$

in the limit $\alpha \to 0$. It is convenient to introduce the dimensionless variable $z = \alpha x$. In order to solve the generalized Gross-Pitaevskii equation (4.52) with ν and g just introduced, we make the Ansatz

$$\psi(x) = A(z)e^{i\phi(z)/\alpha}\,. \tag{4.55}$$

Inserting this form in Eq. (4.52), at first order in α we get the equation

$$2A'(z)\phi'(z) + A(z)\phi''(z) = 0\,, \tag{4.56}$$

where a prime indicate derivative w.r.t. z. This is the mass conservation, which for a stationary flow in one dimension leads to the constancy of the mass current

$$j = \hbar A^2(z)\phi'(z)\,. \tag{4.57}$$

Solving for $\phi'(z)$ and substituting in the zeroth order equation obtained from (4.52) and (4.55), we get

$$A^4(z) = \frac{\mu - U(z) \pm \sqrt{(\mu - U(z))^2 - \sigma^2}}{2g}\,, \tag{4.58}$$

with

$$\sigma = \frac{\pi\hbar j}{m}\,. \tag{4.59}$$

The chemical potential must therefore satisfy the constraint

$$\mu > U(z) + |\sigma| \qquad \forall z\,, \tag{4.60}$$

which allows for two solutions for each compatible choice of μ and j. Recalling that the local velocity $v(z)$ and the sound velocity $c(z)$ for a Tonks gas are

$$v(z) = \frac{j}{m\rho(z)}, \qquad c(z) = \frac{\pi\hbar\rho(z)}{m}\,, \tag{4.61}$$

with equilibrium density $\rho(z) = A^2(z)$, we get for the Mach number $\beta = v/c$

$$\beta(z) = \frac{\sigma}{\mu - U(z) \pm \sqrt{(\mu - U(z))^2 - \sigma^2}}\,. \tag{4.62}$$

The upper and lower signs correspond to a subsonic and a supersonic velocity profile respectively and no transition (horizon) appears in general, for any potential. The only wave function describing a sonic transition is obtained by matching the two solutions at a point z_0 where $\mu = U(z_0) + |\sigma|$. In order to join the solutions keeping $\beta(z)$ real, z_0 must be a maximum for the potential: $U(z_0) = U_{max}$. We can now compare the resulting stationary state of the semiclassical solution with the exact one in the two cases described in the previous Section.

Step potential

Let us consider first a smooth step potential of the form

$$U(z) = \frac{V_0}{2}\left[1 + \tanh z\right] , \qquad U_0 = \frac{\hbar^2 Q^2}{2m} \tag{4.63}$$

in the limit $\alpha \to 0$. In this case there are no local maxima and, then, it is impossible to match the two branches, so we are left with either a fully supersonic or a fully subsonic regime.

When $Q > k_F - k_0$, in the exact solution the Mach number approaches 1 when $x \to +\infty$. Therefore, from (4.62) we have to set $\mu = U_0 + \sigma$. Parametrizing the mass flux in terms of k_F and k_0 as $j = -\frac{\hbar}{4\pi}(k_F + k_0)^2$, we obtain the asymptotic values of the density profile at $z \to \pm\infty$:

$$\rho_+ = \frac{k_F + k_0}{2\pi}, , \tag{4.64}$$

$$\rho_- = \frac{\sqrt{(k_F + k_0)^2 + Q^2} \pm Q}{2\pi} , \tag{4.65}$$

where ± in the second formula correspond to the upper or the lower sign in (4.58). The semiclassical solution reproduces correctly the exact asymptotic density at $+\infty$, while at $-\infty$ it gives the correct profile only for $k_F = k_0$ (choosing the lower sign) or $k_F = k_0 + Q$ (choosing the upper sign).
If $Q < k_F - k_0$ the exact solution is subsonic and we have to choose the upper sign in (4.58) while μ can always be chosen so that the semiclassical solution fully reproduces the exact density profile.

Repulsive barrier

Consider a barrier displaying a unique maximum in z_0:

$$U_{max} = U(z_0) = \frac{\hbar^2 Q^2}{2m} , \tag{4.66}$$

and choose $\mu = \frac{\hbar^2 Q^2}{2m} + |\sigma|$. We can then take the lower sign for $z < z_0$ and the upper sign for $z > z_0$ to get a solution that passes from a supersonic regime on the left of z_0 to a subsonic regime on the right. We can compare this solution with the exact expressions for the potential (4.11) previously discussed. The exact solution shows that a subsonic/supersonic transition is present for $k_F - k_0 < Q < k_F + k_0$. Choosing Q in this range, we parametrize the mass current in terms of k_F and k_0 as $j = \frac{\hbar}{4\pi}[(k_F + k_0)^2 - Q^2]$. The density profile in semiclassical approximation $\rho(x) = A(z)^2$ is monotonic and its asymptotic values at $z \to \pm\infty$ are

$$\rho_\pm = \sqrt{\frac{|j|}{\pi\hbar}} \left(\frac{\mu}{|\sigma| \pm \sqrt{\left(\frac{\mu}{\sigma}\right)^2 - 1}} \right)^{\frac{1}{2}} , \tag{4.67}$$

which for the given values of μ and j give

$$\rho_\pm = \frac{k_0 + k_F \pm Q}{2\pi} \,. \tag{4.68}$$

For a barrier of the form (4.11), ρ_+ coincides with the exact value, while ρ_- is correct only for $k_F = k_0$, when the exact density profile is monotonic. Notice that in this particular case not only the asymptotic values but also also the full density profile coincides with the exact one displaying a sonic horizon at $z = 0$. For future reference we note that the slope of the relative velocity at the horizon $\kappa = \frac{d}{dz}(c(z) + v(z))|_{z=0}$ is $\kappa = \frac{\hbar Q}{m}$. It is interesting to consider also the fully subsonic case $Q < k_F - k_0$, where no matching procedure is required. Correspondingly, we choose the upper sign in (4.58) and set $|j| = \frac{\hbar k_F k_0}{\pi}$. Now μ is unconstrained and if we parametrize μ as $\mu = \frac{\hbar^2}{2m}(k_F^2 + k_0^2)$, we get that the exact density profile is reproduced by the semiclassical solution for any $k_0 < k_F$.

Remarkably, in the fully subsonic case, for both the barrier and the step potential, the exact density profile in the $\alpha \to 0$ limit is always reproduced by the semiclassical one. Instead, if a horizon is present, the semiclassical approximation is correct only for strictly monotonic velocity profiles, i.e. for a very specific (fine tuned) choice of the initial velocity.

Finally, it is worth to mention that we have just looked for the stationary solutions of the semiclassical equations but we have not checked whether the semiclassical dynamics does indeed drive the system towards such a solution. In the Heisenberg formalism the field operator $\widehat{\psi}(x,t)$ evolves in time according to

$$i\hbar \frac{\partial \widehat{\psi}(x,t)}{\partial t} = -[\widehat{H}, \widehat{\psi}(x,t)] \,, \tag{4.69}$$

which, after separating the background configuration from the quantum fluctuations, gives

$$i\hbar \frac{\partial \psi(x,t)}{\partial t} = h_1(x,t)\psi(x,t) \,, \tag{4.70}$$

$$i\hbar \frac{\partial \delta\widehat{\psi}(x,t)}{\partial t} = -[\widehat{H}_2, \delta\widehat{\psi}(x,t)] \,, \tag{4.71}$$

where $h_1(x,t)$ and $\widehat{H}_2(t)$ are formally given by Eqs. (4.49) and (4.51) evaluated in terms of the evolving condensate wave function $\psi(x,t)$. Assuming a uniform condensate $\psi(x) = \sqrt{\frac{k_F}{\pi}} e^{-ik_0 x}$ as initial condition, in the $\alpha \to 0$ limit we can look for a solution of the form

$$\psi(x,t) = \sqrt{\rho(z,t)}\, e^{\frac{i}{\alpha}\phi(z,\tau)} \,, \tag{4.72}$$

expressed in terms of the dimensionless variables

$$z = \alpha x\,, \qquad \tau = \frac{\hbar Q}{m} \alpha t\,. \tag{4.73}$$

The equation of motion for the background field in presence of the barrier (4.11) now becomes

$$Q \frac{\partial \rho}{\partial \tau} = -\frac{\partial}{\partial z} \left[\rho \phi' \right]\,, \tag{4.74}$$

$$Q \frac{\partial \phi'}{\partial \tau} = -\frac{1}{2} \frac{\partial}{\partial z} \left[\phi'^2 + \pi^2 \rho^2 + \frac{Q^2}{\cosh^2 z} \right]\,. \tag{4.75}$$

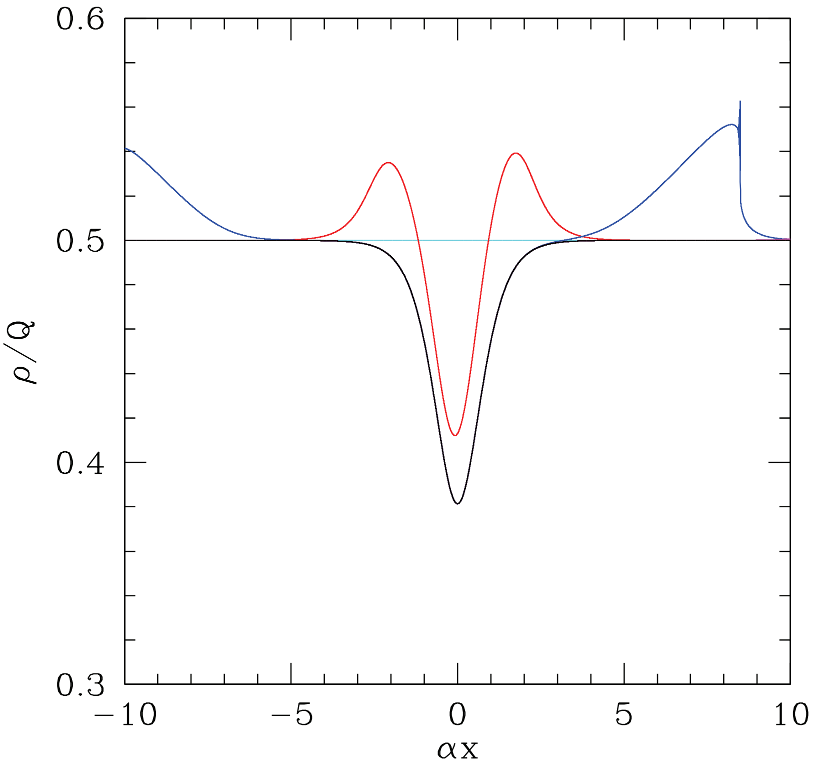

Figure 4.17: Evolution of the density profile for the choice of initial conditions $k_F = \frac{\pi}{2} Q$, $k_0 = \frac{\pi}{15} Q$ obtained by numerical integration of Eqs. (4.74) and (4.75). The density profile converges to the analytical fully subsonic stationary solution (black line). Colours refer to different times: $\tau = 0, 1, 5, 10$, cyan, red, blue, magenta respectively. A localized oscillation is present at $\tau = 5$. The curve at $\tau = 10$ (magenta) is indistinguishable from the stationary solution (black line) in the range shown in figure.

These equations have been numerically solved verifying the approach to the stationary configuration as shown in Figs. (4.17) and (4.18) in the subsonic and supersonic case respectively. The semiclassical dynamics shown in Fig. (4.18)

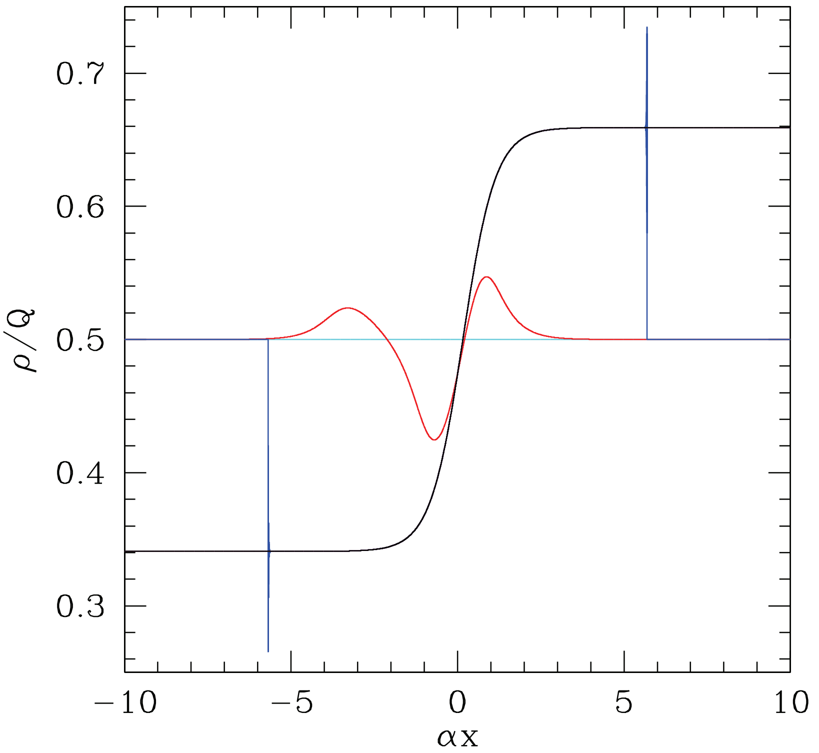

Figure 4.18: Same as Fig. 4.17 for the initial conditions $k_F = k_0 = \frac{\pi}{2}\,Q$. The density profile converges to the analytical fully subsonic stationary solution (black line). Colours refer to different times: $\tau = 0, 1, 10, 20$, cyan, red, blue, magenta respectively. Two shocks (here at $\tau = 10$) develop after the quench and travel towards infinity. The curve at $\tau = 20$ (magenta) is indistinguishable from the stationary solution (black line) in the range shown in figure.

can be compared with the exact one (for a barrier of width $\alpha = 0.1\,Q$) of Fig. (4.10). While in the exact dynamics the density profile is always smooth, in the semiclassical approximation (appropriate for $\alpha \to 0$) two shocks travelling in opposite directions are clearly visible. In both cases, long after the quench, the solution approaches the analytical stationary state profile. Note that in the semiclassical dynamics the time scale for obtaining a stationary state in a given region of space is roughly a factor two smaller than in the exact solution.

4.4.2 The excitation spectrum

According to the semiclassical approach, phonons are expected to be described by the quantum perturbation around the stationary background configuration, governed by the Hamiltonian $\widehat{H}_2$. The strategy is therefore to diagonalize $\widehat{H}_2$

via a Bogoliubov transformation

$$\delta\widehat{\psi}(x) = \int d\lambda \left\{ D_\lambda(x)\widehat{a}_\lambda + E^*_\lambda(x)\widehat{a}^\dagger_\lambda \right\} , \tag{4.76}$$

where the annihilation and creation operators $\widehat{a}_\lambda$, $\widehat{a}^\dagger_\lambda$ satisfy the usual commutation relations

$$[\widehat{a}_\lambda, \widehat{a}^\dagger_\mu] = \delta(\lambda - \mu) , \tag{4.77}$$

whereas the transformation coefficients must be normalized as

$$\begin{aligned} &\int d\lambda \left\{ D_\lambda(x) D^*_\lambda(x') - E^*_\lambda(x) E_\lambda(x') \right\} = \delta(x - x') , \\ &\int d\lambda \left\{ D_\lambda(x) E^*_\lambda(x') - E^*_\lambda(x) D_\lambda(x') \right\} = 0 . \end{aligned} \tag{4.78}$$

The procedure is exactly the one discussed in Section 2.4 but we have now chosen a different notation, so to retrace the one used in the analogue gravity literature. By imposing the diagonalization of $\widehat{H}_2$ in the form

$$\widehat{H}_2 = \epsilon + \int d\lambda \, \hbar\omega_\lambda \, \widehat{a}^\dagger_\lambda \widehat{a}_\lambda , \tag{4.79}$$

where ϵ is the fluctuation energy, we are led to the eigenfunction equations

$$\begin{aligned} h_2(x) D_\lambda(x) + 2g|\psi(x)|^2 \psi(x)^2 E_\lambda(x) &= \hbar\omega_\lambda D_\lambda(x) , \\ h_2(x) E_\lambda(x) + 2g|\psi(x)|^2 \psi(x)^{*2} D_\lambda(x) &= -\hbar\omega_\lambda E_\lambda(x) . \end{aligned} \tag{4.80}$$

Of course, after solving for D_λ, E_λ, and ω_λ, one must impose the normalization conditions (4.78). Notice that if (ω, D, E) is a solution satisfying the normalization condition, then $(-\omega, E^*, D^*)$ is another formal solution of the same equations, but with negative frequency and negative norm. Moreover, a stable equilibrium solution of (4.52) must allow only for positive eigenfrequencies, as discussed in Section 2.4.

The fluctuation energy is expressed in terms of the solution of the eigenvalue problem as:

$$\epsilon = - \int d\lambda \, \hbar\omega_\lambda \int dx |E_\lambda(x)|^2 . \tag{4.81}$$

We can now apply this general procedure to two physically relevant cases: the homogeneous state before the quench and the stationary state solution long after the quench.

Before the quench, in the absence of any external potential, the background configuration is

$$\psi(x) = \sqrt{\frac{k_F}{\pi}} e^{-ik_0 x} , \tag{4.82}$$

corresponding to a uniform density $\rho = \frac{k_F}{\pi}$ flowing with negative velocity $v = -\frac{\hbar}{m}k_0$. Substituting this wave function in the eigenvalue equations, an exact solution for the coefficients $D_p(x)$ and $E_p(x)$ is given by plane waves. Correspondingly the fluctuation operator is

$$\delta\widehat{\psi}(x) = \int_{-\infty}^{\infty} \frac{dp}{N_p} \left[e^{ipx}\widehat{a}_p + \Gamma_p e^{-ipx}\widehat{a}_p^\dagger\right] e^{-ik_0 x}\,, \tag{4.83}$$

$$N_p = \sqrt{2\pi(1-\Gamma_p^2)}\,, \tag{4.84}$$

$$\Gamma_p = \sqrt{\xi^2p^2 + \frac{\xi^4p^4}{4}} - \frac{\xi^2p^2}{2} - 1\,. \tag{4.85}$$

with healing length $\xi = k_F^{-1}$. The dispersion relation for the excitation spectrum is

$$(\omega_p - vp)^2 = c^2\left(p^2 + \frac{\xi^2}{4}p^4\right)\,, \tag{4.86}$$

where $c = \frac{\hbar}{m}k_F$. This form coincides with the known Bogoliubov phonon spectrum in a moving fluid $\omega(p)$ already introduced in Section 2.6.

After the quench, the background solution evolves and at later times is defined by the non-homogeneous asymptotic stationary solution of the generalized Gross-Pitaevskii equation (4.55), (4.57), (4.58). In this state phonons are defined as the normal modes of the fluctuation operator on top of the new background solution. The analysis can be carried out along the same lines followed in the uniform case. In order to solve the eigenfunction equations we make the Ansatz

$$D(x) = D^0(z)e^{i(\phi(z)+\chi(z))/\alpha}, \tag{4.87}$$

$$E(x) = E^0(z)e^{-i(\phi(z)-\chi(z))/\alpha}, \tag{4.88}$$

where we omitted the label λ, and we set, as usual, $z = \alpha x$. Inserting this form in the linear system (4.80), we obtain an algebraic equation for the spatial derivative of the phase $\chi'(z)$:

$$(\omega - v\chi')^2 = c\left(\chi'^2 + \frac{\xi^2}{4}\chi'^4\right)\,, \tag{4.89}$$

where

$$v(z) = \frac{j}{m\rho(z)}\,, \qquad c(z) = \pi\frac{\hbar\rho(z)}{m}\,, \quad \xi(z) = \frac{\hbar}{mc(z)} \tag{4.90}$$

are the velocity profile, the sound velocity and the local healing length respectively. The solution of the secular equation (4.89) gives two branches

$$\omega_\pm = v\chi' \pm c\sqrt{\chi'^2 + \frac{\xi^2}{4}\chi'^4}\,, \tag{4.91}$$

where we omitted the explicit z dependence at right hand side. The corresponding eigenmodes $(D^0_\lambda(z), E^0_\lambda(z))$ are, at fixed ω_λ,

$$E^0_\lambda(z) = \Gamma_\lambda(z) D^0_\lambda(z)\,, \tag{4.92}$$

$$\Gamma_\lambda = \frac{\xi}{c}\left(\omega_\lambda - \frac{\xi c \chi'^2_\lambda}{2} - v\chi'_\lambda - \frac{c}{\xi}\right)\,, \tag{4.93}$$

where the label λ uniquely identifies each solution of the eigenvalue problem and D^0_λ, as determined by the normalization condition (4.78), is

$$D^0_\lambda(z) = \left|\frac{1}{2\pi}\frac{\partial \chi'_\lambda(z)}{\partial\lambda}\right|^{\frac{1}{2}} \left[1 - \Gamma_\lambda(z)^2\right]^{-\frac{1}{2}}\,. \tag{4.94}$$

The normalisation condition leads to the condition $\Gamma^2_\lambda(z) < 1$, which, due to Eq. (4.93), forces the choice of the upper sign in Eq. (4.91). At fixed $\omega > 0$, the analysis of the algebraic equation (4.91) for χ' shows that two solutions are always present both in the subsonic and in the supersonic case. However, in the latter case there are two solutions also for any $\omega > -\omega_{max}(z)$, where

$$\omega_{\max}(z) = \frac{c}{8\xi}\left[3\beta - \sqrt{\beta^2+8}\right]\left[\beta + 4 + \sqrt{\beta^2+8}\right]^{\frac{1}{2}}\left[\beta - 4 + \sqrt{\beta^2+8}\right]^{\frac{1}{2}}, \tag{4.95}$$

and $\beta(z) = \left|\frac{v(z)}{c(z)}\right|$ is the local Mach number. As previously discussed, in the presence of a sonic horizon $\beta(z)$ is monotonic. For negative frequencies $\omega < 0$ the mode amplitude diverges at $z^* > 0$ such that $\omega = -\omega_{\max}(z^*)$ and vanishes for $z > z^*$. This discontinuous behaviour is likely to be an artefact of the $\alpha \to 0$ limit: we expect that for small but non vanishing α the divergence disappears and the mode decays exponentially for $z > z^*$.

The analysis of the Bogoliubov spectrum then shows that the fluctuation operator, long after the quench, is explicitly given in terms of the phonon creation and annihilation operators by

$$\delta\widehat{\psi}(x) = \int \frac{d\lambda}{N_\lambda(z)}\left[\widehat{b}_\lambda + \Gamma_\lambda(z)\,\widehat{b}^\dagger_\lambda\right]\,, \tag{4.96}$$

$$N_\lambda(z) = \sqrt{2\pi\left(1 - \Gamma_\lambda(z)^2\right)}\,, \tag{4.97}$$

$$\tag{4.98}$$

Where $\Gamma_\lambda(z)$ is defined in Eq. (4.93) and $\widehat{b}_\lambda$ and $\widehat{b}^\dagger_\lambda$ are related to the modes $\widehat{a}_\lambda$, $\widehat{a}^\dagger_\lambda$ before the quench by the non-trivial time evolution of the system after switching on the external barrier.

4.4.3 Analogue Hawking radiation

To relate the phonon operator before and long after the quench we have to consider the evolution from the initial uniform flow, at negative times, to the final stationary state long after the sudden switching on of the smooth barrier (4.11). In the Heisenberg picture the state $|\Phi\rangle$ does not evolve and remains the vacuum state of the Bogoliubov modes $\widehat{a}_p$. The fluctuation operator at any time t can be expressed as a linear combination of the bare modes with time dependent coefficients:

$$\delta\widehat{\psi}(x,t) = \int dp \left\{ D_p(x,t)\,\widehat{a}_p + E^*_p(x,t)\,\widehat{a}^\dagger_p \right\} . \tag{4.99}$$

Substituting this expansion into the equation of motion (4.71) we get the equations for the coefficients

$$i\hbar\frac{\partial D_p}{\partial t} = h_2 D_p + 2g|\psi|^2\psi^2 E_p\,, \tag{4.100}$$

$$-i\hbar\frac{\partial E_p}{\partial t} = h_2 E_p + 2g|\psi|^2\psi^{*2} D_p\,. \tag{4.101}$$

with initial condition at $t = 0$ given by (4.83). Looking for a solution that remains regular in the limit $\alpha \to 0$, we are led to the Ansatz

$$D(x,t) = D^0(z,\tau)\, e^{i(\phi(z,\tau)+\chi(z,\tau))/\alpha}\,, \tag{4.102}$$

$$E(x,t) = E^0(z,\tau)\, e^{-i(\phi(z,\tau)-\chi(z,\tau))/\alpha}\,, \tag{4.103}$$

which indeed satisfies the evolution equations (4.101) provided that the local momentum $\chi'_p(z,\tau)$ satisfies

$$-\frac{\hbar Q}{m}\frac{\partial \chi'_p}{\partial \tau} = \frac{\partial}{\partial z}\left(v\chi'_p + c\sqrt{\chi'^2_p + \frac{\xi^2}{4}\chi'^4_p}\right)\,, \tag{4.104}$$

where

$$v(z,\tau) = \frac{\hbar}{m}\phi'(z,\tau)\,, \tag{4.105}$$

$$c(z,\tau) = \pi\frac{\hbar}{m}\rho(z,\tau)\,, \tag{4.106}$$

$$\xi(z,\tau) = \frac{\hbar}{mc(z,\tau)}\,, \tag{4.107}$$

are the time dependent velocity, sound velocity and healing length of the evolving background configuration. $\rho(z,\tau)$ and $\phi'(z,\tau)$ are solutions of the equations (4.74) and (4.75), while the initial condition at the quench $\tau = 0$ is $\chi'_p(z,0) = p$.

For a parameter choice corresponding to a fully subsonic stationary state configuration ($Q < k_F + k_0$) the numerical study of these evolution equations shows that Eq. (4.104) has a smooth, regular solution for both positive and negative quasi-particle momenta p approaching, at long times, the expected positive norm solution (4.91) with the same frequency ω_p (4.86). Two representative examples are shown in Fig. (4.19).

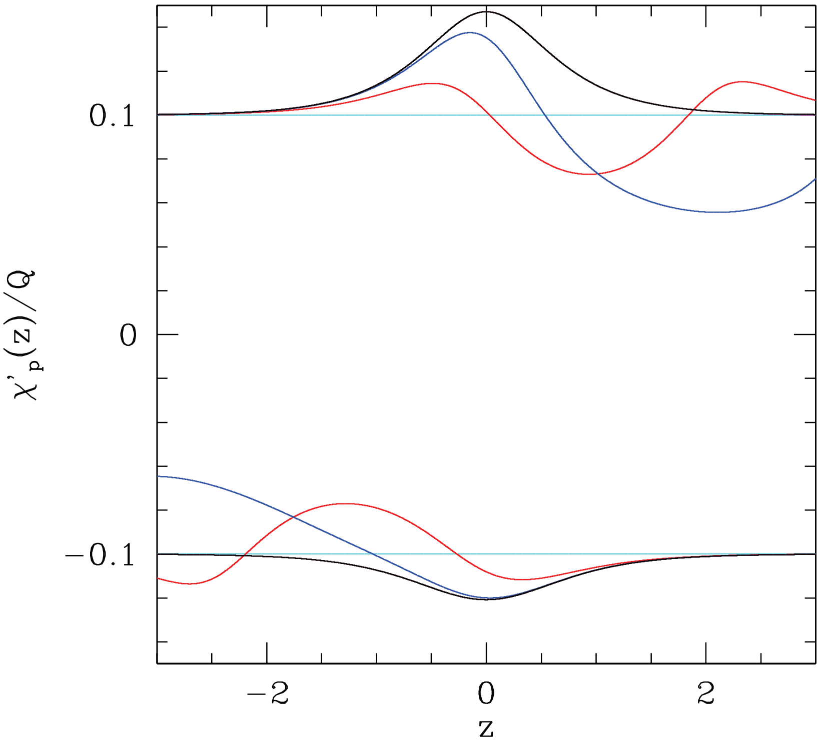

Figure 4.19: Time evolution of the local wave vector after the quench for $k_F = \frac{\pi}{2}\,Q$ and $k_0 = \frac{\pi}{15}\,Q$ according to Eq. (4.104). The upper set of curves correspond to the mode labelled by $p = 0.1\,Q$ at the quench. The lower set refers to $p = -0.1\,Q$. Times are in unit of $\frac{m}{\hbar Q\alpha}$: $\tau = 0$ (cyan), $\tau = 1$ (red), $\tau = 2$ (blue) and $\tau = 6$ (magenta). The last line is not visible on the plot because, in the region displayed in the figure, it coincides with the normal mode of the stationary solution (4.91) corresponding to the same frequency ω_p, shown in black.

In this case we conclude that $\widehat{b}_\lambda = \widehat{a}_p$, with $\omega_\lambda = \omega_p$, so the bare operators coincide with the proper normal modes also in the final stationary solution. The behaviour is qualitatively unchanged also when a sonic horizon forms in the background solution (i.e. for $k_F - k_0 < Q < k_F + k_0$), provided the quasi-particle momentum p is negative. Instead, for positive p the numerical solution of the differential equation (4.104) shows the emergence of singularities, implying that the above Ansatz does not correctly describe the actual evolution of the phonon modes.

A careful numerical study shows that just after the quench, while the background configuration approaches the stationary solution in a neighbourhood of $z = 0$, the excitations $D_p(z,\tau)$, $E_p(z,\tau)$ are regular and $\chi'_p(z,\tau)$ preserves the sign of its initial condition $\chi'_p(z,0) = p$, as illustrated in Fig. (4.20). Singularities develop later in time, suggesting that the bare phonon operators $\widehat{a}_p$ differ from the normal modes defined in the stationary background long after the quench. Thus, in this case, we have to identify the unitary transformation

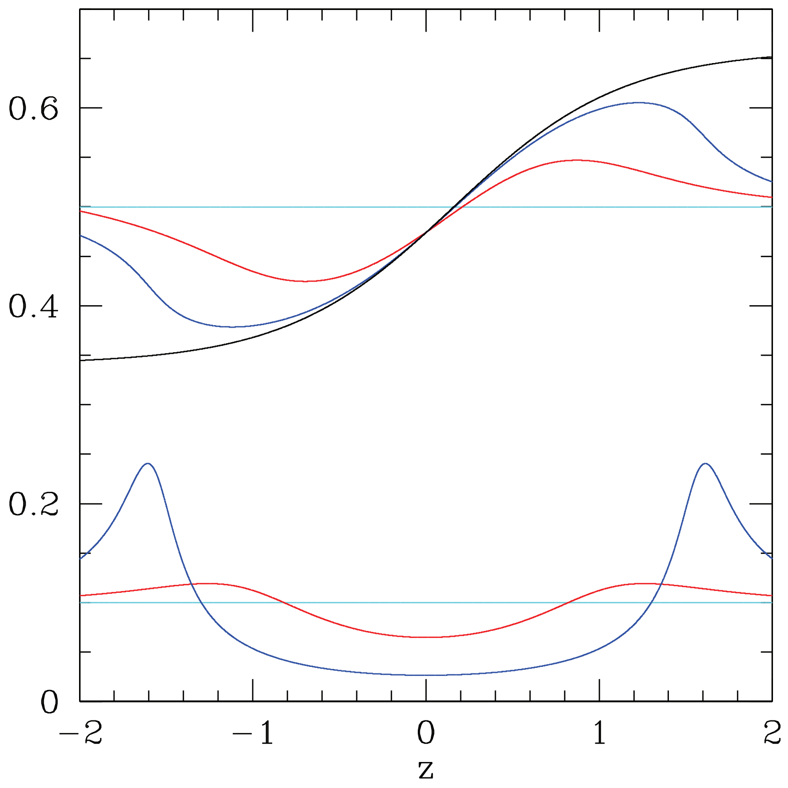

Figure 4.20: Time evolution after the quench for $k_F = k_0 = \frac{\pi}{2}\, Q$ according to the semiclassical dynamics The upper set of curves correspond to the density, the lower set to the local wave vector of the mode labelled by $p = 0.1\, Q$ at the quench. Both density and wave vector are expressed in units of Q. Times are in unit of $\frac{m}{\hbar Q \alpha}$: $\tau = 0$ (cyan), $\tau = 1$ (red), $\tau = 2$ (blue). The density profile at stationary state is shown in black.

relating the initial and the final phonon operators.

To this end we follow the same argument put forward by Hawking in his seminal paper [19], comparing the forward evolution just discussed with the solution of the same equations backward in time, imposing the initial condition at a time $\tau \gg 0$ where the stationary state after the quench has been already reached in a wide portion of space around $z = 0$. The fluctuation field operator can then be expressed at all times either in the form (4.99) or as

$$\delta\widehat{\psi}(x,t) = \int d\lambda \left\{ D_\lambda(x,t) b_\lambda + E^*_\lambda(x,t) \widehat{b}^\dagger_\lambda \right\} . \tag{4.108}$$

Matching these two expressions allows to express the bare modes in terms of the phonon operators long after the quench:

$$\widehat{a}_p = \int d\lambda \left\{ U_{p\lambda} \widehat{b}_\lambda + V_{p\lambda} \widehat{b}^\dagger_\lambda \right\} , \tag{4.109}$$

with

$$U_{p\lambda} = \int dx \left\{ D_p^* D_\lambda - E_p^* E_\lambda \right\} \,, \tag{4.110}$$

$$V_{p\lambda} = \int dx \left\{ D_p^* E_\lambda^* - E_p^* D_\lambda^* \right\} \,. \tag{4.111}$$

In these formulas D and E are functions of both x and t, but the time dependence must disappear in the final expressions. Therefore, we can choose a convenient time to evaluate the transformation matrices. We fix an optimal time τ_0 when the forward evolution after the quench has led the background function to approximate the asymptotic one in a given neighbourhood of $z \sim 0$, let us say $|z| < 0.5$ (see Fig. (4.20)).

To evaluate the unitary transformation (4.111) we have to solve the evolution equations (4.101) both forward and backward in time. It is convenient to consider wave packets of the form

$$\tilde{D}_p(z,\tau) = \int dp' \, f(p'-p) D_{p'}(z,\tau) \,, \tag{4.112}$$

$$\tilde{D}_\lambda(z,\tau) = \int d\lambda' \, g(\lambda'-\lambda) D_{\lambda'}(z,\tau) \,, \tag{4.113}$$

where $f(p)$ and $g(\lambda)$ are weight functions chosen in such a way that, at the initial condition (i.e. $\tau \to -\infty$ for the forward evolution and $\tau \to +\infty$ for the backward one) the wave packet is centred around $z \sim 0$ (i.e. close to the sonic horizon) with momenta p and $\chi'_\lambda(z=0)$, respectively. These wave packets are expected to move away from $z = 0$ with a group velocity given by the derivative of the frequency with respect to the wave vector. Now we have to evaluate expressions like

$$\int dz \, \tilde{D}_p^*(z,\tau_0) \, \tilde{D}_\lambda(z,\tau_0) \,, \tag{4.114}$$

entering the transformation matrices. Note that in order to give a significant contribution to the integral, both wave packets, at time τ_0, must be localized the same region. However, during the time evolution from the initial condition up to the matching time τ_0, the wave packet $\tilde{D}_\lambda$, that moves backward in time, will proceed to the right because waves cannot propagate upstream after the sonic horizon, at least at long wavelengths. Analogously, $\tilde{D}_p^*$, moving forward in time will be dragged inside the black hole. The only possibility to find both $\tilde{D}_\lambda$ and $\tilde{D}_p^*$ centred in the same region is to require that both group velocities are vanishingly small, i.e. that the momenta p and $\chi'_\lambda(z=0)$ are positive and small. For this choice of parameters we can assume that $D_\lambda^0(z,\tau_0)$ is still well-approximated by its value long after the quench, i.e. by the expression (4.94) appropriate for the normal mode corresponding to the stationary state solution

(4.55), (4.57) and (4.58). For $\omega_\lambda \sim 0$, $z \sim 0$ and $\chi'_\lambda(z) > 0$ we get

$$\chi'_\lambda(z) \sim \frac{\omega_\lambda}{\kappa z}, \qquad (\omega_\lambda z > 0) \tag{4.115}$$

$$D^0_\lambda(z) \sim \frac{1}{\sqrt{4\pi\xi(0)|\omega_\lambda|}}\,, \tag{4.116}$$

$$\Gamma_\lambda(z) \sim -1 + \xi(0)\,\chi'_\lambda(z)\,, \tag{4.117}$$

where

$$\kappa = \frac{d}{dz}[c(z) + v(z)]\bigg|_{z=0}\,, \tag{4.118}$$

is the analogue surface gravity (recall that in our model $v(z)$ is negative). The divergence of $\chi'_\lambda(z)$ when $z \to 0$ implies that the leading contribution to the integrals defining $U_{p\lambda}$ and $V_{p\lambda}$ comes from such a region, where we can approximate $D^0_p(z,\tau_0) \sim D^0_p(0,\tau_0)$:

$$U_{p\lambda} = C_{p\lambda}\int_{-\infty}^{\infty} dz\, e^{\frac{i}{\alpha}\left(\frac{\omega_\lambda}{\kappa}\log|z| - \chi'_p(0)z\right)}\,, \tag{4.119}$$

$$V_{p\lambda} = -C_{p\lambda}\int_{-\infty}^{\infty} dz\, e^{-\frac{i}{\alpha}\left(\frac{\omega_\lambda}{\kappa}\log|z| + \chi'_p(0)z\right)}\,, \tag{4.120}$$

$$C_{p\lambda} = \frac{D^0_p(0,\tau_0)}{\alpha\sqrt{4\pi\xi(0)|\omega_\lambda|}}\,, \tag{4.121}$$

which, after integration, give the transformation matrices

$$U_{p\lambda} = -iG^+_{p\lambda}\left|\frac{\chi'_p(0)}{\alpha}\right|^{-\left(1+i\frac{\omega_\lambda}{\alpha\kappa}\right)} e^{\frac{\pi|\omega_\lambda|}{2\alpha\kappa}}\,, \tag{4.122}$$

$$V_{p\lambda} = iG^-_{p\lambda}\left|\frac{\chi'_p(0)}{\alpha}\right|^{-\left(1-i\frac{\omega_\lambda}{\alpha\kappa}\right)} e^{-\frac{\pi|\omega_\lambda|}{2\alpha\kappa}}\,, \tag{4.123}$$

with

$$G^\pm_{p\lambda} = (\text{sign }\omega_\lambda)\,C_{p\lambda}\,\Gamma\left(1 \pm i\frac{\omega_\lambda}{\alpha\kappa}\right)\,. \tag{4.124}$$

Recall that, since we are working in the Heisenberg picture, the ground state $|\Phi\rangle$ is unchanged during the time evolution. However, it is non-trivially related to the vacuum $|0\rangle$ of the phonon operators long after the quench, defined by $\widehat{b}_\lambda|0\rangle = 0$:

$$|\Phi\rangle = e^{-\frac{1}{2}\int d\lambda d\lambda' F_{\lambda\lambda'}\widehat{b}^\dagger_\lambda \widehat{b}^\dagger_{\lambda'}}|0\rangle\,, \tag{4.125}$$

where the symmetric matrix $F_{\lambda\lambda'}$ is defined as the solution of the linear problem

$$\int d\lambda\, U_{p\lambda}\, F_{\lambda\lambda'} = V_{p\lambda'}\,. \tag{4.126}$$

We will demonstrate this equations shortly. Nevertheless, by substituting the previous expressions we finally get

$$F_{\omega\omega'} = \delta(\omega + \omega')e^{-\pi\frac{|\omega|}{\alpha\kappa}}\,, \tag{4.127}$$

and we see that it mixes positive and negative frequencies. The ground state, in terms of the dressed phonon operators, has thus the form of a two mode squeezed state. Notice that the negative frequencies are only defined in the supersonic region and cannot reach the region $z > 0$. By tracing out them [189] we then get a thermal density matrix with the Hawking temperature

$$k_B T_H = \alpha\frac{\hbar\kappa}{2\pi}\,, \tag{4.128}$$

which is the same obtained in the exact solution of the model (4.38).
Let us notice that $|\Phi\rangle$ is written as a linear superposition of excited states including an infinite number of phonons of positive and negative frequencies. Since each pair has zero energy, this combination remains an eigenstate of the fluctuation Hamiltonian $\widehat{H}_2$, which is essential to prove that the asymptotic state is a stationary solution of the evolution equations. Furthermore, we want to stress that this is possible only if a supersonic transition is present, as a subsonic dispersion relation does not allow for such a behaviour of the quasi-particle field.

Before heading to the conclusions, we want to take a little time to prove Eq. (4.125).

Demonstration of Eq. (4.125)

We want to obtain the exact ground state of the quadratic Hamiltonian diagonalized by a Bogoliubov transformation in terms of the original bosonic operators. We will use a discrete notation for simplicity.

Let us define a general Bogoliubov transformation as

$$a_i = U_{i\alpha} b_\alpha + V_{i\beta} b^\dagger_\beta\,, \tag{4.129}$$

where the summation convention is understood and a_i and b_α are bosonic operators related by a canonical transformation defined by the two complex matrices U and V. By imposing that the commutation relations $[a_i, a^\dagger_j]$ are preserved, we find the two conditions

$$UV^T - VU^T = 0\,, \tag{4.130}$$

$$UU^\dagger - VV^\dagger = I\,, \tag{4.131}$$

as already discussed in Section 1.3. Defining $|0\rangle$ the vacuum of the b operators (i.e., $b_\alpha\,|0\rangle = 0$), we want to determine $|\Phi\rangle$, the vacuum of a set of operators a_i

(i.e., $a_i\,|\Phi\rangle = 0$, for a given set of labels i). By writing $|\Phi\rangle = \widehat{X}\,|0\rangle$ we assume that the operator $\widehat{X}$ can be written as

$$\widehat{X} = \sum_{n=0}^{\infty} c_n \left(b^\dagger_\alpha \, X_{\alpha\beta} \, b^\dagger_\beta \right)^n , \tag{4.132}$$

where c_n are complex numbers and $X_{\alpha\beta}$ is a complex and symmetric matrix to be determined. Therefore, the condition is

$$a_i \, \widehat{X}\,|0\rangle = \sum_{n=0}^{\infty} c_n (U_{i\mu} b_\mu + V_{i\mu} b^\dagger_\mu) \left(b^\dagger_\alpha \, X_{\alpha\beta} \, b^\dagger_\beta \right)^n |0\rangle = 0 \, . \tag{4.133}$$

Using the commutation relations and defining $\widehat{K} = \left(b^\dagger_\alpha \, X_{\alpha\beta} \, b^\dagger_\beta \right)$ we obtain

$$\sum_{n=0}^{\infty} \left\{ c_n U_{i\mu} \left(\widehat{K}^n b_\mu + 2n X_{\mu\nu} b^\dagger_\nu \widehat{K}^{n-1} \right) + c_{n-1} V_{i\nu} b^\dagger_\nu \widehat{K}^{n-1} \right\} |0\rangle = 0 \, . \tag{4.134}$$

Since $\widehat{K}$ includes only creation operators, the previous equation implies

$$2n \, c_n U_{i\mu} X_{\mu\nu} + c_{n-1} V_{i\nu} = 0 \qquad \forall n \geq 1 \, . \tag{4.135}$$

By choosing $X = -\frac{1}{2} U^{-1} V$ we get $c_n = 1/n!$, leading to a solution of the form

$$\widehat{X} = e^{-\frac{1}{2}\sum_{\alpha\beta} F_{\alpha\beta} b^\dagger_\alpha b^\dagger_\beta} = e^{-\frac{1}{2} b^\dagger U^{-1} V b^\dagger} , \tag{4.136}$$

which defines our ground state $|\Phi\rangle = \widehat{X}\,|0\rangle$ in terms of the pair wave function F satisfying the matrix equation

$$U_{i\alpha} F_{\alpha\beta} = V_{i\beta} \, . \tag{4.137}$$

These are exactly Eqs. (4.125) and (4.126).

4.5 Experimental configurations

The exhaustive analysis we have just presented refers to the specific case of hard core bosons in one dimension, because only in this limit an analytic solution is available. Although this special system has been already experimentally reproduced several years ago [136, 137], the Tonks-Girardeau limit is rather difficult to obtain due to the tight one-dimensional confinement required. We believe that the strong coupling restriction may be relaxed and the Hawking emission may be seen also under less stringent conditions (see, e.g., [133, 134]). To this aim, we briefly examine the case of a gas of ^{87}Rb atoms confined in a cylindrical trap of radius $a_\perp = 0.25\,\mu$m, as an illustrative example. The trap is assumed to be flat in the longitudinal direction with total length $L \gtrsim 10\mu$m. Let us fix the initial number density of the condensate to $\rho_0 = 3.8\,10^3\,\mu\mathrm{m}^{-1}$ and its initial velocity to $v_0 \sim 18$ mm/s. Now we turn on an external potential of the form $V(x) = V_0\, e^{-(\alpha\, x)^2}$ with $V_0 = \frac{\hbar^2 Q^2}{2m}$ and $\alpha = 0.1\, Q$. The potential amplitude corresponding to $Q = 38\,\mu\mathrm{m}^{-1}$ is $V_0 \sim 3.6\,\mu$K. then, we follow the semiclassical dynamics by integrating the usual (cubic) Gross-Pitaevskii equation in the $\alpha \to 0$ limit. As illustrated in Fig. (4.21) a sonic horizon forms in $x = 0$ and the flow reaches a stationary state in a region of $10\,\mu$m around the horizon after a fraction of a millisecond.

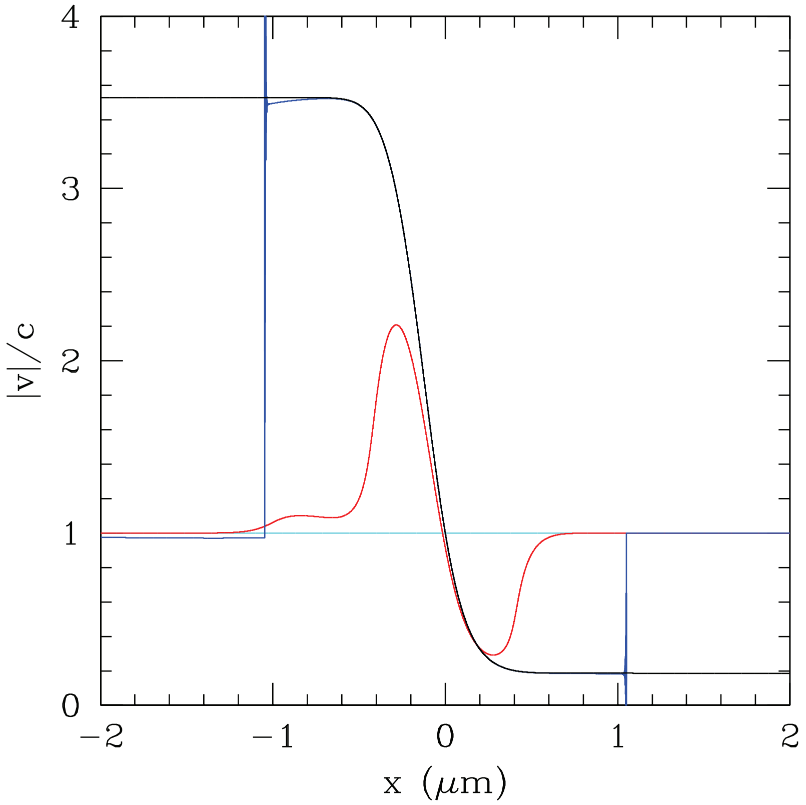

Figure 4.21: Semiclassical time evolution of the Mach ratio after the quench for the parameters discussed in the text. Different colors correspond to different times after the quench: $t = 0$ (cyan), $\tau = 0.02$ ms (red), $\tau = 0.08$ ms (blue), $t = 0.2$ ms (black). The curves gradually approach the stationary state profile in the whole range shown in the figure.

Then, according to Eq. (4.128) we expect the emission of Hawking radiation at a temperature $T_H \sim 100$ nK, which is remarkable. Measuring the momentum distribution in the far upstream region or the density correlations across the horizon, the characteristic signatures of thermal emission should be clearly visible. In an experimental set-up it might be more convenient to maintain the condensate still and move the external barrier, as in the experiments [64–66,96]. This choice is clearly equivalent to the case considered here.

4.6 Conclusions

In this Chapter we have presented the results regarding a flowing Bose gas in the framework of analogue gravity, providing a complete characterization of the analogue Hawking radiation in one-dimensional BECs. Moreover, the results are obtained through a microscopic, exactly solvable model and without relying on the gravitational analogy, something which has not been developed up to date. This also allows to test the limits of validity of the semiclassical methods usually exploited in this field.

In summary, the flow of a fluid past an obstacle is always accompanied by the emission of sound waves in the upstream direction, generally unrelated to the Hawking process. Furthermore, the exact solution shows that the analogue Hawking effect requires additional conditions besides the occurrence of a supersonic transition in the flow: indeed, the obstacle must be a smooth repulsive barrier and the largest kinetic energy of the fluid particles must be bigger than the height of the potential. These conditions rule out other popular choices for the external potential, like the celebrated "waterfall" [65, 66, 96], and emerge as new requirements to be met in order to detect the analogue Hawking radiation in a quantum fluid. In fact, as it was already pointed out [75], if the smoothness condition is not met, finite energy phonons are excited, exposing corrections to the linear dispersion relation and introducing a finite lifetime for the elementary excitations. We have now shown that, even in this case, an observer located far upstream would detect a phonon flux; its energy spectrum, however, would deviate from the predicted thermal distribution which characterizes the Hawking radiation. This result has important consequences in the theoretical interpretation of experiments on flowing condensates. When the previously summarized necessary conditions are satisfied, the thermal character of the analogue Hawking radiation follows directly from the exact solution and reflects in all (static and dynamic) density correlation functions evaluated in the far upstream region. Moreover, weak off-diagonal correlations in the two point function are present even in the limit of smooth potential. While this behaviour is expected in the case of a barrier - where the analogue Hawking radiation appears - it is also found for the case of the step potential, casting doubts on the effectiveness of this probe for the experimental demonstration of the occurrence of the analogue Hawking mechanism.

We also analysed this configuration through a semiclassical approach, showing that the results coincide with the exact solution if the low-energy limit $\alpha \to 0$ is satisfied. While we demonstrate that part of the dynamics is lost in this approximation, the results obtained nevertheless confirm our previous treatment. In particular, the waterfall potential never displays the occurrence of an horizon while an analysis of the excitation spectrum for the case of a barrier potential shows that a thermal flux of phonons with temperature exactly equal to the one predicted by Hawking is emitted in the far upstream region; moreover, the dispersion relation allows the effect to occur only if a sonic horizon is present, as negative frequencies play a key role in the appearance of the radiation.

Finally, we show that a realistic realization of an experimental configuration with a barrier potential would allow for the occurrence of the analogue Hawking radiation with a temperature much higher than the temperature of the gas.

Chapter 5

Future possibilities

In this brief Chapter, we want to illustrate the many open possibilities for future developments of our research. As it is evident from the experimental and theoretical efforts of the past years, the field of analogue gravity (and in particular, of the analogue Hawking effect) is dynamic and very active and this helps the development of new studies and researches. Note that some of the possibilities listed in the following are already under studying at the time of writing, either by author's group or by other teams.

5.1 Including zero-point quantum fluctuations

As we have already mentioned many times, in the past years there have been different attempts at the experimental detection of the analogue Hawking radiation in a BEC sonic black hole [65, 66, 96]. Nevertheless, we still lack a undisputed proof of this phenomenon, as a theoretical interpretation of the experimental data which is consistent with the claims is not available yet. Moreover, the models developed so far have had the effect of disputing some of these assertions, as deeply discussed in Chapter 3. On the other hand, these numerical simulations still lack the fundamental ingredient necessary in order to completely characterize the thermal emission of phonons: that is, a description of quantum fluctuations. Thus, the first and most obvious step needed from a theoretical point of view is the development of a simulation which addresses the challenging problem of including zero-point quantum fluctuations into the theoretical model.

Up to date, a couple of solutions have been developed and they are currently under studying. In fact, the teams of T. Jacobson and J. Steinhauer, who we have mentioned in Chapter 3, have now succeeded in the realization of a fully-quantum simulation of a sonic black hole in a BEC, as they recently announced in a meeting in Haifa[1]. Nevertheless, there are still a few issues regarding their results.

First and foremost, the two numerical models do not completely agree on the results obtained and it is still unclear where the differences lie (i.e., if it is a technical problem or a physical one). Furthermore, the usual way of including quantum fluctuation in a mean-field simulation is to use the Truncated Wigner approximation, which we have mentioned in Section 3.3. This, though, is a non-trivial task as the inhomogeneity of the experimental system adds further complications and, furthermore, the reliability of the technique in these cases is still under debate. We will come back to this point in Section 5.3.

Nevertheless, it is out of question that a development of a quantum numerical simulation is a much needed step in order to unambiguously identify the detection of the analogue Hawking radiation in a BECs.

---

[1] *Analogue Gravity workshop*, *Haifa*, *June 18-20, 2018* (http://phsites.technion.ac.il/analogue-gravity-workshop-2018/).

5.2 The black-hole laser effect: realistic experimental apparatuses

The black-hole laser effect was claimed to be detected in a BEC in 2014 [65] but it was later demonstrated that the phenomena observed in the experimental data were of purely hydrodynamic nature, as deeply discussed in Chapter 3. This achievement immediately led to the quest for a detailed description of an alternative set-up, apt to the observation of this effect; such an experiment would not only give a better insight on the physics of charged black hole but also demonstrate, indirectly, the existence of the Hawking radiation.

The theoretical characterization of such an apparatus requires different steps to be achieved. First of all, one would have to design a longitudinal trap whose shape would allow for two horizons to be present and with characteristics compatible for the effect to happen. Second, there is the challenge of finding a way to bring the system as close as possible to stationary, in order to avoid spurious effects due to the transient nature of the dynamics. Finally, most importantly, there is the need to characterize (and a find a way to trace out) all the possible effects which could mask (or cancel) the black-hole laser effect, like the accumulation of atoms in the region near the horizon, the Bogoliubov-Cerenkov effect and others. Due to the extreme complexity and challenges associated with this kind of experiments, a theoretical insight on how to achieve these goals would be most welcome.

Going further, one last accomplishment could be to determine a way to discriminate the purely quantum laser effect from the semiclassical relative, usually associated with an hydrodynamical instability. For a discussion on how to include quantum fluctuations into the simulations see the previous Section.

Lastly, we need to mention that a work in this direction has been already developed lately [190] but a theoretical characterization which includes the linear effects described in Section 3.4 is still lacking.

5.3 The TG gas model: future directions worth exploring

The Tonks-Girardeau gas model described in Chapter 4 represents an innovative way to approach the matter of the analogue Hawking radiation in Bose-Einstein condensates. As described in the Chapter, thanks to this microscopic, exactly solvable model a different characterization of the Hawking effect in condensed-matter systems can be developed. Our results show, in fact, that further conditions must be met in order to detect a thermal phonon radiation in a sonic black hole (other than the sole occurrence of a sonic horizon) and that the methods currently used (i.e., the density correlation method and the semiclassical approximation) do not completely describe the analogue Hawking effect, as part of the physics is hidden or disregarded.

For these reasons, the first development of this model implicates a deeper understanding of the limit of validity of these approaches. Secondly, it can be employed for a deeper characterization of a realistic experimental set-up, as we have only sketched an raw example so far (see Section 4.5).

Once the fine details of the characterization of the analogue Hawking effect are studied, the horizon of possibilities for this models includes a vast number of effects which could be studied. For example, we could imply the TG model to describe the Dynamical Casimir Effect (DCE) [191], as recent experiments in BECs have tried to characterize [192]. We could otherwise test the limit of validity of the Truncated Wigner method or try to give a better characterization of the black-hole laser effect. Going even further, always in the realm of analogue gravity, we could investigate phenomena related to superfluidity [193], dark matter [194], the state of universe at early times [195] or cosmological particle production (a detailed list on this last aspect can be found in [75]). Nevertheless, it is important to remember that the extension of this model to dimensions higher than (1+1) is challenging.

Conclusions

In this Thesis we have illustrated the results we have obtained in the last years and we attempted a description of the field of the analogue Hawking radiation in Bose-Einstein condensates.

This realm brings together different areas of physics, as it spans from gravitational black holes to the dynamics of quantum fluids. For this reason, a first, fundamental effort, should be devoted to understand the basic concepts from both worlds, trying to find the links connecting the different ideas and to develop one, sole terminology. Even if it does not represent the main purpose of this dissertation, the first Chapters of this Thesis are dedicated to the description of the two realms of physics involved and a particular interest is given in the connection of this two separate worlds. I sincerely hope that the detailed and “from-scratch” approach adopted succeeded in the intent of giving the most complete picture possible, providing the tools necessary in order to grasp the basic notions of the analogue gravity field.

In the following Chapters, we described our researches into details, discussing the two sides of our work which we have developed in the years past. On one side, we have given crucial contributions to the characterization of the experiments that have claimed the first observation of the analogue Hawking radiation in a Bose-Einstein condensate. Moreover, our studies serve also as a starting point for a development of new frameworks in future experimental efforts. On the other hand, through an innovative approach, we have given a complete and new characterization of the analogue Hawking effect in Bose gases, highlighting the limit of validity of the approaches developed up to date and describing the complete set of requirements needed in order to observe this phenomenon. Moreover, this study opens many possibilities for future experimental and theoretical investigations.

At this point we have finally reached the very end. I can only conclude this Thesis hoping the results developed in these years will be of help in understanding a little more of our Nature. In any case, it has been a fascinating journey.

Appendices

Appendix A

The role of the axial confinement

In this Appendix, we discuss the results from the analysis described in Section 3.4. In particular, the different figures refer to the different choices of parameters listed in Fig. (3.19). We study the evolution of the position and of the height of the peaks when we allow the parameters μ and x_0 to vary. We will start from the case of a varying chemical potential.

From the simulations we note that the number of peaks of the standing wave inside the supersonic region does not seem to depend on the number of bosons as it stays the same in the different runs (that is, there are 15-18 fringes, depending on the time one measures). We have also demonstrated (we do not show the results here) that an efficient way to diminish this number is to take a smaller step or a steeper trap. Furthermore, in each run the position of all the peaks changes during the evolution time (Figs. (A.1)). In particular, they all move to the left according to some law which appears to be the same in the different runs; moreover, after an initial time (which decreases as we study the more inner peaks) it seems that the velocity becomes constant. Two things are also interesting to notice: first, this evolution appears to be qualitatively the same for the peak inside the supersonic region and the one outside; second, the peaks all converge to the same position as time passes; the former feature is obvious from the plots of the position of the different peaks as time passes for a given chemical potential (Figures (A.3)).

As far as the height of each peak, the Figures (A.2) show that each peak rises as time passes but the slope of the line (i.e. the velocity of the growth) increases as we increase the chemical potential. Interestingly, the peak outside the lasing region appears to behave differently from the ones inside the lasing region (Figures (A.4)). Finally, the oscillations that appear after a certain time are due to the interference of the wave with itself once it is scattered back by the black-hole horizon.

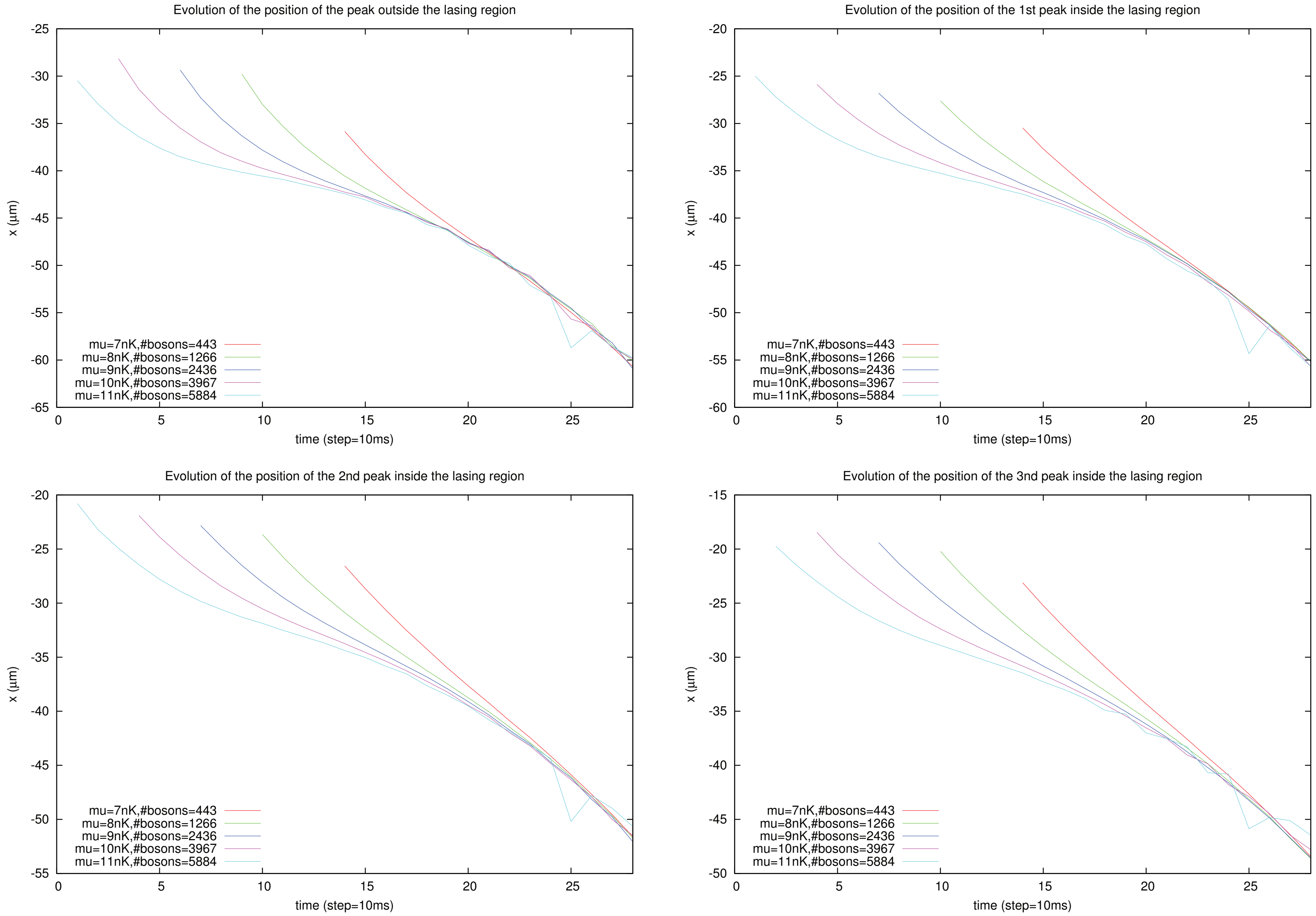

Figure A.1: The evolution of the position of a single peak as μ changes.

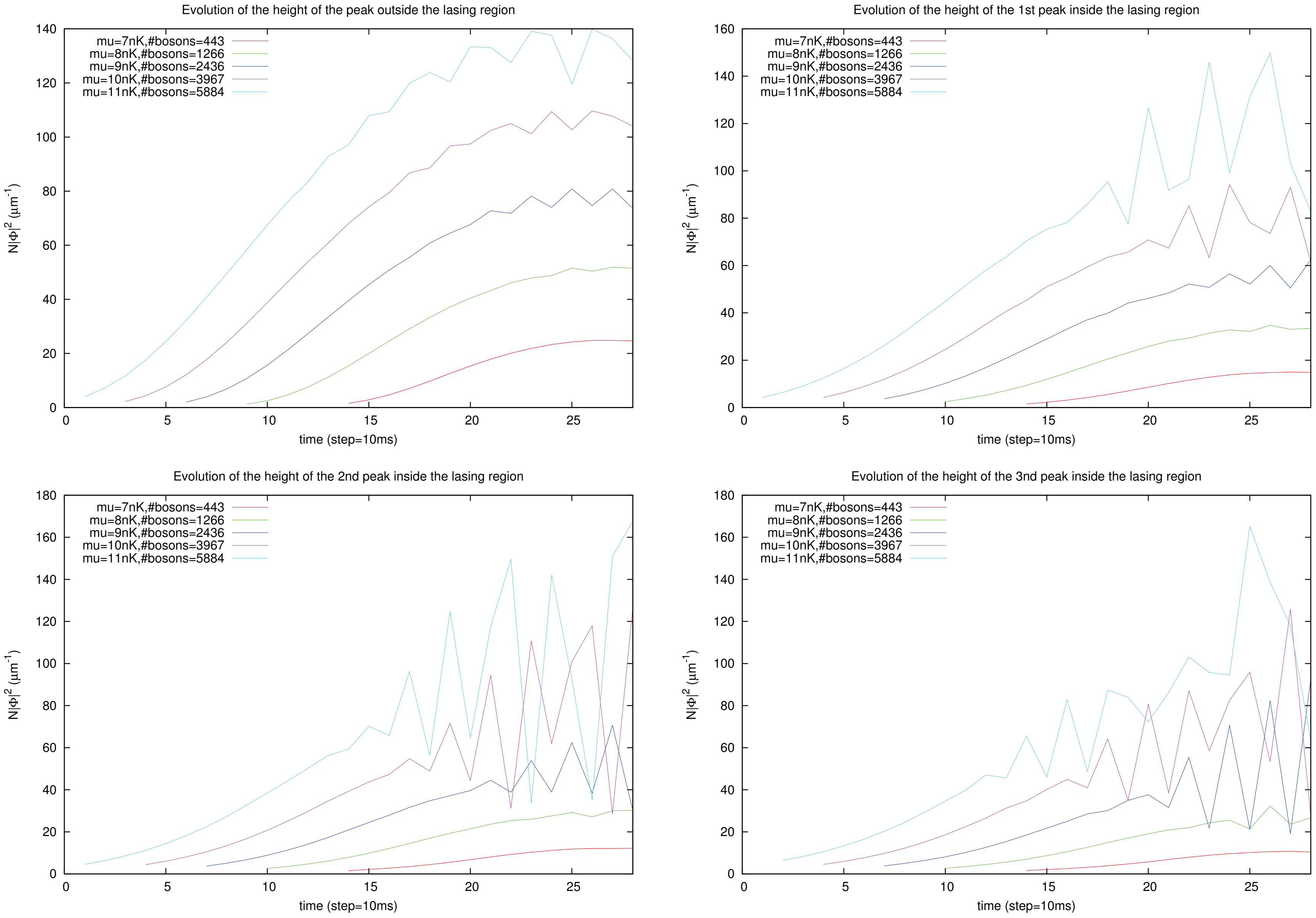

Figure A.2: The evolution of the height of a single peak as μ changes.

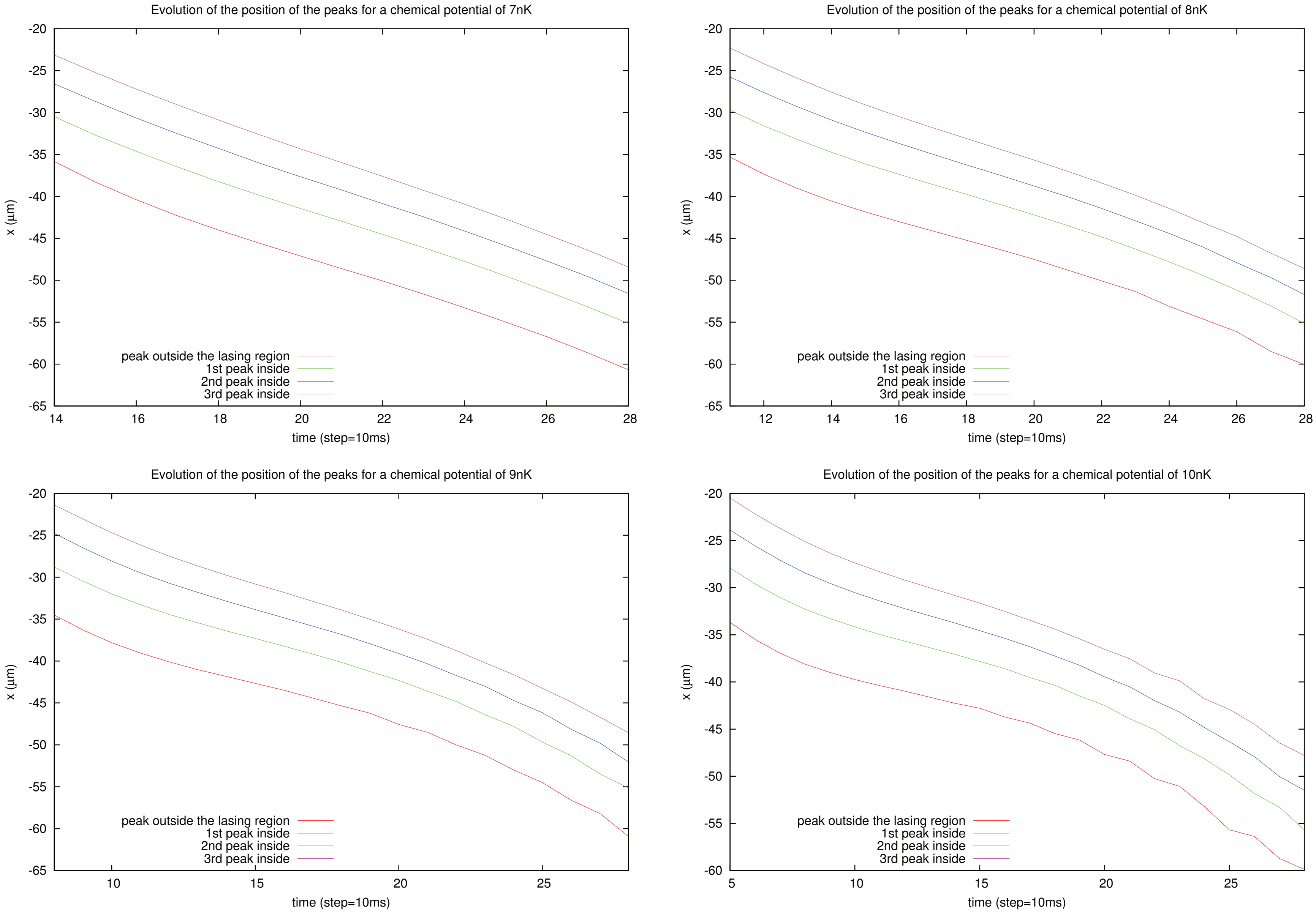

Figure A.3: The evolution of the position of the different peaks with μ fixed.

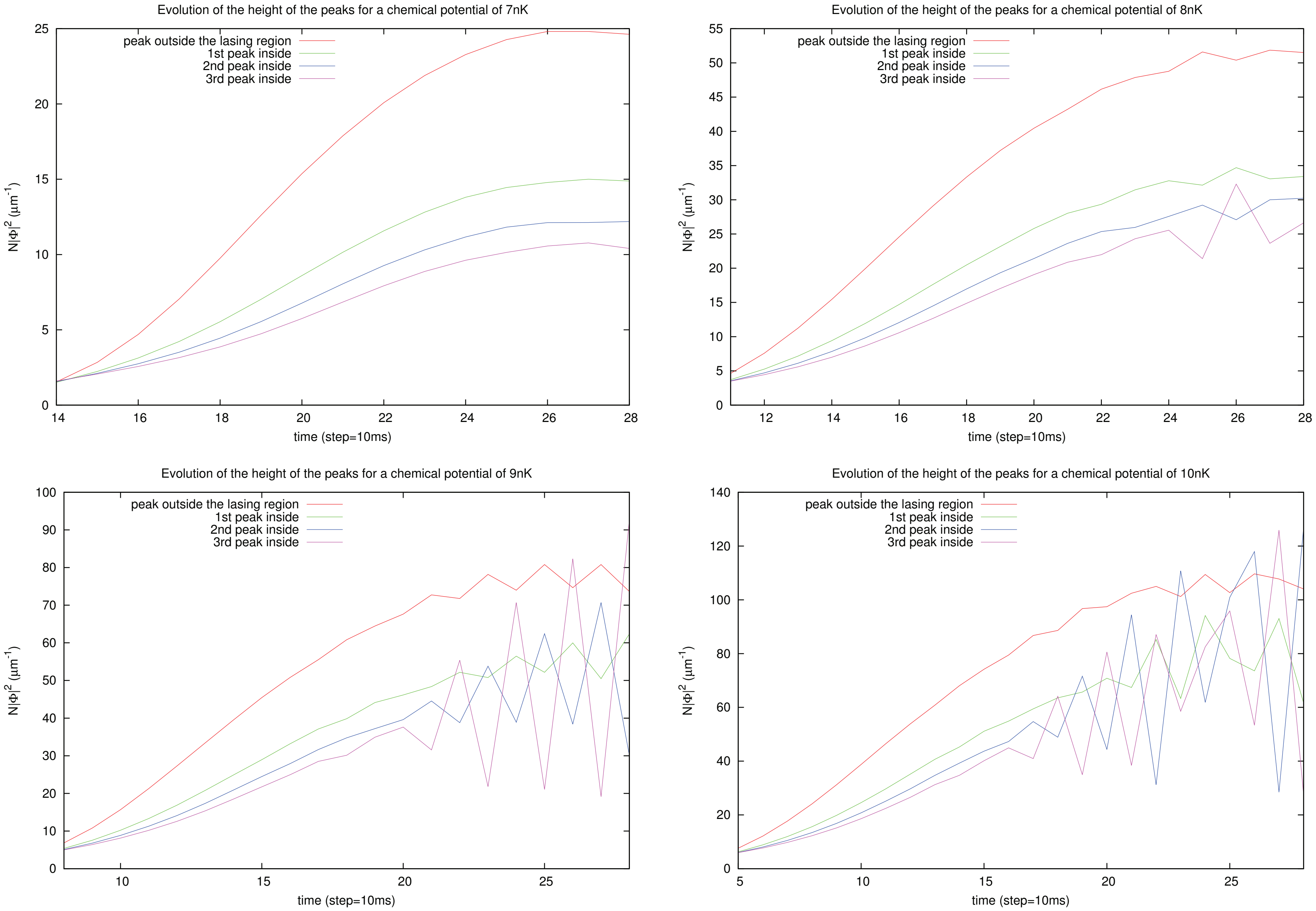

Figure A.4: The evolution of the height of the different peaks with μ fixed.

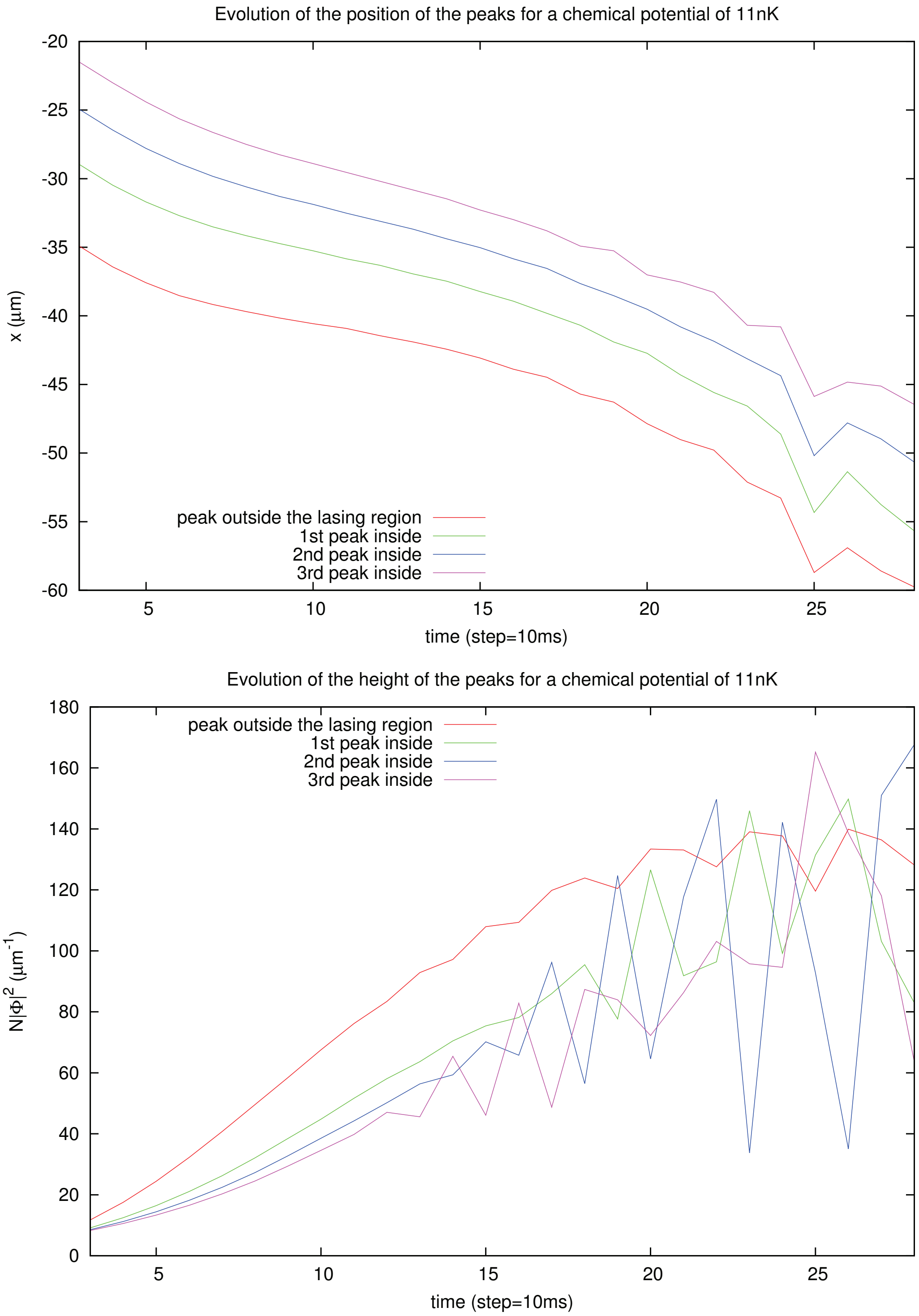

Figure A.5: The evolution of the position and of the height of the different peaks with $\mu = 11$ nK.

We now turn our attention to the case of varying x_0.

From the density profile evolution we see (we have not shown the results here for simplicity) that the number of peaks inside the supersonic region grows as the trap becomes more shallow. In fact, in the case of $x_0 = 37\mu$m the standing wave pattern inside the supersonic region shows 4-5 peaks, for $x_0 = 57\mu$m there are 8-9 peaks, for $x_0 = 77\mu$m 11-12 peaks, for $x_0 = 97\mu$m we have 14-15 peaks and for $x_0 = 117\mu$m there are 18-19 peaks. So, as we were already pointing out in the previous case, another way to manipulate the number of modes inside the cavity (without changing the height of the step) is to tune the tightness of the longitudinal trap. Another (obvious) consequence of changing the parameter x_0 is that the number of bosons varies in each run. This is due to the fact that the chemical potential stays fixed as the traps becomes larger.

Now, as for the peaks position, all the peaks move to the left with a constant velocity (which is different from the condensate constant velocity). Furthermore it seems that, given a single run, all the peaks move with the same velocity and also between runs, given a single peak, the velocity is the same (Figures (A.6) and (A.8)). This is completely different from the case of a varying chemical potential, where the peaks had similar behaviour given a single run but behaved very differently from run to run; there, in fact, the velocity of a single peak in between runs was different at the initial times (in particular, it was not constant) and then converged to the same position (while here the position of the single peak at the final time changes from realization to realization). This is an effect induced by the shape of the trap, as the number of bosons increases in both cases.

Finally, the height of the peaks shows some interesting features also. First of all, it can be seen how, given a single run, the height of the peak outside the lasing region grows more that the height of the peaks inside the lasing region (Figures (A.9)). This was also visible in the previous runs, when we let the chemical potential vary. Second, if we focus our attention to a single peak, it is evident how this grows to a maximum level (which is the same in every run) before starting oscillating - due to the non-zero mode which appears in the cavity. This is interesting for two reasons: first it shows that a change in the trap changes the velocity of the growth of a given peak; second, this behaviour is, again, different from the case of a varying chemical potential as there a single peak grew faster as the number of bosons increased.

In conclusion, we see that variations in the number of atoms or in the shallowness of the potential cause different behaviours of the standing wave pattern present inside the lasing region.

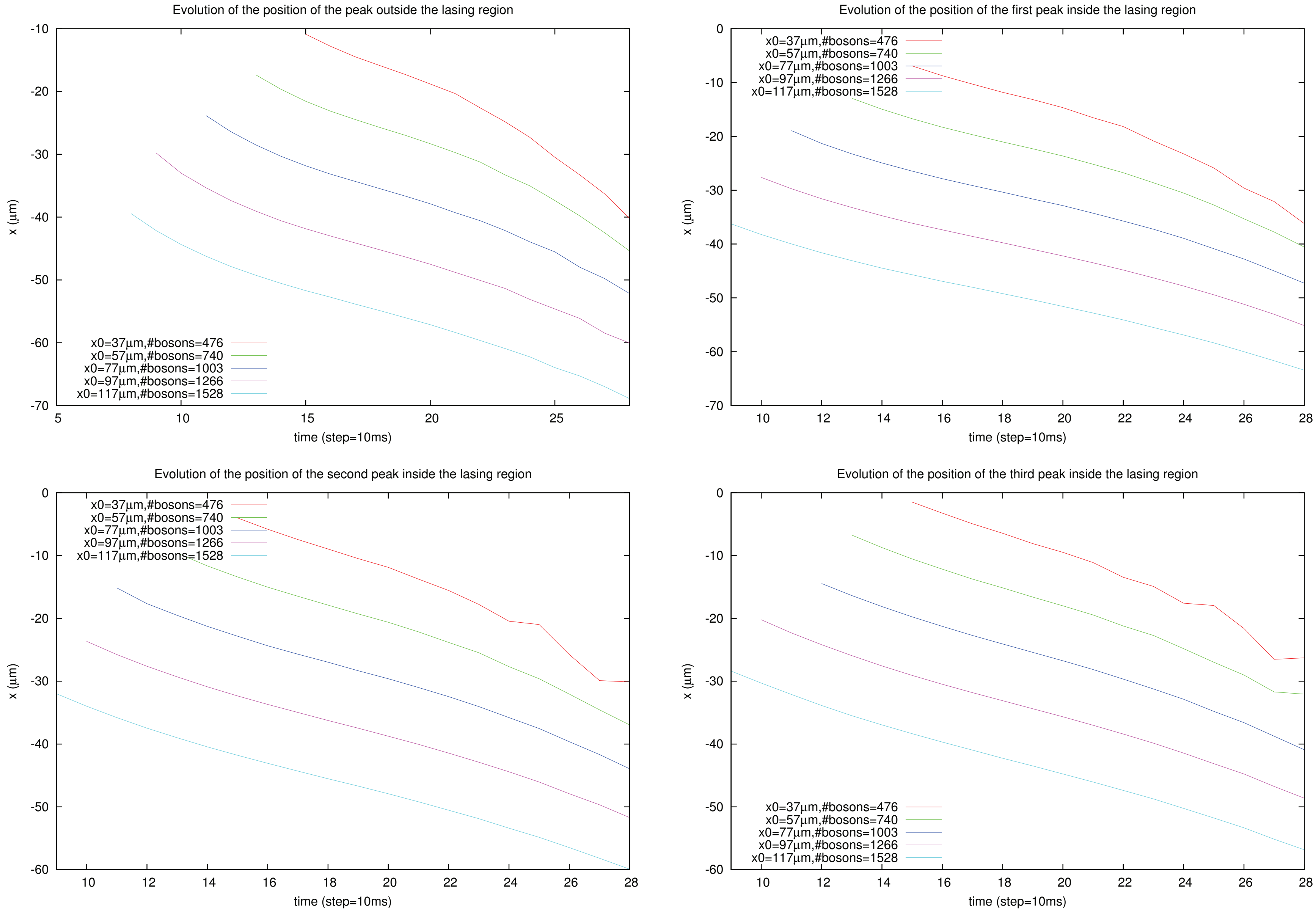

Figure A.6: The evolution of the position of a single peak as x_0 changes.

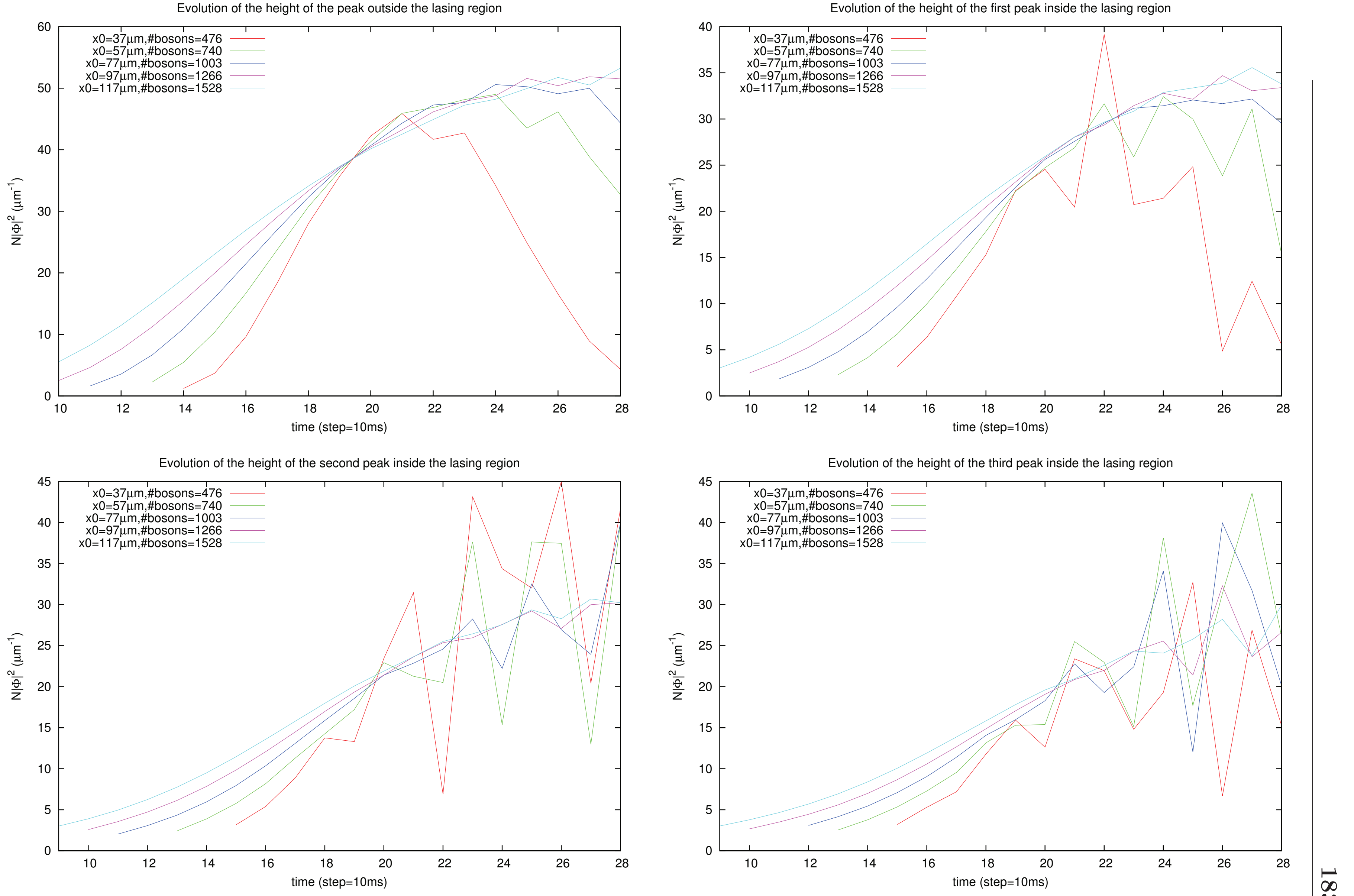
Evolution of the height of the peak outside the lasing region

Evolution of the height of the first peak inside the lasing region

Evolution of the height of the second peak inside the lasing region

Evolution of the height of the third peak inside the lasing region

Figure A.7: The evolution of the height of a single peak as x_0 changes.

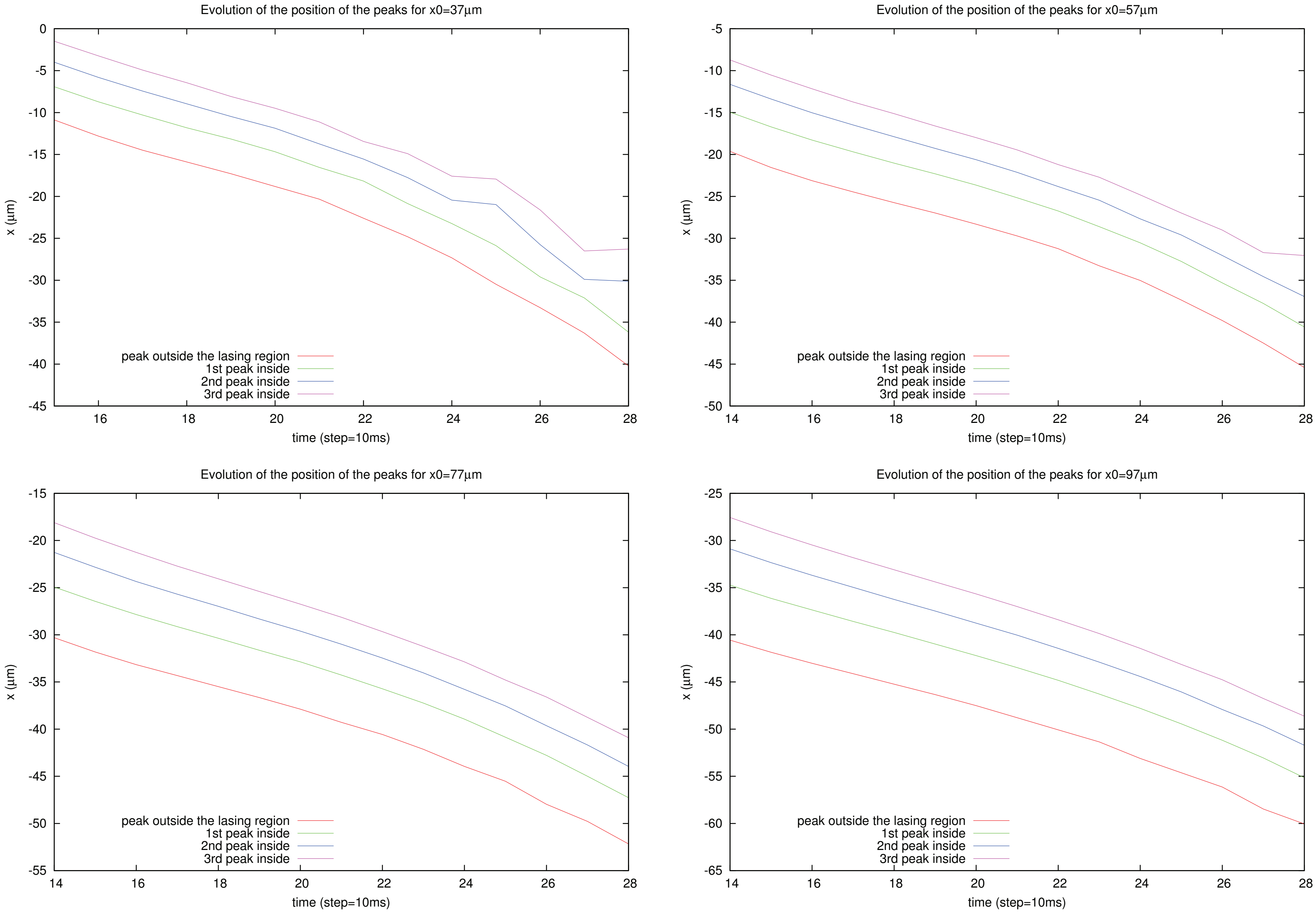

Figure A.8: The evolution of the postition of the different peaks with x_0 fixed.

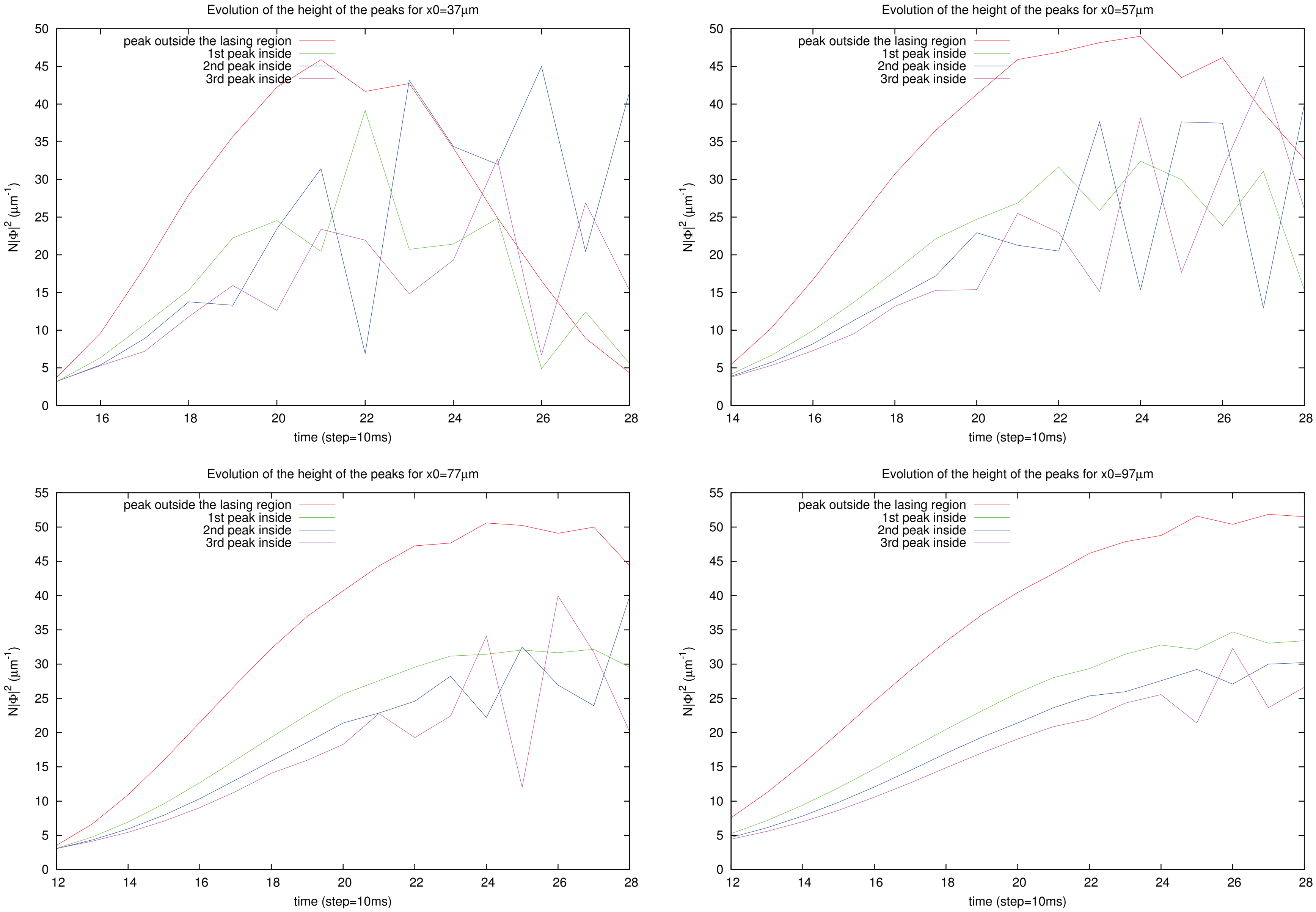

Figure A.9: The evolution of the height of the different peaks with x_0 fixed.

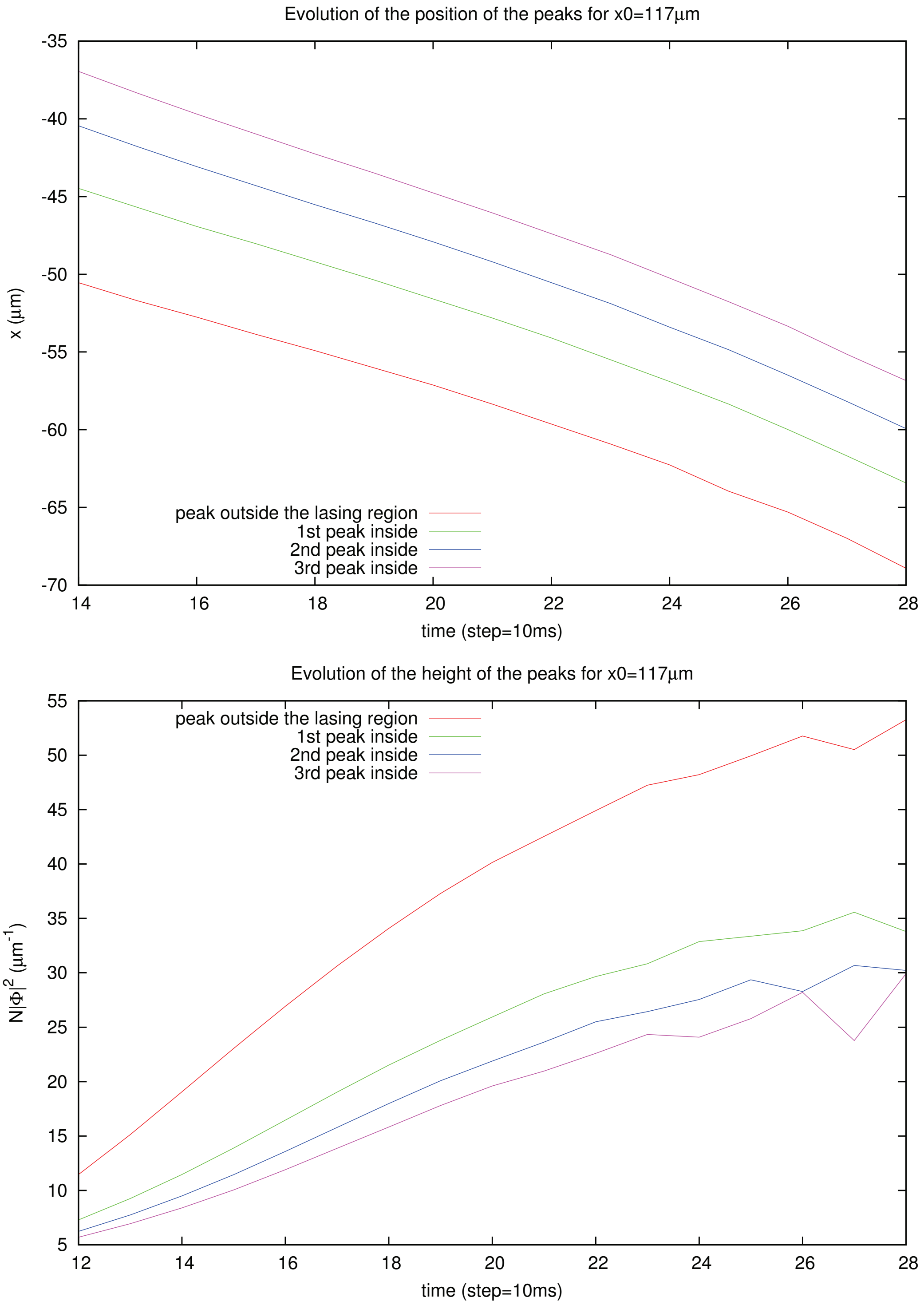

Figure A.10: The evolution of the position and of the height of the different peaks with $x_0 = 117\mu$m.

Finally, we check that the relation theorized in [93, 94] (i.e. Eq (3.24)) for the growth of the peaks holds when we vary the trap parameter x_0. Recall that we label the peak outside the supersonic region n_P (it is the first peak from the left). To the right of this peak the supersonic region begins and we name n_1 the first peak/maximum from the left, n_2 the first valley/minimum from the left (the one between n_P and n_1) and n_3 the second valley/minimum from the left (the one to the right of n_1). Then we see that the strength of the obstacle is just n_P, the actual height of the first peak inside the supersonic region is $N = n_1 - \frac{1}{2}(n_2 + n_3)$ and the background density can be taken as $n_M = (n_1 + n_2)$ approximately. Thus, if the scenario depicted in [93, 94] is correct, we should obtain that $N/(n_P \cdot n_M)$ is constant. The following Figures show three different combinations of the aforementioned parameters for the values of x_0 listed in Fig. (3.19).

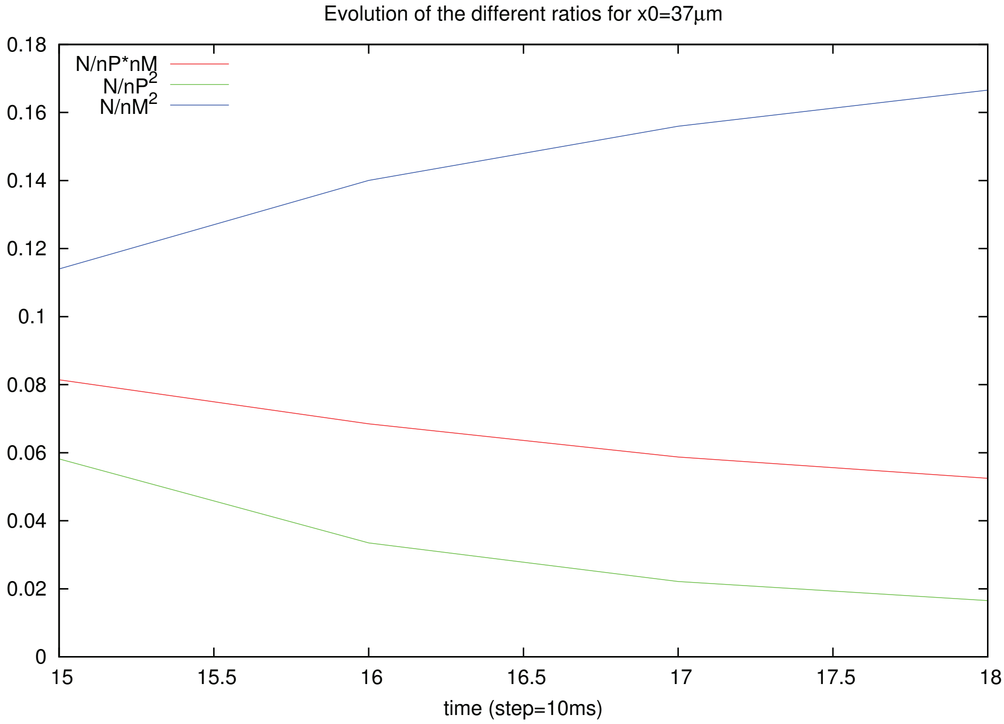

Figure A.11: The evolution of the different ratios studied in Section 3.3.2 when $x_0 = 37\mu$m.

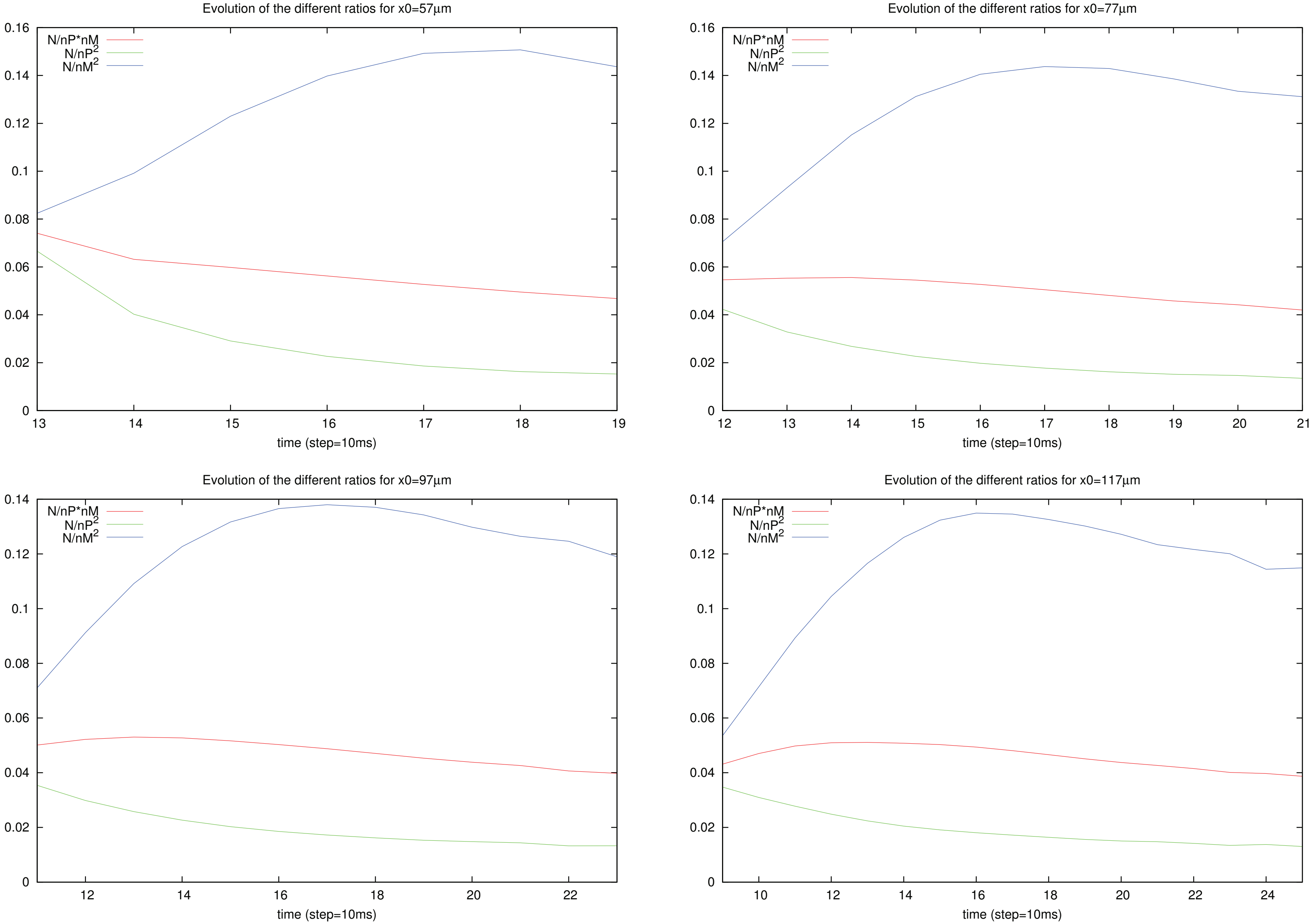

Figure A.12: The evolution of the different ratios studied in Section 3.3.2 when x_0 varies.

Appendix B

Step potential eigenstates

Here we report the spectrum of the non-interacting single particle Hamiltonian

$$h = -\frac{\hbar^2}{2m}\frac{d^2}{dx^2} + V(x) \tag{B.1}$$

with $V(x) = \frac{\hbar^2 Q^2}{2m}\Theta(x)$. The eigenvalues are written in the free particle form $\epsilon_k = \frac{\hbar^2 k^2}{2m}$ while the corresponding wave-functions acquire different forms for $0 < k \leq Q$ or $|k| > Q$:

i) $0 < k \leq Q$. In this regime the spectrum is non degenerate and the eigenfunctions have the form

$$\phi_k(x) = \begin{cases} \frac{1}{\sqrt{2\pi}}\left[e^{ikx} + R_k\, e^{-ikx}\right] & \text{for } x < 0 \\ \frac{1}{\sqrt{2\pi}}\, T_k\, e^{-\lambda_k x} & \text{for } x > 0 \end{cases}, \tag{B.2}$$

where $\lambda_k = \sqrt{Q^2 - k^2}$ and the reflection and transmission coefficients are

$$R_k = \frac{k - i\lambda_k}{k + i\lambda_k}\,, \qquad T_k = \frac{2k}{k + i\lambda_k}\,. \tag{B.3}$$

These states are exponentially trapped in the region $x < 0$. Note that the eigenfunctions $\phi_k(x)$ for $-Q \leq k \leq 0$ are not defined.

ii) $|k| > Q$. Here the spectrum is doubly degenerate. The right moving wave for $k > Q$ is

$$\phi_k(x) = \begin{cases} \frac{1}{\sqrt{2\pi}}\left[e^{ikx} + R_k\, e^{-ikx}\right] & \text{for } x < 0 \\ \frac{1}{\sqrt{2\pi}}\, T_k\, e^{iqx} & \text{for } x > 0 \end{cases}, \tag{B.4}$$

and the left moving wave for $k < -Q$ is

$$\phi_k(x) = \begin{cases} \sqrt{\frac{|k|}{2\pi q}}\, T_k\, e^{ikx} & \text{for } x < 0 \\ \sqrt{\frac{|k|}{2\pi q}}\, [e^{-iqx} + R_k\, e^{iqx}] & \text{for } x > 0 \end{cases}, \tag{B.5}$$

where $q = \sqrt{k^2 - Q^2}$ and the reflection and transmission coefficients are

$$R_k = \frac{k-q}{k+q} \qquad T_k = \frac{2k}{k+q}\,, \tag{B.6}$$

for the right moving and

$$R_k = -\frac{k+q}{k-q} \qquad T_k = -\frac{2q}{k-q} \tag{B.7}$$

for the left moving. The normalization condition between any pair of wave functions reads, as usual

$$\int_{-\infty}^{\infty} dx\, \phi_k(x)^* \phi_{k'}(x) = \delta(k-k')\,. \tag{B.8}$$

The solutions (B.2), (B.4) and (B.5) are easily obtained by solving the stationary Schrödinger equation with the Hamiltonian (B.1) and then imposing the suitable boundary conditions for the scattering coefficients and asymptotic conditions for the normalization of the eigenstates.

Appendix C

Exact results for a potential barrier

Exact results for the barrier (4.11) can be obtained starting from (4.12) and using that

$$|\Gamma(1+ik)|^2 = \frac{k\pi}{\sinh k\pi}\,, \tag{C.1}$$

$$|\Gamma(\tfrac{1}{2}+ik)|^2 = \frac{\pi}{\cosh k\pi}\,, \tag{C.2}$$

as well as the asymptotic expression

$$F(a,b;c;z) \sim \frac{\Gamma(c)\Gamma(c-a-b)}{\Gamma(c-a)\Gamma(c-b)} + \frac{\Gamma(c)\Gamma(a+b-c)}{\Gamma(a)\Gamma(b)}(1-z)^{c-a-b}\,, \tag{C.3}$$

when $z \to 1$ (since in our case $\mathrm{Re}(c-a-b)=0$). These allow to find exact expressions for the asymptotic density $\rho(x)$ when $x \to \pm\infty$:

$$\begin{aligned}\rho_+ = \frac{k_F}{\pi} + \frac{\alpha}{4\pi^2}\Bigg[&\frac{1+\coth\frac{2\pi Q}{\alpha}}{\sinh\frac{2\pi Q}{\alpha}}\log\frac{\frac{\pi}{\alpha}(Q+k_F+k_0)}{\frac{\pi}{\alpha}(Q-k_F-k_0)}\\ &+\coth\frac{\pi Q}{\alpha}\log\frac{\frac{\pi}{\alpha}(Q-k_F+k_0)}{\frac{\pi}{\alpha}(Q+k_F-k_0)}\Bigg]\,,\end{aligned} \tag{C.4}$$

$$\begin{aligned}\rho_- = \frac{k_F}{\pi} + \frac{\alpha}{4\pi^2}\Bigg[&\frac{1+\coth\frac{2\pi Q}{\alpha}}{\sinh\frac{2\pi Q}{\alpha}}\log\frac{\frac{\pi}{\alpha}(Q+k_F-k_0)}{\frac{\pi}{\alpha}(Q-k_F+k_0)}\\ &+\coth\frac{\pi Q}{\alpha}\log\frac{\frac{\pi}{\alpha}(Q-k_F-k_0)}{\frac{\pi}{\alpha}(Q+k_F+k_0)}\Bigg]\,.\end{aligned} \tag{C.5}$$

Appendix D

The density profile for a potential barrier

According to the exact form (4.12) of the scattering states for a barrier of the form (4.11), the Hypergeometric function $F(a,b;c;\zeta)$ has to be evaluated for arguments (a,b,c) whose imaginary part grows large as $\alpha \to 0$. Here we derive the appropriate asymptotic limit of the Hypergeometric function. First we use the identity (see Ref. [184], Eq. 15.3.3)

$$F(a,b;c;\zeta) = (1-\zeta)^{c-a-b} F(c-a, c-b; c; \zeta)\,. \tag{D.1}$$

Then we note that, in the case of interest (4.12), the variable z is real and the parameters are related by $2c-a-b=1$. Therefore, we can express the Hypergeometric function in terms of Legendre functions by (see Ref. [184] Eq. 15.4.17)

$$F(a,b;c;\zeta) = \Gamma(c)\ \left[\zeta(1-\zeta)\right]^{\frac{1-c}{2}}\ P^{1-c}_{a-c}(1-2\zeta)\,. \tag{D.2}$$

Finally, recalling that $\zeta = \frac{1-\tanh(\alpha x)}{2}$ belongs to the interval $(0,1)$, we use the integral representation (see Ref. [196] Eq. 8.714-2) to obtain

$$F(a,b;c;\zeta) = \frac{\Gamma(a+b)}{\Gamma(a)\Gamma(b)} \int_0^\infty dt\, \frac{t^{a-1}}{\left[1+2(1-2\zeta)t+t^2\right]^{c-\frac{1}{2}}}\,. \tag{D.3}$$

Inserting the expressions for $a = \frac{1}{2} - i\frac{k+Q}{\alpha}$ and $b = \frac{1}{2} - i\frac{k-Q}{\alpha}$, the integral can be written as

$$\int_0^\infty dt \frac{e^{i\frac{\varphi(t)}{\alpha}}}{\sqrt{t\left[1+2(1-2\zeta)t+t^2\right]}}\,, \tag{D.4}$$

with

$$\varphi(t) = -(k+Q)\,\log t + k\,\log\left[1+2(1-2\zeta)t+t^2\right]\,. \tag{D.5}$$

These expressions hold for any value of α. However, in the $\alpha \to 0$ limit they considerably simplify because the integral can be explicitly evaluated by use of the stationary phase method. Looking for the extrema of $\varphi(t)$ with $t > 0$, we have to consider two distinct regimes

- If $k > Q$, the unique extremum is given by
$$t_- = \frac{-Q\,\tanh(\alpha x) - \Delta}{Q-k}\,. \tag{D.6}$$
- Instead, if $k < Q$, two solutions exist for $Q\,\tanh(\alpha x) < -\sqrt{Q^2-k^2}$
$$t_\pm = \frac{-Q\,\tanh(\alpha x) \pm \Delta}{Q-k}\,, \tag{D.7}$$
while no extremum is present for $Q\,\tanh(\alpha x) > -\sqrt{Q^2-k^2}$.

In both cases,
$$\Delta = \sqrt{Q^2(\tanh(\alpha x))^2 + k^2 - Q^2}\,. \tag{D.8}$$
The second derivative of the phase, evaluated at the extremum, is given by
$$\varphi''(t_\pm) = \frac{k^2-Q^2}{kt_\pm^2}\frac{\Delta}{\Delta \mp k\,\tanh(\alpha x)}\,. \tag{D.9}$$
Therefore, each extremum (if any) contributes to the integral with a term
$$\sqrt{\frac{\alpha\pi}{\Delta}}\,e^{i\frac{\varphi(t_\pm)}{\alpha}}\,e^{\mp i\frac{\pi}{4}}\,. \tag{D.10}$$
The scattering states (4.12) then acquire an analytic form in the $\alpha \to 0$ limit. By use of the Stirling formula for the asymptotic behaviour of the Γ function, we finally obtain
$$\phi_k(x) = \sqrt{\frac{k}{2\pi\Delta}}\,[\zeta\,(1-\zeta)]^{-i\frac{k}{2\alpha}}\left\{e^{i\frac{\varphi_-}{\alpha}} - ie^{i\frac{\varphi_+}{\alpha}}\right\}\,, \tag{D.11}$$
where we used the shorthand notation $\varphi(t_\pm) = \varphi_\pm$. The second term in curly brackets is present only for $k < Q$ and $Q\,\tanh(\alpha x) < -\sqrt{Q^2-k^2}$, while for $k < Q$ and $Q\,\tanh(\alpha x) > -\sqrt{Q^2-k^2}$, the wave function vanishes to leading order in α. This result has been derived for $k > 0$. The analogous expression for $k < 0$ is simply obtained by changing $k \to |k|$ and $x \to -x$ (or $\zeta \to 1-\zeta$).

As $\alpha \to 0$, the square modulus of the scattering wave function just reduces to
$$|\phi_k(x)|^2 = \frac{1}{2\pi}\frac{k}{\sqrt{Q^2[\tanh(\alpha x)]^2 + k^2 - Q^2}}\,, \tag{D.12}$$
for $k > Q$, while for $k < Q$ and $Q\,\tanh(\alpha x) < -\sqrt{Q^2-k^2}$ an oscillatory term still survives
$$|\phi_k(x)|^2 = \frac{1}{\pi}\frac{k}{\sqrt{Q^2[\tanh(\alpha x)]^2 + k^2 - Q^2}}\left[1 + \sin\frac{\varphi_+ - \varphi_-}{\alpha}\right]\,. \tag{D.13}$$
These rapid oscillations in the single particle scattering wave function are however washed out when we perform the integration over the wave vectors k required to evaluate the averages in the Fermi gas (2.82).

Bibliography

[1] D. Leary. *Metaphors in the History of Psychology.* Cambridge Studies in the History of Psychology. Cambridge University Press (1994).

[2] J. Mill. *A System of Logic, Ratiocinative and Inductive.* Harper & brothers (1858).

[3] G. Polya. *Mathematics and Plausible Reasoning: Induction and analogy in mathematics.* Induction and Analogy in Mathematics. Princeton University Press (1990).

[4] F. Hallyn. *Metaphor and Analogy in the Sciences.* Origins (Dordrecht, Netherlands). Springer Netherlands (2000).

[5] M. Gorman. *Transforming Nature: Ethics, Invention and Discovery.* Springer US (2012).

[6] W. Rindler. *Essential relativity: special, general, and cosmological.* Texts and monographs in physics. Van Nostrand Reinhold Co. (1969).

[7] L. Landau. *The Classical Theory of Fields.* COURSE OF THEORETICAL PHYSICS. Elsevier Science (2013).

[8] J. C. Maxwell. *On Faraday's Lines of Force*, volume 1 of *Cambridge Library Collection - Physical Sciences.* Cambridge University Press (2011).

[9] L. Heng. *Gauge Theory Of Weak And Electromagnetic Interactions.* World Scientific Publishing Company (1981).

[10] D. Gentner. *Analogy in scientific discovery: The case of Johannes Kepler.* Kluwer Academic / Plenum Publishers (2002).

[11] S. Chandrasekhar. *Newton's Principia for the Common Reader.* Clarendon Press (1995).

[12] S. W. Hawking and G. F. R. Ellis. *The Large Scale Structure of Space-Time.* Cambridge Monographs on Mathematical Physics. Cambridge University Press (1973).

[13] S. Schaffer. *John Michell and Black Holes.* Journal for the History of Astronomy **10** (1979)(1), 42–43.

[14] J. R. Oppenheimer and H. Snyder. *On Continued Gravitational Contraction.* Phys. Rev. **56** (1939), 455–459.

[15] J. D. Bekenstein. *Black Holes and Entropy.* Phys. Rev. D **7** (1973), 2333–2346.

[16] J. D. Bekenstein. *Generalized second law of thermodynamics in black-hole physics.* Phys. Rev. D **9** (1974), 3292–3300.

[17] R. Ruffini and J. A. Wheeler. *Introducing the black hole.* Physics Today **24** (1971), 30.

[18] S. W. Hawking. *Black hole explosions.* Nature **248** (1974), 30–31.

[19] S. W. Hawking. *Particle creation by black holes.* Comm. Math. Phys. **43** (1975)(3), 199–220.

[20] J. D. Bekenstein. *Black-hole thermodynamics.* Physics Today **33** (1980), 24–31.

[21] S. W. Hawking. *Black holes and thermodynamics.* Phys. Rev. D **13** (1976), 191–197.

[22] J. B. Hartle and S. W. Hawking. *Path-integral derivation of black-hole radiance.* Phys. Rev. D **13** (1976), 2188–2203.

[23] W. G. Unruh. *Notes on black-hole evaporation.* Phys. Rev. D **14** (1976), 870–892.

[24] T. Damour and R. Ruffini. *Black-hole evaporation in the Klein-Sauter-Heisenberg-Euler formalism.* Phys. Rev. D **14** (1976), 332–334.

[25] N. Sanchez. *Absorption and emission spectra of a Schwarzschild black hole.* Phys. Rev. D **18** (1978), 1030–1036.

[26] K. Fredenhagen and R. Haag. *On the derivation of Hawking radiation associated with the formation of a black hole.* Communications in Mathematical Physics **127** (1990)(2), 273–284.

[27] M. K. Parikh and F. Wilczek. *Hawking Radiation As Tunneling.* Phys. Rev. Lett. **85** (2000), 5042–5045.

[28] L. Susskind. *The Black Hole War: My Battle with Stephen Hawking to Make the World Safe for Quantum Mechanics.* Little, Brown (2008).

[29] A. D. Helfer. *Do black holes radiate?* Reports on Progress in Physics **66** (2003)(6), 943.

[30] G. ’t Hooft. *On the quantum structure of a black hole.* Nuclear Physics B **256** (1985), 727 – 745.

[31] T. Jacobson. *Introductory lectures on black hole thermodynamics* .

[32] P.-H. Lambert. *Introduction to Black Hole Evaporation.* PoS **Modave2013** (2013), 001.

[33] K. Schwarzschild. *On the Gravitational Field of a Mass Point According to Einstein's Theory.* Abh. Konigl. Preuss. Akad. Wissenschaften Jahre 1906,92, Berlin,1907 (1916).

[34] C. Misner, K. Thorne, and J. Wheeler. *Gravitation.* Number pt. 3 in Gravitation. W. H. Freeman (1973).

[35] W. Kaufmann. *The Cosmic Frontiers of General Relativity.* Peregrine books. Penguin (1979).

[36] D. J. Griffiths and D. F. Schroeter. *Introduction to Quantum Mechanics.* 3 edition. Cambridge University Press (2018).

[37] N. Birrell, N. Birrell, and P. Davies. *Quantum Fields in Curved Space.* Cambridge Monographs on Mathematical Physics. Cambridge University Press (1984).

[38] F. D. Belgiorno, S. L. Cacciatori, and D. Faccio. *Hawking Radiation.* WORLD SCIENTIFIC (2018).

[39] N. N. Bogoliubov. *On a new method in the theory of superconductivity.* Il Nuovo Cimento (1955-1965) **7** (1958)(6).

[40] J. G. Valatin. *Comments on the theory of superconductivity.* Il Nuovo Cimento (1955-1965) **7** (1958)(6), 843–857.

[41] R. Adler, M. Bazin, and M. Schiffer. *Introduction to general relativity.* International series in pure and applied physics. McGraw-Hill (1965).

[42] R. P. Kerr. *Gravitational Field of a Spinning Mass as an Example of Algebraically Special Metrics.* Phys. Rev. Lett. **11** (1963), 237–238.

[43] L. Ryder. *Introduction to General Relativity.* Cambridge University Press (2009).

[44] P. Fré, V. Gorini, G. Magli, and U. Moschella. *Classical and Quantum Black Holes.* Series in High Energy Physics, Cosmology and Gravitation. Taylor & Francis (1999).

[45] D. N. Page. *Particle emission rates from a black hole: Massless particles from an uncharged, nonrotating hole.* Phys. Rev. D **13** (1976), 198–206.

[46] S. Dimopoulos and G. Landsberg. *Black Holes at the Large Hadron Collider.* Phys. Rev. Lett. **87** (2001), 161602.

[47] W. G. Unruh. *Has Hawking Radiation Been Measured?* Foundations of Physics **44** (2014)(5), 532–545.

[48] S. A. Fulling. *Nonuniqueness of Canonical Field Quantization in Riemannian Space-Time.* Phys. Rev. D **7** (1973), 2850–2862.

[49] P. C. W. Davies. *Scalar production in Schwarzschild and Rindler metrics.* Journal of Physics A: Mathematical and General **8** (1975)(4), 609.

[50] W. Gordon. *Zur Lichtfortpflanzung nach der Relativitätstheorie.* Annalen der Physik **377**(22), 421–456.

[51] D. Peregrine. *Interaction of Water Waves and Currents.* volume 16 of *Advances in Applied Mechanics.* Elsevier (1976), pp. 9 – 117.

[52] W. G. Unruh. *Experimental Black-Hole Evaporation?* Phys. Rev. Lett. **46** (1981), 1351–1353.

[53] L. Landau and E. Lifshits. *Fluid Mechanics, by L.D. Landau and E.M. Lifshitz.* Teoreticheskaia fizika. Pergamon Press (1959).

[54] T. G. Philbin, C. Kuklewicz, S. Robertson, S. Hill, F. König, and U. Leonhardt. *Fiber-Optical Analog of the Event Horizon.* Science **319** (2008)(5868), 1367–1370.

[55] F. Belgiorno, S. L. Cacciatori, M. Clerici, V. Gorini, G. Ortenzi, L. Rizzi, E. Rubino, V. G. Sala, and D. Faccio. *Hawking radiation from ultrashort laser pulse filaments.* Phys. Rev. Lett. **105** (2010), 203901.

[56] S. Finazzi and I. Carusotto. *Spontaneous quantum emission from analog white holes in a nonlinear optical medium.* Phys. Rev. A **89** (2014), 053807.

[57] I. Carusotto and C. Ciuti. *Quantum fluids of light.* Rev. Mod. Phys. **85** (2013), 299–366.

[58] D. Gerace and I. Carusotto. *Analog Hawking radiation from an acoustic black hole in a flowing polariton superfluid.* Phys. Rev. B **86** (2012), 144505.

[59] H. S. Nguyen, D. Gerace, I. Carusotto, D. Sanvitto, E. Galopin, A. Lemaître, I. Sagnes, J. Bloch, and A. Amo. *Acoustic Black Hole in a Stationary Hydrodynamic Flow of Microcavity Polaritons.* Phys. Rev. Lett. **114** (2015), 036402.

[60] M. Elazar, V. Fleurov, and S. Bar-Ad. *All-optical event horizon in an optical analog of a Laval nozzle.* Phys. Rev. A **86** (2012), 063821.

[61] I. Carusotto. *Superfluid light in bulk nonlinear media.* Proceedings of the Royal Society of London A **470** (2014)(2169).

[62] L. J. Garay, J. R. Anglin, J. I. Cirac, and P. Zoller. *Sonic Analog of Gravitational Black Holes in Bose-Einstein Condensates.* Phys. Rev. Lett. **85** (2000), 4643–4647.

[63] I. Carusotto, S. Fagnocchi, A. Recati, R. Balbinot, and A. Fabbri. *Numerical observation of Hawking radiation from acoustic black holes in atomic Bose-Einstein condensates.* New J. Phys. **10** (2008)(10), 103001.

[64] O. Lahav, A. Itah, A. Blumkin, C. Gordon, S. Rinott, A. Zayats, and J. Steinhauer. *Realization of a Sonic Black Hole Analog in a Bose-Einstein Condensate.* Phys. Rev. Lett. **105** (2010), 240401.

[65] J. Steinhauer. *Observation of self-amplifying Hawking radiation in an analogue black-hole laser.* Nature Physics **10** (2014), 864–869.

[66] J. Steinhauer. *Observation of quantum Hawking radiation and its entanglement in an analogue black hole.* Nature Phys. **12** (2016), 959.

[67] S. Giovanazzi. *Hawking Radiation in Sonic Black Holes.* Phys. Rev. Lett. **94** (2005), 061302.

[68] S. Giovanazzi. *The sonic analogue of black hole radiation.* Journal of Physics B: Atomic, Molecular and Optical Physics **39** (2006)(10), S109.

[69] A. Parola, M. Tettamanti, and S. L. Cacciatori. *Analogue Hawking radiation in an exactly solvable model of BEC.* EPL (Europhysics Letters) **119** (2017)(5), 50002.

[70] S. Weinfurtner, E. W. Tedford, M. C. Penrice, W. G. Unruh, and G. A. Lawrence. *Measurement of stimulated Hawking emission in an analogue system.* Phys. Rev. Lett. **106** (2011)(2), 021302.

[71] F. Michel and R. Parentani. *Probing the thermal character of analogue Hawking radiation for shallow water waves?* Phys. Rev. D **90** (2014), 044033.

[72] L.-P. Euvé, F. Michel, R. Parentani, and G. Rousseaux. *Wave blocking and partial transmission in subcritical flows over an obstacle.* Phys. Rev. D **91** (2015), 024020.

[73] T. Torres, S. Patrick, A. Coutant, M. Richartz, E. W. Tedford, and S. Weinfurtner. *Observation of superradiance in a vortex flow.* Nature Phys. **13** (2017), 833–836.

[74] L.-P. Euvé, S. Robertson, N. James, A. Fabbri, and G. Rousseaux. *Scattering of surface waves on an analogue black hole* (2018).

[75] C. Barcelo, S. Liberati, and M. Visser. *Analogue gravity.* Living Rev. Rel. **8** (2005), 12.

[76] T. Jacobson. *Black-hole evaporation and ultrashort distances.* Phys. Rev. D **44** (1991), 1731–1739.

[77] W. G. Unruh. *Sonic analogue of black holes and the effects of high frequencies on black hole evaporation.* Phys. Rev. D **51** (1995), 2827–2838.

[78] S. Corley and T. Jacobson. *Hawking spectrum and high frequency dispersion.* Phys. Rev. D **54** (1996), 1568–1586.

[79] S. J. Robertson. *The theory of Hawking radiation in laboratory analogues.* J. Phys. B.: At. Mol. Opt. Phys. **45** (2012), 136001.

[80] A. Coutant. *On the phenomenology of quantum gravity : stability properties of Hawking radiation in the presence of ultraviolet violation of local Lorentz invariance.* Ph.D. thesis, Orsay, LPT (2012).

[81] G. Rousseaux, P. Maïssa, C. Mathis, P. Coullet, T. G. Philbin, and U. Leonhardt. *Horizon effects with surface waves on moving water.* New Journal of Physics **12** (2010)(9), 095018.

[82] T. Jacobson. *On the origin of the outgoing black hole modes.* Phys. Rev. D **53** (1996), 7082–7088.

[83] R. Parentani. *Quantum metric fluctuations and Hawking radiation.* Phys. Rev. D **63** (2001), 041503.

[84] R. Brout, S. Massar, R. Parentani, and P. Spindel. *Hawking radiation without trans-Planckian frequencies.* Phys. Rev. D **52** (1995), 4559–4568.

[85] M. Visser. *Hawking Radiation without Black Hole Entropy.* Phys. Rev. Lett. **80** (1998), 3436–3439.

[86] W. G. Unruh. *Origin of the particles in black-hole evaporation.* Phys. Rev. D **15** (1977), 365–369.

[87] R. Schützhold and W. G. Unruh. *Origin of the particles in black hole evaporation.* Phys. Rev. D **78** (2008), 041504.

[88] G. Rousseaux, C. Mathis, P. Maïssa, T. G. Philbin, and U. Leonhardt. *Observation of negative-frequency waves in a water tank: a classical analogue to the Hawking effect?* New Journal of Physics **10** (2008)(5), 053015.

[89] L.-P. Euvé, F. Michel, R. Parentani, T. G. Philbin, and G. Rousseaux. *Observation of Noise Correlated by the Hawking Effect in a Water Tank.* Phys. Rev. Lett. **117** (2016), 121301.

[90] R. Schützhold and W. G. Unruh. *Comment on "Hawking Radiation from Ultrashort Laser Pulse Filaments".* Phys. Rev. Lett. **107** (2011), 149401.

[91] F. Belgiorno, S. L. Cacciatori, M. Clerici, V. Gorini, G. Ortenzi, L. Rizzi, E. Rubino, V. G. Sala, and D. Faccio. *Belgiorno et al. Reply:.* Phys. Rev. Lett. **107** (2011), 149402.

[92] M. Tettamanti, S. L. Cacciatori, A. Parola, and I. Carusotto. *Numerical study of a recent black-hole lasing experiment.* EPL (Europhysics Letters) **114** (2016)(6), 60011.

[93] Y.-H. Wang, T. Jacobson, M. Edwards, and C. W. Clark. *Mechanism of stimulated Hawking radiation in a laboratory Bose-Einstein condensate.* Phys. Rev. A **96** (2017), 023616.

[94] Y.-H. Wang, T. Jacobson, M. Edwards, and C. W. Clark. *Induced density correlations in a sonic black hole condensate.* SciPost Phys. **3** (2017), 022.

[95] U. Leonhardt. *Questioning the Recent Observation of Quantum Hawking Radiation.* Annalen der Physik **530**(5), 1700114.

[96] J. R. M. de Nova, K. Golubkov, V. I. Kolobov, and J. Steinhauer. *Observation of thermal Hawking radiation at the Hawking temperature in an analogue black hole* (2018).

[97] J. Drori, Y. Rosenberg, D. Bermudez, Y. Silberberg, and U. Leonhardt. *Observation of Stimulated Hawking Radiation in an Optical Analogue.* Phys. Rev. Lett. **122** (2019), 010404.

[98] H. Lamb. *Hydrodynamics.* Dover Books on Physics. Dover publications (1945).

[99] M. Visser. *Acoustic propagation in fluids: An Unexpected example of Lorentzian geometry* (1993).

[100] R. W. White. *Acoustic ray tracing in moving inhomogeneous fluids.* The Journal of the Acoustical Society of America **53** (1973)(6), 1700–1704.

[101] J. L. Anderson and E. A. Spiegel. *Radiative transfer through a flowing refractive medium.* Astrophysical Journal **202** (1975), 454–464.

[102] V. Moncrief. *Stability of stationary, spherical accretion onto a Schwarzschild black hole.* Astrophysical Journal **235** (1980), 1038–1046.

[103] M. Visser. *Essential and inessential features of Hawking radiation.* Int. J. Mod. Phys. **D12** (2003), 649–661.

[104] P. Painlevé. *Le Mécanique Classique et la Théorie de la Relativité.* L'Astronomie **36** (1922), 6–9.

[105] A. Gullstrand. *Allgemeine Lösung des statischen Einkörperproblems in der Einsteinschen Gravitationstheorie.* Mat. Astron. Fys. **16** (1922), 1–15.

[106] G. Lemaître. *L'Univers en expansion.* Annales de la Société Scientifique de Bruxelles **53** (1933).

[107] L. Susskind. *Black holes and the information paradox.* Scientific American (April issue) (1997).

[108] A. Cho. *Test of Hawking's Prediction on the Horizon With Mock 'White Hole'.* Science **319** (2008)(5868), 1321–1321.

[109] L. Pítajevskíj, L. S. Stringari, L. Pitaevskii, S. Stringari, S. Stringari, and O. U. Press. *Bose-Einstein Condensation.* Comparative Pathobiology - Studies in the Postmodern Theory of Education. Clarendon Press (2003).

[110] M. H. Anderson, J. R. Ensher, M. R. Matthews, C. E. Wieman, and E. A. Cornell. *Observation of Bose-Einstein Condensation in a Dilute Atomic Vapor.* Science **269** (1995)(5221), 198–201.

[111] K. B. Davis, M. O. Mewes, M. R. Andrews, N. J. van Druten, D. S. Durfee, D. M. Kurn, and W. Ketterle. *Bose-Einstein Condensation in a Gas of Sodium Atoms.* Phys. Rev. Lett. **75** (1995), 3969–3973.

[112] Bose. *Plancks Gesetz und Lichtquantenhypothese.* Zeitschrift fur Physik **26** (1924), 178–181.

[113] A. Einstein. *Quantentheorie des einatomigen idealen Gases.* Sitzungsberichte der Preussischen Akademie der Wissenschaften **1** (1925).

[114] J. F. Allen and A. D. Misener. *Flow Phenomena in Liquid Helium II.* Nature **142** (1938), 643–644.

[115] P. Kapitza. *Viscosity of Liquid Helium below the λ-Point.* Nature **141** (1938), 74.

[116] F. London. *On the Bose-Einstein Condensation.* Phys. Rev. **54** (1938), 947–954.

[117] L. Landau. *Theory of the Superfluidity of Helium II.* Phys. Rev. **60** (1941), 356–358.

[118] N. N. Bogoliubov. *On the theory of superfluidity.* J. Phys.(USSR) **11** (1947), 23–32. [Izv. Akad. Nauk Ser. Fiz.11,77(1947)].

[119] F. Dalfovo, S. Giorgini, L. P. Pitaevskii, and S. Stringari. *Theory of Bose-Einstein condensation in trapped gases.* Rev. Mod. Phys. **71** (1999), 463–512.

[120] C. C. Bradley, C. A. Sackett, J. J. Tollett, and R. G. Hulet. *Evidence of Bose-Einstein Condensation in an Atomic Gas with Attractive Interactions.* Phys. Rev. Lett. **75** (1995), 1687–1690.

[121] M. R. Andrews, M.-O. Mewes, N. J. van Druten, D. S. Durfee, D. M. Kurn, and W. Ketterle. *Direct, Nondestructive Observation of a Bose Condensate.* Science **273** (1996)(5271), 84–87.

[122] W. Pauli. *The Connection Between Spin and Statistics.* Physical Review **58** (1940), 716–722.

[123] E. Fermi. *Sulla quantizzazione del gas perfetto monoatomico. (Italian) [On the Quantization of the Ideal Monatomic Gas].* Rendiconti dell'Accademia Nazionale dei Lincei **3** (1926)(6), 145–149.

[124] *On the theory of quantum mechanics.* Proceedings of the Royal Society of London A: Mathematical, Physical and Engineering Sciences **112** (1926)(762), 661–677.

[125] E. P. Gross. *Structure of a quantized vortex in boson systems.* Il Nuovo Cimento (1955-1965) **20** (1961)(3), 454–477.

[126] E. P. Gross. *Hydrodynamics of a Superfluid Condensate.* Journal of Mathematical Physics **4** (1963)(2), 195–207.

[127] L. P. Pitaevskii. *Vortex lines in an imperfect Bose gas.* Sov. Phys. JETP **13** (1961)(3), 451–454.

[128] L. Salasnich, A. Parola, and L. Reatto. *Effective wave equations for the dynamics of cigar-shaped and disk-shaped Bose condensates.* Phys. Rev. A **65** (2002), 043614.

[129] C. J. Pethick and H. Smith. *Bose-Einstein Condensation in Dilute Gases.* Cambridge University Press (2008).

[130] D. C. Mattis. *The Many-Body Problem.* WORLD SCIENTIFIC (1993).

[131] E. H. Lieb and W. Liniger. *Exact Analysis of an Interacting Bose Gas. I. The General Solution and the Ground State.* Phys. Rev. **130** (1963), 1605–1616.

[132] E. H. Lieb. *Exact Analysis of an Interacting Bose Gas. II. The Excitation Spectrum.* Phys. Rev. **130** (1963), 1616–1624.

[133] D. Iyer and N. Andrei. *Quench Dynamics of the Interacting Bose Gas in One Dimension.* Phys. Rev. Lett. **109** (2012), 115304.

[134] D. Iyer, H. Guan, and N. Andrei. *Exact formalism for the quench dynamics of integrable models.* Phys. Rev. A **87** (2013), 053628.

[135] M. Girardeau. *Relationship between Systems of Impenetrable Bosons and Fermions in One Dimension.* Journal of Mathematical Physics **1** (1960)(6), 516–523.

[136] T. Kinoshita, T. Wenger, and D. S. Weiss. *Observation of a one-dimensional Tonks-Girardeau gas.* Science **305 5687** (2004), 1125–8.

[137] B. Paredes, A. Widera, V. Murg, O. Mandel, S. Fölling, I. Cirac, G. V. Shlyapnikov, T. W. Hänsch, and I. Bloch. *Tonks–Girardeau gas of ultracold atoms in an optical lattice.* Nature **429** (2004)(6989), 277.

[138] S. Blundell, S. Blundell, and K. Blundell. *Concepts in Thermal Physics.* OUP Oxford (2010).

[139] A. Fetter and J. Walecka. *Quantum Theory of Many-particle Systems.* Dover Books on Physics. Dover Publications (2003).

[140] L. J. Garay, J. R. Anglin, J. I. Cirac, and P. Zoller. *Sonic Analog of Gravitational Black Holes in Bose-Einstein Condensates.* Phys. Rev. Lett. **85** (2000), 4643–4647.

[141] M. Visser and S. Weinfurtner. *Analogue spacetimes: Toy models for "quantum gravity".* PoS **QG-PH** (2007), 042.

[142] C. Barcelo, A. Cano, L. J. Garay, and G. Jannes. *Quasi-normal mode analysis in BEC acoustic black holes.* Phys. Rev. **D75** (2007), 084024.

[143] W. G. Unruh and R. Schutzhold. *On the universality of the Hawking effect.* Phys. Rev. **D71** (2005), 024028.

[144] C. Barcelo, S. Liberati, and M. Visser. *Towards the observation of Hawking radiation in Bose-Einstein condensates.* Int. J. Mod. Phys. **A18** (2003), 3735.

[145] J. Macher and R. Parentani. *Black-hole radiation in Bose-Einstein condensates.* Phys. Rev. A **80** (2009)(4), 043601.

[146] S. J. Robertson. *Hawking Radiation in Dispersive Media.* Ph.D. thesis, St. Andrews U., Phys. Astron. (2011).

[147] J. Macher and R. Parentani. *Black/white hole radiation from dispersive theories.* Phys. Rev. D **79** (2009), 124008.

[148] R. Balbinot and A. Fabbri. *Amplifying the Hawking signal in BECs.* Adv. High Energy Phys. **2014** (2014), 713574.

[149] I. Carusotto, S. Fagnocchi, A. Recati, R. Balbinot, and A. Fabbri. *Numerical observation of Hawking radiation from acoustic black holes in atomic Bose-Einstein condensates.* New Journal of Physics **10** (2008)(10), 103001.

[150] R. Balbinot, A. Fabbri, S. Fagnocchi, A. Recati, and I. Carusotto. *Nonlocal density correlations as a signature of Hawking radiation from acoustic black holes.* Phys. Rev. A **78** (2008), 021603.

[151] A. Fabbri. *Observing Hawking radiation in Bose-Einstein condensates via correlation measurements.* Nuovo Cim. **C036** (2013)(04), 99–108.

[152] C. Mayoral. *Correlation Functions for Black Holes and White Holes in Bose-Einstein Condensates.* Ph.D. thesis, Universitat de València (2011).

[153] A. Vilenkin. *Exponential amplification of waves in the gravitational field of ultrarelativistic rotating body.* Physics Letters B **78** (1978), 301–303.

[154] S. Corley and T. Jacobson. *Black hole lasers.* Phys. Rev. **D59** (1999), 124011.

[155] A. Coutant and R. Parentani. *Black hole lasers, a mode analysis.* Phys. Rev. **D81** (2010), 084042.

[156] S. Finazzi and R. Parentani. *Black hole lasers in Bose-Einstein condensates.* New Journal of Physics **12** (2010)(9), 095015.

[157] S. Finazzi, F. Piazza, M. Abad, A. Smerzi, and A. Recati. *Instability of the Superfluid Flow as Black-Hole Lasing Effect.* Physical Review Letters **114** (2015)(24), 245301.

[158] D. Bermudez and U. Leonhardt. *Resonant Hawking radiation as an instability* (2018).

[159] F. Michel and R. Parentani. *Saturation of black hole lasers in Bose-Einstein condensates.* Phys. Rev. **D88** (2013), 125012.

[160] J. R. M. de Nova, S. Finazzi, and I. Carusotto. *Time-dependent study of a black-hole laser in a flowing atomic condensate.* Phys. Rev. **A94** (2016), 043616.

[161] S. Finazzi. *Analogue gravitational phenomena in Bose-Einstein condensates.* Ph.D. thesis, SISSA, Trieste (2011).

[162] J. Steinhauer and J. R. M. de Nova. *Self-amplifying Hawking radiation and its background: a numerical study.* Phys. Rev. **A95** (2017)(3), 033604.

[163] J. Steinhauer. *Comment on "Questioning the Recent Observation of Quantum Hawking Radiation" [Ann. Phys. (Berlin) 2018, 530, 1700114].* Annalen der Physik **530** (2018)(5), 1700459.

[164] I. Shammass, S. Rinott, A. Berkovitz, R. Schley, and J. Steinhauer. *Phonon Dispersion Relation of an Atomic Bose-Einstein Condensate.* Phys. Rev. Lett. **109** (2012), 195301.

[165] R. Schley, A. Berkovitz, S. Rinott, I. Shammass, A. Blumkin, and J. Steinhauer. *Planck Distribution of Phonons in a Bose-Einstein Condensate.* Phys. Rev. Lett. **111** (2013), 055301.

[166] C. Mayoral, A. Recati, A. Fabbri, R. Parentani, R. Balbinot, and I. Carusotto. *Acoustic white holes in flowing atomic Bose-Einstein condensates.* New J. Phys. **13** (2011), 025007.

[167] A. Coutant, A. Fabbri, R. Parentani, R. Balbinot, and P. R. Anderson. *Hawking radiation of massive modes and undulations.* Phys. Rev. D **86** (2012), 064022.

[168] W. Press, S. Teukolsky, W. Vetterling, and B. Flannery. *Numerical Recipes in Fortran 77: The Art of Scientific Computing, 933 pp* (1992).

[169] I. Carusotto, S. X. Hu, L. A. Collins, and A. Smerzi. *Bogoliubov-Čerenkov Radiation in a Bose-Einstein Condensate Flowing against an Obstacle.* Physical Review Letters **97** (2006)(26), 260403.

[170] A. Sinatra, C. Lobo, and Y. Castin. *The truncated Wigner method for Bose-condensed gases: limits of validity and applications.* Journal of Physics B: Atomic, Molecular and Optical Physics **35** (2002)(17), 3599.

[171] L. Isella and J. Ruostekoski. *Quantum dynamics in splitting a harmonically trapped Bose-Einstein condensate by an optical lattice: Truncated Wigner approximation.* Phys. Rev. A **74** (2006), 063625.

[172] S. Wüster, B. J. Dąbrowska-Wüster, A. S. Bradley, M. J. Davis, P. Blair Blakie, J. J. Hope, and C. M. Savage. *Quantum depletion of collapsing Bose-Einstein condensates.* Phys. Rev. A **75** (2007), 043611.

[173] J. Ruostekoski and A. D. Martin. *The Truncated Wigner Method for Bose Gases.* Imperial College Press (2013), pp. 203–214.

[174] Y.-H. Wang. *Pair creation and pair annihilation in Bose-Einstein condensates.* Ph.D. thesis, UMD (2017).

[175] G. El and M. Hoefer. *Dispersive shock waves and modulation theory.* Physica D: Nonlinear Phenomena **333** (2016), 11 – 65. Dispersive Hydrodynamics.

[176] T. Congy, G. El, M. Hoefer, and M. Shearer. *Nonlinear Schrödinger equations and the universal description of dispersive shock wave structure.* Studies in Applied Mathematics .

[177] R. Balbinot, I. Carusotto, A. Fabbri, C. Mayoral, and A. Recati. *Understanding Hawking radiation from simple models of atomic Bose-Einstein condensates.* Lect. Notes Phys. **870** (2013), 181–219.

[178] H. Liu, J.-T. Sun, H. Huang, F. Liu, and S. Meng. *Fermionic analogue of black hole radiation with a super high Hawking temperature.* ArXiv e-prints (2018).

[179] T. Kinoshita, T. Wenger, and D. S. Weiss. *Local Pair Correlations in One-Dimensional Bose Gases.* Phys. Rev. Lett. **95** (2005), 190406.

[180] E. Haller, M. Gustavsson, M. J. Mark, J. G. Danzl, R. Hart, G. Pupillo, and H.-C. Nägerl. *Realization of an Excited, Strongly Correlated Quantum Gas Phase.* Science **325** (2009)(5945), 1224–1227.

[181] J. Plemelj. *Problems In the Sense of Riemann and Klein.* New York: Interscience Publishers (1964).

[182] P. Engels and C. Atherton. *Stationary and Nonstationary Fluid Flow of a Bose-Einstein Condensate Through a Penetrable Barrier.* Phys. Rev. Lett. **99** (2007), 160405.

[183] L. Landau and E. Lifshitz. *Quantum Mechanics: Non-Relativistic Theory.* Course of Theoretical Physics. Elsevier Science (1981).

[184] M. Abramowitz and I. A. Stegun. *Handbook of mathematical functions: with formulas, graphs, and mathematical tables.* New York: Dover Publications (1970).

[185] F. Michel and R. Parentani. *Nonlinear effects in time-dependent transonic flows: An analysis of analog black hole stability.* Phys. Rev. A **91** (2015), 053603.

[186] F. Michel, R. Parentani, and R. Zegers. *No-hair theorems for analogue black holes.* Phys. Rev. D **93** (2016), 065039.

[187] P. Nozieres and D. Pines. *Theory Of Quantum Liquids.* Advanced Books Classics. Avalon Publishing (1999).

[188] C. Menotti and S. Stringari. *Collective oscillations of a one-dimensional trapped Bose-Einstein gas.* Phys. Rev. A **66** (2002), 043610.

[189] V. Gorini and A. Frigerio. *Fundamental Aspects of Quantum Theory,* volume 144. NATO ASI Series, Series B: Physics (1986).

[190] J. R. M. de Nova. *Non-linear stationary solutions in realistic models for analog black-hole lasers.* Universe **3** (2017)(3), 54.

[191] X. Busch. *Dispersive and dissipative effects in quantum field theory in curved space-time to model condensed matter systems.* Ph.D. thesis, Orsay, LPT (2014).

[192] J.-C. Jaskula, G. B. Partridge, M. Bonneau, R. Lopes, J. Ruaudel, D. Boiron, and C. I. Westbrook. *Acoustic Analog to the Dynamical Casimir Effect in a Bose-Einstein Condensate.* Phys. Rev. Lett. **109** (2012), 220401.

[193] M. C. Diamantini, C. A. Trugenberger, and V. M. Vinokur. *Confinement and Asymptotic Freedom with Cooper pairs* (2018).

[194] J. Khoury. *A Dark Matter Superfluid.* In *Proceedings, 50th Rencontres de Moriond Gravitation : 100 years after GR: La Thuile, Italy, March 21-28, 2015* (2015), pp. 35–42.

[195] S. Eckel, A. Kumar, T. Jacobson, I. B. Spielman, and G. K. Campbell. *A Rapidly Expanding Bose-Einstein Condensate: An Expanding Universe in the Lab.* Phys. Rev. X **8** (2018), 021021.

[196] I. Gradshteyn and I. Ryzhik. *Table of Integrals, Series, and Products.* Elsevier Science (2014).